On the Excited States Formed During Interfacial Charge Transfer and Recombination in Organic Bulk Heterojunction Photovoltaic Devices

Dana B. Sulas

A dissertation

submitted in partial fulfillment of the

requirements for the degree of

Doctor of Philosophy

University of Washington

2017

Reading Committee:

Cody W. Schlenker, Chair

Alshakim Nelson

Munira Khalil

Program Authorized to Offer Degree:

Chemistry

University of Washington

Abstract

On the Excited States Formed During Interfacial Charge Transfer and Recombination in Organic Bulk Heterojunction Photovoltaic Devices

Dana B. Sulas

Chair of the Supervisory Committee:
Cody W. Schlenker
Department of Chemistry

The optimization and implementation of organic photovoltaic (OPV) devices as low-cost and highly modular power sources are complicated by the intricacies of materials design and processing. Small variations in molecular structure and packing can lead to drastic changes in the photophysical pathways that enable or detract from optical-to-electrical energy conversion. This thesis outlines progress in understanding functional OPV device operation by characterizing these photophysical pathways using optical spectroscopy. With both optical and electrical perturbations to the photovoltaic systems, we relate the spatial properties of organic semiconductors with their thermodynamic energy landscapes and the kinetic processes that mediate energy conversion. We probe interactions between electron-donating and electron-accepting molecules whose energy level offsets must overcome coulombic binding energies of excitonic states in the low dielectric media, driving separation of charge carriers to produce power through generation of photocurrent and photovoltage. We highlight the roles of energetics and kinetics, while further elucidating the influences of electronic coupling, spin character, excited-state density, and delocalization for optimizing interfacial charge transfer and lessening photovoltaic loss through recombination.

TABLE OF CONTENTS

LIST OF FIGURES

LIST OF TABLES

ACKNOWLEDGEMENTS

I thank my advisor, Prof. Cody Schlenker, for his support throughout my graduate studies and his dedicated contribution to all of the work presented in this thesis. I thank Prof. David Ginger for advising some of the work in this thesis. I am very grateful for the support of my committee members: Prof. Robert Synovec, Prof. Munira Khalil, Prof. Alshakim Nelson, and Prof. Peter Pauzauskie. I thank my lab mates, Emily Rabe, Katie Corp, Jarred Olson, Tim Pollock, Sarah Pristash, and Matt Rigsby for keeping the lab afloat and for their friendship that keeps me afloat. I am grateful for Prof. Alex Jen and his lab for creating the fascinating polymers that I have had the opportunity to study. Dr. Matthew Sfeir has been an important mentor for me and a wonderful role model for the person that I would like to become. The work that I have prepared for this thesis would not have been possible without the support of current and past graduate students. For enlightening conversations on science, reconstructive input on self-worth, and broadening my understanding of our place in this life, I thank: Adam Colbert, Micah Glaz, Matt Gliboff, Stephanie Hemmingston, Marie Clement, Sarah Vorpahl, Mark Ziffer, Chu-Chen Chueh, Chang-Zhi Li, Sae Byeok Jo, Phil Cox, Durmus Karatay, Liz Strein, Liam Bradshaw, and Lucas Flagg.

I also thank my closest friends and family whose love reminds me why we try hard in the first place. My parents, Dalia Suliene and Leonas Sulas, have endeavored more in life than I will ever know, and I thank them for always looking to the future. They have moved their lives to America, worked long hours, and built a bright future for me and my siblings. I thank my sisters, Diana and Daiva, and my brother, Linas, for growing with me and questioning everything I do out of both love and curiosity. Finally, I thank my partner in life and in love, Michael Kern, for seeing me as I am and opening me to who I can be.

DEDICATION

To Diana Sulas Thompson, whose life is intertwined with my every failure and success.

Chapter 1. AN OVERVIEW OF ORGANIC SOLAR CELLS AND THE PHOTOEXCITED STATES INVOLVED IN OPTICAL-TO-ELECTRICAL ENERGY CONVERSION

1.1 THESIS STATEMENT

This thesis describes progress toward understanding organic photovoltaic (OPV) device operation by characterizing the photophysical pathways that enable or detract from optical-to-electrical energy conversion. In Chapter 1, we discuss the importance of developing emergent photovoltaic technologies, and we provide background information on the photovoltaic process in organic solar cell materials. We outline the device configuration, electrical characteristics, and the various excited states formed following light absorption and charge generation. In particular, we highlight the significance of charge-transfer states that form at interfaces of electron-donating and electron-accepting molecules within an organic solar cell's light-absorbing active layer. We further study the essential roles that these interfacial states play in defining an organic photodiode's current-voltage characteristics in Chapter 2 – Chapter 4. We note that Chapter 1 provides an abbreviated overview of the physical properties of excited states directly relevant to the central discussion in this thesis, and we direct the interested reader to more in-depth texts for further details on semiconductor physics, molecular dynamics, and quantum chemistry.[1-4]

In Chapter 2, we use an analysis based on Marcus theory to characterize open-circuit voltage (V_{OC}) losses in OPV devices caused by changes in charge-transfer state energy, electronic coupling, and spatial density. We make structure-function correlations by studying a series of molecularly-related polymer electron donors blended with fullerene acceptors. We combine measurements of the devices' current-voltage characteristics with spectroscopic characterization of the charge-transfer states (including sub-gap photocurrent, electroluminescence, and time-

resolved charge-transfer state photoluminescence), allowing us to isolate values for charge-transfer state electronic coupling to the ground state and values for the density of charge-transfer states (N_{CT}). We show that these charge-transfer state properties explain V_{OC} losses that cannot be justified by changes in the charge-transfer state energy alone. We find values for N_{CT} that are surprisingly large (~ 4.5×10^{21} – 6.2×10^{22} cm^{-3}), and we correlate a significant increase in N_{CT} upon selenium substitution in the donor polymers with lower V_{OC} in bulk heterojunction devices. We show that the increase in N_{CT} upon selenium substitution is also consistent with increased nanoscale donor/acceptor mixing in these blends by characterizing the nanoscale morphology with transmission electron microscopy, selected area electron diffraction, and grazing incidence wide angle X-ray scattering. This chapter provides an important step toward understanding the spatial nature of charge-transfer states and their effect on the open-circuit voltages of polymer/fullerene solar cells.

In Chapter 3, we examine the role of charge-transfer states' spin character in mediating charge generation and photocurrent loss. Although the role of charge-transfer states is most often inferred by characterizing singlet charge-transfer state properties, we address the equilibrium – or lack thereof – between both singlet and triplet charge-transfer states. We investigate the voltage dependence of these interfacial singlet and triplet intermediate states using *operando* photoinduced absorption and photoluminescence spectroscopy on working photodiodes. Interestingly, we measure dissimilar voltage dependence for singlet and triplet charge-transfer state spectroscopic indicators, and we conclude that the singlet and triplet charge-transfer states mediate photocurrent to different extents and do not rapidly interconvert in the polymer/fullerene solar cells that we study. By processing the same donor/acceptor components under different solvent conditions, we highlight a morphology-dependent role of triplet charge-transfer states in mediating photocurrent.

This chapter gives important understanding of charge-transfer states' spin character and the prospects for harnessing the differing roles of singlet and triplet interfacial states for optimizing photocurrent extraction.

In Chapter 4, we use transient absorption spectroscopy, time-resolved photoluminescence, and device measurements to study the kinetic competition between charge separation and recombination to triplet states in small-molecule OPV blends. We find that increasing small-molecule aggregation in bulk heterojunction active layer configurations aids in sustaining the free charge population and inhibiting recombination to low-energy triplet excitons that do not contribute to photocurrent. While aggregation appears to decrease charge-transfer state recombination to triplets, we further highlight an additional thermodynamically-accessible energy-transfer pathway to populate triplet excitons, which would bypass charge-transfer state formation. Importantly, the energy-transfer pathway is kinetically outcompeted by charge transfer in the condensed blends employed in device applications. This chapter suggests new avenues for increasing photocurrent yields by employing excited-state delocalization over molecular aggregates and kinetically avoiding recombination to triplet states, despite the presence of multiple thermodynamically accessible pathways for photovoltaic loss to triplets.

Finally, in Chapter 5 we summarize the implications of our work. We provide an outlook for future investigations into the varying roles that interfacial charge-transfer states play in mediating the photocurrent and photovoltage responses of organic photodiodes, and we discuss the path toward optimization and wide-spread implementation of this promising technology.

1.2 MOTIVATION BEHIND THE DEVELOPMENT OF PHOTOVOLTAICS

The world's energy consumption in 2014 has reached an average power of approximately 12.5 TW, representing a continual increase of approximately 1 – 3 % per year since 2010.[5-9] This increase in worldwide energy consumption tracks with a healthy and growing global economy represented by increases in the aggregate gross domestic product (GDP) of 3 – 5 % per year since 2010.[10] In the past, air pollution by greenhouse gas emission (primarily CO_2) has followed the trends in GDP and energy production, where any significant decreases or stagnation in emission typically correlate with economic recession. Encouragingly, there has been a departure from this trend in recent years (2014 – 2016), where the global energy-related CO_2 emission has stood constant at 32.1 gigatons despite increasing GDP and energy production.[11-12] The recent stagnation in CO_2 emissions is in large part due to the decline of coal consumption (decreasing by 1.8 % in 2015), with increasing energy demand supplemented by rising use of cleaner energy sources such as natural gas and renewables.[11-12] This recent shift in the mix of energy-producing sources comes following concerted worldwide efforts encouraging cleaner activities with lower carbon footprints. The cooperative global intentions to reduce carbon emissions are reflected in various international promises such as the Paris Agreement adopted by 55 countries in 2015 along with explicit goals in 173 countries toward increasing the fraction of energy coming from renewables.[13-14]

Although the global focus on expanding renewable energy sources is extremely inspiring, the fraction of energy coming from photovoltaics still lags behind other energy sources, highlighting an opportunity for substantial decrease in CO_2 emissions and increased national energy independence if developing photovoltaic technologies can be optimized and deployed. While renewable sources now account for ~ 23.7 % of global electricity supply, this total is dominated by hydropower (16.4 %), wind power (3.5 %), and biomass (2.2 %), with a much

smaller contribution from photovoltaics (1.1 %).[11] Beyond the obvious benefit of being a clean and renewable energy source, photovoltaics provide additional advantages as they are highly customizable energy sources, ranging from single-device chargers to gigawatt solar farms, and their implementation has relatively low impact and dependence on geographical location and geological features. For these reasons, photovoltaics are one of the most practical energy sources for local power generation and consumption, with prospects of improving homeland energy security and providing direct benefits for local environment and local economy.[15]

Still an emerging photovoltaic technology, organic devices promise an additional range of applications and benefits along with the silicon photovoltaics that currently dominate the market. Silicon is a brittle material with an indirect band gap leading to weak absorption of incident sunlight. Organic semiconductors exhibit much stronger absorption coefficients, requiring 1000 times thinner active layers (only ~ 100 nm) to absorb appreciable sunlight. This enables deposition of organics on thin, flexible substrates via high-throughput and low-waste roll-to-roll manufacturing techniques.[16] This is in comparison to typical silicon devices, which require thermally and structurally robust substrates to endure high-temperature processing and support a ~ 140 – 200 μm thick layer of the weakly absorbing material.[17]

Taking into account the cost of materials and overall energy input to generate a module, organic photovoltaics are one of the most promising photovoltaic technologies with a low anticipated energy payback time on the order of 3 – 6 months, in comparison with the 1.5 – 3.5 years required to recoup costs from fabrication of silicon modules.[18] Though the technology is now available on the market and has even begun testing in small-scale commercial building applications,[19] several challenges remain for the development of organic photovoltaics and their wider-spread implementation. Necessary research efforts focus on improving device stability,[20]

designing and synthesizing high efficiency materials,[21-22] optimizing processing conditions and electrode contacts,[23] developing appropriate structures for modules and up-scaling,[16, 24] and analyzing possible areas for cost saving.[18] This thesis outlines novel research aimed toward improving materials and device performance by developing structure-function relationships linking nanoscale materials properties to the relevant photophysical processes that enable or detract from optical-to-electrical energy conversion. The remainder of this chapter provides background information on the basic principles of organic photovoltaic device operation with a goal of building a framework for intelligently designing these materials to harness the beneficial pathways of excited-state evolution for optimal photovoltaic function.

1.3 ORGANIC PHOTOVOLTAIC DEVICE ARCHITECTURE AND PERFORMANCE METRICS

Figure 1.1 shows a schematic representation of the typical device architecture for an organic solar cell along with the current-voltage characteristics for a representative photodiode. As we discuss in further detail in Section 1.4, an organic solar cell's active layer generally contains electron-donating and electron-accepting molecular components whose energy-level offsets enable the separation of coulombically bound electron-hole pairs (excitons) formed upon photoexcitation. The donor/acceptor components are interfaced either as a blended nanoscale donor/acceptor mixture (bulk heterojunction, BHJ), or as stacked layers of pure donor and acceptor material (bilayer). In this thesis we discuss BHJ devices. Although the first modern donor/acceptor organic photovoltaics developed by Tang in 1986 employed a planar bilayer heterojunction,[25] bulk heterojunctions have gained popularity for the ability to solution process the mixed active layer and for the higher photocurrent generation efficiencies generally obtained from these devices,

which results from the greater interfacial donor/acceptor area for charge transfer and the shorter distance that neutral excitons must travel to reach a heterojunction where they dissociate.

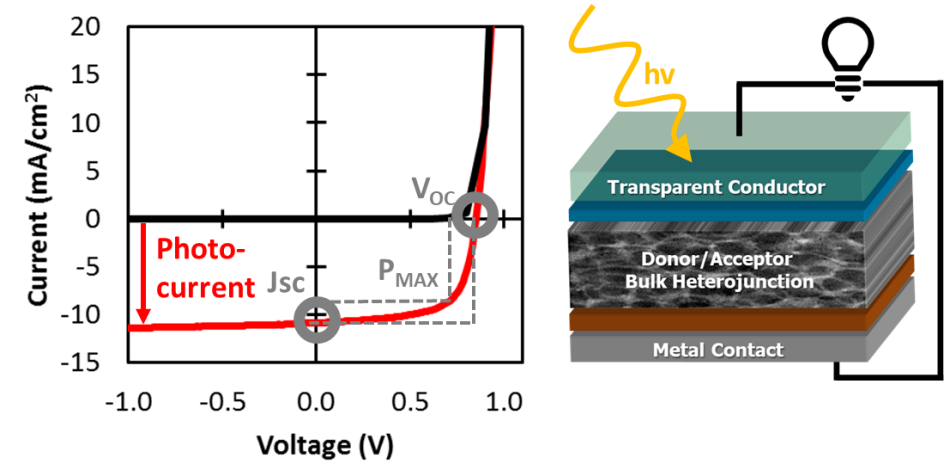

Figure 1.1. Current-voltage characteristics in the dark (black) and under simulated solar illumination (red), indicating the short-circuit current (J_{SC}), open-circuit voltage (V_{OC}), maximum power point (P_{MAX}), and the two boxes whose ratio is used to calculate the fill factor (FF), along with a schematic representation of a typical organic solar cell device architecture.

Once the excitons are separated at the donor/acceptor interfaces, the free charge carriers are transported tens to hundreds of nanometers through the thin-film active layer to reach the appropriate electrode having an energetically-favorable work function for charge extraction. In typical (non-inverted) device architectures, the anode selectively extracts positive charge carriers and is most often comprised of a transparent conducting oxide, such as indium tin oxide (ITO) or fluorine-doped tin oxide (FTO). The anode is often coated with a thin layer (~ 5 – 30 nm) of material to improve selectivity toward hole extraction. The hole-selective interlayer is almost always poly(3,4-ethylenedioxythiophene) polystyrene sulfonate (PEDOT:PSS) or molybdenum oxide. PEDOT:PSS is the most popular anode interlayer because of its facile solution processing, high work function, and ability to make good contact with ITO and FTO. However, a major disadvantage of PEDOT:PSS as a hole-extraction layer is its intrinsic acidity, which causes device

degradation by etching away the metal oxide.[26] To mitigate this stability issue and produce longer-lasting devices, PEDOT layers can be formed through chemical vapor deposition, which would eliminate the acidic PSS component that is necessary for solution processing.[27]

The cathode is typically a vapor-deposited metal contact (usually silver or aluminum) with a lower work function to extract electrons. Before deposition of the metal electrode, an additional layer is sometimes deposited between the active layer and metal contact to selectively transport electrons, to serve as an optical spacer, or to act as a buffer layer that prevents the metal from penetrating into the active layer during thermal vapor deposition. In comparison to anode interlayers, there is a much more diverse range of materials employed at cathode interfaces.[28-30] The most common materials for the electron selective buffer layer at the cathode interface include small molecules (bathocuproine, bathophenanthroline, hydroxyquinolatolithium), polymers (polyethylenimine), lithium fluoride, fullerene derivatives, and metal oxides (ZnO, TiO_2).[28-30]

In addition to the device architecture, Figure 1.1 shows the current-voltage characteristics for a representative photodiode in the dark and under simulated solar illumination. In the dark, an ideal photodiode exhibits minimal current under reverse-bias (negative) voltages and exponentially increasing current under forward-bias (positive) voltages. This current-voltage relationship is generally similar to that derived by Shockley for inorganic photodiodes in 1949,[31] given as $J(V) = J_0 [e^{qV/kT} - 1]$ where J(V) is the voltage-dependent current leaving the device, J_0 is the dark saturation current, q is the elemental charge, k is Boltzmann's constant, and T is temperature. In the light, the photodiode exhibits a constant photocurrent offset (J_{ph}), and the ideal diode equation becomes $J(V) = J_0 [e^{qV/kT} - 1] - J_{ph}$. Figure 1.1 additionally highlights the properties relevant for calculating the device's power conversion efficiency. The open-circuit voltage (V_{OC}) is the forward-bias voltage under which zero total current flows through the device,

meaning that the photogenerated current (J_{ph}) exactly balances the recombination current at this voltage. The V_{OC} is limited by the energy gap between the electron and hole quasi fermi levels. The short-circuit current density (J_{SC}) is related to the number of extractable charge carriers under zero applied voltage. The quadrant between $0 < V < V_{OC}$ represents the power generating region, where the product of current multiplied by voltage gives the photogenerated power produced by the solar cell. The maximum power attainable from the photodiode (P_{MAX}) is depicted by the smaller dotted gray box in Figure 1.1. The fill factor (FF), also called the quality factor, of the photodiode is given by the ratio $P_{MAX} / J_{SC} \times V_{OC}$. The power conversion efficiency (PCE) is calculated using these device performance metrics as $PCE = P_{MAX} / P_{IN} = FF \times J_{SC} \times V_{OC} / P_{IN}$, where P_{IN} is the incident power that shines on the solar cell (typically ~ 100 mW/cm^2 for non-concentrated solar illumination). Currently, state-of-the-art single-junction lab-scale organic solar cells often reach PCEs of 7 – 10 %,[29, 32-33] with the highest efficiency devices recently achieving 11.7 %.[34]

Models based on the ideal Shockley diode equation have been extended to describe organic photodiodes, and in many cases reasonable electrical descriptions of the organic devices can be obtained.[35] However, the photophysical processes leading to current generation are drastically different between organic and inorganic photodiodes. For this reason, several models have been derived to specifically include the molecular parameters and the bound photoexcited states mediating photocurrent generation in organic devices.[36-38] Most notably, inorganic semiconductors differ from organics as they contain delocalized energy bands encompassing an extended lattice of highly ordered atoms, where free carriers are formed by thermal or optical promotion across the band gap. In typical inorganic devices, the preferential motion of charge carriers is driven by a planar p-n junction, where the interface between positively and negatively doped semiconductor

layers creates a built-in electric field and a concentration imbalance inducing the motion of electrons and holes to their respective electrodes. The process for organic semiconductors differs as photoexcitation initially yields neutral electron-hole pairs (excitons) which diffuse only approximately 10 nm from their initial location,[39-40] and are generally unaffected by electric fields.[41] BHJ devices address this short exciton diffusion length by employing nanoscale donor/acceptor interfaces, where the energy level offsets between the donor/acceptor molecular orbitals provide a driving force to overcome the coulombic attraction between the opposite charges. Thus, the successful operation of organic devices must overcome additional challenges related to free charge generation and extraction from inherently disordered semiconductors with low carrier mobilities and low dielectric screening between opposite charge carriers.

In addition to the drastically different process of charge carrier generation for organic versus inorganic photodiodes, the origin of internal electric fields that drive charges to the electrodes also differ. In BHJ devices with nanoscale donor/acceptor mixing, it is unphysical to describe carrier drift to the electrodes caused by a built-in electric field generated in the depletion region at a planar p-n junction as occurs for inorganic devices. Instead, the electrical characteristics of organic devices are often described by considering the BHJ as an effective homogeneous medium sandwiched between two electrodes, where the relevant built-in field is generated either by a Schottky junction at the BHJ/cathode interface[42-43] or by the difference between anode and cathode work functions.[44-45]

Importantly, understanding and improving the function of organic photovoltaics requires careful consideration of the various excited states formed following photoexcitation as well as the accessible pathways that mediate charge generation or recombination. In Section 1.4, we provide a more detailed description of the photoexcited states that influence organic solar cell operation.

1.4 PHOTOEXCITED STATES AND PHYSICAL PROCESSES LEADING TO CHARGE GENERATION

Under solar illumination, a typical organic solar cell has a steady-state population of 10^{16} – 10^{17} photoexcited states per cubic centimeter. Due to the low dielectric constants and complex energy landscape of organic semiconductor materials, these photoexcited states range from bound excitons to free charge carriers, and the interactions between states as well as their productivity toward photocurrent generation vary significantly. In this section, we outline the various states formed upon photoexcitation of an organic photovoltaic material and the roles of these states toward production of electricity.

1.4.1 *Solar Radiation and Photon Absorption*

Figure 1.2 shows the extraterrestrial spectrum of solar radiation along with the terrestrial spectrum of light that reaches the earth after passing through the atmosphere. The air mass 1.5 (AM1.5) spectrum represents the distribution of solar radiation that hits a surface tilted at 37 degrees toward the sun after traveling through the atmosphere at 1.5 times the optical path length compared to the zenith. The AM1.5 solar spectrum represents the average conditions of light reaching the surface in the contiguous United States, and this spectral profile at a total integrated power density of 100 mW/cm^2 has become the international standard for evaluating photovoltaic device performance.

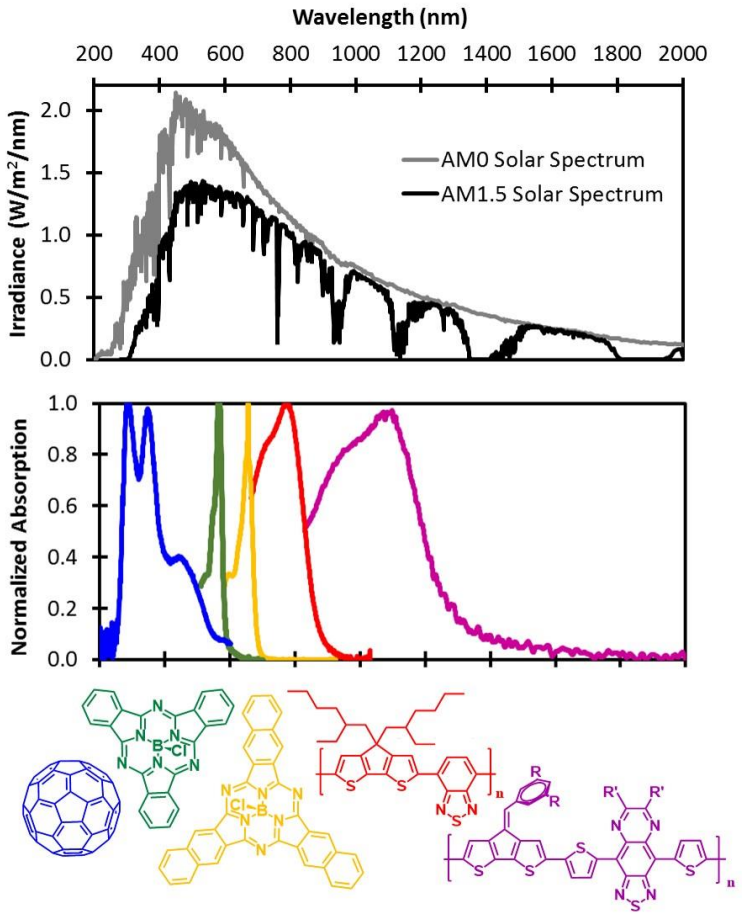

Figure 1.2. Solar irradiance spectra for air mass zero (extraterrestrial) and air mass 1.5 (terrestrial) provided by the National Renewable Energy Laboratory,[46] along with absorption spectra of common small molecule and polymer semiconductors, showing good spectral coverage of available sunlight. We show normalized absorption spectra for C_{60} fullerene (blue), chloroboron subphthalocyanine (green), chloroboron subnaphthalocyanine (yellow), "push-pull" polymer with cyclopentadithiophene push unit and benzothiadiazole pull unit (red), and "push-pull" polymer with bridgehead olefin substituted cyclopentadithiophene push unit and thiophene-flanked thiadiazoloquinoxaline pull unit (purple).

A good photovoltaic material should absorb light in the ~ 300 – 1400 nm range where sunlight is most abundant. The lower panel of Figure 1.2 shows the normalized absorption spectra of several organic photovoltaic materials, highlighting the wide spectral range of molecular absorbers covering the most intense portion of the solar spectrum. A distinct advantage of organic

semiconductors is the ability to tune the optical gap by small variations in molecular structure as well as molecular packing. The absorption spectrum of C_{60} fullerene in the 250 – 600 nm range is a good example of variations in absorption due to molecular packing. The peaks at 290 and 350 nm are attributable to absorption by the individual C_{60} molecules and the peak at 450 nm arises when there is significant molecular aggregation leading to intermolecular charge-transfer interactions.[47-48] In the 450 – 750 nm range, we show another strategy for tuning the absorption, in this case by modifying the molecular structure to extend the π-conjugation system.[49] The conjugation in chloroboron subnaphthalocyanine (SubNc) is extended relative to chloroboron subphthalocyanine (SubPc), resulting in a redshifted absorption maximum shifting from 570 nm for SubPc to 650 nm for SubNc. Finally, the most common materials for lower-energy visible and near-infrared absorption are conjugated polymers, where band gaps as low as 0.6 eV (absorbing out to ~ 2000 nm) have been achieved by employing a "push-pull" design strategy.[50-51] These copolymers consist of electron-rich "push" units linked with electron-deficient "pull" units, where the band gap generally narrows with the increasing polarity along the molecules' backbone.[52-55] The narrowing of the band gap due to intramolecular charge-transfer transitions between the "push" and "pull" units can be understood analogously to the lower energy of intermolecular charge-transfer states at electron donor/acceptor interfaces described in Section 1.4.4. In the 700 – 1300 nm range of Figure 1.2, we show the absorption spectra of two structurally-related "push-pull" copolymers. Both polymers have a "push" unit consisting of a cyclopentadithiophene core. The polymer containing the weaker benzothiadiazole "pull" unit exhibits a higher-energy absorption spectrum, with a maximum around 780 nm. The polymer containing the stronger thiophene-flanked thiadiazoloquinoxaline "pull" unit has a redshifted absorption spectrum with a maximum near 1080 nm. Additionally, the redshift for the cyclopentadithiophene-

thiadiazoloquinoxaline copolymer is also partially attributable to planarization of the polymer backbone caused by the cyclopentadithiophene bridgehead olefin, which reduces backbone torsion and extends the π-conjugation system similar to the SubPc/SubNc case.[55]

As described in Section 1.3, the excited states produced upon light absorption in organic semiconductors differ from inorganic semiconductors due to the more localized nature of excitations in organic materials. In inorganic semiconductors, light absorption promotes an electron across the band gap into a continuum of states delocalized over an extended lattice of covalently bonded atoms. However, in molecular systems the onset of absorption is described by the optical transitions between a molecule's highest occupied molecular orbital (HOMO) and lowest unoccupied molecular orbital (LUMO). The HOMO and LUMO represent the energy of electrons occupying the π network of p_z orbitals extending above and below the plane of the semiconductor molecules' backbone, which is primarily comprised of sp^2 hybridized carbon atoms. Such excitations reside on a single π-conjugation center, most often described by an individual molecule or a portion of a molecule. However, in some cases electronic coupling between neighboring molecular π systems can allow delocalization of excited states over 10's of molecules.[56-57] In the following section (1.4.2), we describe the absorption of light and the bound excited state (singlet exciton) that is most often considered to be the initial product of photoexcitation.

1.4.2 *Singlet Excitons*

The excitonic nature of photogenerated excited states is at the core of optical characterization and understanding of energy conversion processes organic semiconductors. Due to the low dielectric constants ($\varepsilon \sim 2 - 5$) of organic materials, optically excited electrons are

largely unscreened from coulombic attraction to the positively charged vacancies (holes) they leave behind, resulting in coulombically bound electron-hole pairs called excitons.[58] These excitons exhibit singlet spin character upon photoexcitation and experience a stabilization (or binding energy) of 0.4 – 1.5 eV relative to unbound positive and negative charge carriers on the same molecule.[59]

Figure 1.3 shows a schematic representation of the potential energy surfaces associated with exciton formation via photon absorption. We highlight pathways of exciton deactivation through either photon emission or charge transfer in a blend of electron-donating (D) and electron-accepting (A) semiconductor molecules. In our schematic, the minima of the electronic states' potential energy surfaces along the nuclear coordinate represent the optimal molecular geometries for a given state. Following an optical or electronic transition, the molecules must reorganize their nuclei to minimize the total energy of the system. Importantly, under the Born-Oppenheimer approximation, the time scale of nuclear motion is much slower than the time scale for electronic transitions, allowing for the separation of the electronic and nuclear wavefunctions and estimation of the optical transition intensities from the lowest-energy molecular conformation.

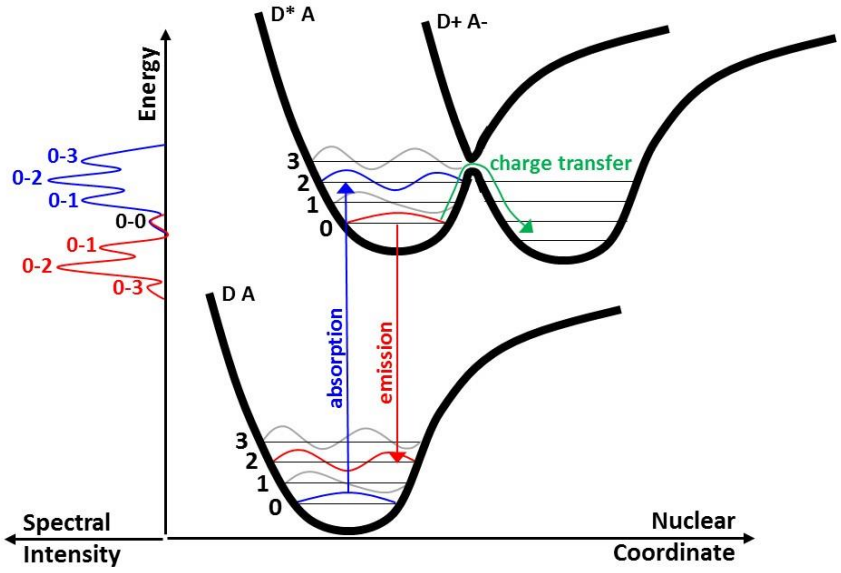

Figure 1.3. Energy level diagram demonstrating the processes of absorption, emission, and charge transfer in organic donor (D) / acceptor (A) blends along with a schematic of the spectral intensity for absorption (blue) and emission (red) determined from the overlap between the initial and final vibronic states for each transition.

In Figure 1.3, we depict the first four vibrational energy levels within each electronic potential energy surface, where the vibrational eigenstates are represented as quantized states within a harmonic oscillator or Morse potential. As described separately by Franck and Condon in 1926,[60-61] the spectral shape of exciton absorption and emission is determined by the overlap of the initial and final vibronic wavefunctions. The left-hand side of our schematic depicts the relative spectral intensities associated with the absorption (blue) and emission (red) optical transitions. The arrow on the right-hand side highlights the transition corresponding to the highest spectral intensity. Figure 1.3 shows that absorption from DA to D^*A originates in the lowest energy vibronic state and has the highest probability of occurring when the vertical overlap between the initial and final vibronic wavefunctions is maximized. After an absorption event has occurred, the excitation quickly relaxes to the lowest energy vibrational state within the D^*A excited electronic

potential energy surface, following Kasha's rule. Emission then originates in the lowest energy vibrational state within the excited D^*A surface and gains the most spectral intensity when the vertical overlap between the initial and final vibronic wavefunctions is maximized.

In blended D/A films, exciton relaxation by emission is greatly quenched as the dominant exciton deactivation pathway becomes charge transfer. Photoinduced charge transfer results in exciton (D^*A) dissociation to form donor cations (D^+) and acceptor anions (A^-). We illustrate the pathway for charge transfer in Figure 1.3, which becomes accessible when the potential energy surface associated with charge transfer (D^+A^-) crosses over the potential energy surface of the excitonic state (D^*A). If the crossing potential energy surfaces electronically couple to each other, then the diabatic states (i.e. the electronic wavefunctions under the Born-Oppenheimer approximation) mix with each other to form new adiabatic surfaces separated by an energy gap that is proportional to the coupling. This phenomenon is called an avoided crossing, and it enables the possibility for a smooth transition from the excitonic potential energy surface to the charge-transfer state after overcoming any necessary activation energy and undergoing nuclear reorganization. We discuss the resulting charge-transfer states and their evolution to free carriers in more detail in sections 1.4.4 and 1.4.5, respectively.

1.4.3 *Triplet Excitons*

In addition to singlets, excitons of triplet spin also form in organic semiconductors and profoundly affect device performance. In some cases, spin conversion to triplet states is desirable. For example, singlet fission is a process allowing generation of two triplet excitons from one singlet exciton, presenting the opportunity for multiple carrier generation from one photoexcitation.[62-63] In addition, some organic light emitting diode (OLED) applications harness

long-lived phosphorescence or harness photoluminescence from delayed reactivation of singlet states, where both of these longer-lived emission processes are linked to the slower, spin-forbidden decay of triplet excited states to the singlet ground state.[64-65] However, in many photovoltaic device applications, formation of triplet excitons is considered a detrimental loss pathway. Population of triplet states following photoexcitation of singlet excitons represents an energetic loss (typically by an exchange energy of 0.1 – 1.5 eV), and the resulting energetic barrier is often sufficient to prevent further charge dissociation.[65-70] Nevertheless, regardless of whether one aims to prevent triplet population or utilize triplet excitons in device applications, understanding triplets and their formation pathways is essential to optimizing device performance.

In Section 1.4.2 we described optical transitions originating in a molecule's singlet ground state and leading to formation of the molecule's singlet excitonic state. However, photoexcitation of triplet excitons is forbidden. Conservation of electronic spin upon light absorption is required because the interacting photons carry zero spin angular momentum. For this reason, triplet excitons are formed either by recombination of spin-uncorrelated charge carriers, or by a change in the total spin angular momentum from $|\vec{S}| = 0\hbar$ for singlet excitons to $|\vec{S}| = \sqrt{2}\hbar$ for triplets.

In order to discuss how a change in spin angular momentum can occur for conversion of a singlet exciton to a triplet exciton, we show the vector representations for pair of electrons with singlet or triplet spin in Figure 1.4. We represent the individual electron spins as black vectors $\vec{S}_i$ (where i is an arbitrary label of 1 or 2). The length of each $\vec{S}_i$ vector is equal to $\sqrt{3}\hbar/2$, corresponding to a projected length along the z axis of $\hbar/2$ or $-\hbar/2$. As a consequence of the Heisenberg uncertainty principle, it is not possible to simultaneously characterize all momentum and spatial coordinates of the spin vectors, so the x and y orientations of the spin vectors are indeterminable and we represent all possible azimuthal orientations of $\vec{S}_i$ by an uncertainty cone.

Despite the uncertainty in the exact xy orientation, the relative orientation between the $\vec{S}_1$ and $\vec{S}_2$ vectors is an important parameter that determines the total spin angular momentum of the correlated electron pair. For a singlet, the $\vec{S}_1$ and $\vec{S}_2$ vectors are oriented 180° from each other, and cancelling of the vectors leads to zero total spin angular momentum ($\vec{S}$ = 0ħ). The spin multiplicity is determined by the number of possible orientations of $\vec{S}$ in a hypothetical magnetic field, which is given by 2S+1 (where S is the spin quantum number according to $|\vec{S}| = \sqrt{S(S+1)}\hbar$). Unsurprisingly, the $\vec{S}$ vector of zero length has only one possible orientation, leading to a singlet spin multiplicity and no interaction with a magnetic field.

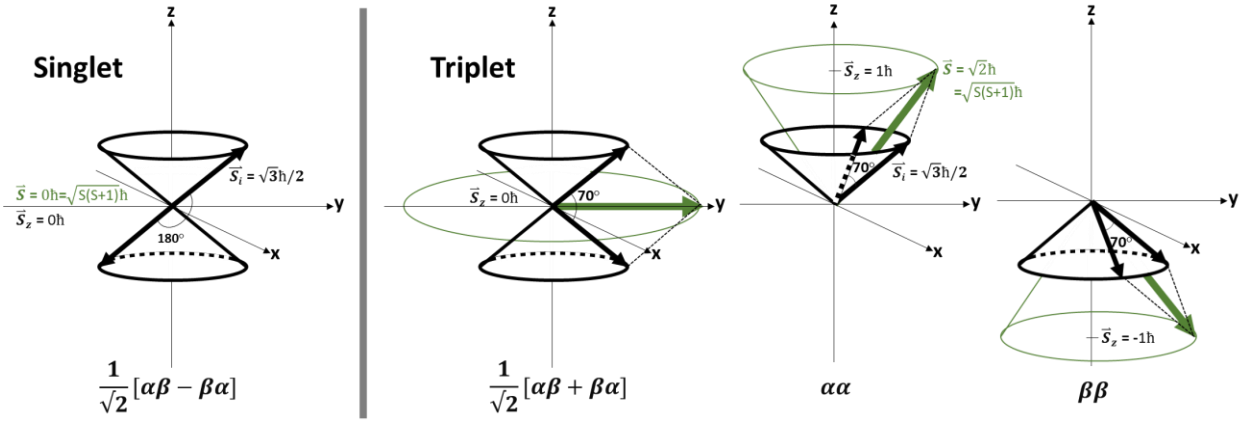

Figure 1.4. Singlet and triplet eigenstates of a two-particle system such as an exciton in an organic semiconductor, where the expressions for each of the four eigenstates contain the one-electron spin wavefunctions α and β. Vector addition of two individual spins ($\vec{S}_i$, illustrated as black arrows) yields the total spin vector ($\vec{S}$, illustrated as green arrows). Singlet states have one total spin projection with total spin angular momentum $\vec{S}$ equal to 0ħ and projection along the z axis ($\vec{S}_z$) of 0ħ. Triplet states have three projections for the total spin vector with $\vec{S}$ with length equal to $\sqrt{2}$ħ and $\vec{S}_z$ equal to 0ħ, 1ħ, and -1ħ.

Triplet states arise when the spins $\vec{S}_i$ are oriented at 70° from each other, summing to a total $|\vec{S}|$ length of $\sqrt{2}\hbar$, as shown by the green vector in Figure 1.4. The triplet spin multiplicity (2S+1 = 3, where S = 1 according to $|\vec{S}| = \sqrt{S(S+1)}\hbar$) is a result of the three possible orientations for the magnetic quantum number m_s. The m_s values of 1, 0, and -1 correspond to the projection $\vec{S}_z$ along the z axis for $\vec{S}$ orientations of 45°, 90°, or 135° relative to the z axis.

The change in the total spin angular momentum to convert from singlet to triplet states can occur, for example, through spin dephasing, where the individual spin vectors $\vec{S}_i$ process at different rates causing variation in the angle between them thereby altering the sum $\vec{S}$. The relative orientation between the $\vec{S}_i$ vectors may also change as a result of intersystem crossing, where coupling of an electronic spin vector to a nuclear spin induces a more rapid conversion of the angular momentum. In addition to interconversion from singlets, triplet states may also from through recombination of initially uncorrelated charge pairs, where bimolecular coulomb recapture of conjugate charge carriers is typically considered to occur in a statistical 1:3 singlet:triplet ratio.

Several important and device-relevant properties of triplet excitons arise from their spin character. One significant property is much longer lifetimes for triplet excitons compared to singlet states, which results from the spin-forbidden relaxation of triplet excited states to the singlet ground state. Although triplet decay to the ground state is strictly forbidden, weak spin-orbit interactions permit triplet decays over time scales of microseconds to minutes compared to singlet states which decay over picosecond to nanosecond time scales.[68, 71-72] Another important result of the spin interaction is the indirect effect on the energy of singlet versus triplet excitonic states. In general, the energies of triplet excitons are 2K ~ 0.1 – 1.5 eV lower than singlet excitons,[65-70] where K represents the exchange energy. This energetic stabilization of triplets relative to singlets is due to the antisymmetric nature of the spatial part of the triplet's electronic wavefunction, which

decreases the coulombic repulsion between the charged particles relative to a symmetric spatial wavefunction.

Since the lower energy of triplet states arises from the spatial part of the wavefunction, it is important to understand the role of electronic spin in determining the symmetric versus antisymmetric nature of the spatial wavefunction. Fundamentally, the exchange energy originates from the central idea that interchanging indistinguishable quantum mechanical particles cannot change the total probability density of the excited state. This basic assumption mathematically divides all particles into two classes – fermions (half-integer spin) and bosons (integer spin). An exciton consists of electrons (which are fermions), leading to the requirement for the total wavefunction to be antisymmetric upon exchange of the electrons. This means that both singlet and triplet excitons must have antisymmetric total wavefunctions, including the spin part of the wavefunction multiplied by the spatial part of the wavefunction. As illustrated in Figure 1.4 singlets have antisymmetric spin wavefunctions, where exchange of the arbitrary electron labels 1 and 2 returns the negative of the wavefunction expression, $\frac{1}{\sqrt{2}}$ [α(1) β(2) – β(1) α(2)] = – $\frac{1}{\sqrt{2}}$ [α(2) β(1) – β(2) α(1)]. Analogously, triplets have symmetric spin wavefunctions where exchange of the arbitrary labels 1 and 2 returns an unchanged expression (see expressions in Figure 1.4). In order to maintain an antisymmetric total wavefunction, singlet excitons must have a symmetric spatial wavefunction while triplet excitons must have an antisymmetric spatial wavefunction.

Because the Hamiltonian only depends on the spatial part of the wavefunction and not on spin, the difference in energy between singlet and triplet excitons arises from the symmetric or antisymmetric nature of the spatial wavefunction. Qualitatively, we can understand that triplets are lower in energy by noting that an antisymmetric spatial wavefunction becomes zero for the hypothetical scenario of both electrons occupying the same space, while a symmetric function is

nonzero. That is, for an antisymmetric triplet spatial wavefunction, $\frac{1}{\sqrt{2}}[\ \psi_a(r_1)\ \psi_b(r_2) - \psi_b(r_1)\ \psi_a(r_2)\ ] = 0$ when $r_1 = r_2$, where ψ_i is a spatial wavefunction component and r_i is the electron position. This result implies a lower probability for electrons to come into close proximity when occupying an antisymmetric spatial wavefunction. When electrons have a lower probability of coming into close proximity, as is the case for triplet excitons, the excited state has a lower overall energy due to decreased electron-electron repulsion. This is the origin of the principle known as Hund's rule, which states that the highest multiplicity term for a given electron configuration lies lowest in energy.[3]

The properties of triplet excitons outlined in this section, including lower energies relative to singlets, longer lifetimes due to spin-forbidden decay to the ground state, and triple degeneracy all have important consequences for the operation of organic electronics. We provide examples of the roles of triplet states in device operation in Chapter 3 and Chapter 4, and we further discuss triplet spin in the context of charge-transfer states in Section 1.4.4.

1.4.4 *Charge-Transfer States*

Charge-transfer states form at electron donor/acceptor interfaces and play important roles in organic photovoltaic device operation. In the simplest case, the energy of the charge-transfer state limits the open-circuit voltage,[38, 73-75] and increasing efficiency of charge-transfer state dissociation improves the short-circuit current.[37, 76-77] However, more detailed understanding of charge-transfer state properties, the photophysical pathways involving charge-transfer states, and their impact on device performance is still lacking and remains under active investigation. Often, charge-transfer states are considered to be a necessary intermediate between initially photoexcited singlet excitons and free carriers.[76-78] However, other studies suggest that carrier generation ideally

bypasses the localized interfacial states, where relaxation to the lowest-energy charge-transfer states may primarily lead to photovoltaic loss.[79] Once free carriers are formed, coulomb recapture may repopulate charge-transfer states of both singlet and triplet spin character.[73, 79-80] It then remains unclear how efficiently the charge-transfer states re-dissociate to useful carriers, undergo spin interconversion, or further relax to the ground state or other non-productive low-energy states.[73, 80] In this light, the equilibrium of charge-transfer states with both bound excitonic states as well as free carriers is central to our understanding of device operation. Importantly, several parameters have been identified that appear to affect the branching between charge-transfer state decay and dissociation to free carriers. While the earliest studies focused primarily on characterizing the energies of charge-transfer states,[81] newer studies additionally highlight the importance of charge-transfer state density,[73, 75, 82] electronic coupling,[38, 75, 83-84] lifetime,[73, 75, 85] delocalization,[73, 75, 77, 79, 86] binding energy,[76, 86] voltage dependence,[41, 87-88] and spin character.[80, 89-93]

To understand the influence of these charge-transfer state properties on device performance, it is first important to conceptualize the donor/acceptor interactions that lead to the formation of the interfacial states. Figure 1.5 shows a schematic representation of the energy-level offsets at electron donor/acceptor interfaces that are required to drive charge separation. The lower-energy LUMO level of the electron acceptor relative to the donor ($E_{LUMO,A} < E_{LUMO,D}$) corresponds to a deeper electron affinity for the acceptor ($A + e^- \rightarrow A^-$) compared to the excited-state ionization potential of the donor ($D^* \rightarrow D^+ + e^-$). Therefore, following generation of donor singlet excitons (D^*) by light absorption, electron transfer to the acceptor is exothermic ($A + D^* \rightarrow A^- + D^+$), typically by 100 – 300 meV.[73] Similarly, the energy level alignment $E_{HOMO,A} < E_{HOMO,D}$ drives hole transfer from excited acceptors to ground-state donors ($A^* + D \rightarrow A^- + D^+$).

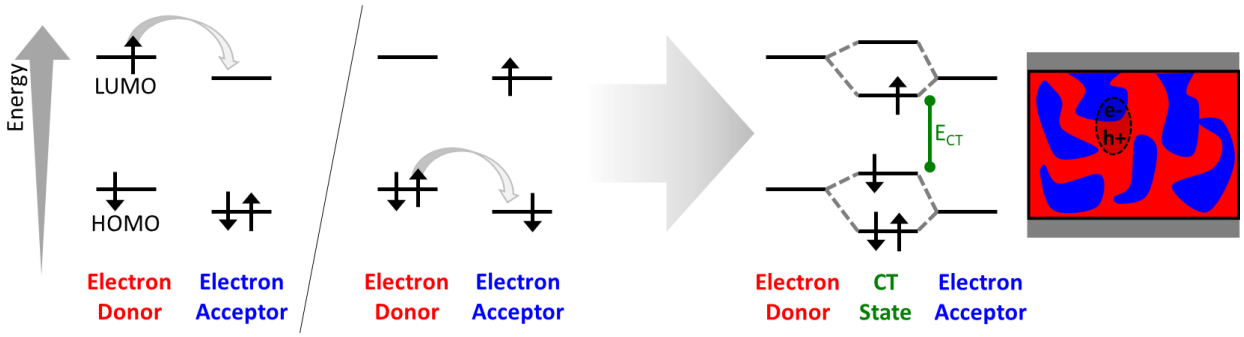

Figure 1.5. Energy level offsets at electron donor/acceptor interfaces, where electron transfer from excited donors to acceptors and hole transfer from excited acceptors to donors are both favorable reactions to create interfacial charge-transfer states. Charge-transfer state energies (E_{CT}) are depicted as the gap between singly occupied molecular orbitals at electron donor/acceptor interfaces. Cartoon of a bulk heterojunction morphology (not to scale) shows that charge-transfer states form at donor/acceptor interfaces and remain coulombically bound.

Following charge transfer, the interfacial electron-hole pairs most likely remain coulombically bound. This results in a decrease in the charge-transfer state energy relative to the difference between the electron donor HOMO (or ionization potential) and the acceptor LUMO (or electron affinity). This binding energy (E_B) is estimated by Coulomb's law as $E_B = q^2 / 4\pi\varepsilon_0\varepsilon_r r$, where q is the elementary charge, ε_0 is the permittivity of vacuum, ε_r is the relative dielectric constant (usually 2 – 5), and r is the distance between the electron and hole. Since charge-transfer states have a larger electron-hole separation (r) compared to the excitons that are generated in the neat materials, charge-transfer states are reported to have lower binding energies of 0.05 – 0.4 eV[73, 94-98] compared to singlet exciton binding energies of 0.4 – 1.5 eV.[98-99]

Despite these estimates of charge-transfer state binding energies, the actual extent of coulombic binding within the interfacial electron-hole pairs that contribute to photocurrent is still debated.[41, 95, 97, 100] Notably, in the most promising OPV systems, charge-transfer state dissociation

approaches 100% efficiency,[78, 101] and free carrier generation approaches sub-100 femtosecond time scales.[102-105] We may turn to several different factors to explain this seemingly paradoxical ability to efficiently dissociate charge-transfer states with binding energies up to ~10 times higher than the available thermal energy. For example, the inherent morphological and associated energetic disorder in molecular films[106] may decrease the barrier to charge separation by providing an entropic driving force favoring unbound carriers.[97, 107] In addition, recent studies,[73] including our own discussed in Chapter 2,[75] suggest that charge-transfer interactions extend beyond nearest-neighbor donor/acceptor pairs. These results point to excited-state delocalization over multiple chromophores as a key factor in decreasing the attraction between electron-hole pairs and sustaining free charge.[77]

We have described the energetic driving force for generating charge-transfer states through exciton dissociation at donor/acceptor interfaces as depicted in Figure 1.5. However, as we now illustrate using a state diagram in Figure 1.6, the various kinetic and thermodynamic processes that dictate charge-transfer state populations, decay rates, and spin character are significantly more complicated. Typically, the earliest geminate charge-transfer state populations initially have singlet spin character. This is because spin-conserved singlet exciton dissociation to form singlet charge-transfer states (process 1 in Figure 1.6) kinetically outcompetes singlet exciton intersystem crossing to triplet excitons. The kinetic avoidance of intersystem crossing largely removes the possibility of geminate triplet charge-transfer state population from triplet exciton dissociation. Even if triplet excitons did form through intersystem crossing, dissociation of the low-energy triplet excitons is most often thermodynamically inaccessible. However, triplet charge-transfer states are known to form at later times through either direct spin interconversion from singlet charge-transfer states (process 2 in Figure 1.6) or recombination of spin-uncorrelated charge

carriers (process 3 in Figure 1.6). The predominant pathways for triplet charge-transfer state population have important implications for organic photovoltaic device operation and the possible strategies for avoiding photocurrent loss to low-energy triplet excitons.

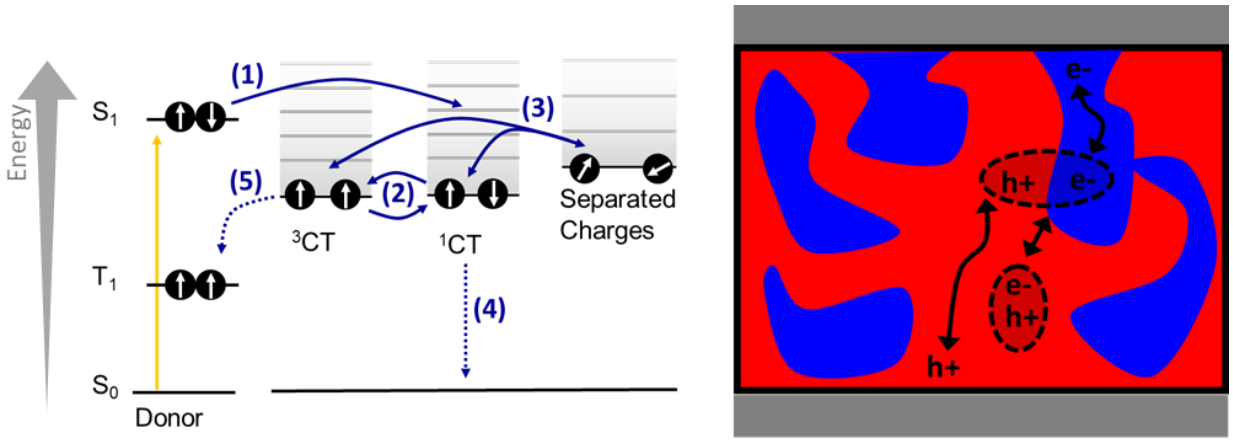

Figure 1.6. State diagram showing the process of photoexcitation (yellow arrow) of singlet excitons (S_1) from the singlet ground state (S_0) followed by spin-conserved dissociation to the singlet charge-transfer manifold (1). Spin interconversion within the charge-transfer manifold (2) may possibly populate triplet charge-transfer states (^{3}CT) from singlet charge-transfer states (^{1}CT). Alternatively, dissociation to separated charge carriers may allow carrier recombination to both singlet and triplet charge-transfer states (3). Singlet charge-transfer states may decay to the ground state (4), and triplet charge-transfer states may decay to localized triplet excitons (5). Our cartoon depicts the equilibrium between free carriers, interfacial charge-transfer states, and bound excitonic states.

Most likely, the majority of triplet charge-transfer states are populated through bimolecular recombination of uncorrelated charge carriers (process 3 in Figure 1.6) rather than spin interconversion within the charge-transfer manifold (process 2 in Figure 1.6). Indeed, several studies have verified that bimolecular recombination is the dominant triplet formation pathway when charge transfer is accessible, since triplet exciton populations in OPV donor/acceptor blends

typically rise with kinetics dependent on photoexcitation intensity.[80, 96, 108] In this case, interconversion between singlet and triplet charge-transfer states proceeds through dissociation to uncorrelated charge carriers followed by recombination. This pathway highlights the importance of extracting free carriers before recombination to triplet states occurs, as well as the importance of carrier delocalization for suppressing charge-transfer state (re)population. We further discuss the implications of equilibrium between charge carriers with singlet and triplet charge-transfer states in Chapter 3.

The extent of direct spin interconversion between singlet and triplet charge-transfer states (process 2 in Figure 1.6) is debated.[92] Rapid singlet/triplet interconversion implies that the rate of spin interconversion within the charge-transfer manifold outpaces both the decay of singlet charge-transfer states to the ground state (process 4, $^1CT \rightarrow S_0$ typically 0.4 – 6.8 ns[75]) as well as the decay of triplet charge-transfer states to energetically-accessible triplet excitons (process 5, $^3CT \rightarrow T_1$ typically 10 – 100 ps[89, 96]). If this is the case, then population of the charge-transfer state manifold would immediately open a pathway for photovoltaic loss to low-energy triplet excitons, regardless of the initial charge-transfer state spin.[92] In fact, once the charge-transfer manifold is populated, the ratio of decay via each pathway would be fixed by the relaxation rates as $k_{1CT \rightarrow S0} / k_{3CT \rightarrow T1}$. In this case, the faster rate of $^3CT \rightarrow T_1$ would be responsible for the enhanced triplet population often observed in donor/acceptor blends relative to neat materials.[92] Importantly, the ratio of decay via ^1CT or ^3CT in this scenario would not be restricted to the statistical 1:3 singlet:triplet ratio. This is different from typical analysis of OLEDs, where coulomb recapture of injected charge carriers is expected to generate a 1:3 singlet:triplet ratio. However, even in some OLED materials, exciplex-mediated interconversion has been invoked to explain thermally activated delayed fluorescence, in which the singlet fraction exceeds the statistical limit.[90, 109]

While the assumption of rapid spin interconversion within the charge-transfer manifold is often based on near-degeneracy of these states, recent results suggest that these states may not be degenerate.[110-111] Near-degeneracy would be attributed to the small static exchange integral, which is insignificant in charge-transfer states compared to the exchange energy in more tightly bound excitons (see Section 1.4.3). However, additional factors beyond static exchange may be necessary to accurately depict singlet/triplet splitting for charge-transfer states.[110-111] In particular, an additional kinetic exchange term could stabilize singlet charge-transfer states through a hopping mechanism across the interface in which electrons are exchanged through a spin-paired intermediate.[110-111] This uncertainty in the singlet/triplet energy splitting for charge-transfer states also sheds further uncertainty onto whether rapid singlet/triplet interconversion occurs to a significant extent.

1.4.5 *Polarons*

If opposite charge carriers overcome the coulombic binding energy at electron donor/acceptor interfaces, they may separate to form unbound cations on the donor material and anions on the acceptor material.[73, 94-96] Importantly, charge carriers generated in organic semiconductors interact strongly with the surrounding molecules, causing structural lattice reorganization away from the relaxed ground-state molecular geometries to better accommodate the excess charge. Thus, "free" carriers in π-conjugated semiconductor molecules are more accurately described as polarons, where the distortion of the local molecular configurations stabilizes and localizes the charge relative to a rigid or non-interacting system.

Figure 1.7 shows that the polaronic nature of charge in organic semiconductors leads to a characteristic absorption pattern including two sub-gap absorption features. As we will further

discuss in Chapter 3 and Chapter 4, characterizing and tracking polaron absorption profiles has proven essential for elucidating the photophysical processes in organic photovoltaic materials with optical spectroscopy. For illustration, Figure 1.7 displays a transient absorption spectrum highlighting the two polaron absorption bands (P_1 and P_2) for a positive carrier on a small-molecule organic semiconductor that has been employed in both OLEDs and in OPV devices, N,N′-bis(1-naphthyl)-N,N′-diphenyl-1,1′-biphenyl-4,4′-diamine (NPD). As we further outline in Chapter 4, transient absorption is a pump-probe optical spectroscopy technique allowing the characterization of excited-state absorption profiles at various time delays following laser photoexcitation of the system. In the present example, we blend NPD with the electron acceptor [6,6]-phenyl-C_{61}-butyric acid methyl ester ($PC_{61}BM$) in order to drive charge separation following photoexcitation with a 400 nm laser pulse. Less than one picosecond after photoexcitation, we observe ultrafast charge transfer between NPD and $PC_{61}BM$ yielding two polaron absorption bands associated with NPD cations centered around 510 nm and 1600 nm in addition to a $PC_{61}BM$ anion absorption band at 1050 nm.

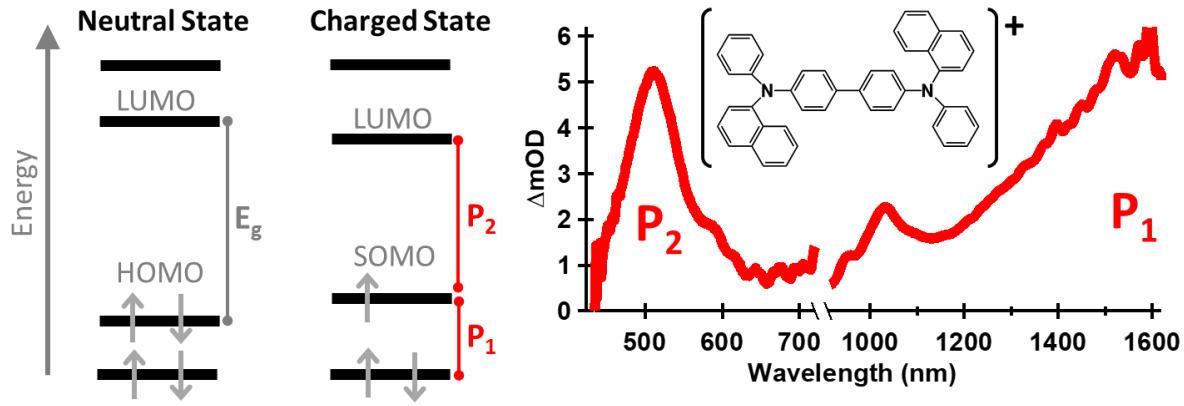

Figure 1.7. Schematic illustration of the shift in energy landscape associated with polaronic charge generation in organic semiconductor molecules along with an example of polaron absorption given by the transient absorption spectrum at 1 ps for N,N′-bis(1-naphthyl)-N,N′-diphenyl-1,1′-biphenyl-4,4′-diamine blended with [6,6]-phenyl-C_{61}-butyric acid methyl ester following 400 nm photoexcitation. The difference between the highest occupied molecular orbital (HOMO) and lowest unoccupied molecular orbital (LUMO) in the neutral state gives the optical gap (E_g) of the material. In the positively charged state, the polaron absorption bands (P_1 and P_2) are the transition between the new highest fully occupied state and the singly occupied state (SOMO) and the transition between the SOMO and LUMO. The transient absorption spectrum is plotted as the change in optical density (ΔmOD) relative to the ground-state absorption.

The absorption profile that we observe for NPD positive polarons is typical for carriers generated in organic semiconductors, where one higher energy absorption peak is 0.1 – 1.0 eV redshifted of the ground state absorption and another lower energy polaron absorption peak is often observed in the infrared region (0.1 – 1.2 eV, 1000 – 4000 nm).[112-115] We schematically illustrate the origin of this absorption pattern on the left hand side of Figure 1.7, where structural relaxation of the molecular lattice to accommodate the localized charge causes the frontier molecular orbitals to shift into the optical band gap (E_g).[112, 116-120] For positive charge carriers (holes), the lower energy absorption P_1 corresponds to a transition from the highest energy fully occupied molecular orbital to the singly occupied molecular orbital (SOMO) within the optical band gap. The higher

energy feature P_2 corresponds to absorption from the singly occupied orbital to the lowest energy unoccupied molecular orbital (LUMO). Negative charge carriers (electrons), would similarly be characterized by two absorption features, but the relevant transitions differ due to changed occupancy of the molecular orbitals. The higher energy absorption feature for negative polarons would correspond to the transition denoted as P_2, but in this case the absorption occurs from a fully occupied molecular orbital to a singly occupied molecular orbital. The lower energy absorption feature for electron polarons corresponds to absorption from the singly occupied molecular orbital to the lowest energy unoccupied molecular orbital in the charged state. It is important to note that electron and hole polaron absorption spectra for a given material may not be identical, since the spectra depend on the differing occupancies of the molecular orbitals during the absorption transition, differing molecular distortions under positive or negative charge, and differing abilities of the electrons and holes to delocalize within the material.[121-123]

Polaron formation represents energetic loss for the carriers extracted from OPV materials relative to the case of a rigid lattice that does not distort in the presence of charge. In addition to decreasing the attainable open-circuit voltages, this also affects the magnitude of extractable current. That is, lower carrier mobilities arise from the activation barrier that polarons must overcome to move through the material.[124] We further discuss polarons along with examples of polaron spectral signatures in Chapter 3 and Chapter 4 and their voltage dependence in Chapter 3.

Chapter 2. OPEN-CIRCUIT VOLTAGE LOSSES IN SELENIUM-SUBSTITUTED ORGANIC PHOTOVOLTAIC DEVICES FROM INCREASED DENSITY OF CHARGE-TRANSFER STATES

Adapted From:
Sulas, D.B.; Yao, K.; Intemann, J.; Williams, S.; Li, C.-L.; Chueh, C.-C.; Richards, J.; Xi, Y.; Pozzo, L.D.; Schlenker, C.W.; Jen, A.K.-Y.; Ginger, D.S. Chem. Mater. ***2015****, 27, p. 6583-6591.*

2.1 INTRODUCTION

Organic photovoltaics (OPVs) have the potential to reduce the costs and environmental impacts associated with power generation by serving as lightweight, flexible, and easily processed solar power conversion devices made from abundant and non-toxic materials. OPV power conversion efficiencies (PCEs) have been steadily increasing, with a number of materials exhibiting efficiencies in the 7-10% range.[125-128] Nevertheless, many calculations indicate that OPVs should be able to reach much higher efficiencies, suggesting substantial room for improvement if one can understand the factors that limit device performance.[129-130]

The general path toward higher efficiency OPVs seems straightforward: it involves harvesting a broader range of the solar spectrum with lower band gap materials while maintaining energetic landscapes that favor exciton dissociation.[131] The task is complicated by the need to simultaneously optimize donor/acceptor phase morphology for efficient charge transport[132-133] as well as suppress recombination losses both in the bulk[73, 80, 134] and at electrode interfaces.[135-137] Despite significant progress in this field, successful strategies to achieve these goals remain elusive, and in many cases depend on a deeper understanding of the mechanisms underpinning the loss processes.

The highest efficiency OPVs at present are bulk heterojunction (BHJ) cells that make use of photoinduced charge transfer between electron donor (typically a conjugated polymer) and electron acceptor (often a fullerene derivative) materials. Numerous reports have identified the formation of charge-transfer (CT) states at the polymer/fullerene interface in these blends, which can be excited directly with light, or formed by recombination of electron-hole pairs.[38, 78, 81, 138-139] While spectroscopic evidence of charge-transfer states is observed in most polymer/fullerene blends, its spatial form and role in charge separation are still debated. Some studies have proposed that successful photocurrent generation likely bypasses the charge-transfer state in favor of direct free charge formation across the donor/acceptor interface,[79, 140] but others report that charge generation via the lowest energy charge-transfer state proceeds with high efficiency.[78, 141] Regardless of whether the charge-transfer state is a key intermediate for charge formation, whether it is a trap state that mediates charge carrier recombination, or both, there is a large body of empirical evidence (such as the relationship between open-circuit voltage and charge-transfer state energy) indicating that charge-transfer state properties correlate with device performance.[73, 83, 142-143]

Many studies have concluded that charge carrier recombination via charge-transfer states limits the open-circuit voltage (V_{OC}).[38, 73, 82-84, 144] Initially, the energy of the excited charge-transfer state (E_{CT}) and the electronic coupling between the initial and final states of charge transfer were thought to dominate recombination losses.[38, 83-84, 144] However, more recent work has gone beyond the role of energetics to study the spatial density of recombination centers.[73] For instance, Vandewal and co-workers studied the effects of donor/acceptor interfacial area, showing that a reduction in the spatial density of charge-transfer states (N_{CT}) could lead to increased V_{OC}.[82] However, most studies have not reported measurements of N_{CT} because the most common

experimental probes measure the product of N_{CT} and donor/acceptor electronic coupling.[83] Even those studies that report qualitative changes in N_{CT} usually do so in systems with low donor/acceptor ratios and by the implicit assumption that under specific film fabrication conditions the degree of electronic coupling will remain invariant, allowing the authors to attribute variations in sub-gap photocurrent to variations in N_{CT}.[82]

Here, we investigate V_{OC} losses in organic photovoltaic devices made from selenium-substituted polymer donors blended with fullerene acceptors. We individually evaluate the effects of charge-transfer state energy, spatial density of charge-transfer states, and electronic coupling between the ground-state polymer/fullerene complex and excited charge-transfer state. We find that N_{CT} and electronic coupling both increase upon Se substitution, but the increase in N_{CT} is more substantial and has a significant impact on V_{OC}. The increase in N_{CT} that we calculate from device performance is consistent with the more intermixed polymer/fullerene morphology that we observe by electron microscopy and electron diffraction.

2.2 RESULTS AND DISCUSSION

2.2.1 *Selenium Substitution in an Indacenodithiophene Polymer Electron Donor Series*

Figure 2.1 shows the series of four structurally similar polymers that we studied. The polymers are distinguished by varying either the selenium substitution on the indacenodithiophene unit or by aromatic ring fusion of the diphenyl substituents of the quinoxaline. We synthesized PIDT-PhanQ and PIDT-PhQ following previous reports,[145] and prepared PIDSe-PhanQ and PIDSe-PhQ via Stille coupling. The detailed synthetic methods and structural characterization are given in Section 2.4.

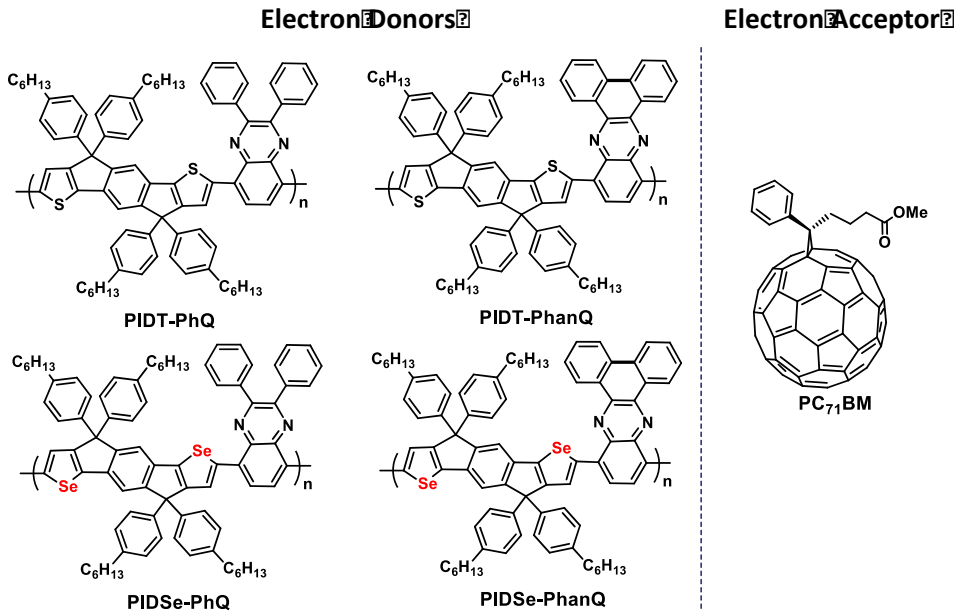

Figure 2.1. Molecular structures of the donor polymers and acceptor fullerene used in this study.

Figure 2.2a shows UV-Vis absorption spectra of the neat polymer films, showing that Se atom substitution leads to a lower energy onset of the thin film absorption spectra. This corresponds to a lower energy optical band gap of 1.53 eV for PIDSe-PhanQ compared to 1.70 eV for PIDT-PhanQ, and 1.65 eV for PIDSe-PhQ compared to 1.79 eV for PIDT-PhQ. Figure 2.2b shows a similar trend of redshifting for the polymer emission spectra with Se substitution. This decrease in optical gap upon Se substitution for S on the indacenodithiophene unit is consistent with previous reports and is generally attributed to a lower LUMO energy arising from increased Se atom polarizibility compared to S.[146] In Table 2.1, we summarize the UV-Vis absorption and cyclic voltammetry data, confirming that the drop in band gap energy for both Se-substituted polymers corresponds mainly to a decrease in reduction potential (LUMO position).

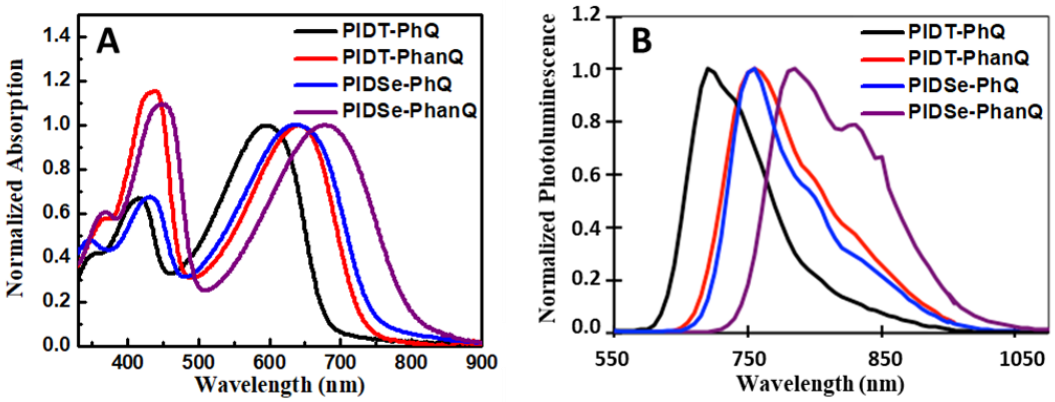

Figure 2.2. Normalized (a) absorption and (b) photoluminescence spectra of PIDT-PhQ, PIDT-PhanQ, PIDSe-PhQ and PIDSe-PhanQ neat polymers in thin films.

Table 2.1. Molecular weight (Mw), polydispersity index (PDI), highest occupied molecular orbital (HOMO) energy, lowest unoccupied molecular orbital (LUMO) energy, and optical band gap for polymers PIDSe-PhanQ, PIDT-PhanQ, PIDSe-PhQ, and PIDT-PhQ.

Polymer	**Mw** (k)	**PDI**	**HOMO** (eV)[a]	**LUMO** (eV)[a]	**Band Gap** (eV)
PIDSe-PhanQ	61.1	1.75	-5.11	-3.47	1.64[b] (1.53)[c]
PIDT-PhanQ	82.4	2.84	-5.14	-3.36	1.78 (1.70)
PIDSe-PhQ	62.5	1.66	-5.10	-3.36	1.74 (1.65)
PIDT-PhQ	68.2	2.42	-5.13	-3.31	1.82 (1.79)

[a] The HOMO and LUMO energies are approximated from cyclic voltammetry. [b] Calculated from the difference between HOMO and LUMO values. [c] Calculated from absorption onset of the thin film spectra.

2.2.2 *Polymer:Fullerene Bulk Heterojunction Device Performance*

We study the effect of these small variations in polymer structure on photovoltaic device performance. Figure 2.3 and Table 2.2 summarize the photovoltaic external quantum efficiencies (EQE_{PV}), current-voltage (JV) characteristics, and power conversion efficiency (PCE) averaged over 20 devices of each type for the four polymers in bulk heterojunction (BHJ) device structures.

We observe lower overall efficiency along with a significant open-circuit voltage (V_{OC}) loss of 120 – 130 mV upon Se substitution. Figure 2.3b also shows redshifted photocurrent generation in Se-substituted devices. While this redshift is partly due to the lower band gap in the Se-substituted polymers, Figure A.1 shows that the absorption features in the BHJ blends extend to even lower energies than the onset of the neat materials' absorption. We attribute this low-energy absorption feature to direct excitation from the neutral ground state to the excited charge-transfer state.

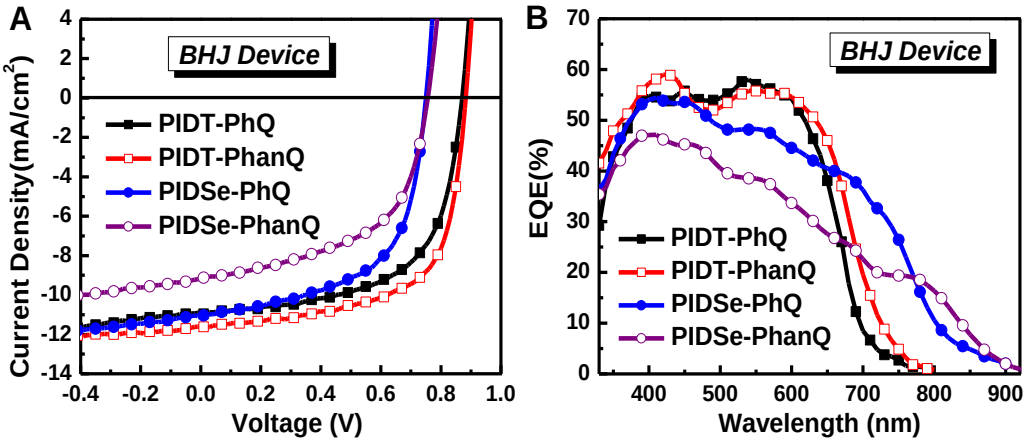

Figure 2.3. a) Current-voltage curves taken under 1 sun illumination and b) photovoltaic external quantum efficiency (EQE_{PV}). The current-voltages curves show a large open-circuit voltage (V_{OC}) drop upon selenium-substitution in the donor polymer when the donor and acceptor materials are intimately mixed in the bulk heterojunction (BHJ) device configuration.

Table 2.2. Short-circuit current density (J_{sc}), open-circuit voltage (V_{OC}), fill factor (FF), and power conversion efficiency (PCE) for bulk heterojunction polymer/fullerene devices under 1 sun illumination.

Active Layer	$\mathbf{J_{sc}}$ (mA cm^{-2})	$\mathbf{V_{oc}}$ (V)	**FF**	**PCE** (%)[a]
PIDSe-PhanQ:$PC_{71}BM$	9.16 ± 0.17	0.75 ± 0.01	0.57 ± 0.02	3.93 ± 0.18
PIDT-PhanQ:$PC_{71}BM$	11.61 ± 0.18	0.88 ± 0.01	0.65 ± 0.02	6.63 ± 0.22
PIDSe-PhQ:$PC_{71}BM$	11.04 ± 0.22	0.75 ± 0.01	0.59 ± 0.02	4.89 ± 0.20
PIDT-PhQ:$PC_{71}BM$	10.86 ± 0.20	0.87 ± 0.01	0.62 ± 0.02	5.91 ± 0.24

[a] Error values represent the standard deviation of the mean for 20 devices.

2.2.3 *Characterizing Charge-Transfer State Energies by Fitting Sub-Gap Photocurrent*

Since the energy,[38] number density,[73, 82] and electronic coupling[83-84] of charge-transfer states have all been linked to V_{OC}, we next explore the relative importance of these parameters in explaining the 120 – 130 mV lower V_{OC} of selenophene versus thiophene polymers in the bulk heterojunction devices.

Based on the electroluminescence spectra of the charge-transfer states and the sub-gap EQE_{PV} spectra (Figure 2.4), we determine that the energies of the charge-transfer states are similar within ~10 meV for PhanQ systems irrespective of Se substitution, suggesting that the 130 mV drop in V_{OC} cannot be explained by a change in charge-transfer state energy in the PhanQ blends. We find that the charge-transfer state energy changes by about 60 meV upon Se substitution in PhQ systems, which may account for up to ~50 % of the V_{OC} drop in the PhQ blends. In both cases, more than energetics must be responsible for the lower V_{OC} upon Se substitution.

Figure 2.4 shows the lock-in detected EQE_{PV} curves and the normalized charge-transfer state electroluminescence spectra that we use to extract the charge-transfer state energies and quantify the voltage deficit, defined as $q^{-1}E_{CT} - V_{OC}$,[73] for each BHJ device.[38] We observe infrared charge-transfer state emission at similar energies and peak widths commonly measured for polymer/fullerene blends.[81] The peak electroluminescence intensity occurs near the EQE_{PV} onset, as is expected for charge-transfer state emission.[74] We observe a distinct shoulder in the low energy portion of the EQE_{PV} spectrum for PhQ blends and a steeper low energy EQE_{PV} drop off in PhanQ blends. The energy difference of ~350 meV between the EQE_{PV} shoulder and the peak electroluminescence intensity is consistent with Stokes shifts previously reported for charge-transfer states in polymer/fullerene blends.[87]

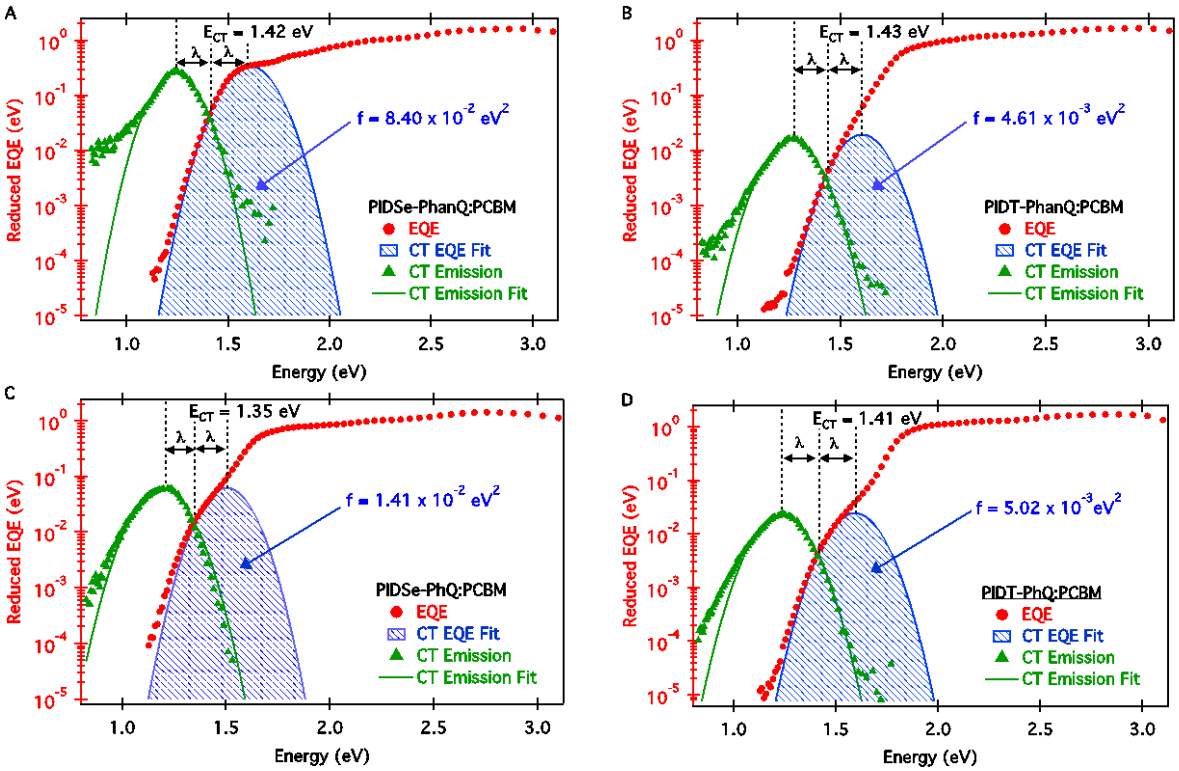

Figure 2.4. Reduced external quantum efficiencies (EQE, red circles) and normalized electroluminescence spectra (green triangles) for bulk heterojunction devices of a) PIDSe-PhanQ:PCBM b) PIDT-PhanQ:PCBM c) PIDSe-PhQ:PCBM and d) PIDT-PhQ:PCBM. Charge-transfer state absorption fit by Equation 2.3 (blue curves) demonstrates increased charge-transfer state absorption intensity and coupling constant (f) value for Se-substituted devices. Fits of electroluminescence spectra according to Equation 2.1 (green curves) are used to constrain the charge-transfer state energy (E_{CT}) and reorganization energy (λ) during the charge-transfer state absorption fit. Electroluminescence spectra are scaled to the height of the respective CT absorption band in order to emphasize the definitions of E_{CT} and λ.

We extract the charge-transfer state energies and reorganization energies (λ) by fitting *both* the charge-transfer state electroluminescence and EQE_{PV}. Literature reports commonly find E_{CT} and λ by fitting the low energy portion of the EQE_{PV} spectrum,[82-83, 86, 143] though a smaller number of studies report simultaneous fits of both data sets.[38, 87] To reduce the error associated with fitting

only part of the Gaussian curve in the charge-transfer state absorption region of EQE_{PV}, we first constrain the sum $E_{CT} + \lambda$ by fitting the electroluminescence spectrum according to the reduced equation for the charge-transfer state radiative decay rate (I_{rad}) derived from Marcus theory (Equations 2.1 – 2.2).[147-148] Using these constrained values, we then fit the low energy portion of the EQE_{PV} spectrum with the reduced equation for photocurrent generation from direct excitation of the charge-transfer complex (Equations 2.3 – 2.4).[38] We provide additional electroluminescence spectra and further explanation of our fitting procedure in Appendix A.

$$\frac{I_{rad}(E)}{E} = \frac{f_{emission}}{\sqrt{4\pi\lambda kT}} \exp\left(\frac{-(E_{CT}-\lambda-E)^2}{4\lambda kT}\right) \quad (2.1)$$

$$f_{emission} = \frac{64\,\pi^4}{3h^4c^3} n^3 V^2 \Delta\mu^2 \left[6.24 * 10^{-25} \frac{eVcm^3}{D^2}\right] \quad (2.2)$$

$$EQE_{PV}(E)E = \frac{f}{\sqrt{4\pi\lambda kT}} \exp\left(\frac{-(E_{CT}+\lambda-E)^2}{4\lambda kT}\right) \quad (2.3)$$

$$f = \eta N_{CT} 2d \frac{8\pi^3}{3hc} nV^2 \Delta\mu^2 \left[6.24 * 10^{-25} \frac{eVcm^3}{D^2}\right] \quad (2.4)$$

In Equations 2.1-2.4, E is the photon energy [eV], k is Boltzmann's constant [eV K^{-1}], T is temperature [K], λ is the reorganization energy [eV], E_{CT} is the excited CT state energy [eV], $f_{emission}$ is the coupling constant associated with the emission process [eV^{-1} s^{-1}],[38] f is the coupling constant associated with the absorption process [eV^2],[38] h is Planck's constant [eV s], c is the speed of light [cm s^{-1}], n is the refractive index, η is the internal photon to electron conversion efficiency, N_{CT} is the available density of charge-transfer states [cm^{-3}], d is the film thickness [cm], V is the electronic coupling matrix element [eV] between the initial and final states of electron transfer (i.e. the neutral ground state and CT exciton), and Δμ is the difference in dipole moment between the

initial and final states of electron transfer [D]. In Section A.4 of Appendix A, we give an explanation of the unit conversion included in Equations 2.2 and 2.4.

Popularized by Vandewal and co-workers, the Marcus formalism is currently widely used to characterize charge-transfer state properties in polymer/fullerene blends.[38, 82-83, 86, 143, 149] While there is general agreement that the sub-gap absorption features are associated with interfacial charge-transfer states, the width of these features also likely has contributions from energetic disorder in the band tails.[150-152] While a deeper comparison of the available models is beyond the scope of the current discussion, we note that the effect of disorder can be represented in analyses based on Equations 2.1 – 2.4 as fixed deviations in E_{CT} and λ from the ideal case.[149] In other words, increased disorder lowers the E_{CT} extracted from a Marcus analysis, having the effect of decreasing the expected V_{OC}. It should therefore be noted that, under the current model, changes in E_{CT} upon Se substitution represent a combined change in E_{CT} and disorder. However, our main conclusions are unaffected by our use of the classic formalism rather than separately extracting disorder, since our analysis focuses on cases where changes in V_{OC} cannot be accounted for solely by changes in the experimentally measured E_{CT} (which folds in changes in disorder).

Figure 2.4 gives the values of E_{CT} for each BHJ device. Our fits indicate that PIDT-PhQ, PIDSe-PhanQ, and PIDT-PhanQ BHJ devices all have similar charge-transfer state energies (1.41, 1.42, and 1.43 eV, respectively), while the PIDSe-PhQ BHJ device has a lower charge-transfer state energy (1.35 eV). However, both Se-substituted devices have a higher voltage deficit ($q^{-1}E_{CT} - V_{OC}$) compared to their thiophene counterparts, indicative of larger recombination losses. Most notably, PIDSe-PhanQ has significantly larger V_{OC} loss than the other three devices, despite having a charge-transfer state energy comparable to the thiophene devices. We next turn to investigate the

origin of the increased recombination in the selenophene systems, especially the PIDSe-PhanQ blend.

2.2.4 *Characterizing Recombination Loss Using the Coupling Constant Value*

Though previous reports have identified both electronic coupling[84] and spatial density of charge-transfer states[73, 82] as possible factors affecting recombination losses, few studies are able to separately measure these values.[83] Most studies rely on coupling constant (f) values, which contain the product of electronic coupling with the spatial density of charge-transfer states (see Equation 2.4).[38, 82-83, 153] A few experimental[84] and computational[154-156] studies have estimated values for electronic coupling, and only one study to our knowledge has determined a range of possible values for the spatial density of charge-transfer states.[73] We therefore present a comprehensive experimental study using the coupling constant to quantitatively assess the magnitudes of charge-transfer state density and electronic coupling as well as their effects on the open-circuit voltage.

We calculate the coupling constant using two separate approaches, and we find that both give increased coupling constant values for the Se-containing blends. First, we obtain coupling constant values by numerically integrating the EQE_{PV} fits to Equation 2.3, and we give the results in Figure 2.4.[38] Consistent with the increased recombination losses measured in the selenophene devices, we extract a larger coupling constant value for Se-substituted BHJ blends, with a ~2× increase (from 5.02×10^{-3} eV^2 to 1.41×10^{-2} eV^2) in PhQ systems and a nearly ~20× increase (from 4.61×10^{-3} eV^2 to 8.40×10^{-2} eV^2) in the PhanQ systems.

We also apply a second approach to calculate the coupling constants by using the voltage deficit ($q^{-1}E_{CT} - V_{OC}$) along with the charge-transfer state electroluminescence quantum yield (EQE_{EL}), as outlined in Equation 2.5 and previously described by Vandewal et al.[38]

$$V_{oc} = \frac{E_{\mathrm{CT}}}{q} + \frac{kT}{q}\ln\left(\frac{J_{\mathrm{sc}}h^3c^2}{fq2\pi(E_{\mathrm{CT}}-\lambda)}\right) + \frac{kT}{q}\ln(EQE_{\mathrm{EL}}) \quad (2.5)$$

As we will show, we obtain similar trends using this approach, confirming that the coupling constant increases upon Se substitution whether determined from photovoltaic EQE or electroluminescence quantum yield data.

We note that there are two separate terms in Equation 2.5 that can contribute to the $q^{-1}E_{CT} - V_{OC}$ loss, and we present their values in Table 2.3. We find that the majority of V_{OC} loss upon Se-substitution is caused by the term including the coupling constant, and the portion of V_{OC} loss caused by the term involving EQE_{EL} hardly changes upon Se substitution. Table 2.3 shows a significantly voltage drop of 50 – 100 mV upon Se-substitution for the f-dependent recombination term. Conversely, the difference in EQE_{EL} can only account for a V_{OC} drop of 20 mV, though there is certainly a measurable decrease in EQE_{EL} upon Se substitution (Figure 2.5). This observation further supports our method of using the coupling constant to quantify the major differences between the selenophene and thiophene OPV systems leading to V_{OC} loss.

Table 2.3. Recombination losses causing the open-circuit voltage (V_{OC}) to decrease compared to the charge-transfer state energy (E_{CT}) partitioned into terms depending on the electroluminescence quantum yield (EQE_{EL}) or coupling constant (f) according to Equation 2.5.

Active Layer	$q^{-1}E_{CT}$-V_{OC} (V)	$\frac{kT}{q}\ln(EQE_{EL})$ (V)	$\frac{kT}{q}\ln\left(\frac{J_{sc}h^3c^2}{fq2\pi(E_{CT}-\lambda)}\right)$ (V)
PIDSe-PhanQ:$PC_{71}BM$	0.67	0.35	0.32
PIDT-PhanQ:$PC_{71}BM$	0.55	0.33	0.22
PIDSe-PhQ:$PC_{71}BM$	0.60	0.33	0.27
PIDT-PhQ:$PC_{71}BM$	0.54	0.31	0.23

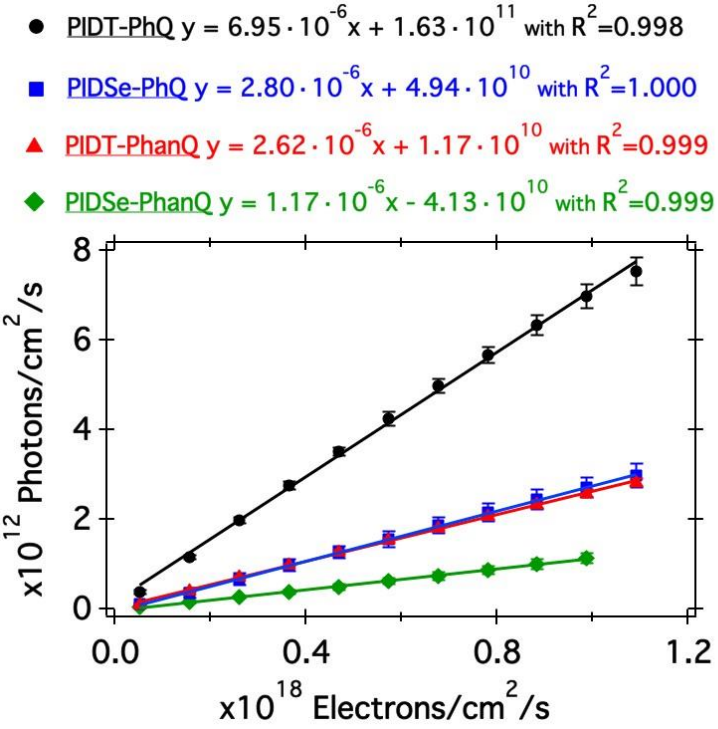

Figure 2.5. Electroluminescence quantum yields for PIDT-PhQ, PIDT-PhanQ, PIDSe-PhQ, and PIDSe-PhanQ blended with $PC_{71}BM$ in BHJ device structures, presented as emitted photon flux integrated over the charge-transfer state electroluminescence spectra given in Section A.3 of Appendix A plotted over a range of injected current density. We show very small variation in the electroluminescence quantum yield over the range in current densities that we probe, corresponding to a linear relationship.

The careful reader may notice that the recombination term including EQE_{EL} in Equation 2.5 analytically quantifies the magnitude of voltage loss due to nonradiative recombination, and the f-containing term has been described as a measure of radiative recombination.[157-158] Consistent with previous studies, our analysis summarized in Table 2.3 shows that nonradiative charge-transfer state recombination may account for over half of the total V_{OC} loss for a given system.[153, 158] However, it appears that the nonradiative term is not significantly affected by Se-substitution, despite the fact that > 99 % of charge-transfer state recombination is nonradiative. We find this to be an intriguing observation for future investigation. In the current study, we focus on the loss term dependent on the coupling constant, which accounts the most significant voltage decrease upon Se substitution relative to the S-containing systems.

We solve Equation 2.5 in order to calculate the coupling constant from electroluminescence quantum yield data and the experimentally observed V_{OC} (f_2, Table 2.4), and we give the resulting equation as Equation 2.6. We use this value of f_2 to verify the f value we obtain in Figure 2.4 from fitting the low energy portion of the EQE_{PV} spectrum.

$$f_2 = \frac{J_{sc}h^3c^2}{q2\pi(E_{CT}-\lambda)EQE_{EL}}\mathrm{Exp}\left(\frac{E_{CT}-V_{oc}}{kT}\right) \quad (2.6)$$

Table 2.4 shows that f_2 is similar to the f value from our fitting procedure in Figure 2.4, with percent variation of only 15 – 48 %. All values are the same order of magnitude regardless of the calculation method, and the trend of increasing f upon Se substitution is consistent across both methods of finding the f value.

Table 2.4. Comparison of the coupling constant value from Equation 2.6 using the experimental V_{OC} deficit and electroluminescence quantum yield (f_2) with the coupling constant value obtained in Figure 2.4 by fitting the low-energy intersection between the EQE_{PV} and electroluminescence spectrum (f).

Active Layer	$\mathbf{f_2}$ (eV^2)	**f** (eV^2)	**Percent Variation**
PIDSe-PhanQ:$PC_{71}BM$	9.81×10^{-2}	8.40×10^{-2}	15.4
PIDT-PhanQ:$PC_{71}BM$	2.82×10^{-3}	4.61×10^{-3}	48.4
PIDSe-PhQ:$PC_{71}BM$	1.67×10^{-2}	1.41×10^{-2}	16.9
PIDT-PhQ:$PC_{71}BM$	4.07×10^{-3}	5.02×10^{-3}	20.9

2.2.5 *Separating the Effects of Electronic Coupling and Density of Charge-Transfer States on Open-Circuit Voltage Losses*

While the coupling constant values obtained in Section 2.2.4 depend on both electronic ($V\Delta\mu$) and spatial (N_{CT}) molecular interactions, we next show that the higher coupling constant value upon Se substitution mainly results from increased N_{CT}. Based on the charge-transfer state photoluminescence lifetime and photoluminescence quantum yield, we separate the effects of electronic coupling and N_{CT}, and we conclude that a significant portion of V_{OC} loss upon Se substitution is due to increased spatial density of charge-transfer states, while electronic coupling plays a smaller role.

Figure 2.6b and Figure 2.6d show the photoluminescence spectra for each BHJ blend. We observe two photoluminescence peaks near 1.25 eV and 1.70 eV. As is commonly observed in OPV blends, we find that the photoluminescence signatures of the individual donor/acceptor components are highly quenched in all blends, though not completely eliminated.[81, 85] The peak near 1.25 eV closely matches the charge-transfer state emission peak measured by electroluminescence (see Figure A.5 – Figure A.8 in Appendix A), and the peak near 1.70 eV corresponds to unquenched emission from the neat materials (Figure 2.2b). We measure the

photoluminescence spectra using lock-in techniques, and we find that the photoluminescence quantum yield of the charge-transfer state is around 100 times lower than that of the neat polymers. We observe similar luminescence intensities for all BHJ films with no clear trend in photoluminescence quantum yield upon Se substitution.

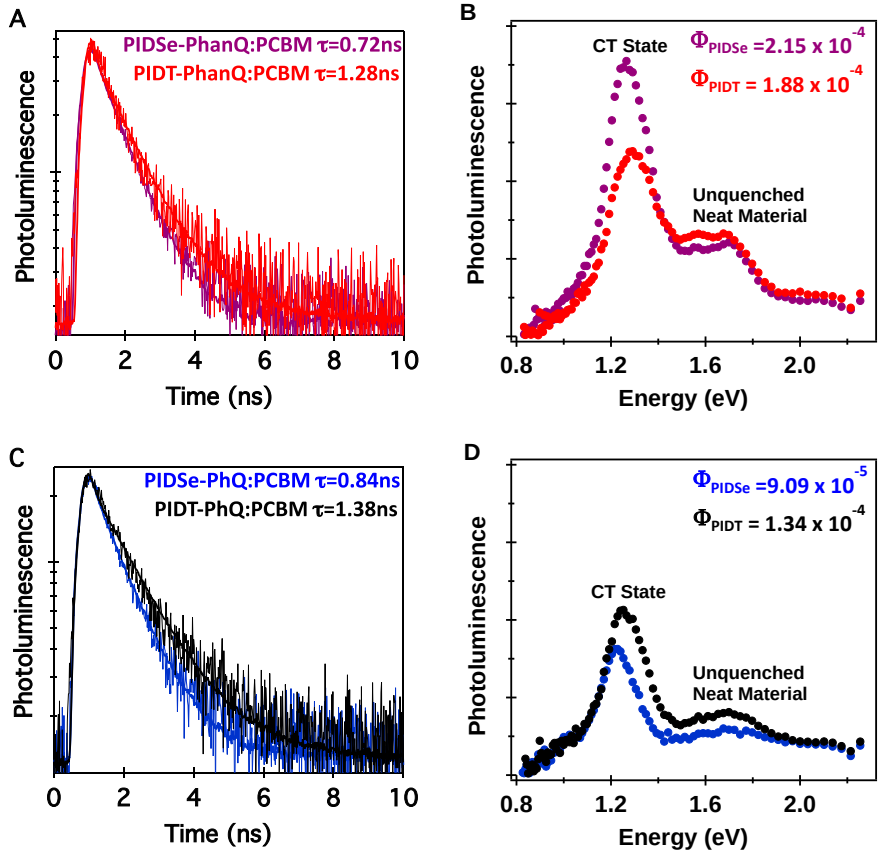

Figure 2.6. Normalized time-resolved photoluminescence of the charge-transfer state for a) PIDSe-PhanQ:PCBM and PIDT-PhanQ:PCBM and b) PIDSe-PhQ:PCBM and PIDT-PhQ:PCBM with lifetimes extracted from a monoexponential decay fit. The charge-transfer state photoluminescence quantum yields for c) PIDSe-PhanQ:PCBM and PIDT-PhanQ:PCBM and d) PIDSe-PhQ:PCBM and PIDT-PhQ:PCBM estimated by the relative intensity of the 1.24 eV peak. Combining lifetimes and photoluminescence quantum yield in Equation 2.7 gives a slightly faster radiative charge-transfer state lifetime for Se-substituted blends.

We measure time-resolved photoluminescence decays for both the charge-transfer state (Figure 2.6a and Figure 2.6c) and the unquenched neat materials (Figure A.11). Figure 2.6a and Figure 2.6c show normalized photoluminescence decays probed at energies below 1.18 eV, which exhibit monoexponential decays with nanosecond-scale lifetimes. These lifetimes are similar to previously reported results for polymer/fullerene charge-transfer states, which range from 0.4 – 6.8 ns.[73, 85, 156, 159-161] The single-exponential fits (performed as reconvolution fits of a single-exponential with the instrument response function, see Section A.8 of Appendix A) yield faster photoluminescence decays for Se-substituted blends, corresponding to a faster total charge-transfer state lifetime including both radiative and nonradiative processes. Figure A.11 in Appendix A shows the photoluminescence decays of the unquenched neat materials probed at 1.77 eV, which are distinct from the charge-transfer state lifetime.

Equations 2.1 and 2.2 show that the rate of charge-transfer state emission depends on electronic coupling, but not the spatial density of charge-transfer states. Measuring the rate of charge-transfer state emission therefore allows us to isolate variations in electronic coupling from the spatial density of charge-transfer states and obtain numeric values for both variables. Integrating Equation 2.1 with respect to energy gives the rate constant for radiative charge-transfer state decay (k_{rad}), which we experimentally quantify using the charge-transfer state lifetime (τ) and the photoluminescence quantum yield (Φ_{rad}).[148]

$$k_{rad} = \frac{64\,\pi^4}{3\mathrm{h}^4 c^3} n^3 V^2 \Delta\mu^2 E_{rad} \left[6.24 * 10^{-25}\,\frac{eV cm^3}{D^2}\right] = \frac{\Phi_{rad}}{\tau} \qquad (2.7)$$

In Equation 2.7, E_{rad} is the average emission energy [eV], and $\Delta\mu$ represents the change in dipole moment between the ground-state charge-transfer complex and the excited charge-transfer

exciton, which we approximate as 15 D for all blends. This Δμ value has been used in previous reports when estimating electronic coupling in organic contact radical ion pairs.[162-163] The value of 15 D for Δμ is also slightly larger than the intramolecular dipole moment for excited polymer donors commonly used in organic photovoltaic systems.[164] We further support 15 D as a good estimate for Δμ by estimating an upper limit of Δμ for nearest neighbor D/A pairs, in the case where charge transfer is absolute. This value would be given as q × r, where q is a unit of charge and r is the separation of the electron/hole pair upon photoexcitation. We estimate r as 0.5 nm, which is on the order of lattice parameters measured for polymer/fullerene cocrystals.[165] The upper limit would thus be given as $\Delta\mu = q \times r = (1.602 \times 10^{-19}\ C) \times (0.5 \times 10^{-9}\ m) / (3.34 \times 10^{-30}\ Cm/D) = 24$ D.

We note that the numerical value that we estimate for Δμ has no effect our main conclusion, which is that N_{CT} dominates recombination losses. With the photoluminescence lifetime experiment, we measure the quantity VΔμ (see Equation 2.7). We then calculate the value of N_{CT} using the total quantity VΔμ. We estimate a numerical value for Δμ only for illustrative purposes to aid readers in more direct comparison to current literature discussions by estimating a reasonable value for the electronic coupling matrix element (V).

We summarize the electronic coupling values in Table 2.5 and find that electronic coupling does increase slightly upon Se substitution. However, the increase in electronic coupling could only account for a small portion of the observed V_{OC} loss if N_{CT} were to remain constant. We estimate that this slight increase in electronic coupling would account for 14 +/- 3.0 % of the 130 mV V_{OC} decrease upon Se substitution in PhanQ blends and 4.6 +/- 1.4 % of the 120 mV V_{OC} decrease in PhQ blends (see discussion in Section A.5 of Appendix A).

We find that increased N_{CT} is responsible for a larger portion of V_{OC} loss. By inserting our measured V and f values into equation 2.3, we find that N_{CT} is tripled upon Se substitution in PhQ blends and increases by over an order of magnitude upon Se substitution in PhanQ blends (values given in Table 2.5). This substantial increase in N_{CT} would account for 52 +/- 20% of the 130 mV V_{OC} decrease upon Se substitution in PhanQ blends and 29 +/- 11% of the 120 mV V_{OC} decrease in PhQ blends (see discussion in Section A.5 of Appendix A). The remaining V_{OC} loss is primarily due to the decrease in charge-transfer state energy and the decrease in electroluminescence quantum yield.

Table 2.5. Values for electronic coupling (V) and spatial density of charge-transfer states (N_{CT}) as determined by time-resolved photoluminescence and EQE_{PV} measurements.

Active Layer	**N_{CT}** ($\times 10^{21}$ cm^{-3})	**Electronic Coupling, V** (meV)
PIDSe-PhanQ:$PC_{71}BM$	62 ± 27	30 ± 6
PIDT-PhanQ:$PC_{71}BM$	4.5 ± 1.8	21 ± 4
PIDSe-PhQ:$PC_{71}BM$	19 ± 9.8	19 ± 5
PIDT-PhQ:$PC_{71}BM$	5.8 ± 4.3	17 ± 6

2.2.6 *Relating the Density of Charge-Transfer States to Thin-Film Morphology*

We note that the N_{CT} values in Table 2.5 are large compared to the expected fullerene density in the film (~10^{21} molecules cm^{-3}). However, it is important to distinguish that N_{CT} corresponds to the total density of available charge-transfer states (i.e. the total number of possible donor-acceptor interactions), not the density of simultaneously occupied charge-transfer states.[149] Therefore, the results suggest that ~5 – 60 fullerene states may be spatially accessible to each polymer donor unit.[149] While it seems surprising that N_{CT} could be ~5 – 60 times larger than the molecular density, Burke et al. similarly concluded that ~32 charge-transfer states per molecule

were necessary to account for common $q^{-1}E_{CT} - V_{OC}$ deficits, and Street et al. estimated that electronic states may be delocalized over 20 – 30 molecules in polymer/fullerene blends.[151] The consistency between these separate results might imply a manifold of charge-transfer states involving donor/acceptor interactions beyond the nearest-neighbor pairs.[73] This further implies that even molecules not directly located at a heterojunction may participate in a charge-transfer state. Though the values are high, we note that these N_{CT} values are comparable to densities of states in inorganic materials with delocalized band structures, which range from $10^{19} - 10^{23}$ cm^{-3}.[166-169] While we take our results to be in experimental agreement with the analysis of Burke et al., we believe that future work is needed to evaluate the origin of these high N_{CT} densities in organic systems.

Finally, we turn to speculate on a possible cause for the higher N_{CT} values for the selenophene blends. Several reports imply that the degree of molecular mixing, as well as the interaction range between donor/acceptor pairs may both contribute to N_{CT}.[73, 142, 165, 170] Figure 2.7 depicts this relationship schematically. The green arrow represents a possible charge-transfer complex, which forms between a donor/acceptor pair. N_{CT} may increase when donor/acceptor molecules are more intimately mixed, because a given donor molecule would have access to more acceptor molecules within the CT delocalization area, and vice versa. N_{CT} may also increase if the degree of molecular mixing does not change, but the charge-transfer state is delocalized over a larger area. One possible cause of CT state delocalization is increased crystallinity.[86] Although carrier delocalization in organic electronics is generally viewed as beneficial,[79-80] if both molecular mixing and CT state delocalization increase simultaneously, we may expect N_{CT} to be relatively high. This speculative hypothesis is qualitatively consistent with our morphological studies on the polymer/fullerene BHJ blends, which we present below.

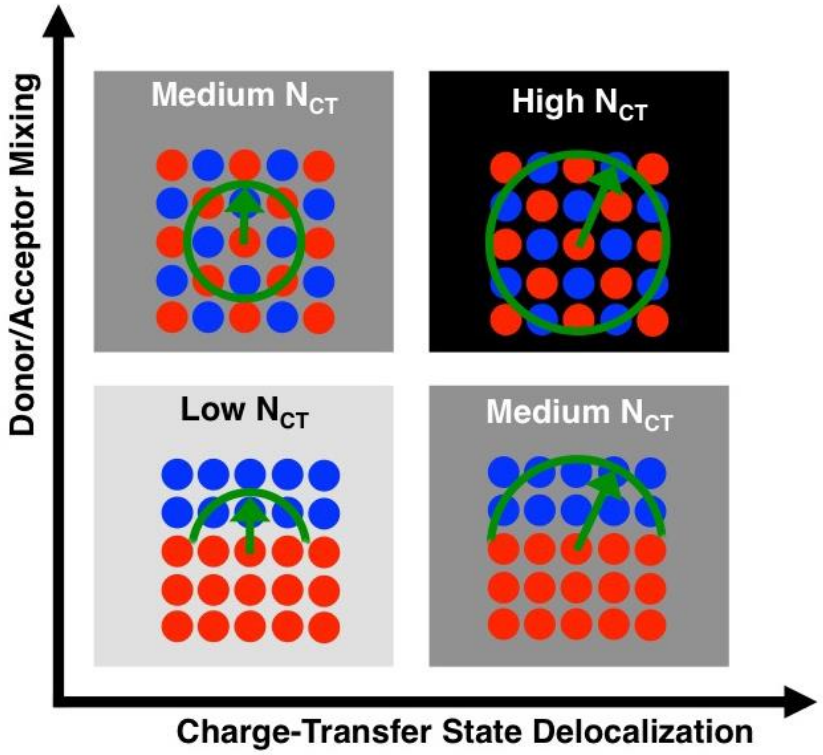

Figure 2.7. Schematic representation of a possible relationship between donor/acceptor morphology and charge-transfer state density (N_{CT}). We propose that N_{CT} may increase due to more intimate donor/acceptor mixing, increased charge-transfer state delocalization, or both.

Figure 2.8 shows bright field transmission electron microscopy (TEM) images for the BHJ blends as well as the selected area electron diffraction (SAED) patterns with a comparison of the SAED radial intensity profiles. The TEM images show 10 – 100 nm scale phase regions in the thiophene blends. We do not observe phase segregation on this scale in the selenophene blends, despite the higher Z-contrast of Se compared to S. This result suggests that there is finer donor/acceptor mixing in the selenophene blends. Increased mixing upon Se substitution would be consistent with the higher N_{CT} values that we observe and would place the selenophene blends on the upper portion of our cartoon in Figure 2.7 compared to the thiophene blends.

Figure 2.8 also shows a sharp diffraction ring at Q = 0.613 nm^{-1} (1.63 nm) for the PIDSe-PhanQ:PCBM blend, the BHJ with the largest voltage deficit and largest N_{CT} value. The diffraction ring indicates a highly ordered feature. It is important to note that the ring is not present in the radial profiles for either neat PIDSe-PhanQ or neat fullerene. The diffraction ring is entirely absent in the PIDT-PhanQ:PCBM blend, and both the PIDSe-PhQ:PCBM and the PIDT-PhQ:PCBM blends show only a weak signal near Q = 0.59 – 0.73 nm^{-1} (1.7 – 1.4 nm). This sharp diffraction ring in the PIDSe-PhanQ BHJ indicates that there is some molecular ordering in this system that is mostly absent in the other BHJ blends and entirely absent in the neat materials. We confirm the presence of this uniquely ordered feature in the PIDSe-PhanQ:PCBM blend using grazing incidence wide angle x-ray scattering (GIWAXS) experiments (discussed in Section A.9 of Appendix A). We may interpret the highly-ordered feature as a polymer/fullerene cocrystalline structure or as polymer packing induced by the presence of fullerene.[165, 171-172] The increase in molecular ordering may place the PIDSe-PhanQ:PCBM blend on the right side of our cartoon in Figure 2.7 and would be consistent with the increased N_{CT} value that we observe.

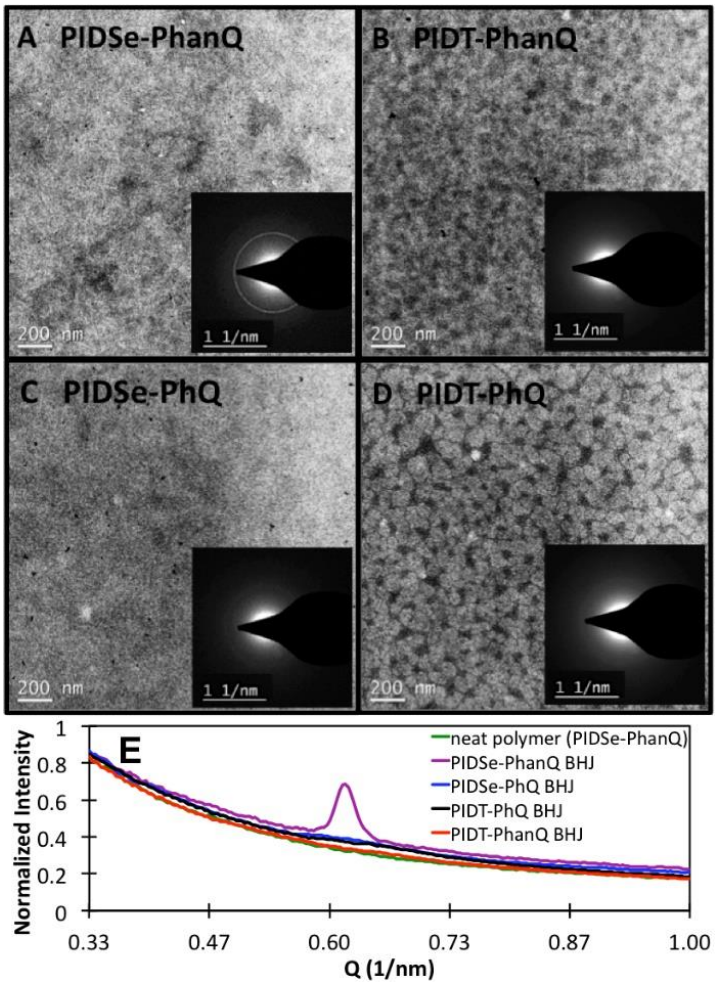

Figure 2.8. Transmission electron microscopy images and selected area electron diffraction profiles for a) PIDSe-PhanQ:PCBM b) PIDT-PhanQ:PCBM c) PIDSe-PhQ:PCBM and d) PIDT-PhQ:PCBM showing reduced phase separation in Se-substituted blends and a higher degree of fullerene-induced crystallization for the PIDSe-PhanQ:PCBM blend; e) radial intensity profile of SAED images, showing a sharp diffraction peak for PIDSe-PhanQ BHJ.

Taken together, we find that disrupted phase separation upon Se substitution and a fullerene-induced crystalline feature in the PIDSe-PhanQ BHJ blend are suggestive that N_{CT} may qualitatively correlate with thin-film morphology as depicted in Figure 2.7 and that rational morphological control of N_{CT} may be a viable route to reduce V_{OC} loss. Indeed, Figure 2.9 shows

that the Se-induced voltage deficit is substantially decreased in planar heterojunction devices with intentionally suppressed donor/acceptor mixing.

Figure 2.9 shows the current-voltage curves and EQE_{PV} for bilayer device structures, which must have reduced donor/acceptor interface area compared to the BHJ blends. We summarize the device performance metrics for the bilayer devices in Table 2.6. We observe lower EQE_{PV} signal from direct charge-transfer state absorption as well as a 30 – 40 mV drop in V_{OC} upon Se substitution for bilayer devices, which is significantly smaller than the 120 – 130 mV drop that we observe for the bulk heterojunction blends (Figure 2.3). The decreased voltage deficit in bilayer devices would be consistent with lower N_{CT} compared to the BHJ blends.

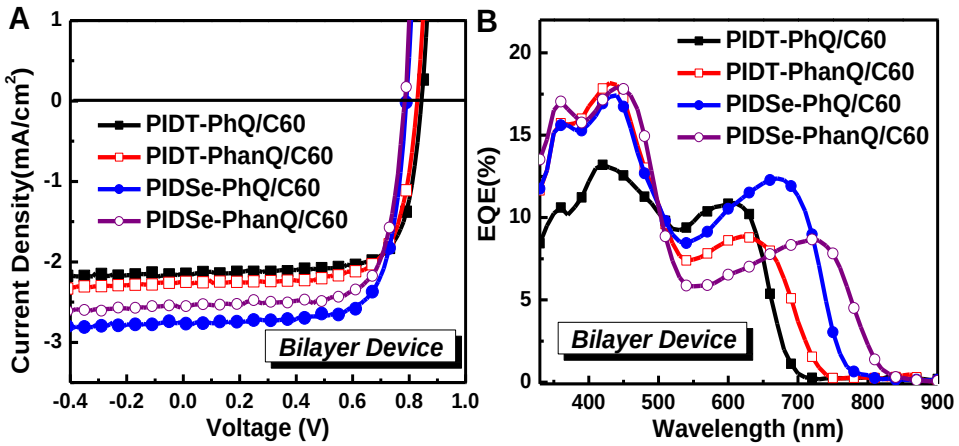

Figure 2.9. Bilayer device measurements, including a) current-voltage curves taken under 1 sun illumination and b) photovoltaic external quantum yield (EQE_{PV}). The current-voltages curves show a minimal open-circuit voltage (V_{OC}) drop upon selenium substitution in the donor polymer when interfacial area between the donor and acceptor materials is minimized in the bilayer structure.

Table 2.6. Bilayer device characteristics including short circuit current (J_{SC}), open-circuit voltage (V_{OC}), fill factor (FF) and power conversion efficiency (PCE).

Configuration	**Active Layer**	**Jsc** (mA cm^{-2})	**Voc** (V)	**FF**	**PCE** (%)
Bilayer	PIDT-PhQ/C_{60}	2.15 ± 0.12	0.84 ± 0.01	0.74 ± 0.01	1.34 ± 0.08
	PIDT-PhanQ/C_{60}	2.21 ± 0.13	0.83 ± 0.01	0.74 ± 0.01	1.36 ± 0.09
	PIDSe-PhQ/C_{60}	2.75 ± 0.15	0.80 ± 0.01	0.74 ± 0.01	1.63 ± 0.12
	PIDSe-PhanQ/C_{60}	2.56 ± 0.12	0.80 ± 0.01	0.73 ± 0.01	1.49 ± 0.10

2.3 CONCLUSIONS

We present a unique separation of the contributions of electronic coupling and density of charge-transfer states to open-circuit voltage losses in a series of polymer/fullerene blends. After evaluating a number of device and spectroscopic properties, our data suggest that increased recombination in Se-substituted devices leading to V_{OC} loss is strongly affected by a higher spatial density of charge-transfer states (N_{CT}). We first find the product of electronic coupling and N_{CT} by fitting the low energy portion of the EQE_{PV} spectrum. We show that this product increases for blends with higher V_{OC} loss. We then separate this product into electronic coupling and N_{CT} by measuring charge-transfer state photoluminescence lifetime and quantum yield. Using the time-resolved photoluminescence decays for charge-transfer state emission, we find that electronic coupling does increase upon Se substitution, but that a larger portion of the experimental V_{OC} loss is attributable to increased N_{CT}. Consistent with a recently published proposal,[73] the N_{CT} values extracted from our analysis ($4.51 \times 10^{21} – 6.22 \times 10^{22}$ cm^{-3}) seem uncomfortably large for a weakly interacting molecular system. To explain this discrepancy, we finally take the liberty to speculate on the spatial nature of charge-transfer states by correlating high N_{CT} values with intermixed morphology *and* fullerene-induced crystallization in the selenophene BHJ blends. Our work implies that both electronic coupling and N_{CT} are tunable with small changes in molecular

structure, and it implies that controlling these parameters is a route to intelligent molecular design for higher efficiency OPV devices. Future studies may find fruitful ground in focusing on understanding the relationship between N_{CT} and thin-film morphology in more detail.

2.4 SYNTHETIC DETAILS

2.4.1 *Materials*

4,4,9,9-tetrakis(4-hexylphenyl)-2,7-bis(trimethylstannyl)indaceno [1,2-*b*:5,6-*b*']diselenophene, 10,13-Dibromodibenzo[*a*,*c*]phenazine, 5,8-Dibromo-2,3-diphenylquinoxaline, PIDT-PhanQ, and PIDT-PhQ were made according to literature procedures.[145, 173] All other reagents were purchased from Sigma-Aldrich and used without further purification.

2.4.2 *Polymerization of PIDSe-PhQ*

To a degassed mixture of 4,4,9,9-tetrakis(4-hexylphenyl)-2,7-bis(trimethylstannyl) indaceno [1,2-*b*:5,6-*b*']diselenophene (139.3 mg, 0.105 mmol) and 5,8-Dibromo-2,3-diphenylquinoxaline (44.0 mg, 0.100 mmol), dissolved in toluene (3.5 mL), was added $Pd_2(dba)_3$ (1.8 mg, 2 μmol) and tri-o-tolylphosphine (2.4 mg, 8 μmol). The mixture was heated to reflux under a nitrogen atmosphere for 24 h. The mixture was cooled to room temperature and poured into methanol. The precipitated polymer was collected and washed in a Soxhlet extractor sequentially with methanol, acetone, and hexane, followed by extraction with chloroform. The chloroform extract was then passed through a plug of silica gel (2 cm dia., 4 cm long), eluting with chloroform. The polymer solution was then concentrated to ~10 mL and then poured into methanol. The precipitated polymer was collected and dried to yield the polymer as a blue-green

solid (119.2 mg, 94% yield). ^{1}H NMR (300 MHz, $CDCl_3$, δ): 8.05 (s, 2H), 7.87 (s, 2H), 7.64 (br m, 4H), 7.42 (br m, 8H), 7.25 (br d, 8H), 7.09 (br d, 8H), 2.58 (br t, 8H), 1.60 (br m, 8H), 1.28 (br m, 24H) 0.86 (br t, 12H); GPC (*o*-dichlorobenzene): M_n = 62,500 g/mol, PDI = 1.66.

2.4.3 *Polymerization of PIDSe-PhanQ*

To a degassed mixture of 4,4,9,9-tetrakis(4-hexylphenyl)-2,7-bis(trimethylstannyl) indaceno [1,2-*b*:5,6-*b*']diselenophene (139.3 mg, 0.105 mmol) and 10,13-Dibromodibenzo[a,c] phenazine (43.8 mg, 0.100 mmol), dissolved in toluene (3.5 mL), was added $Pd_2(dba)_3$ (1.8 mg, 2 μmol) and tri-o-tolylphosphine (2.4 mg, 8 μmol). The mixture was heated to reflux under a nitrogen atmosphere for 24 h. The mixture was cooled to room temperature and poured into methanol. The precipitated polymer was collected and washed in a Soxhlet extractor sequentially with methanol, acetone, and hexane, and chloroform, followed by extraction with chlorobenzene. The polymer solution was passed through a plug of silica gel (2 cm dia., 4 cm long), eluting with chlorobenzene. The solution was then concentrated to ~10 mL and poured into methanol. The precipitated polymer was collected to dried to yield the product as a green solid (227.1 mg, 89% yield). ^{1}H NMR (300 MHz, $CDCl_3$, δ): 9.87 (d, 2H), 8.36 (br s, 4H), 7.80 (br m, 6H), 7.53 (br s, 2H), 7.21 (br m, 12H), 7.00 (br s, 4H); GPC (*o*-dichlorobenzene): M_n = 61,100 g/mol, PDI = 1.75.

2.5 EXPERIMENTAL METHODS

2.5.1 *Device Fabrication*

Bulk heterojunction OPVs were fabricated using ITO-coated glass substrates (15 Ω sq^{-1}), which were cleaned with detergent, deionized water, acetone, and isopropyl alcohol. In the

conventional structure devices, a thin layer (≈35 nm) of PEDOT:PSS (Baytron PVP AI 4083, filtered at 0.45 μm) was first spin-coated on the pre-cleaned ITO-coated glass substrates at 5000 rpm and baked at 140 °C for 10 min under ambient conditions. The substrates were then transferred into a nitrogen filled glovebox. Subsequently, the polymer:PCBM (20 mg mL^{-1}, 1:3, w/w) dissolved in 1,2-dichlorobenzene (o-DCB) was spin-coated on the PEDOT:PSS layer to obtain the active layer (≈90 nm). The active layer films were annealed at 110°C for 10 minutes. The fullerene surfactant layer was spun onto the active layer and subsequently thermally annealed at 110 °C for 5 min. Finally, Ag (120 nm) was thermally evaporated under high vacuum ($<2\times10^{-6}$ Torr) to serve as the cathode.

For the bilayer device structures, the PEDOT:PSS layer were coated onto the cleaned ITO substrate with the same conditions. The polymers were dissolved in DCB (8mg ml^{-1}) and spin-coated on the PEDOT:PSS layer with thickness around 50 nm. Then the C_{60} layer (30 nm) was formed by thermal deposition under high vacuum. Finally Ca (10 nm) and Al (100 nm) were thermally evaporated as the top electrode.

2.5.2 *Cyclic Voltammetry*

Cyclic voltammetry of the polymer film was conducted in acetonitrile with 0.1 M tetrabutylammonium hexafluorophosphate using a scan rate of 100 mV s^{-1}. ITO, Ag/AgCl and Pt mesh were used as the working electrode, reference electrode and counter electrode, respectively.

2.5.3 *Photovoltaic External Quantum Efficiency*

Photocurrent was detected by a Stanford Research Systems SR830 lock-in amplifier. Excitation light was produced by a monochromated tungsten-halogen lamp and modulated at 200 Hz using a Stanford Research Systems SR540 chopper. External quantum efficiency values were calculated using an OSI optoelectronics calibrated silicon photodiode. The lock-in phase was set using photocurrent generated at 550 nm excitation such that the photocurrent signal was entirely in the positive X-channel (in-phase). Y-channel (quadrature) photocurrent was simultaneously monitored and remained at base line. The calibrated photodiode and device pixels were masked to identical 1.6 mm^2 area. The devices were held under active 20 mTorr vacuum during the measurement.

2.5.4 *Current-Voltage Characteristics*

All *J–V* curves were recorded using a Keithley 2400 source meter. The device photocurrent was measured under AM1.5 illumination condition at intensity of 100 mW cm^{-2}. The illumination intensity of the light source was calibrated employing a standard Si photodiode detector equipped with a KG-5 filter, which can be traced back to the standard cell of the National Renewable Energy Laboratory (NREL).

2.5.5 *Photoluminescence*

Steady-state photoluminescence spectra were recorded on a home-built spectrometer using standard lock-in techniques. Luminescence was modulated at 200 Hz by an Aligent 33120A arbitrary waveform generator using a 447 nm LED (Luxeon Rebel, 700mW, LXML-PR01-0425)

excitation. Spectra were resolved using an Acton monochromator and Si/InGaAs dual-band photodiode (ThorLabs, DSD2). Luminescence was amplified with a Stanford Research Systems SR570 low-noise current preamplifier and measured with a Stanford Research Systems SR830 lock-in amplifier. The lock-in phase was set using reflected pump light such that the signal was entirely in the positive X-channel (in-phase). Y-channel (quadrature) signal was monitored and remained at base line during the measurement. Photoluminescence spectra were corrected for detector response using a calibrated LS-1-CAL Ocean Optics light source. Samples were held under active 20 mTorr vacuum during the photoluminescence measurement.

2.5.6 *Photoluminescence Quantum Yield*

Neat polymer photoluminescence quantum yield was recorded using the Hamamatsu integrating sphere and photonic multi channel analyzer (C10027) with 470 nm excitation from a fiber optic coupled monochromated Xenon/Mercury light source. Charge-transfer state photoluminescence quantum yield was measured from the ratio of the integrated photoluminescence peak area to the neat polymer integrated photoluminescence peak area, when both spectra were recorded under identical conditions on our home-built spectrometer. Photoluminescence spectra were measured and corrected for detector response as described in the previous section. The integrated area of the charge-transfer state peak corresponds to a Gaussian fit excluding any unquenched polymer emission. This method gives close agreement with previously measured values for charge-transfer state photoluminescence quantum yield.[85]

2.5.7 *Visible Photoluminescence Lifetime*

Time-resolved photoluminescence decays at visible wavelengths were measured using a PicoQuant FluoTime100 compact fluorescence lifetime spectrometer. Data were collected and processed using the PicoHarp300 time-correlated single-photon counting module. For unquenched neat materials' lifetimes, a 700 nm band-pass filter and was placed in the detection path. The sample was excited with 467 nm laser pump pulses at 10 MHz repetition rate. Data analysis was carried out using FluoFit software (PicoQuant). Figure S13 shows the instrument response function obtained using scattered laser light reflected off of a glass slide.

2.5.8 *Infrared Photoluminescence Lifetime*

Time-resolved photoluminescence decays at infrared wavelengths were measured using an IDQ ID220 free running InGaAs/InP avalanche photodiode single photon detector. Data were collected and processed using the PicoHarp300 time-correlated single-photon counting module. For charge-transfer state lifetimes, a 1050 nm long-pass filter and focusing lens were placed in the detection path. The sample was excited with 467 nm laser pump pulses at 10 MHz repetition rate. Data analysis was carried out using FluoFit software (PicoQuant). Figure S12 shows the instrument response function obtained using 0.3mM 1-ethyl-2-(4-(p- dimethylaminophenyl)-1,3-butadienyl)-quinolinium perchlorate (LDS 798) fluorophore in H_2O with 27 ps lifetime purchased from Exciton.[174]

2.5.9 *Electroluminescence*

Steady-state electroluminescence spectra were recorded on a home-built spectrometer using standard lock-in techniques. Electroluminescence was produced by direct current bias from a Kiethley 2400 sourcemeter, and luminescence was modulated at 200 Hz using a Stanford Research Systems SR540 chopper. Spectra were resolved using an Acton monochromator and Si/InGaAs dual-band photodiode (ThorLabs, DSD2). Luminescence was amplified with a Stanford Research Systems SR570 low-noise current preamplifier and measured with a Stanford Research Systems SR830 lock-in amplifier. The lock-in phase was set using electroluminescence signal from the sample at 2 V direct current bias such that the signal was entirely in the positive X-channel (in-phase). Y-channel (quadrature) signal was simultaneously monitored and remained at base line for all measurements. Electroluminescence spectra were corrected by calibrating the instrument using a calibrated LS-1-CAL Ocean Optics light source. Samples were held under active 20 mTorr vacuum during the electroluminescence measurement.

2.5.10 *Electroluminescence Quantum Yield*

Electroluminescence quantum yield was estimated by dividing the integrated peak area (in photons/cm^2/s) by forward biased direct current (in electrons/cm^2/s) measured on a Kiethley 2400 sourcemeter. Calculations were adjusted by a factor of 0.87 to account for the difference in emitter area between the calibrated LS-1-CAL Ocean Optics light source and the sample pixel as well as the fraction of light that would not have been collected by the focusing lenses assuming cosine-corrected Lambertian emission.

2.5.11 *Transmission Electron Microscopy and Selected Area Electron Diffraction*

BHJ films for TEM characterization were deposited onto PEDOT:PSS using the same procedure as device fabrication. The films were slowly immersed in water to dissolve the PEDOT:PSS and render the film freely floating on the water's surface. This film was mounted on a Tecnai G2 F20 TEM grid for analysis. An accelerating voltage of 120 kV was used for bright field imaging. An accelerating voltage of 200 kV and select area aperture of 100 μm was used for diffraction measurements.

2.5.12 *Grazing Incidence Wide Angle X-Ray Scattering*

Grazing Incidence Wide Angle X-Ray Scattering (GIWAXS) measurements were made on an Anton Paar Saxsess instrument. Thin films were deposited onto mechanical grade silicon and cleaved into 15mm x 15mm squares. Samples were aligned using a pin diode to an incident angle, alphai = 0.2 deg. Sample scattering was recorded for 16 hours on image plate detectors and the resulting images reduced to Intensity vs Qy, Qz using custom IGOR Pro reduction macros.[175] Intensity was normalized with respect to sample area and scattering time. From the two dimensional Qy Qz plots, 1-D integration was performed with an azimuthal angle of 20 degrees with respect to the specular rod to obtain Intensity vs Qbar in order to characterize the wide-angle scattering features in the sample. The scattering patterns were then deconvoluted assuming Gaussian scattering with a power-law background subtraction to obtain the peak intensities and full-width-half-maxima for each feature in the scattering patterns.

Chapter 3. UNEQUILIBRATED SINGLET AND TRIPLET CHARGE-TRANSFER STATES IN ORGANIC BULK HETEROJUNCTIONS

Adapted from:
Sulas, D.B.; Chueh, C.-C.; Collins, B.A.; Jen, A.K.-Y.; Schlenker, C.W.; Ginger, D.S., in preparation.

3.1 **INTRODUCTION**

The most successful organic photovoltaic devices employ nanostructured mixtures of electron-donating and electron-accepting components, in which energy level offsets at donor/acceptor interfaces provide the necessary driving force for exciton dissociation and photocurrent generation.[128, 176] It is widely accepted that loosely bound intermolecular charge pairs, or charge-transfer states, form at these donor/acceptor interfaces and play important roles in device performance.[68, 73, 75, 78, 92, 141] Certain properties of charge-transfer states, such as energies and lifetimes, have been characterized and suggest that charge-transfer states mediate photocurrent generation and charge recombination.[75, 85, 143, 149, 160] However, the importance of other charge-transfer state properties such as spin multiplicity remain open questions with important implications for optimizing materials to efficiently produce photocurrent.[68, 80, 92, 96, 111]

Charge-transfer states may affect the photovoltaic process at two different stages. At early times, a manifold of charge-transfer states (initially with singlet spin multiplicity) may act as an intermediate between neutral photogenerated excitons and free charge carriers.[177-180] At later times, bimolecular recapture of charge carriers is commonly thought to form a distribution of singlet and triplet charge-transfer states, which either further relax and lead to photocurrent loss or re-dissociate to free charge carriers that contribute to photocurrent.[80, 93, 96, 110] The resulting quasi-equilibrium between free carriers and charge-transfer states under illumination and bias has become an important component of our understanding of organic solar cell operation.[41, 87, 92, 96]

Despite the reported presence of both singlet and triplet charge-transfer states,[38, 75, 81, 93, 96, 108, 181-182] the spin multiplicity of charge-transfer states in organic photovoltaic devices is often neglected based on the assumption of rapid singlet/triplet interconversion.[90, 92] This assumption implies that spin interconversion within the charge-transfer manifold outpaces the nanosecond decay of singlet charge-transfer states to the ground state ($^1CT \rightarrow S_0$)[73, 75, 85, 159] as well as sub-nanosecond relaxation of triplet charge-transfer states to triplet excitons ($^3CT \rightarrow T_1$).[89, 96] Rapid singlet/triplet charge-transfer state equilibrium could accelerate formation of low-energy triplet excitons,[92] which have been implicated in photocurrent loss.[68, 80, 181, 183-185] Importantly, both the $^1CT \rightarrow S_0$ and $^3CT \rightarrow T_1$ pathways in this case would proceed in a fixed proportion, and charge extraction from the charge-transfer manifold would proportionately counteract both pathways. For this reason, most studies infer charge-transfer states' role in photocurrent generation by measuring singlet charge-transfer state characteristics, such as their luminescent decay and voltage dependence.[38, 41, 179]

However, several recent results point toward the possibility that singlet and triplet charge-transfer states do not always rapidly equilibrate, and that spin character does in fact affect the role of charge-transfer states in photocurrent extraction. For example, the trends of singlet charge-transfer state luminescence quenching under an applied voltage do not necessarily correlate with extractable photocurrent.[41, 87] Bakulin et al. recently addressed this discrepancy by separately evaluating the time-averaged and sub-picosecond singlet charge-transfer state populations.[179] Bakulin et al. proposed that fast geminate charge-transfer state decay limits extractable photocurrent in the thiophene-quinoxaline/fullerene devices that they studied, suggesting that later formation of singlet and triplet charge-transfer states by bimolecular charge recombination affects photocurrent to a lesser extent.[179] However, Chow et al. found that bimolecular formation of triplet

charge-transfer states accounts for the majority of recombination in their cyclopentadithiophene-benzothiodiazole/fullerene systems, where recombination via singlet charge-transfer states is entirely suppressed.[108] Chow et al. further demonstrated that the percentage of photoexcitations decaying via either singlet or triplet charge-transfer states varies with solvent processing of the active layer.[108] These combined results suggest that singlet and triplet charge-transfer states mediate photocurrent to different extents, and that variations in nanoscale donor/acceptor interfacial properties can affect the role of charge-transfer state spin character in device operation.

Here, we investigate the voltage dependence of singlet and triplet charge-transfer states and their relation to extractable photocurrent in organic solar cells made from an indacenodithiophene-quinoxaline copolymer electron donor blended with a fullerene acceptor. We consider whether photovoltaic loss to triplet states in these materials must proceed through bimolecular recombination of uncorrelated charge carriers or if rapid singlet/triplet interconversion within the charge-transfer manifold plays a significant role. We compare the trends in extractable photocurrent under reverse bias voltage with trends in the polaron, triplet exciton, and singlet charge-transfer state populations using *operando* bias-dependent photoinduced absorption and photoluminescence spectroscopy. We conclude that the singlet and triplet charge-transfer states do not rapidly interconvert under our experimental conditions, as we observe dissimilar voltage dependence for their spectroscopic indicators. Interestingly, the extent to which an external voltage affects the singlet or triplet charge-transfer state populations appears to depend on nanoscale morphology. Our results suggest that the singlet and triplet charge-transfer states are not in rapid equilibrium and may mediate photocurrent to different extents in the polymer/fullerene devices studied here, which can reach high internal quantum efficiencies of 80 – 95 % in the visible range.[93]

3.2 RESULTS AND DISCUSSION

3.2.1 *Molecular Structures, Device Configuration, and AM1.5 Current-Voltage Curves*

To study the relationship between interfacial charge-transfer state populations and photocurrent generation, we fabricated devices with different nanoscale morphologies using different solvent processing on the same donor/acceptor components. Figure 3.1 shows the molecular structures for the electron donor (poly(indacenodithiophene-cophananthrene-quinoxaline), PIDT-PhanQ) and electron acceptor ([6,6]-Phenyl C_{71} butyric acid methyl ester, $PC_{71}BM$) that we used, along with the device architecture and current-voltage characteristics under simulated AM1.5 solar illumination.[186] We prepared devices with the architecture of [indium tin oxide / PEDOT:PSS / 1:3 PIDT-PhanQ:$PC_{71}BM$ / bis-fulleropyrrolidinium ion surfactant / Ag][186] where the active layer was spin-coated either from dichlorobenzene (DCB) or chloroform ($CHCl_3$). We observe increased short-circuit current and fill factor for the DCB-processed devices compared to the $CHCl_3$-processed devices. We summarize the device performance metrics in Table 3.1.

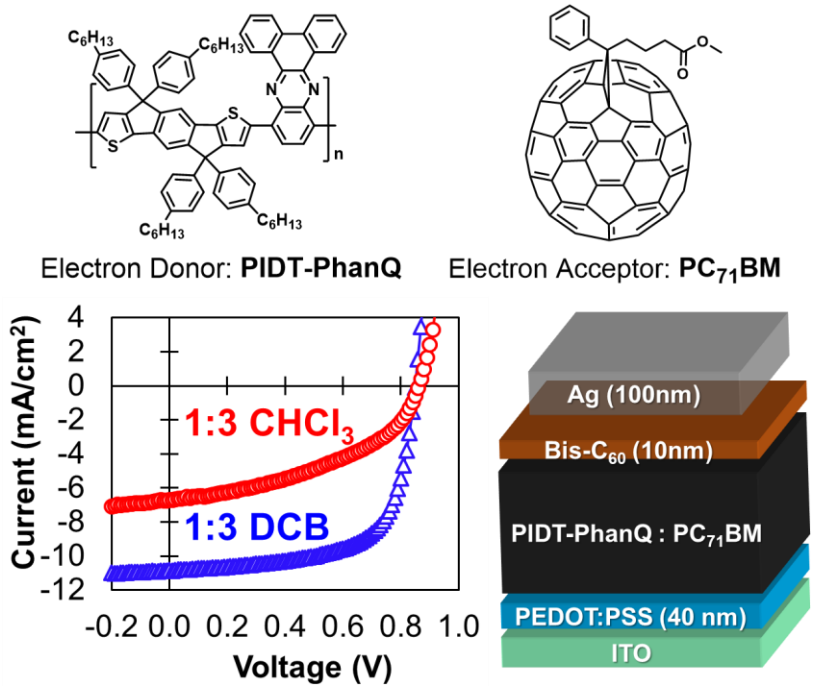

Figure 3.1. Current-Voltage curves under AM1.5 solar illumination for devices of 1:3 PIDT-PhanQ:PCBM spin-coated from chloroform ($CHCl_3$, red circles) or dichlorobenzene (DCB, blue triangles), along with the device architecture and molecular structures for the electron donor (PIDT-PhanQ) and electron acceptor ($PC_{71}BM$). DCB-processed devices show higher short-circuit current and fill factor compared to $CHCl_3$-processed devices.

Table 3.1. Device characteristics under simulated AM1.5 solar illumination for PIDT-PhanQ:$PC_{71}BM$ devices with 1:3 ratio processed in dichlorobenzene (DCB) or chloroform ($CHCl_3$), including open-circuit voltage (V_{OC}), short-circuit current (J_{SC}), fill factor (FF), and power conversion efficiency (PCE).

Solvent Processing Condition	**V_{OC}** (V)	**J_{SC}** (mA/cm^2)	**FF**	**PCE** (%)
1:3 DCB	0.86 ± 0.001	10.85 ± 0.250	0.66 ± 0.001	6.14 ± 0.082
1:3 $CHCl_3$	0.86 ± 0.011	6.52 ± 0.163	0.45 ± 0.002	2.51 ± 0.082

3.2.2 *Lock-In Detected Photocurrent Under Applied Bias*

We aim to understand the equilibrium of charge carriers with singlet and triplet charge-transfer states under varying applied voltage biases for the solar cells fabricated using DCB or $CHCl_3$ solvent processing. Figure 3.16 in the Section 3.5 shows our experimental setup, where we use lock-in techniques to detect modulated photocurrent, luminescence, or excited-state absorption in the operating solar cells. This instrumentation allows us to compare the magnitude of photocurrent generated from ground-state photoexcitations with the quasi-steady-state populations of singlet charge-transfer states, polarons, and triplet excitons at different applied voltages.

Figure 3.2 shows the lock-in detected photocurrent at reverse-bias voltages for the DCB and $CHCl_3$ processed devices excited at 500 nm at 180 K. Both devices show an increase in photocurrent under reverse bias. However, we measure different voltage-dependent trends for the photocurrent extracted from the $CHCl_3$ devices compared to the DCB-processed devices. The $CHCl_3$-processed devices exhibit a more pronounced relative increase in photocurrent under reverse bias, though the initial magnitude of photocurrent is lower. That is, we observe six-fold increase in photocurrent from 0 to -7 V in the $CHCl_3$-processed devices, in contrast to less than two-fold increase in photocurrent from the DCB devices. Moreover, we measure continuous increase in photocurrent from the $CHCl_3$-processed devices over this voltage range, while photocurrent from the DCB devices increases 1.6 times from 0 to -2 V, followed by minimal change from -2 to -7 V. We give a more detailed discussion including full external quantum efficiency curves under applied bias as well as the room temperature data in Sections 3.2.3 and 3.2.4.

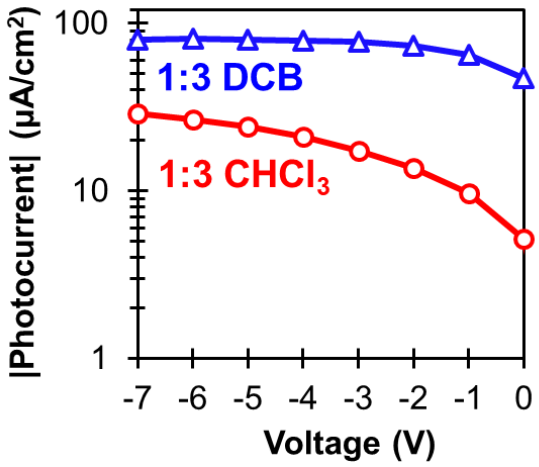

Figure 3.2. Lock-in detected photocurrent at 180 K using 500 nm photoexcitation, showing higher overall photocurrent from the 1:3 PIDT-PhanQ:PCBM devices processed in dichlorobenzene (DCB, blue triangles) compared to the devices processed in chloroform ($CHCl_3$, red circles). Photocurrent in the $CHCl_3$-processed devices increases more strongly under reverse bias than photocurrent in the DCB-processed devices.

3.2.3 *External Quantum Efficiency Curves Under Applied Bias*

Figure 3.3a and Figure 3.3b show the full photovoltaic external quantum efficiency (EQE) curves at 180 K for the $CHCl_3$ and DCB processed devices, respectively. As we discuss in Section 3.2.2, the EQE increases to some extent under reverse bias in both types of devices. We find that the EQE for the $CHCl_3$ devices increase continuously from 0 to -10 V. The EQE for the DCB devices increase from 0 to -3 V, and then remains constant after -3 V. Importantly, Figure 3.3 shows that we are able to reproduce the original EQE curves measured at 0 V after completing all measurements under applied bias.

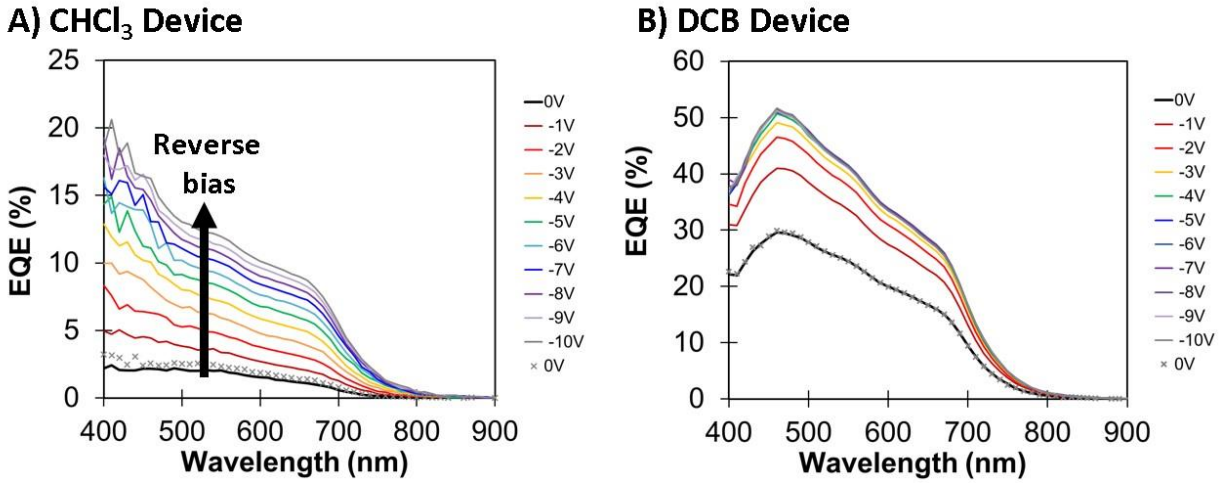

Figure 3.3. External quantum efficiency (EQE) curves measured at 180 K under varying applied voltage bias for the 1:3 PIDT-PhanQ:$PC_{71}BM$ devices processed in (a) chloroform ($CHCl_3$) and (b) dichlorobenzene (DCB).

Figure 3.2 from Section 3.2.2 shows the photocurrent values under 500 nm monochromatic light excitation. However, in Figure 3.3 we observe a slight change in the EQE shape under applied bias. Nevertheless, in Figure 3.4a we show that the voltage-dependent photocurrent trends are similar for both the 500 nm probe and the total integrated EQE. This is important because we will further characterize the voltage dependence of photoexcited states following photoexcitation with an LED in the 400 – 500 nm range. Based on Figure 3.4, we conclude that the trends under 400 – 500 nm light excitation are representative of the overall bias dependence of photocurrent extracted from the devices.

To emphasize the change in extractable photocurrent under reverse bias relative to the value at short circuit, Figure 3.4b and Figure 3.4c show the photocurrent (PC) normalized to the photocurrent at 0 V (PC_0) for the 500 nm probe and total integrated EQE, respectively. For the 500 nm probe, we observe a significant ~ 5.6 times increase in the photocurrent from the $CHCl_3$ devices relative to short circuit, and a smaller ~1.6 times increase in the photocurrent from the DCB devices

relative to short circuit. Figure 3.4c shows similar ~ 6.4 times increase in photocurrent for the integrated photocurrent from the $CHCl_3$ devices, and ~ 1.7 times increase in integrated photocurrent for the DCB devices.

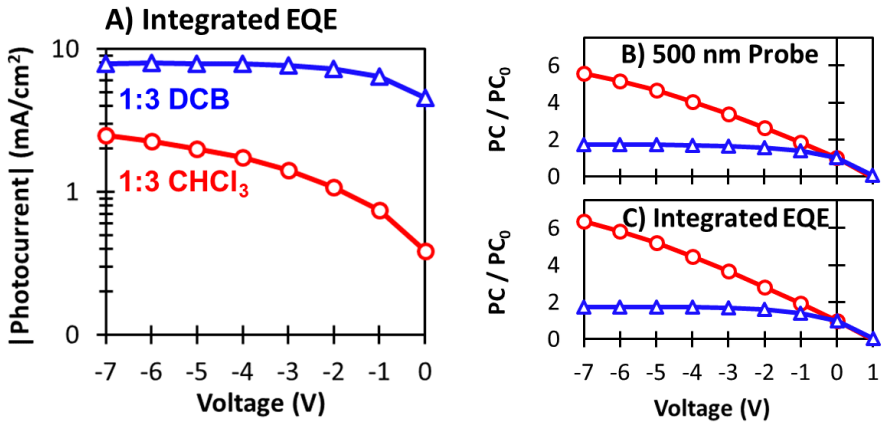

Figure 3.4. (a) Total photocurrent under applied bias obtained by integrating over the lock-in detected external quantum efficiency (EQE) curves multiplied by the AM1.5 solar spectrum for 1:3 PIDT-PhanQ:$PC_{71}BM$ devices processed in chloroform ($CHCl_3$) or dichlorobenzene (DCB). We compare (b) the photocurrent (PC) collected under 500 nm photoexcitation normalized to the photocurrent at 0 V (PC_0) with (c) the normalized plot for the integrated photocurrent values, showing a similar trend in both cases with larger relative increase in photocurrent for the $CHCl_3$ devices, despite a lower overall magnitude of photocurrent.

3.2.4 *Temperature Dependence of Lock-in Detected Photocurrent Under Applied Bias*

We present room-temperature photocurrent measurements to show that the trends discussed in Sections 3.2.2 – 3.2.3 are also valid at room temperature. Figure 3.5a and Figure 3.5b show the room-temperature EQE curves for the $CHCl_3$ and DCB processed devices, respectively. Similar to the trends at 180 K, we find that the EQE increases to some extent under reverse bias in both cases. The EQE for the $CHCl_3$ device increases continuously from 0 to -15 V. The EQE for the DCB device increases from 0 V to -3 V, and then remains constant after -3 V. Importantly, we

are able to reproduce the original EQE curve measured at 0 V after completing all measurements under applied bias.

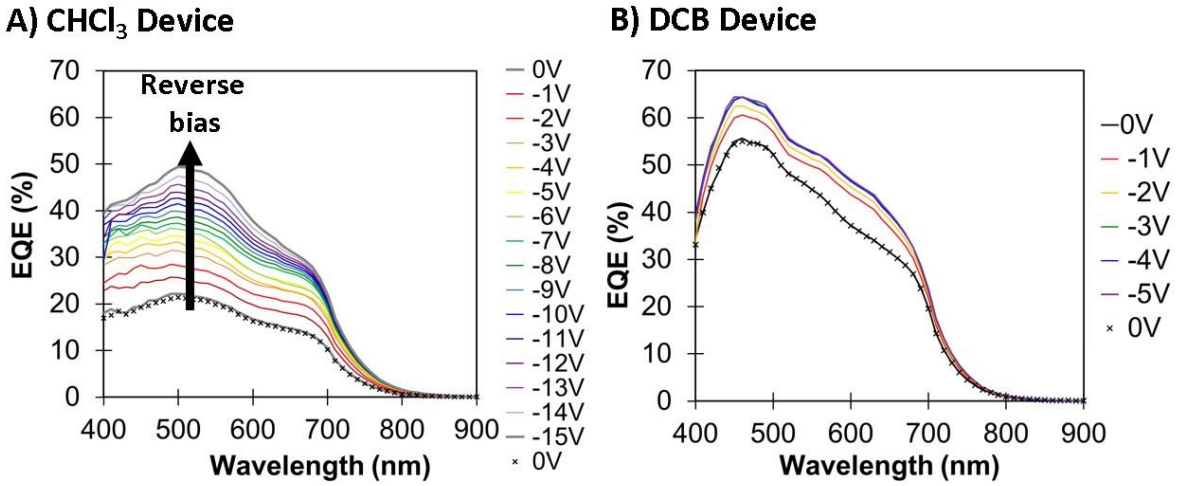

Figure 3.5. Photovoltaic external quantum efficiency (EQE) curves measured at room temperature under varying applied voltage bias for 1:3 PIDT-PhanQ:PCBM devices processed in (a) chloroform ($CHCl_3$) and (b) dichlorobenzene (DCB).

We note that the shape of the EQE curves for the $CHCl_3$-processed devices is different at room temperature compared to that measured at 180 K (compare with Figure 3.3a). This change in shape implies that conductivities within the polymer and fullerene phases are not equally affected by changes in temperature. The more significant change in shape of the $CHCl_3$ devices' EQE curves with varying temperature compared to the DCB devices implies that charge extraction plays a more significant role in limiting device performance for the $CHCl_3$ devices.

In Figure 3.6, we show the EQE curves on a log-scale y-axis in order to discuss the sensitivity limits of our measurement techniques. We measure sub-gap photocurrent in both devices, consistent with our previous studies in Chapter 2.[75] We note that our previous measurements in Chapter 2 gave photocurrent out to 1100 nm for similar devices,[75] while in this study our instrumentation limits our photocurrent measurement to 900 nm. Our measurement

technique in this study is less sensitive compared to that in Chapter 2, since we use the lock-in amplifier to detect a voltage drop across a 100 Ohm resistor instead of setting the lock-in amplifier to measure current directly (see experimental setup in Section 3.5). We note this limitation on the sensitivity of the technique simply for the benefit of future studies aiming to design similar experiments.

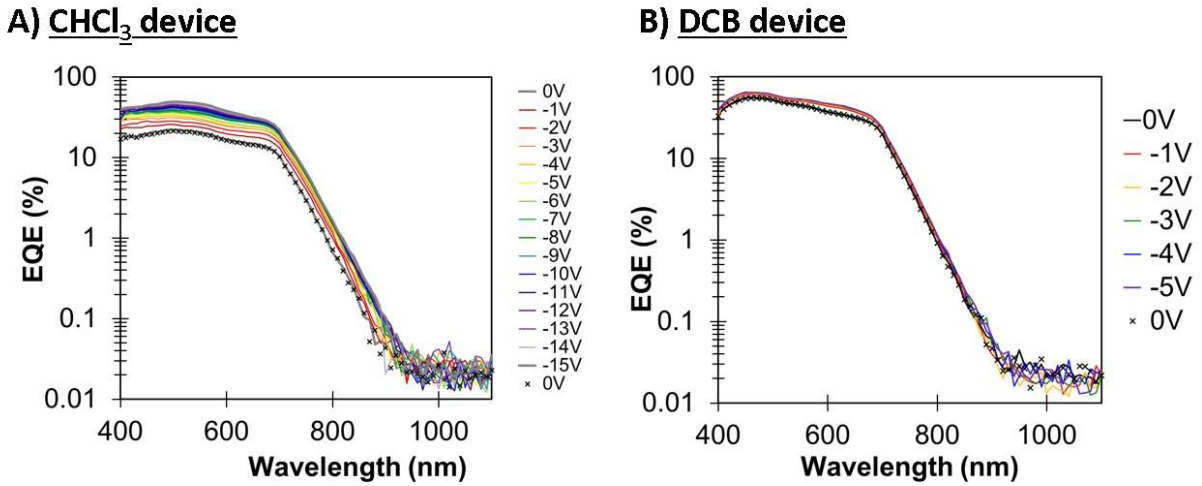

Figure 3.6. Log-scale plots of external quantum efficiency (EQE) data for 1:3 PIDT-PhanQ:$PC_{71}BM$ devices processed in (a) chloroform ($CHCl_3$) and (b) dichlorobenzene (DCB), showing sub-gap photocurrent detected out to 900 nm.

In Figure 3.7, we present the photocurrent measured at a single wavelength (600 nm) for both devices at room temperature from 0 to -12 V. This measurement confirms that the photocurrent for the $CHCl_3$ devices continually increases over the measured voltage range while the photocurrent for the DCB devices remains nearly constant at room temperature. Error bars represent standard deviation among three devices. We note that the nearly unchanged value for photocurrent extracted from the DCB devices at room temperature is consistent with these devices already being optimized for photocurrent generation. Indeed, earlier observations report 80-95% internal quantum efficiency (IQE) across the visible range in this type of device.[93]

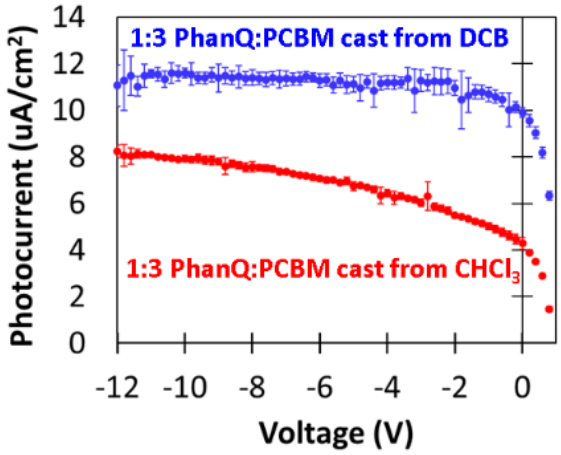

Figure 3.7. Photocurrent measured at room temperature under monochromated light at 600 nm from +1 V to -12 V for the 1:3 PIDT-PhanQ:$PC_{71}BM$ devices processed in dichlorobenzene (DCB, blue) and chloroform ($CHCl_3$, red).

We find that photocurrent from both devices is more strongly voltage dependent at low temperature (see Sections 3.2.2 – 3.2.3) compared to room temperature (Figure 3.7). For example, the DCB devices show ~13 % increase in photocurrent from 0 to -7 V at room temperature, and a more significant ~50 % increase in photocurrent over the same voltage range at 180 K. Similarly, the $CHCl_3$ devices show ~43 % increase in photocurrent from 0 to -7 V at room temperature, with a more significant ~600 % increase at 180 K.

Interestingly, the temperature dependence is more severe for the $CHCl_3$ devices compared to the DCB devices. Bakulin et al. recently concluded that charge extraction is more severely affected by decreasing temperature than geminate recombination of singlet charge-transfer states at early times.[179] Therefore, the greater temperature dependence for the $CHCl_3$ devices likely suggests that charge extraction plays a more significant role in limiting $CHCl_3$ device performance.

3.2.5 *Bimolecular Polymer Triplet Formation Through Triplet Charge-Transfer States*

In order to gain insight into the equilibrium between free charge carriers and charge-transfer states in the PIDT-PhanQ:PCBM system, we characterize the voltage dependence of polarons and charge-transfer states of both singlet and triplet spin (Sections 3.2.6 – 3.2.8). We begin by measuring the photoinduced absorption signatures of polarons and polymer triplet excitons in the DCB and $CHCl_3$ processed devices. We use the polymer triplet absorption as a proxy for the number of carriers passing through the triplet charge-transfer manifold, consistent with the approach of Chow et al.[108] Importantly, previous studies suggest that the majority of polymer triplets in these devices are formed through bimolecular carrier recombination, where carriers pass through triplet charge-transfer states before relaxing to localized polymer triplets.[80, 89, 93, 110] In this section, we provide time-resolved induced absorption data showing fluence-dependent rise times for the polymer triplets, consistent with the bimolecular formation pathway.[80] Once carriers recombine to triplet charge-transfer states, Chen et al. predict strong coupling between the triplet charge-transfer (^{3}CT) and triplet exciton (T_1) manifolds, yielding fast (~10^{11} s^{-1}) $^3CT \rightarrow T_1$ relaxation when localized triplet excitons are thermodynamically accessible.[89]

In order to distinguish between monomolecular and bimolecular triplet formation, we compare the transient absorption kinetics corresponding to triplet formation at varying excitation fluence in Figure 3.8. Figure 3.8a and Figure 3.8b show the polaron and triplet kinetics for the $CHCl_3$-processed thin films at higher (2.3×10^{18} cm^{-3}) and lower (2.3×10^{17} cm^{-3}) absorbed photon densities out to 5.5 ns. Similarly, Figure 3.8c and Figure 3.8d show the polaron and triplet kinetics for the DCB-processed thin films at higher (2.2×10^{18} cm^{-3}) and lower (3.7×10^{17} cm^{-3}) absorbed photon densities. We characterize the triplet kinetics by averaging the transient absorption signal from 1300 – 1450 nm, and we characterize the polaron kinetics using the

transient absorption signal at 1000 nm. We discuss the full induced absorption spectral shapes in further detail in Section 3.2.6. We find that the rise of the triplet signal appears to be correlated with polaron decay. Both the triplet rise times and polaron decay times vary with pump fluence.

For the higher pump fluence ($2.2 – 2.3 \times 10^{18}$ absorbed photons cm^{-3}), the triplet transient absorption signal in the 1300 – 1450 nm spectral region reaches a maximum amplitude around 100 – 350 ps. At lower fluence ($2.3 – 3.7 \times 10^{18}$ absorbed photons cm^{-3}), the signal rises more slowly and appears to still be growing at the end of our time window at 5.5 ns. We interpret the fluence dependence in Figure 3.8 as evidence for triplet formation via bimolecular recombination in these blends. We note that our finding of sub-ns triplet formation by bimolecular recombination at room temperature is consistent with other recent reports.[187] Importantly, we measure our kinetics showing fluence-dependent triplet rise times over a comparable range of excitation densities to those used by Dimitrov et al., where they observed fluence-independent triplet formation in a different polymer/fullerene system.[92]

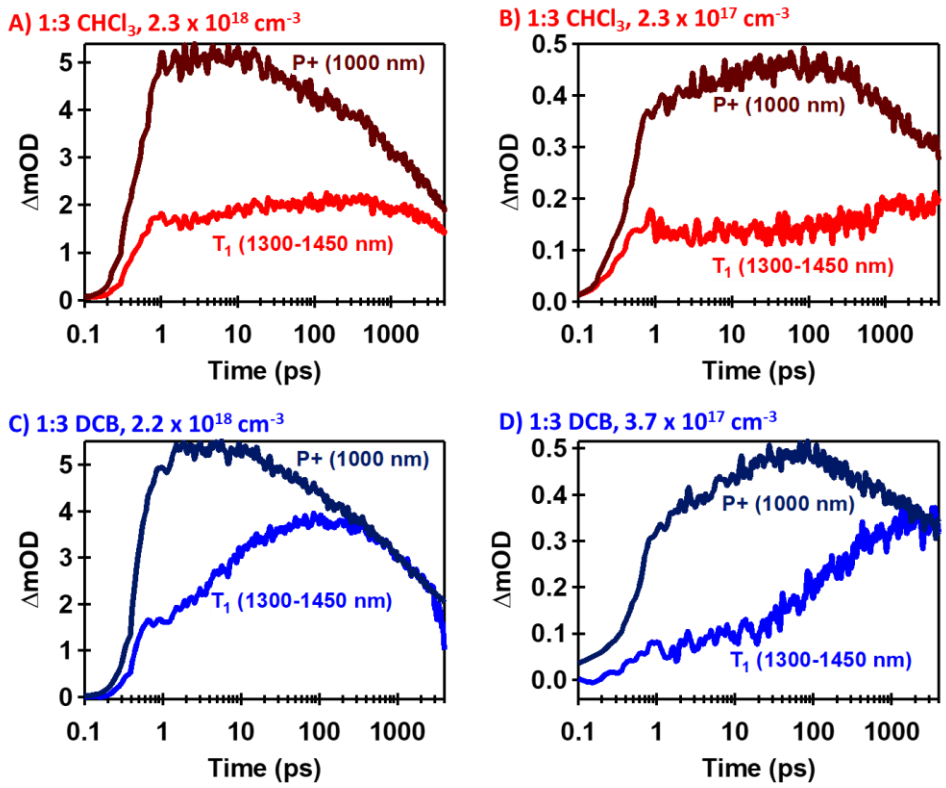

Figure 3.8. Triplet and polaron kinetics using the 450 nm pump for1:3 PIDT-PhanQ:PCBM films processed in chloroform ($CHCl_3$) at fluences of (a) 2.3×10^{18} absorbed photons cm^{-3} and (b) 2.3×10^{17} absorbed photons cm^{-3} and processed in dichlorobenzene (DCB) at (c) 2.2×10^{18} absorbed photons cm^{-3} and (d) 3.7×10^{17} absorbed photons cm^{-3}.

We note that the triplet kinetics in Figure 3.8a and Figure 3.8b for the $CHCl_3$-processed films appear to have a faster rise times in the 1300 – 1450 nm spectral region compared to the DCB films. We attribute this faster rise to the contribution in this spectral region from unquenched PIDT-PhanQ singlet excitons, which overlap with the polymer triplet signal. As we discuss later in Section 3.2.9, the $CHCl_3$-processed active layers have large and pure phases, resulting in a significant amount of unquenched PIDT-PhanQ singlet excitons that are unable to diffuse to a donor/acceptor interface. Figure 3.9 shows the kinetics in a neat PIDT-PhanQ thin film at 1300 nm (~2×10^{18} absorbed photons cm^{-3} with 450 nm excitation). We attribute the kinetics in the neat

films to singlet excitons. We observe a fast rise time followed by a decay reaching zero intensity by ~ 400 ps.

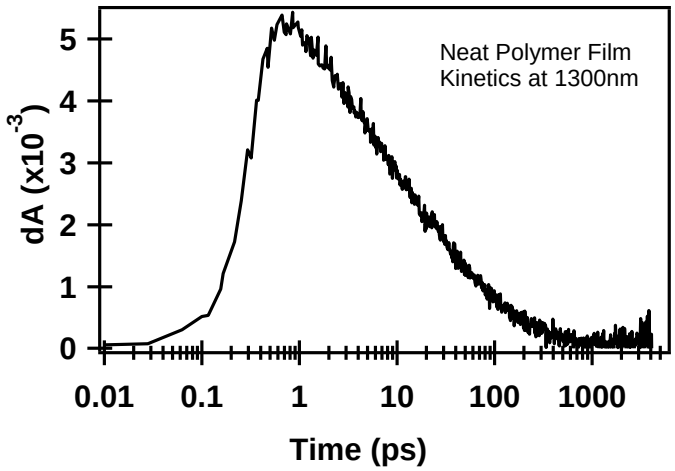

Figure 3.9. Kinetics at 1300 nm for neat PIDT-PhanQ thin films under 450 nm photoexcitation.

3.2.6 *Voltage-Dependent Photoinduced Absorption Spectra*

The striking differences in magnitude and shape between the DCB and $CHCl_3$ processed devices' bias dependence for photocurrent generation in Sections 3.2.2 – 3.2.4 point to the strong influence of film morphology on the balance between recombination and charge extraction, consistent with a wide range of literature.[41, 43, 87, 92, 179, 181, 188] However, the related influence of morphology and bias on the interconversion between free carriers, singlet charge-transfer states, and triplet states remains unclear.[68, 90, 92-93, 110-111] While free carriers are known to recombine to both singlet and triplet charge-transfer states, it is debated whether the resulting charge-transfer state populations follow 1:3 spin statistics[96, 111] and how readily the bound states re-dissociate.[93] Indeed, morphology-related factors causing changes in donor/acceptor orbital overlap have been proposed to alter the singlet/triplet energy splitting and disrupt the recombination ratios.[109-111] It is further unclear whether charge-transfer state spin interconversion can kinetically outcompete the

nanosecond $^1CT \rightarrow S_0$[73, 75, 85, 159] and the sub-nanosecond $^3CT \rightarrow T_1$ relaxation pathways.[89, 96] Understanding the extent of spin interconversion and the influence of morphology and bias is critical for avoiding photovoltaic loss to low-energy triplet excitons.

We investigate whether singlet/triplet charge-transfer state interconversion occurs to a significant extent by comparing the voltage dependence of singlet charge-transfer states (Section 3.2.8) with triplet charge-transfer states (Sections 3.2.6 – 3.2.7). In this section, we show the voltage dependence of the quasi-steady-state photoinduced absorption signatures of polarons and polymer triplet excitons in the DCB and $CHCl_3$ devices. As discussed in Section 3.2.5, we use the polymer triplet exciton as a proxy for the voltage dependence of triplet charge-transfer states in these blends, which are formed through relaxation of triplet charge-transfer states.

Figure 3.10a and Figure 3.10b show the near-steady-state voltage-dependent photoinduced absorption (PIA) spectra at 180 K for the $CHCl_3$ and DCB devices, respectively. For both devices, we observe positive signals from 600 – 800 nm, corresponding to bleaching of the ground state absorption. We observe an induced absorption signal from 800 – 1600 nm, including a peak centered around 1000 nm and a broad absorption region from 1200 – 1600 nm. Consistent with previous studies, we assign the peak at 1000 nm to positive polymer polaron absorption and the broad absorption around 1200 – 1600 nm to localized polymer triplet absorption.[80, 93] The polaron and triplet induced absorption bands respond differently to bias. For the $CHCl_3$ devices, the triplet signal reaches its maximum amplitude under forward bias and exhibits a strong decrease going from +2 to -4 V. In contrast to the $CHCl_3$ blends' triplet, the polaron signal in the $CHCl_3$ devices is most intense around 0 V and shows the strongest decrease under forward bias. For the DCB devices, the triplet signal shows very little variation under applied bias. However, the polaron

signal in the DCB blends reaches a maximum amplitude under reverse bias and decreases under forward bias.

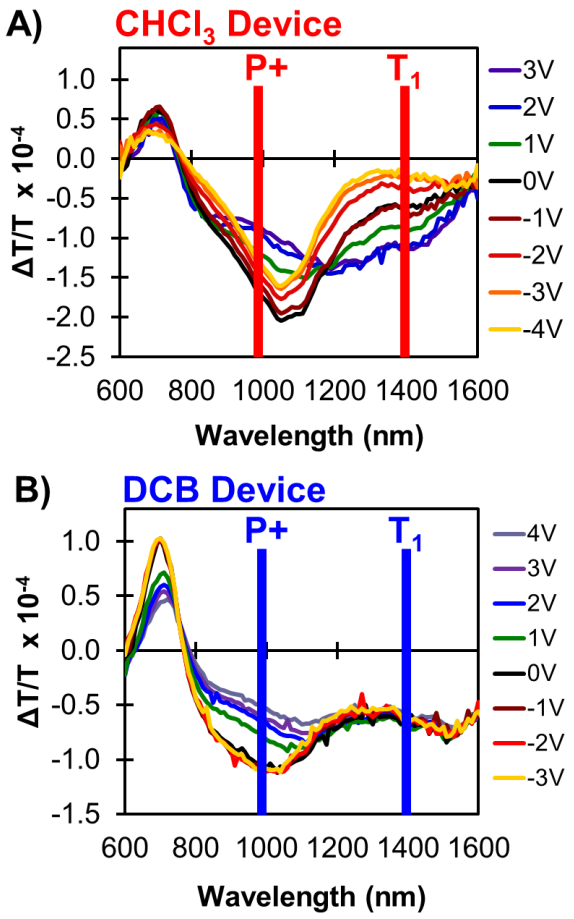

Figure 3.10. Voltage-dependent photoinduced absorption (PIA) spectra for 1:3 PIDT-PhanQ:PCBM devices processed in a) chloroform ($CHCl_3$) and b) dichlorobenzene (DCB) measured at 180 K, showing different voltage dependence for regions corresponding to polaron (P+) and triplet (T_1) absorption.

The difference in voltage dependence between the 1000 nm and 1400 nm spectral regions confirms that the spectra consist of two overlapping absorption bands (polaron and triplet).[80, 93] Interestingly, the overall voltage dependence of polarons and triplets under applied bias appears to be different in the DCB devices compared to the $CHCl_3$ devices. This result suggests that

interfacial polymer/fullerene morphology plays an important role in the voltage dependent pathways populating triplet states.

3.2.7 *Comparison of Triplet and Polaron Voltage Dependence in Dichlorobenzene and Chloroform Processed Devices*

In Figure 3.11a and Figure 3.11b, we compare the normalized PIA signals for triplets and polarons, respectively, that we measure in the $CHCl_3$ and DCB processed devices over +3 to -7 V at 180 K. In Figure 3.11a, we highlight very different voltage dependence for the triplet states in the $CHCl_3$ and DCB processed devices. We find that the triplet PIA is almost completely quenched at -7 V for the $CHCl_3$ devices while the triplet PIA is nearly invariant for the DCB devices over the measured voltage range. For both types of devices, the polaron signal in Figure 3.11b exhibits the largest decrease in the power-generating region from 0 to +1 V, and the signal changes less drastically at both higher forward and reverse biases.

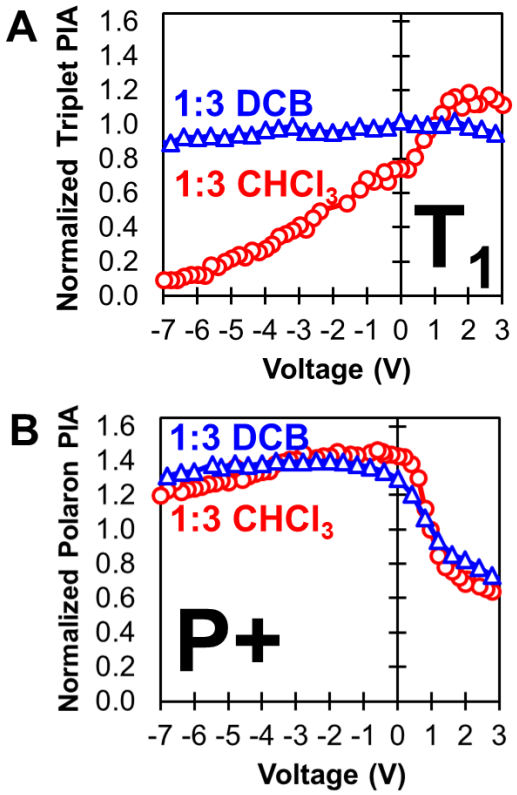

Figure 3.11. Normalized photoinduced absorption signals at 180 K corresponding to a) polaron (P+) absorption at 980 nm and b) triplet (T_1) absorption at 1400 nm for the chloroform ($CHCl_3$, red circles) and dichlorobenzene (DCB, blue triangles) processed devices with 1:3 PIDT-PhanQ:PCBM ratio. Curves are normalized at +1 V (~V_{OC}).

Based on the trends in Figure 3.11, we consider whether triplet formation in these blends primarily proceeds through bimolecular recombination of uncorrelated charge carriers or if rapid singlet/triplet interconversion within the charge-transfer manifold plays a significant role.

Since previous results suggest that the majority of triplets in PIDT-PhanQ:PCBM films form through bimolecular polaron recombination, even at low temperature,[80] we first discuss the voltage dependence in Figure 3.11 in the context of polaron recombination. In the $CHCl_3$ devices under forward bias, the triplet signal increases as the polaron signal decreases. We interpret this trend to suggest that photogenerated polarons recombine with injected carriers to form triplets.

Under reverse bias in the $CHCl_3$ devices, we attribute the decrease of the triplet signal to extraction of polarons that would otherwise recombine via the triplet charge-transfer manifold. Interestingly, we do not see a similar voltage dependence for the triplets in the DCB devices. However, it is still possible that triplets form via bimolecular charge recombination in the DCB devices. In this case, any increase in triplet signal upon charge injection may be masked by triplet-charge annihilation, which is known to occur in PIDT-PhanQ:PCBM blends.[80]

Alternatively, if rapid singlet/triplet charge-transfer state interconversion occurs to a significant extent, we could attribute the decrease in triplet population in the $CHCl_3$ devices under reverse bias to field-dependent separation of singlet charge-transfer states at early times.[179] This possible pathway for triplet formation would only be consistent with the voltage-invariant triplet signal in the DCB devices if *both* singlet and triplet charge-transfer state populations show no voltage dependence.

We note that characterizing the singlet charge-transfer state voltage dependence is crucial to elucidate whether or not singlet/triplet charge-transfer state interconversion is significant in these blends. Importantly, the qualitatively similar voltage dependence that we observe for the polaron PIA in both devices (Figure 3.11b) could be consistent with either pathway for triplet formation. Under forward bias, the polaron signal strongly decreases. On one hand, we may attribute the decrease in polaron signal to bimolecular recombination as the carrier density increases and extraction rates decrease.[189-193] On the other hand, we may attribute the decrease in polaron signal under forward bias to decreasing efficiency of charge-transfer state dissociation under a weaker field.[41, 87] Under reverse bias, we observe minimal change in the polaron signal. Based on Figure 3.2, we expect charge extraction to decrease the polaron density. However, spatial separation of the positive and negative carriers under reverse bias may also decrease recombination

rates and increase the polaron lifetimes. In addition, the reverse bias may assist charge-transfer state dissociation,[41, 87, 92, 194] generating polarons rather than decay products such as triplet excitons.

3.2.8 *Voltage-Dependent Photoluminescence Spectra*

In order to distinguish between these two possible pathways for triplet formation (i.e. polaron recombination or rapid equilibrium with singlet charge-transfer states), we next evaluate the voltage dependence of the singlet charge-transfer states. If the singlet and triplet charge-transfer states are in rapid equilibrium (as previously suggested for different systems[92]), then we would expect to measure similar voltage dependence for the singlet charge-transfer state photoluminescence and triplet state PIA. This would result in minimal voltage dependence for the singlet charge-transfer states in the DCB devices and significant quenching of the singlet charge-transfer states under reverse bias in the $CHCl_3$ devices. If the singlet and triplet charge-transfer states are not in rapid equilibrium, then we may expect to measure different voltage dependence for the singlet and triplet charge-transfer states. By measuring the *in situ* photoluminescence of the singlet charge-transfer states under applied bias (Figure 3.12), we infer that the singlet and triplet charge-transfer states do not have the same voltage dependence and we conclude that they are not likely to rapidly equilibrate in this system at 180 K.

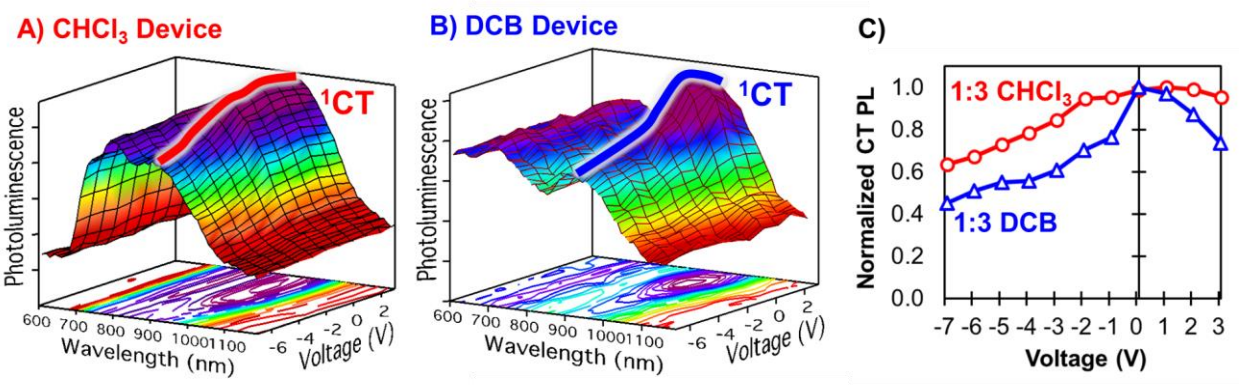

Figure 3.12. Voltage dependent photoluminescence spectra for 1:3 PIDT-PhanQ:PCBM devices processed in a) chloroform ($CHCl_3$) and b) dichlorobenzene (DCB), where the colored line highlights the voltage dependence of the singlet charge-transfer state (^1CT) photoluminescence peak centered at 980 nm. c) Line scans of the 980 nm luminescence peaks normalized at 0 V, showing that the singlet charge-transfer state photoluminescence is more strongly affected by an applied bias in the DCB device (blue triangles) compared to the $CHCl_3$ device (red circles).

Figure 3.12a and Figure 3.12b show the photoluminescence spectra under applied bias for the $CHCl_3$ and DCB processed devices, respectively. Consistent with previous studies, we observe a low-energy charge-transfer state luminescence peak centered around 950 – 1000 nm along with a small amount of unquenched luminescence from the donor and acceptor materials from 600 – 900 nm.[75, 93] We confirm that the 950 – 1000 nm peak is charge-transfer state photoluminescence by measuring charge-transfer state electroluminescence (Figure 3.13) in the same spectral region. We confirm that the 600 – 900 nm photoluminescence is unquenched singlet exciton emission by measuring the emission from the neat polymer in Figure 3.14. Importantly, in Figure 3.14 we show that the singlet exciton emission in neat polymer devices is largely unaffected by an applied bias from +6 to -7 V, consistent with the voltage independence that we observe in the 600 – 900 nm spectral region for the bulk heterojunction devices in Figure 3.12.[41, 85, 87, 179] In contrast, the charge-transfer state photoluminescence is significantly quenched under both forward and reverse bias.[41,

[85, 87, 179] In Figure 3.12c, we compare the voltage dependence for the charge-transfer state photoluminescence signals for both devices (after subtracting off the residual luminescence from the unquenched polymer). We find that the singlet charge-transfer state photoluminescence decreases more strongly under a reverse bias in the DCB devices compared to the $CHCl_3$ devices.

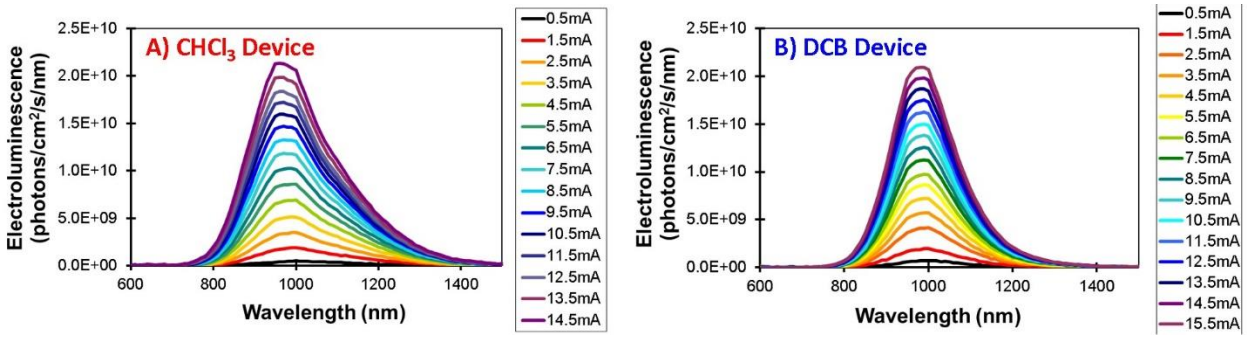

Figure 3.13. Electroluminescence spectra for a) chloroform ($CHCl_3$) devices and b) dichlorobenzene (DCB) devices over a range of 0.5 – 15.5 mA injected current measured at room temperature.

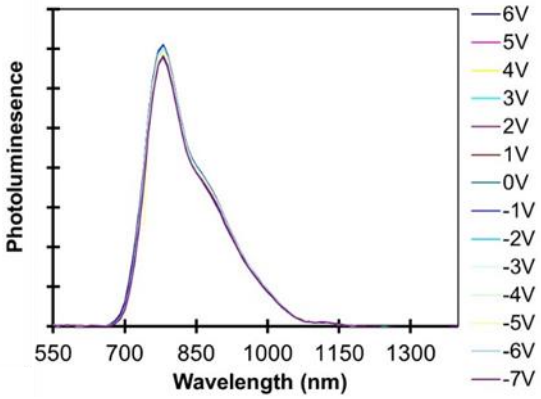

Figure 3.14. Photoluminescence under external applied voltage for neat PIDT-PhanQ devices, showing minimal voltage dependence for singlet excitons over the +6 to -7 V range.

The decreasing charge-transfer state photoluminescence intensity under reverse bias for both blends suggests that it is possible to diminish the singlet charge-transfer state population by applying an external voltage to some extent in both cases. This result is different from the voltage dependence of the triplet charge-transfer states. In particular, the triplet signal for DCB devices shows minimal voltage dependence, while the singlet charge-transfer state luminescence shows ~60 % decrease under reverse bias. On the other hand, the $CHCl_3$ device shows nearly complete quenching of the triplet signal under reverse bias with only ~40 % decrease of singlet charge-transfer state signal at the same reverse-bias voltage. The dissimilar trends of the singlet and triplet charge-transfer state spectroscopic signals suggests that the charge-transfer states of different spin are not in rapid equilibrium in our measurements.

Based on our combined spectroscopy and photocurrent results, we conclude that the singlet and triplet charge-transfer states mediate photocurrent to differing extents in the PIDT-PhanQ:PCBM devices. We propose that the six-fold increase in photocurrent extracted from the $CHCl_3$ devices under reverse bias is predominately due to decreasing recombination to triplet charge-transfer states, and to a lesser extent due to decreasing recombination through singlet charge-transfer states. On the other hand, we attribute the weaker increase in photocurrent in the DCB devices under reverse bias primarily to decreasing recombination through singlet charge-transfer states.

3.2.9 *Relating Singlet and Triplet Charge-Transfer State Voltage Dependence to Thin-Film Morphology*

Finally, we turn to the possible origins for the differing voltage dependence of singlet and triplet charge-transfer states that we observe in our DCB and $CHCl_3$ processed devices by

considering the different nanoscale morphologies in these blends. In Figure 3.15a and Figure 3.15b, we display bright field transmission electron microscopy (TEM) images, showing significantly larger phase separation in the $CHCl_3$-processed blends compared to fine polymer/fullerene mixing in the DCB-processed blends. Indeed, our resonant soft X-ray scattering (RSoXS) measurements in Figure 3.15c suggest a characteristic domain spacing $l_c = 2\pi/Q$ in the $CHCl_3$ blends of 420 nm, corresponding to the Q-position at 0.015 nm^{-1}. We interpret the additional scattering peaks at 0.03 and 0.05 nm^{-1} in the $CHCl_3$ blends to represent the domain form factor, mirrored in the TEM images as circular domains. The DCB blends exhibit significantly less scattering intensity and smaller domain spacing of 52 nm (Q-position of 0.12 nm^{-1}). The less pronounced structure in the scattering profile for the DCB blends suggests more intermixed domains without a clear form factor. Additionally, we estimate that the polymer/fullerene phases are nearly 100% pure in the $CHCl_3$ blends while being more intermixed in the DCB blends. We arrive at this estimate by comparing the total scattering intensities from RSoXS and by spatially resolving the polymer/fullerene contrast function with scanning transmission X-ray microscopy (see discussion in Section B.3 of Appendix B). Using atomic force microscopy (Appendix B), we confirm the change in morphology with the different solvent processing conditions, and we measure an increase in film thickness for the $CHCl_3$ films (~200 nm) compared to the DCB films (~100 nm).

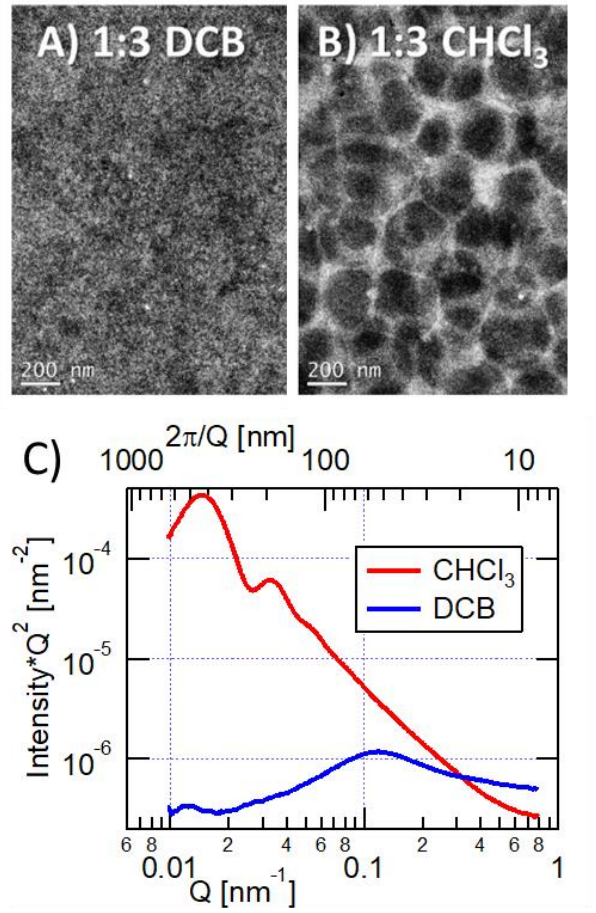

Figure 3.15. Transmission electron microscopy images of 1:3 PIDT-PhanQ:PCBM thin films processed in (a) dichlorobenzene (DCB) and (b) chloroform ($CHCl_3$) along with resonant soft X-ray scattering (RSoXS) profiles acquired with a photon energy of 283 eV (corresponding to the best polymer/fullerene contrast), showing significantly larger polymer/fullerene phases in the $CHCl_3$-processed blends compared to the DCB-processed blends. The characteristic length is defined as $l_c = 2\pi/Q$ at the peak intensity of the scattering profile.

In the $CHCl_3$ devices, we attribute the lower overall photocurrent to poor charge separation when excitons are photogenerated within large and pure polymer or fullerene regions. For the fraction of excitons that reach the donor/acceptor interfaces and dissociate, extraction of the resulting charge carriers is strongly dependent on external reverse-bias voltage. In this case, we propose that the reverse bias prevents charge recombination through both singlet and triplet

charge-transfer states. The stronger voltage dependence for the triplet PIA that we observe compared to the singlet charge-transfer state emission is consistent with the spin statistics of bimolecular recombination.

We may explain the strong voltage dependence for photocurrent extraction in the $CHCl_3$ devices with several factors influenced by both the coarse morphology and increased film thickness in $CHCl_3$-processed blends. For example, discontinuous polymer/fullerene regions are unconducive to carrier diffusion to the electrodes, and the external voltage may extract carriers from these unconnected interfacial regions.[195] Similarly, the reverse bias may extract charge that is generated directly from fullerene autoionization, as has been previously reported for devices with large fullerene phases.[188] Furthermore, in thick active layers, drift-diffusion models predict stronger external voltage dependence for photocurrent extraction due to non-uniform built-in electric fields that do not penetrate the device.[43] We speculate that several of these factors contribute to the stronger voltage dependence for carrier extraction in the $CHCl_3$ devices.

The DCB devices show higher overall photocurrent and less voltage dependence for photocurrent extraction, which we attribute to the optimized phase morphology. In this case, we propose that the more continuous and intermixed network of polymer and fullerene phases allows a greater fraction of charge carriers to reach their respective electrodes. For this reason, the reverse bias plays a lesser role in decreasing bimolecular charge recombination, and we observe minimal voltage dependence for the triplet states formed through carrier recombination. We propose that the stronger voltage dependence of the singlet charge-transfer states in the DCB devices is due to avoided polaron pair recombination at early times.[85, 179] This scenario is consistent with a recent study by Bakulin et. al on a different polymer/fullerene system, where they conclude that voltage-dependent geminate formation of singlet charge-transfer states on the sub-picosecond time scale

limits photocurrent generation in their devices.[179] Importantly, the voltage-invariance of the triplet signal that we observe in the DCB devices suggests that the singlet charge-transfer states that are avoided under reverse bias are not in rapid equilibrium with triplet charge-transfer states.

3.3 CONCLUSION

We conclude that singlet and triplet charge-transfer states are not in rapid equilibrium in the PIDT-PhanQ/PCBM system under our experimental conditions, and that their contributions to photocurrent under applied bias differ depending on nanoscale morphologies and film thicknesses. To arrive at this conclusion, we investigate the photoexcited states associated with voltage-dependent photocurrent extracted from 1:3 PIDT-PhanQ:PCBM bulk heterojunction solar cells at 180 K where the active layer is spin-coated from $CHCl_3$ or DCB. By evaluating the polaron and triplet PIA signatures under applied bias, we find that only the $CHCl_3$ devices exhibit a voltage-dependent polymer triplet signal (a proxy for triplet charge-transfer states). Importantly, the photoluminescence of singlet charge-transfer states shows a different bias dependence compared to the triplet PIA. This is particularly evident in the DCB devices, which show ~60% decrease in the photoluminescence signal under reverse bias in contrast to a voltage-invariant triplet signal. We interpret this result as indicating that the singlet and triplet charge-transfer states are not in rapid equilibrium. Finally, we speculate on the relationship between charge-transfer state voltage dependence and thin-film morphology. We propose that large, pure polymer/fullerene phases and thick active layers in the $CHCl_3$ devices yield bias-dependent charge recombination to both singlet and triplet charge-transfer states. Conversely, in the DCB devices we propose that the optimized morphology lessens the voltage dependence for carrier recombination, so the bias primarily diminishes decay of initially photogenerated singlet polaron pairs. Our results provide an important

example of the differing roles that singlet and triplet charge-transfer states play in mediating extractable photocurrent.

3.4 MATERIALS

PIDT-PhanQ was synthesized according to the previously reported procedure.[145] All other reagents were purchased from Sigma-Aldrich and used without further purification.

3.5 EXPERIMENTAL METHODS

3.5.1 *Device Fabrication*

ITO-coated (15 Ω/sq) glass substrates were cleaned sequentially with a detergent, DI-water, acetone, and isopropanol, and finally treated by UV-Ozone. PEDOT:PSS (Baytron 4083) was first spin-cast onto the ITO substrate and annealed at 140 ºC for 10 min in air to create a ~ 40 nm thick layer. Afterward, the samples were transferred into an N_2-filled glovebox. The PIDT-PhanQ:$PC_{71}BM$ (1:3 wt) BHJ layers (80-90 nm) were deposited from precursor solutions with a total material concentration of 20 mg/ml in dichlorobenzene or chloroform and annealed at 110 ºC for 10 min. A thin bis-C_{60} surfactant layer (~10 nm) was then spin-cast onto the BHJ layer and annealed at 110 °C for 5 min prior to electrode deposition. For the opaque device, 100 nm Ag was thermally evaporated under high vacuum (< 2 x 10^{-6} Torr) onto the surfactant layer through shadow masks to define the active area (10.08 × 10^{-2} cm^2) of the devices. For the semitransparent device, 30 nm Ag was thermally evaporated as the cathode for decent transparency. The rate of Ag evaporation is 2 Å/s.

3.5.2 *Current-Voltage Curves*

The current-voltage curves were measured using a Keithley 2400 source meter under AM1.5 illumination conditions with light intensity of 100 mW cm^{-2}. The intensity of the light source was calibrated using a Si photodiode detector equipped with KG-5 filter, which can be traced back to the standard cell of the National Renewable Energy Laboratory (NREL).

3.5.3 *Overview of Voltage-Dependent Photocurrent and Spectroscopy Methods*

The individual methods are described in more detail in the following sections. Figure 3.16 gives an overview of the lock-in detected photocurrent and spectroscopy measurements. Both types of measurements (photocurrent or spectroscopy) utilized the monochromator and sourcemeter shown in gray in Figure 3.16 to photoexcite the sample and simultaneously apply a DC voltage bias. For photocurrent measurements, the lock-in amplifier shown in green measured modulated photocurrent excited by chopped monochromatic light. Due to the nature of the lock-in amplifier, the modulated photocurrent measurement is insensitive to any dark current from the DC voltage applied by the sourcemeter, allowing the calculation of photovoltaic external quantum efficiency (EQE) at different applied biases.[67, 196-198] The instruments shown in blue in Figure 3.16 were used to measure the voltage-dependent photoinduced absorption spectra for the polymer triplet exciton and polaron states. CW-monochromatic light was transmitted through a device with semi-transparent electrodes, and photoinduced absorption (PIA) was recorded using the modulated change in the transmission spectrum induced by absorption of the pulsed 450 nm LED light. The PIA spectrum was corrected for luminescence by concurrently measuring the modulated PL signal by blocking the probe light with a shutter at each measured wavelength. All quasi-steady state measurements were carried out under positive nitrogen pressure at 180 K in an open-flow cryostat,

or under static vacuum for room-temperature measurements. The reduced temperature improved signal-to-noise for the spectroscopy measurements and may also have enhanced the differences between singlet and triplet charge-transfer state voltage dependence by reducing thermally-assisted interconversion and dissociation.

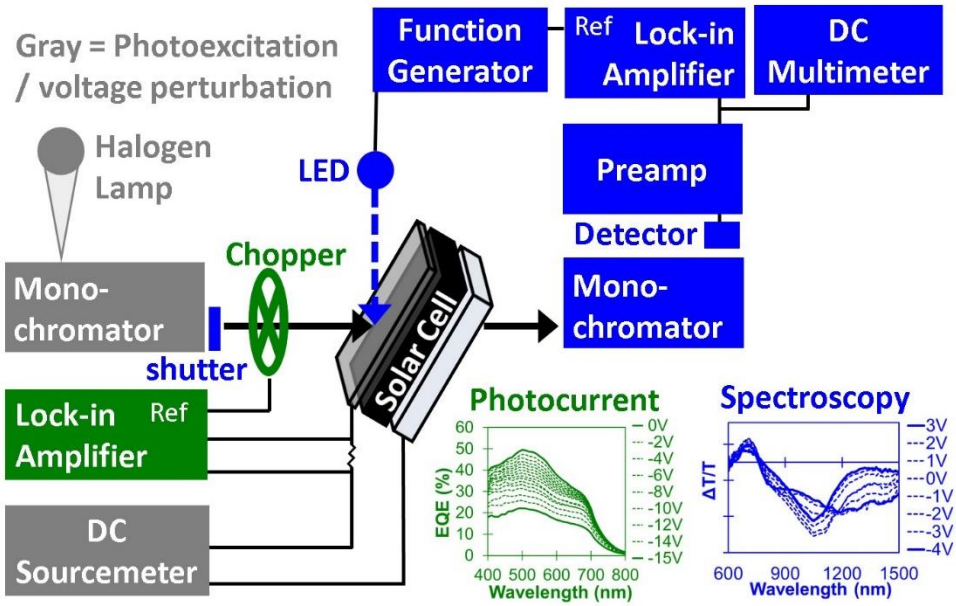

Figure 3.16. Experimental setup, where voltage dependent external quantum efficiency (EQE) measurements are made using the instruments shown in green, and voltage dependent spectroscopy measurements are made using the instruments shown in blue. Both experiments utilize the instruments shown in gray for photoexcitation under a DC voltage perturbation. The solar cell is kept either under positive nitrogen pressure at 180 K in an open-flow cryostat or under static vacuum for room temperature measurements. Insets show representative plots of voltage-dependent data in this study, including photocurrent measured as external quantum efficiency (EQE) and spectroscopy (photoinduced absorption or photoluminescence).

3.5.4 *Photovoltaic External Quantum Efficiency Under Applied Voltage*

Photocurrent was detected using a Stanford Research Systems SR830 lock-in amplifier, according to the schematic shown in Figure 3.16. A 100 Ohm resistor was placed across a BNC-

to-banana plug adapter on the input of the SR830, and the measurement mode was set to measure the voltage drop across the resistor. A Kiethley 2400 sourcemeter was used in parallel with the SR830 to apply a DC voltage to the solar cell. The sample was photoexcited using monochromated light from a tungsten-halogen lamp modulated at 200 Hz using a Stanford Research Systems SR540 chopper. A calibrated OSI optoelectronics silicon photodiode was used to record the lamp power density and calculate external quantum efficiency values. The lock-in phase was set using the measured signal at 550 nm excitation, such that the photocurrent signal was entirely in the positive X-channel (in-phase). The calibrated photodiode and device pixels were each masked to 1.2 mm^2 area. For measurements at 180 K, the devices were held under positive nitrogen flow in an open-flow cryostat. For measurements at room temperature, the devices were held under static 40 mTorr vacuum during the measurement.

3.5.5 *Photoluminescence Spectroscopy Under Applied Voltage*

Steady-state photoluminescence spectra were measured according to the schematic shown in Figure 3.16. A Kiethley 2400 sourcemeter was used to apply a DC voltage to the solar cell over the course of the measurement. The sample was photoexcited using a 447 nm LED (Luxeon Rebel, 700mW, LXML-PR01-0425) modulated at 200 Hz by an Agilent 33120A arbitrary waveform generator. Samples for photoluminescence measurements were prepared with a thin (30 nm) Ag electrode contact, allowing excitation light to pass through the electrode and photoexcite the active layer. Luminescence was recorded through an Acton monochromator using a Si/InGaAs dual-band photodiode (ThorLabs, DSD2). The current response from the photodiode was amplified and converted to a voltage signal using a Stanford Research Systems SR570 low-noise current preamplifier, and the signal was measured on a Stanford Research Systems SR830 lock-in

amplifier. The lock-in phase was set using reflected LED light such that the signal was entirely in the positive X-channel (in-phase). A calibrated LS-1-CAL Ocean Optics light source was used to correct the photoluminescence spectra for detector response. The device pixels were masked to 1.2 mm^2 area in order to avoid photoexcitation of the surrounding material not in contact with the electrode. The devices were held at 180 K under positive nitrogen flow in an open-flow cryostat.

3.5.6 *Photoinduced Absorption Spectroscopy Under Applied Voltage*

Steady-state photoinduced absorption was measured using standard lock-in techniques, according to the schematic shown in Figure 3.16. A Kiethley 2400 sourcemeter was used to apply a DC voltage to the solar cell over the course of the measurement. The sample was photoexcited using a 447 nm LED (Luxeon Rebel, 700mW, LXML-PR01-0425) modulated at 200 Hz by an Agilent 33120A arbitrary waveform generator. Samples for photoinduced absorption measurements were prepared with a thin (30 nm) Ag electrode contact, allowing excitation light to pass through the electrode and photoexcite the active layer. Monochromated CW light from a tungsten-halogen light source was incident on the same area and transmitted through the device. Transmitted light was recorded through an Acton monochromator using a Si/InGaAs dual-band photodiode (ThorLabs, DSD2). The current response from the photodiode was amplified and converted to a voltage signal using a Stanford Research Systems SR570 low-noise current preamplifier. The output from the preamplifier was measured on a Keithley 2000 sourcemeter to obtain the total DC transmission signal (T). The output from the preamplifier was simultaneously measured on a Stanford Research Systems SR830 lock-in amplifier to obtain the AC (dT) signal. The photoluminescence (PL) signal was simultaneously measured by blocking the monochromated CW light from the tungsten-halogen light source with a shutter at each

wavelength. The PIA signal was corrected for PL and total transmission intensity as (dT – PL) / T. The lock-in phase was set using reflected LED light. The device pixels were masked to 1.2 mm^2 area in order to avoid photoexcitation of the surrounding material not in contact with the electrode. The devices were held at 180 K under positive nitrogen flow in an open-flow cryostat.

3.5.7 *Atomic Force Microscopy*

AFM measurements were performed on an Asylum Research MFP-3D Bio atomic force microscope. All images were acquired using 300 kHz resonance frequency BudgetSensor silicon cantilevers with a Pt/Cr conductive coating.

3.5.8 *Transmission Electron Microscopy*

Films for TEM characterization were spin-cast onto PEDOT:PSS as described for device fabrication. The films were separated from the substrate by immersing the sample in water and dissolving the PEDOT:PSS layer. The film was mounted on a TEM grid without a support film. Bright field imaging was carried out using a Tecani G2 F20 TEM with an accelerating voltage of 120 kV.

3.5.9 *Soft X-Ray Characterization*

Films were spin-cast onto PEDOT:PSS as described for device fabrication and were separated from the substrate by immersing in water and dissolving the PEDOT:PSS layer. For X-ray microscopy, the films were mounted on a TEM grid without a support film. For scattering, films were mounted onto a 100nm thick SiN window.

3.5.10 *Transient Absorption Spectroscopy*

The fundamental for the pump and probe pulses was generated from a Libra amplified Ti:Sapphire femtosecond laser system purchased from Coherent Inc (50 fs, 800 nm, 1 kHz). The Libra laser system consists of the Vitesse mode-locked Ti:Sapphire seed laser (100 fs, 800 nm, 80 MHz) and Evolution pump laser (250 ns, 527 nm, 1 kHz). After passing the seed pulse through a stretcher, the two pulses are co-incident on a Ti:Sapphire crystal within a regenerative amplifier system containing two Pockels cells. The Ti:Sapphire output then passes through a compressor before the fundamental output pulse is split by an 80/20 beam splitter to generate the probe and pump, respectively. The wavelength for the pump pulse was set using the OperAsolo optical parametric amplifier purchased from Coherent Inc. The NIR white light for the probe pulse was generated by focusing the fundamental onto a sapphire crystal in the Helios transient absorption system purchased from Ultrafast Systems. Delay between the pump and probe pulse was set using the Thorlabs optical delay line within the Helios system. Data acquisition and instrument control were carried out using the Helios software from Ultrafast Systems.

3.5.11 *Laser Spot Characterization*

Pump and probe beams were characterized at the sample position using the BC106N-VIS CCD Camera Beam Profiler purchased from Thorlabs (see Figure S20). Spatial beam images and spot size calculations were obtained from Thorlabs' standard beam profiler software package. Average power was measured using the Coherent FieldMate laser power meter equipped with the OP-2 VIS high sensitivity sensor purchased from Edmond Optics.

Figure 3.17 shows the beam profiles for the 450 nm laser excitation (lower left) along with the NIR white light (upper right) near the sample position for transient absorption experiments. We obtain a spot size of 0.0026 cm^2 for the 450 nm pump by calculating the area of the ellipse with radii defined by $1/e^2$ of the peak intensities of the Gaussian fits shown in Figure 3.17. Importantly, Figure 3.17 shows that the white light has a smaller spot size than the 450 nm pump, allowing the pump to photoexcite the full area that is probed by the white light when the pump and probe are overlapped.

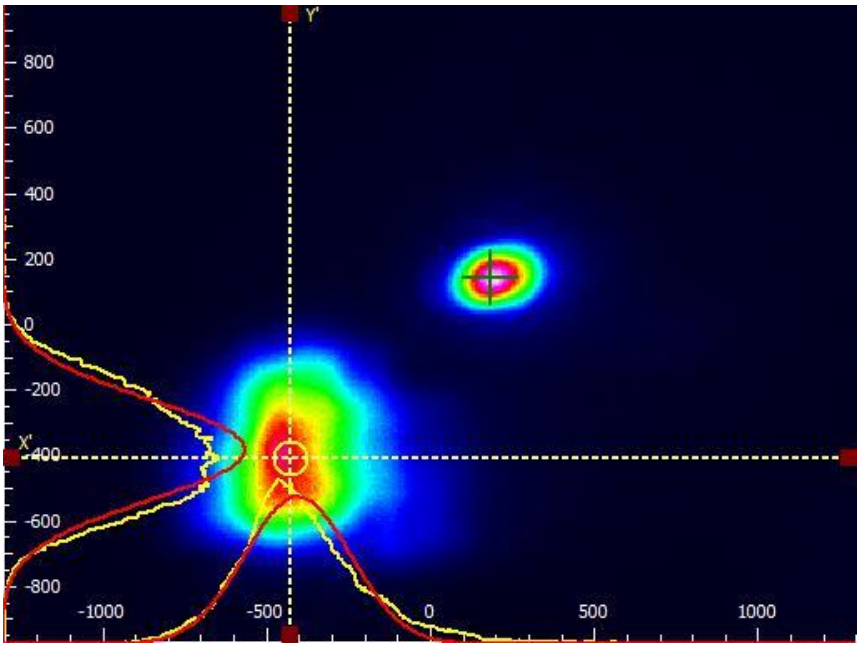

Figure 3.17. Beam profiles of the 450 nm pump (lower left) and NIR white light (upper right) at the sample position (Note: beams would be overlapped during the transient absorption measurement). Axes are in units of micrometers.

Chapter 4. KINETIC COMPETITION BETWEEN CHARGE SEPARATION AND TRIPLET FORMATION IN SMALL-MOLECULE PHOTOVOLTAIC BLENDS

Adapted From:
Sulas, D.B.; Rabe, E.J.; Schlenker, C.W. J. Phys. Chem. C ***2017****, 121, p. 26667-26676.*

4.1 INTRODUCTION

In high-performance organic photovoltaic (OPV) materials, charge separation at electron donor/acceptor interfaces and carrier extraction must kinetically outcompete relaxation to low-energy excited states that do not contribute to photocurrent.[68, 80, 181, 183-185] In several materials systems, relaxation to localized triplet excitons has been identified as a severe and sometimes dominant loss pathway.[68, 80, 181, 183-185] The 0.1 – 1.5 eV exchange energy that stabilizes triplets relative to photogenerated singlet excitons in these materials is frequently sufficient to create a thermodynamic barrier to charge (re)dissociation at the donor/acceptor interfaces.[65-67, 69] The inability to dissociate triplet states often decreases device efficiency, with the notable exception of devices designed to harness the lower-energy triplets produced by singlet exciton fission.[62, 199] More commonly, however, charge-transfer state energies in non-fission devices are higher than triplet exciton energies.[199] As a result, triplet formation by charge recombination or intersystem crossing must be kinetically avoided in order to avert photocurrent loss.[68, 80, 181, 183-185] Indeed, the most promising OPV materials systems exhibit charge generation approaching sub-100 femtosecond time scales,[102-105] significantly faster than the nanosecond intersystem crossing times that are typical for the pristine donor and acceptor components.[200-202] Nevertheless, several studies report *enhanced* triplet formation in donor/acceptor blends compared to the pristine materials, suggesting that donor/acceptor interactions provide alternative pathways to generate triplet

excitons that are not accessible in the separated materials.[69, 181, 183-184, 203-205] These reports of photovoltaic loss via triplets, even in many state-of-the-art materials systems, represent an area for improvement in OPV design if the factors influencing triplet formation can be better understood and ultimately suppressed.[65, 67-69, 91, 181, 183, 203-204]

Although the time-resolved photophysics of enhanced triplet formation in polymer/fullerene bulk heterojunction films has received recent attention,[68-69, 91-92, 206] the corresponding processes in small-molecule photovoltaic blends are surprisingly underexplored.[184, 205] The understanding of triplet formation pathways has tracked with the popularity of polymer-based devices due to their facile solution processing and the perceived benefits of longer polymer chain lengths for charge transport.[207-208] However, the inherent energetic and spatial disorder resulting from polydispersity and polymorphism in polymer films may also influence the pathways of triplet formation.[106] Small-molecule organic semiconductors represent an attractive alternative model system, where the well-defined molecular units allow the relationship between triplet formation and local chromophore environment to be more systematically characterized and controlled. Decreased disorder due to greater structural rigidity, both within the molecules and their lattice structures, may additionally promote beneficial properties in small-molecule systems such as excited-state delocalization,[106, 115] fewer and shallower trap sites,[106] and high carrier mobilities.[209]

Importantly, excited-state delocalization over multiple chromophores has recently been linked to efficient charge generation in polymer/fullerene blends,[102] which appears to suppress recombination to triplet states in these materials.[80] In this study, we investigate the effect of molecular aggregation on triplet formation in small-molecule donor/acceptor blends, including both the extent of loss via triplet states and the photophysical pathways for triplet formation. We

use C_{60} fullerene as the electron acceptor and chloroboron subphthalocyanine (SubPc) as the electron donor. SubPc/C_{60} interfaces serve as a popular model system for understanding photovoltaic processes,[39, 104, 210-218] and solar cells employing SubPc have achieved up to 8.4 % power conversion efficiency.[211]

We perform transient absorption and time-resolved photoluminescence spectroscopy to evaluate the photophysics leading to triplet formation in blended SubPc:C_{60} films. We find that SubPc triplets are formed via charge recombination in vapor-deposited SubPc:C_{60} films, but that losses to triplets are markedly decreased in films with higher fullerene ratio (1:2 versus 1:1 blends). Based on the enhanced fullerene aggregate peak in the photovoltaic external quantum efficiency curves, we attribute the decrease in triplet formation to excited-state delocalization over aggregate states, which favors charge generation instead of recombination. We further evaluate the influence of molecular aggregation and charge-transfer states on triplet formation by studying dilute films of SubPc and C_{60} in polystyrene, where aggregation is suppressed. In the dilute films, SubPc triplets are populated via an energy transfer pathway with intersystem crossing centered on C_{60}. Though thermodynamically accessible, this pathway is kinetically out-competed by charge transfer in the vapor-deposited blends.

4.2 Results and Discussion

4.2.1 *Energy Landscape in SubPc:C_{60} Blends*

Since the efficiencies of SubPc:C_{60} devices are likely affected by the branching between charge generation and triplet formation, we investigate the thermodynamically accessible pathways to create triplets. We illustrate the energy landscape for SubPc:C_{60} blends in Figure 4.1a, emphasizing two pathways for possible SubPc triplet exciton formation. Path 1 depicts SubPc

triplets forming through charge-transfer state relaxation, which is thermodynamically favorable as SubPc triplets are lower in energy than both charge-transfer states and fullerene triplets. It is possible for the localized molecular triplet states to be populated via free charge recombination to triplet charge-transfer states or following spin interconversion within the charge-transfer state manifold.[92, 219-221] Path 2 depicts an energy transfer pathway including the following processes: (i) singlet-singlet energy transfer from SubPc to C_{60}, (ii) intersystem crossing on C_{60}, and (iii) triplet-triplet energy transfer from C_{60} to SubPc. Importantly, the spectral overlap of the SubPc singlet fluorescence spectrum with the weak C_{60} singlet absorption out to 650 nm indicates that singlet-singlet energy transfer is possible via Förster resonance energy transfer (FRET) from SubPc to C_{60}.[210, 222]

We obtain the singlet and triplet energies in Figure 4.1a from the absorption and emission spectra of dilute SubPc or C_{60} in polystyrene (PS) films (Figure 4.1b-c). We employ polystyrene as an inert matrix allowing us to characterize native molecular spectra without contributions from aggregate states, similar to the methods in previous photophysical studies.[200, 223]

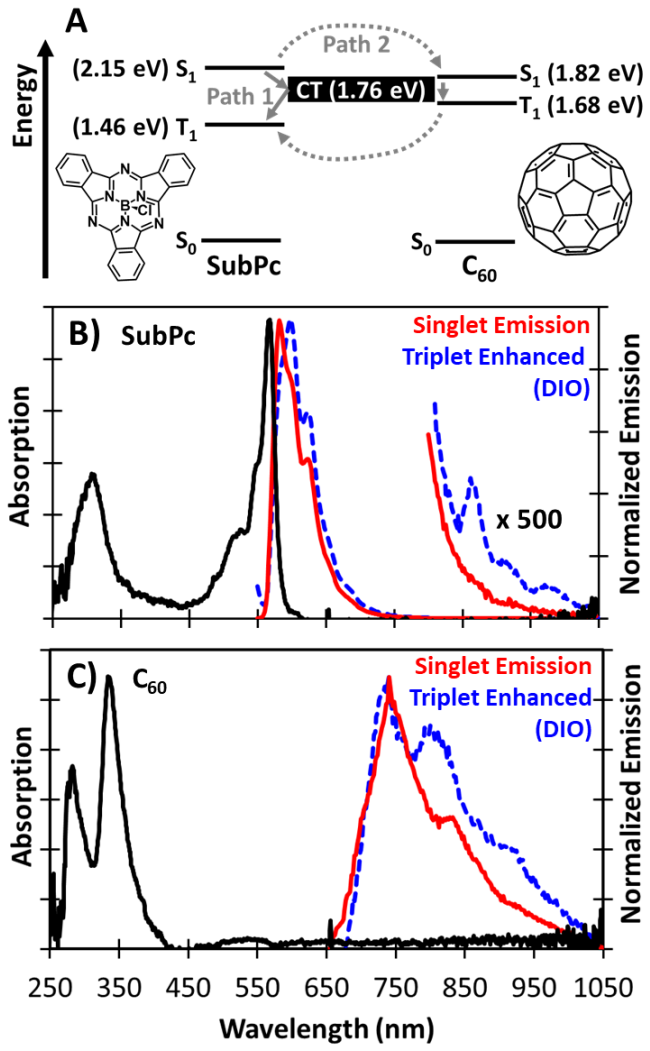

Figure 4.1. (a) Molecular structures and energy levels for SubPc and C_{60}, including accessible fullerene-mediated pathways for populating SubPc triplet states. Charge-transfer state (CT) energy is approximated from emission of vapor-deposited SubPc:C_{60} blends (Figure S5) and fitting the sub-gap region of external quantum efficiency curves (Figure 4.3).[38,45-46] Singlet (S_1) energies are determined from the intersection of normalized absorption (black) and photoluminescence (red) spectra for (b) SubPc and (c) C_{60} in polystyrene films. Triplet (T_1) energies are determined from the onset of phosphorescence in dilute films with diiodooctane (DIO, blue dotted traces). Emission spectra are recorded at 80 K.

Figure 4.1b shows emission spectra for SubPc:PS films at 80 K, measured with and without diiodooctane (DIO) as a non-emissive external heavy-atom source to promote triplet phosphorescence. The SubPc singlet fluorescence in the films without DIO shows emission maxima centered around 600 and 625 nm, with the intersection between the normalized absorption and fluorescence spectra yielding a singlet energy of 2.15 eV.[224] The SubPc:PS films with DIO exhibit new emission peaks at lower energy in addition to the singlet emission. We assign these new peaks to triplet phosphorescence at 860, 915, and 975 nm, corresponding to a SubPc triplet energy of 1.46 eV. While we are not aware of a prior report showing SubPc phosphorescence, we find our SubPc triplet energy to be commensurate with those of chemically functionalized SubPc derivatives estimated from phosphorescence or from the rate of singlet luminescence quenching.[225-227] We are able to measure the weak SubPc phosphorescence signal using sensitive lock-in techniques, where the triplet emission intensity is more than an order of magnitude larger than the noise floor of our instrument.

Figure 4.1c displays the absorption and emission spectra for C_{60}:PS films that we use to obtain the C_{60} energy levels in Figure 4.1a. The dilute C_{60} absorption spectrum contains peaks at 282 and 336 nm with a weak symmetry-forbidden transition from 450 to 650 nm (see Figure C.1 of Appendix C).[210, 228-230] We obtain a singlet energy of 1.82 eV from the C_{60} fluorescence in films without DIO, where emission maxima are centered around 740 and 830 nm.[231-232] For C_{60}:PS films with DIO, we observe new peaks corresponding to triplet emission maxima at 800 and 910 nm, in addition to residual singlet luminescence at 740 nm. From the phosphorescence, we estimate the triplet energy for C_{60} in our samples to be 1.68 eV.[231, 233-234]

We assign the intermolecular SubPc/C_{60} charge-transfer state energy as 1.76 eV by measuring emission spectra of vapor-deposited SubPc:C_{60} blends (Figure 4.2), by fitting the sub-

gap region of the external quantum efficiency curves for our SubPc:C_{60} devices (Figure 4.3),[75, 217] and from literature reports.[37, 217, 235]

Figure 4.2 shows the emission spectra that we use to estimate a lower limit for the charge-transfer state energy, including a comparison of the emission from 1:1 SubPc:C_{60} vapor-deposited films with the singlet emission spectra of dilute SubPc and C_{60} in dispersed in polystyrene. We measure the emission maximum from 1:1 SubPc:C_{60} films at 790 nm, which is lower energy compared to both pristine SubPc and C_{60} singlet emission spectra. While previous studies have reported SubPc-C_{60} charge-transfer state emission in this spectral region, we note that our emission spectrum for the 1:1 SubPc:C_{60} films exhibits a non-gaussian line shape. This result suggests that our measurement for the SubPc:C_{60} films at low temperature may instead correspond to C_{60} triplet emission, which is enhanced due to energetic co-incidence with the charge-transfer state. Based on this data, we assign a minimum possible value of the charge-transfer state energy as ~1.7 eV (i.e. at or greater than the C_{60} triplet).

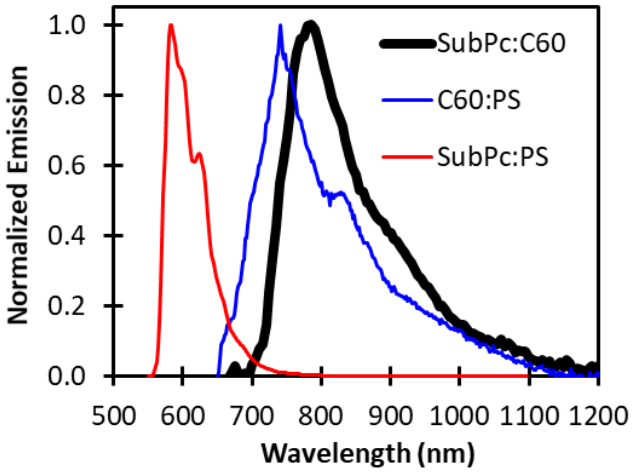

Figure 4.2. Comparison of normalized emission spectra for SubPc:PS (red), C_{60}:PS (blue), and vapor-deposited 1:1 SubPc:C_{60} (black).

We provide a more direct measure of the charge-transfer state energy in Figure 4.3 by fitting the sub-gap region of the external quantum efficiency curves for the 1:1 and 1:2 SubPc:C_{60} devices, showing similar charge-transfer state energies of 1.76 eV for both blend ratios. We fit the low-energy part of the external quantum efficiency (EQE) curves according to Equation 4.1, which is derived from Marcus Theory and represents photocurrent generation from direct excitation of donor/acceptor charge-transfer complexes, as discussed in Chapter 2.[38, 75, 217]

$$EQE\ (E) = \frac{f}{E\sqrt{4\pi\lambda kT}} Exp\left(\frac{-(E_{CT}+\lambda-E)^2}{4\lambda kT}\right) \quad (4.1)$$

In Equation 4.1, E is energy [eV], f is the coupling constant [eV^2] that is proportional to electronic coupling to the ground state and the available density of charge-transfer states,[38, 75] λ is the reorganization energy [eV], k is Boltzmann's constant [eV K^{-1}], T is temperature [K], and E_{CT} is the charge-transfer state energy [eV].

In Figure 4.3, we show that the photocurrent generation in our EQE curves extends to lower energies past the edge of the SubPc absorption spectrum. We attribute the sub-gap EQE to charge-transfer state absorption. By fitting the low-energy EQE region with Equation 4.1, we obtain similar charge-transfer state energies of 1.76 eV and similar reorganization energies of 0.19 – 0.22 eV for both the 1:1 and 1:2 SubPc:C_{60} devices. Importantly, we observe minimal change in the E_{CT} for the SubPc:C_{60} blends studied here, although charge-transfer state energies are known in some cases to vary for a given donor/acceptor pair with different blend ratios and film morphologies.[86, 236-237]

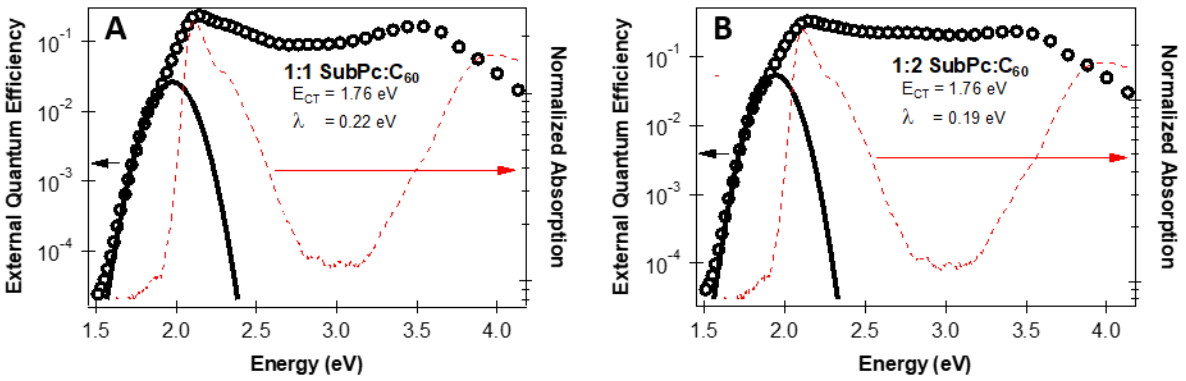

Figure 4.3. External quantum efficiency (black circles) for (a) 1:1 and (b) 1:2 SubPc:C_{60} devices reproduced from Figure 2 along with fits to the sub-gap EQE region according to Equation S1 (black solid line), yielding charge-transfer state energies (E_{CT}) of 1.76 eV and reorganization energies (λ) of 0.19 – 0.22 eV. We overlay the normalized absorption spectrum for 15 nm vapor-deposited SubPc thin films (red dotted line), showing that the 1.5 – 2.0 eV region corresponds to sub-gap charge-transfer state absorption.

Previous solution-phase studies of covalently linked SubPc-C_{60} diads suggest that C_{60} facilitates SubPc triplet formation through one or both of the pathways depicted in Figure 4.1a, where the predominate pathway depends on the polarity of the solvent environment and the electron-donating character of substituents on the SubPc.[201, 222, 227, 238] This dependence on solvent polarity observed in diad solutions indicates that the local molecular environment may also affect the branching of kinetic processes in thin-film devices, altering populations of triplets, charge-transfer states, and free charge carriers.

In fact, aggregation in thin films has been shown to profoundly influence device performance.[86, 215] The importance of aggregation stems from changes in the underlying photophysics, which is influenced by factors such as variation of the local dielectric constant,[86] wave function delocalization,[77, 115, 239-240] the presence of lower-energy aggregate states,[239, 241] charge-transfer states,[69, 217, 227, 240] and enhanced intermolecular interactions causing exciton self-

quenching and charge recombination.[242-244] Some of these factors, such as the dielectric environment, are known to alter the photophysics of triplet formation in solution-phase diads.[201, 222, 227, 238] However, the additional influences in condensed films cannot be inferred from solution-phase measurements of covalently linked donor-acceptor pairs. Hence, the goal of this work is to investigate the influence of small-molecule aggregation on the kinetic processes relevant for photocurrent generation in solid-state devices.

4.2.2 *Photovoltaic Device Performance in SubPc:C_{60} Blends*

In Figure 4.4 and Table 4.1, we demonstrate that photovoltaic device performance in SubPc:C_{60} vapor-deposited blends is strongly influenced by varying the SubPc:C_{60} ratio, which affects the aggregation and ordering of SubPc and C_{60} molecules.[215] In devices with higher fullerene ratio (1:2 blends), we measure increased photovoltaic external quantum efficiency (EQE), with improvements in both the C_{60} absorption region (300 – 475 nm) and the SubPc absorption region (475 – 650 nm). Notably, the 1:2 devices show a new EQE peak at 450 nm associated with enhanced C_{60} aggregate absorption, which is not present in the 1:1 EQE curve. This peak corresponds to intermolecular C_{60}-C_{60} charge-transfer transitions in C_{60} aggregates (see Figure C.3 in Appendix C).[47-48, 223, 245-246] The increase in EQE for the 1:2 blends is also reflected in the current-voltage characteristics in Figure 4.4b and Table 4.1 displaying enhanced power conversion efficiency due to an increase in the short-circuit current for 1:2 devices.

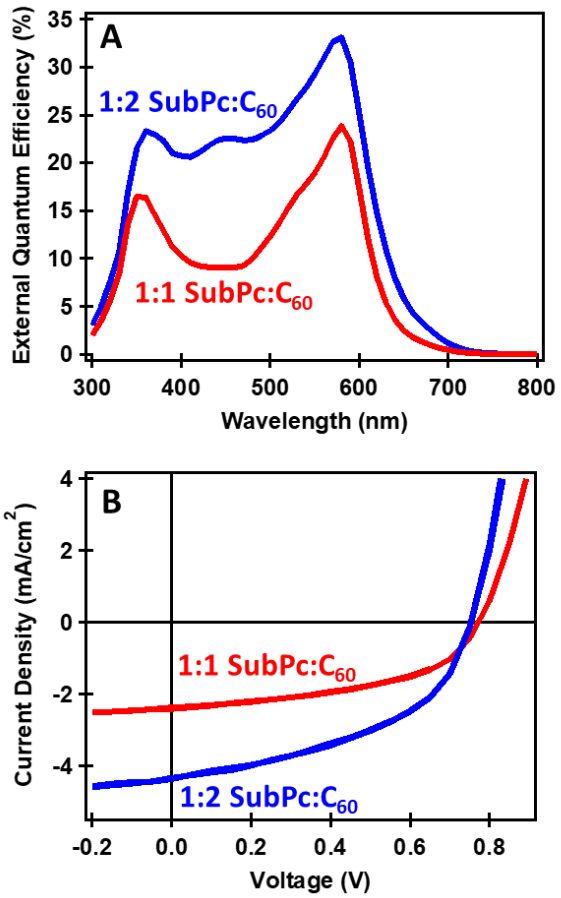

Figure 4.4. Photovoltaic device performance, including (a) external quantum efficiency and (b) current-voltage curves under AM1.5G simulated solar illumination for 1:1 SubPc:C_{60} (red) and 1:2 SubPc:C_{60} (blue) active layers in a device structure consisting of [indium tin oxide / molybdenum oxide (10 nm) / SubPc:C_{60} / bathocuproine (5 nm) / aluminum (100 nm)] where the SubPc:C_{60} active layer is 26 or 39 nm for 1:1 or 1:2 active layers, respectively. The active layers have constant SubPc content for both devices (constant SubPc optical density) and varying C_{60} content.

Table 4.1. Device performance metrics including short-circuit current (J_{SC}), open-circuit voltage (V_{OC}), fill factor (FF), and power conversion efficiency (PCE), where error is reported as the standard deviation of the mean.

	J_{SC} (mA/cm^2)	**V_{OC}** (V)	**FF**	**PCE** (%)
1:1 blend	2.42 +/- 0.04	0.72 +/- 0.03	0.50 +/- 0.01	0.87 +/- 0.03
1:2 blend	4.36 +/- 0.08	0.76 +/- 0.02	0.45 +/- 0.01	1.48 +/- 0.06

The enhanced C_{60} aggregate EQE peak in the 1:2 blends that appears near 450 nm suggests that molecular aggregation plays a role in photocurrent generation in this blend. The goal of this study is to understand how such aggregation behavior correlates with the underlying photophysics of charge generation and triplet formation. We note that the increased fullerene ratio is not only implicated in the formation of nanocrystalline fullerene phases, but also appears to induce orthorhombic packing in SubPc phases.[215] We hypothesize that excited-state delocalization over these ordered phases favors charge generation,[77] and may prevent recombination loss to triplets,[80] leading to the improved device performance that we observe.

By performing transient absorption spectroscopy and interpreting the kinetics with global target analysis (Section 4.2.6), we show that the increase in photocurrent that we measure in the 1:2 devices correlates with suppressed charge recombination to SubPc triplets (Path 1, Figure 4.1a). Additionally, in very dilute blends where both SubPc and C_{60} components are dispersed in an inert matrix to intentionally disrupt aggregation and charge generation (Section 4.2.8), we show that the SubPc triplet state is populated primarily through Path 2.

4.2.3 *Characterization of SubPc Singlet and Triplet Spectra*

In order to evaluate the photophysical processes that occur in mixed SubPc:C_{60} films, we first identify the native rates of intersystem crossing and characterize the singlet and triplet spectral signatures for each of the separate materials dispersed in polystyrene. We choose to initially study dilute films of the materials in polystyrene for several reasons. First, the dilute polystyrene films allow us to study the materials behavior when the molecules are largely isolated rather than aggregated. Suppressing aggregation in order to characterize the native molecular processes is important because, as we previously discussed in Section 4.2.1, aggregation strongly affects

photophysical processes and resulting excited state populations. Additionally, the polystyrene matrix acts as an encapsulating layer, excluding oxygen from penetrating into the film and thus helping to avoid oxygen quenching of triplet excitons. As shown in Figure 4.5, this allows us to cleanly characterize triplet spectral signatures at long time scales, well after singlet excitons have fully decayed. We find that triplet excitons are significantly longer lived in polystyrene films compared to dilute solutions, even when we follow stringent procedures to keep both types of samples under inert atmosphere. We attribute the longer-lived signal in the polystyrene films to better exclusion of oxygen and decreased molecular diffusion. Figure 4.6 shows that the triplet transient absorption signal in the dilute polystyrene films persists past the 9 μs time window that we probe, while the signal reaches zero intensity by 400 ns for dilute solutions of SubPc in tetrahydrofuran (THF).

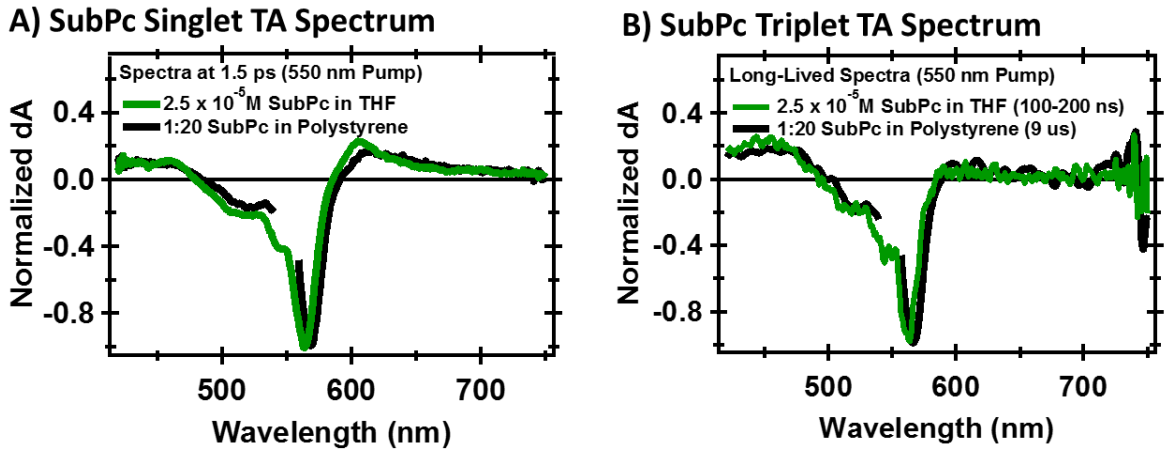

Figure 4.5. Comparison of transient absorption spectra at (a) 1.5 ps and (b) longer time scales (100 – 200 ns or 9 us) for dilute SubPc in THF or in a polystyrene film. We assign the spectral shape at short time scales to initially photoexcited SubPc singlets, and we assign the spectral shape at longer time scales to SubPc triplets formed following intersystem crossing.

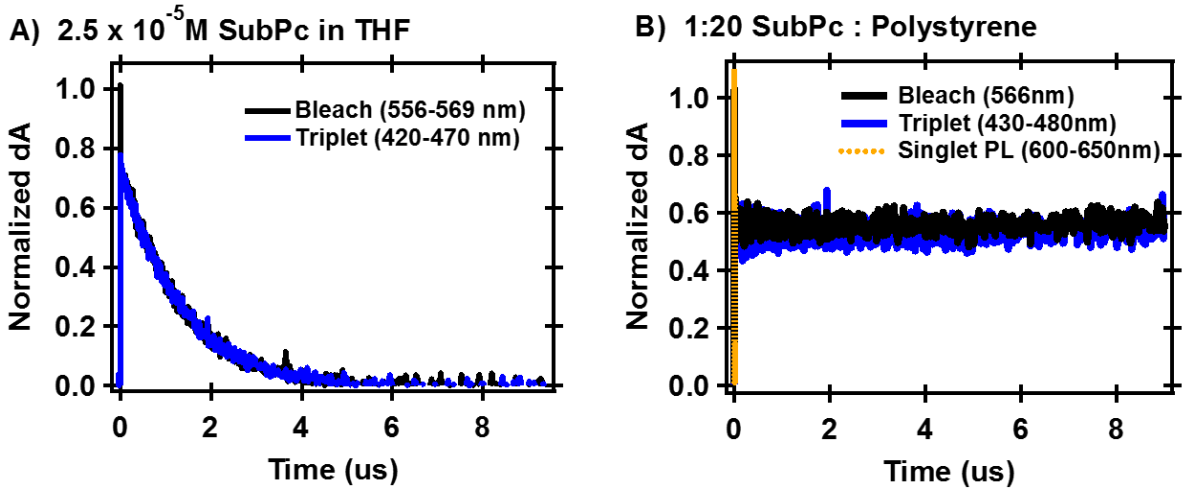

Figure 4.6. Normalized kinetics at the SubPc bleach and at the TA region assigned primarily to SubPc triplets for (a) 2.5 × 10^{-5} M SubPc in tetrahydrofuran (THF) and (b) SubPc:polystyrene dilute films, showing longer-lived triplets in the polystyrene matrix compared to dilute THF solutions.

In addition to our characterization of the SubPc triplet spectral shape by observing long-lived transient absorption signal in Figure 4.5, we also characterize the singlet and triplet spectral shapes by fitting the spectral evolution associated with intersystem crossing through a singular value decomposition method using the GloTarAn software.[247] Figure 4.7a shows the transient absorption spectra for SubPc:PS films between 1 ps and 9 μs following 550 nm photoexcitation. Similar to Figure 4.5, we observe negative signal at 500 – 600 nm corresponding to the ground state bleach and positive signals maximized around 460 and 612 nm. The 612 nm induced absorption significantly decays over 5.5 ns, and is almost completely quenched by 9 μs. On the contrary, the 460 nm induced absorption shows minimal change over 5.5 ns, and is still present at 9 μs. Figure C.4 in Appendix C shows that we measure minimal signal from SubPc:polystyrene films in the near infrared at wavelengths greater than 800 nm.

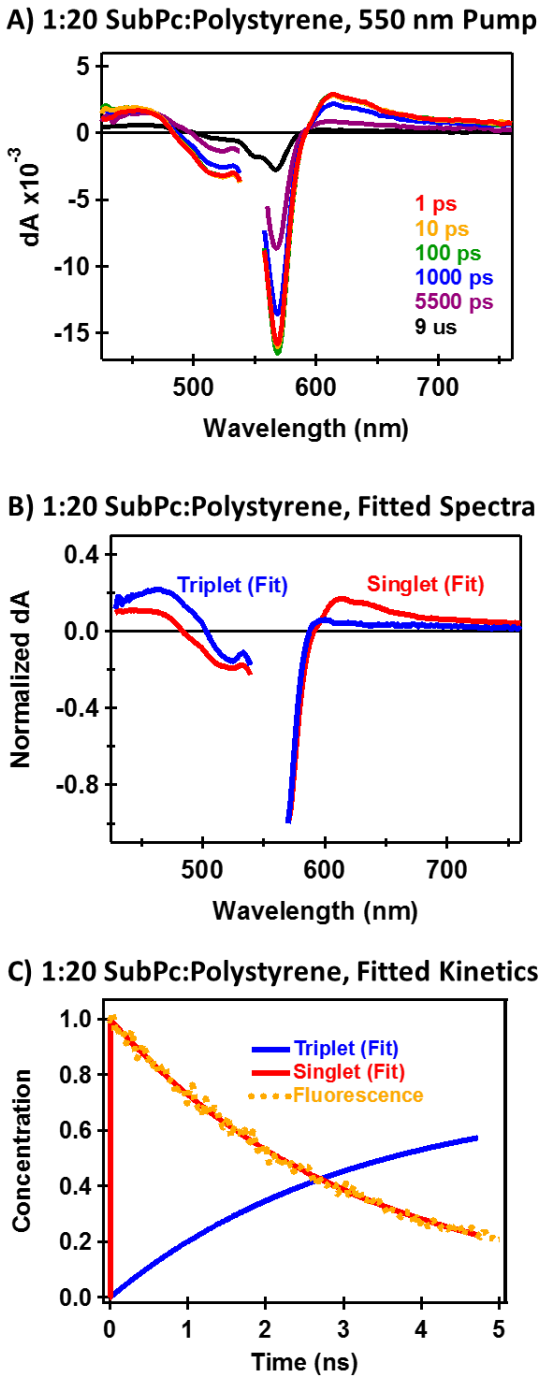

Figure 4.7. (a) Transient absorption spectra under 550 nm photoexcitation for a SubPc:polystyrene film taken at 1ps (red), 10 ps (orange), 100 ps (green), 1000 ps (blue), and 5500 ps (purple) (b) Species associated spectra of the singlet (red) and triplet (blue) signatures from global target analysis fitting using GloTarAn software, and (c) fitted kinetics of the singlet (red) and triplet (blue) spectra from global target analysis overlaid with the normalized SubPc fluorescence decay (orange dots).

We show the results of our global target analysis in Figure 4.7b and Figure 4.7c. Our model assumes that fixed spectral shapes contribute to the overall transient absorption spectrum with time-dependent concentrations according to $\psi_{Total}(\lambda) = C_{Singlet}(t)\ \sigma_{Singlet}(\lambda) + C_{Triplet}(t)\ \sigma_{Triplet}(\lambda)$, where $\sigma(\lambda)$ represents the wavelength-dependent spectral components and C(t) represents the time-dependent concentrations of each species. Figure 4.7b shows the spectral shapes $\sigma(\lambda)$ that we assign to the singlet and triplet states. The singlet induced absorption contains a peak at 612 nm and weaker peak at 450 nm, while the triplet induced absorption contains greater intensity in the 460 nm region.[201-202, 222, 227] Importantly, the SubPc:PS films show a significant fluorescence quantum yield of 26%. For this reason, our model allows the singlet population to decay either radiatively to the ground state or via intersystem crossing to populate triplets. Figure 4.7c shows the corresponding kinetics C(t) overlaid with the normalized fluorescence signal. From both our transient absorption analysis and the SubPc singlet fluorescence decay, we obtain a total singlet lifetime of 3.15 ns.

4.2.4 *Characterization of C_{60} Singlet and Triplet Spectra*

Figure 4.8a shows transient absorption spectra for C_{60}:PS films photoexcited at 365 nm, which we use to characterize the C_{60} singlet and triplet spectral features. At early times (1 – 100 ps) we observe peak maxima at 980 nm and 500 nm, corresponding primarily to singlet absorption. At later times (1000 – 5500 ps) the signal at 980 nm approaches zero, and a triplet-associated induced absorption signal grows in with a maximum at 760 nm. We model the spectral evolution by global target analysis using the GloTarAn software,[247] and we present the results in Figures Figure 4.8b and Figure 4.8c. We model the transient absorption data according to $\psi_{Total}(\lambda) = C_{Singlet}(t)\ \sigma_{Singlet}(\lambda) + C_{Triplet}(t)\ \sigma_{Triplet}(\lambda)$. For the C_{60}:PS films, the majority of singlets decay via

intersystem crossing to triplets, consistent with our observation of < 1% fluorescence quantum yield for these films.

Figure 4.8b shows the resulting line shapes that we assign to the C_{60} singlet and triplet associated spectra, which are in good agreement with previous reports.[200] Figure 4.8c shows the corresponding kinetics for intersystem crossing, where singlets decay and triplets concomitantly rise with a 1.20 ns time constant.[200, 248] We overlay the fitted kinetic traces with the normalized fluorescence decay, measured using sensitive detection employing a streak camera despite the low fluorescence quantum yield (< 1%). We find good agreement between the fluorescence kinetics and the singlet decay from our transient absorption analysis.

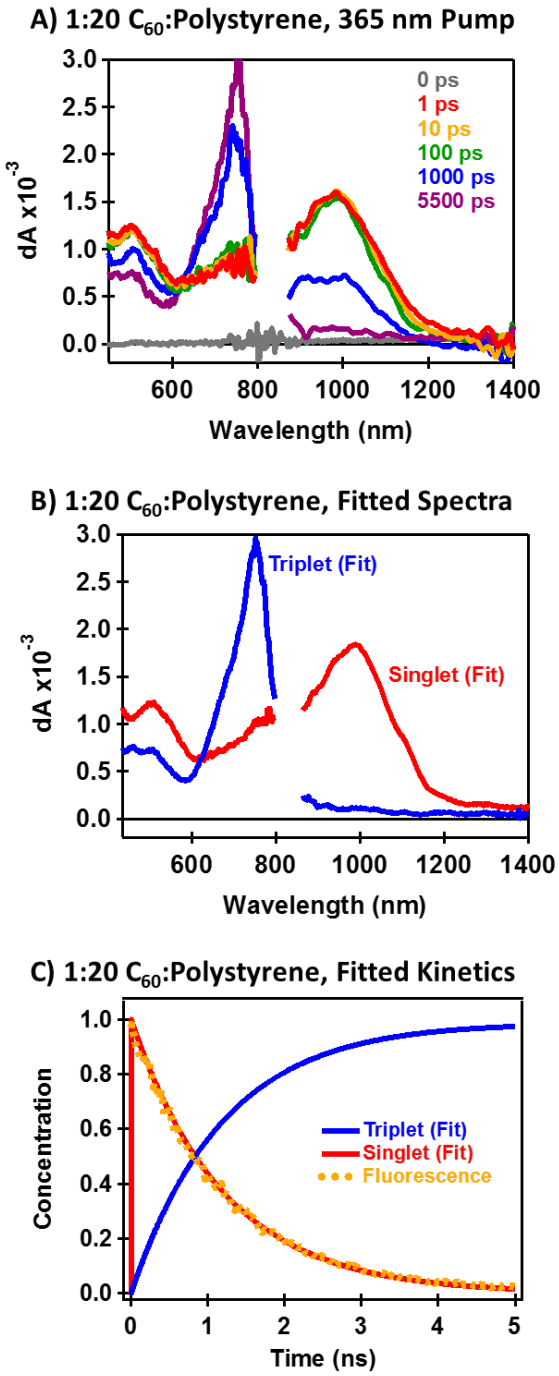

Figure 4.8. (a) Transient absorption spectra under 365 nm photoexcitation for a C_{60}:polystyrene film taken at 0 ps (gray), 1ps (red), 10 ps (orange), 100 ps (green), 1000 ps (blue), and 5500 ps (purple) showing induced absorption regions centered around 980 nm for the singlet exciton and 760 nm for the triplet exciton (b) the kinetics of the singlet (980 nm, red) and triplet (730 nm, blue) induced absorption regions, where the singlet decay is overlaid with the normalized C_{60} photoluminescence kinetics measured over 710 – 800 nm (orange, right axis).

4.2.5 *Characterization of SubPc Cation Spectra*

We characterize the SubPc cation absorption spectral signatures in Figure 4.9 and Figure 4.10 through chemical oxidation of SubPc using triethyloxonium hexachloroantimonate in dichloromethane. Figure 4.9 shows that we observe a decrease in the SubPc ground state absorption at 550 nm upon addition of the oxidizing agent (OA), along with the rise of a new peak at 610 nm. The increase in absorption upon addition of the OA at wavelengths < 400 nm is due to OA absorption. Figure 4.10 shows a comparison of the normalized ground state absorption spectrum with the differential absorption spectrum of chemically oxidized SubPc. We assign the peak at 610 nm to SubPc cations. We also observe a deviation around 520 nm for the chemically oxidized spectrum in comparison to the ground state absorption. This result suggests that the cation absorption overlaps the bleach and has an additional peak around 520 nm.

We note that the solution-phase cation spectra that we obtain by chemical oxidation of SubPc solutions are blue shifted relative to our cation assignment from transient absorption spectroscopy of SubPc:C_{60} thin films (see Section 4.2.6 and Figure 4.11). We attribute this blue shift in solutions to stronger localization of the cations to individual SubPc molecules because of attraction to the OA counter ion as well as the fact that the molecules are dissolved rather than aggregated.

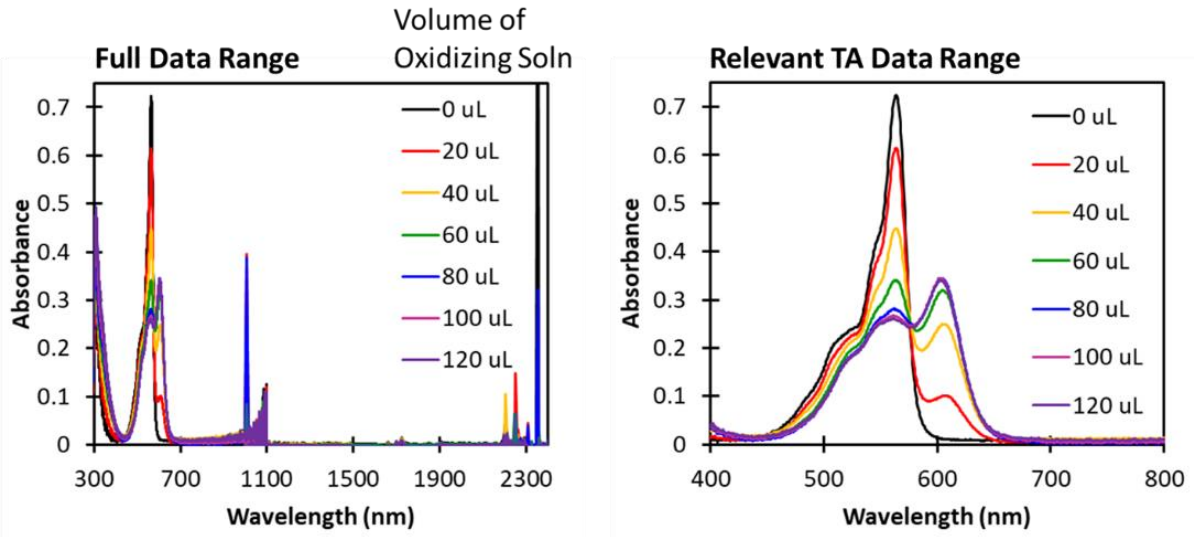

Figure 4.9. Solution-phase chemical oxidation of SubPc in dichloromethane using triethyloxonium hexachloroantimonate as the oxidizing agent (OA).

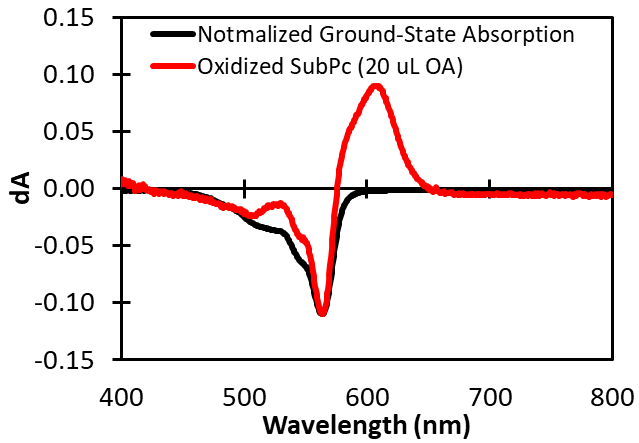

Figure 4.10. Comparison of SubPc ground state absorption with the chemically oxidized SubPc spectrum, showing cation absorption peaks around 610 and 520 nm.

We further characterize SubPc cation induced absorption peaks at 520 and 710 nm through transient absorption measurements of vapor-deposited SubPc:C_{60} films. Figure 4.11 supports this assignment by showing a distinct fluence dependence for the 520 and 710 nm induced absorption peaks in vapor-deposited 1:1 SubPc:C_{60} films. At increasing pump fluence, we observe a relative

decrease in the intensities for the 520 and 710 nm peaks, suggesting that the excited state giving rise to these peaks decays via bimolecular recombination, as expected for free charge carriers.

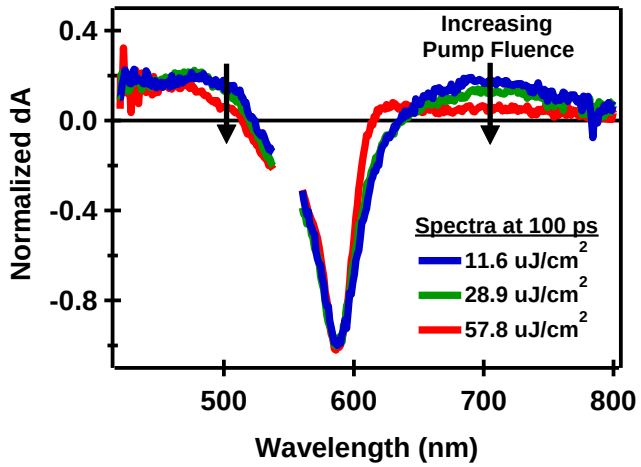

Figure 4.11. Spectral shape at 100 ps in 1:1 SubPc:C_{60} films under varying pump fluences, showing decrease in spectral features associated with SubPc cations at high fluence.

4.2.6 *Triplet Formation by Charge Recombination in Vapor-Deposited SubPc:C_{60} Blends*

We next investigate the excited states formed in vapor-deposited SubPc:C_{60} blends following SubPc photoexcitation with a 550 nm laser pulse. Figure 4.12a shows that the longest-lived signal that we observe in 1:1 SubPc:C_{60} films at 5.5 ns corresponds to SubPc triplet excitons (compare with Figure 4.7), including an induced absorption at 460 nm and the SubPc ground-state bleach at 515 – 615 nm.[201-202, 227, 249] Interestingly, we observe no triplet signal in vapor-deposited SubPc-only thin films under the same excitation conditions (Figure 4.12a), suggesting that SubPc triplet population in the blends is enhanced by the presence of C_{60}.

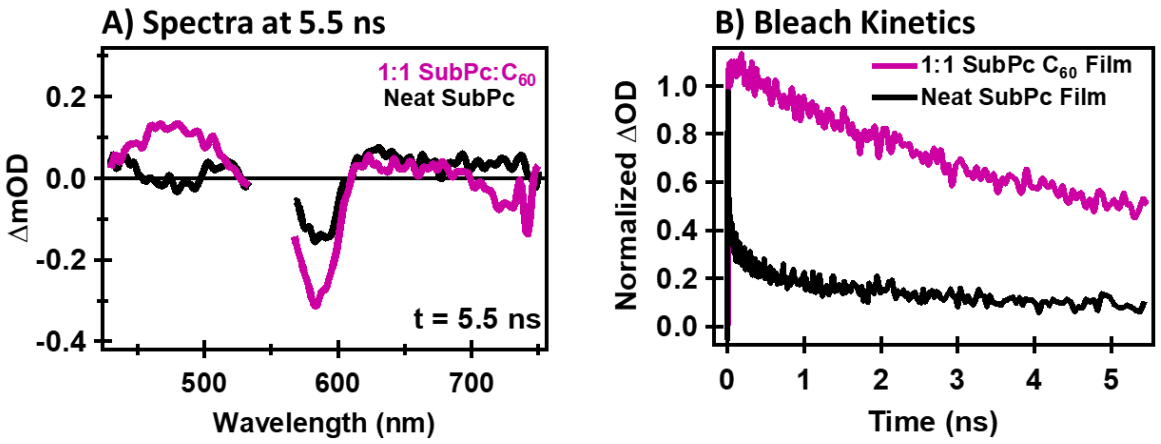

Figure 4.12. Comparison of (a) transient absorption spectra at 5.5 ns and (b) bleach kinetics for 1:1 SubPc:C_{60} (purple) and neat SubPc (black) vapor-deposited thin films, showing longer-lived kinetics and enhanced triplet induced absorption at 460 nm for the blends.

Figure 4.12b shows that the decay kinetics for the neat SubPc films are significantly faster than the 1:1 SubPc:C_{60} films. We attribute the longer-lived signal in the 1:1 SubPc:C_{60} films both to charge generation and long-lived SubPc triplets. However, we note that the neat SubPc film decays are much faster than the decays in dilute polystyrene films (Section 4.2.3). We hypothesize that the vapor-deposited SubPc-only films show very fast decays under these excitation conditions due to exciton-exciton annihilation of the initially photoexcited singlets. We note that the neat SubPc films show a small amount of long-lived signal at 580 – 610 nm in Figure 4.12a, which we attribute to electroabsorption. We propose that the electroabsorption peak in the neat SubPc films is caused by carrier generation following dissociation of excess-energy excitons formed through exciton-exciton annihilation.

We further support our hypothesis of exciton-exciton annihilation in the vapor-deposited SubPc thin films by measuring the singlet photoluminescence lifetimes under increasing incident photon flux (Figure 4.13). We measure faster decays with increasing pump fluence, suggesting a bimolecular decay mechanism (such as annihilation) for SubPc singlet excitons. Taken together,

our data suggests that the lack of triplet induced absorption in SubPc-only vapor-deposited films is due to accelerated singlet decay by processes such as annihilation or internal conversion, which outcompete intersystem crossing.

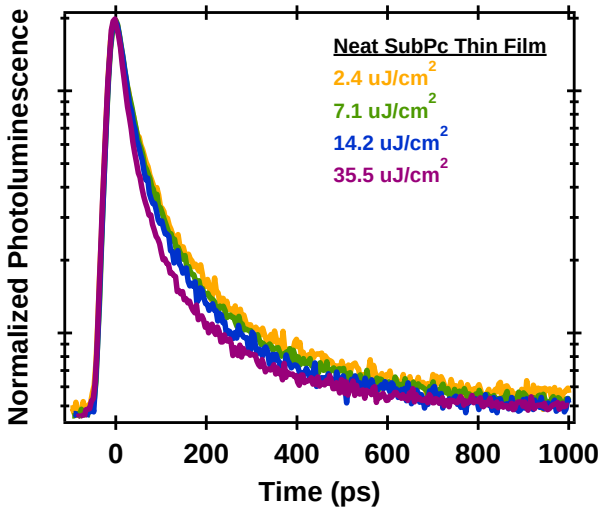

Figure 4.13. Photoluminescence decays for neat SubPc vapor-deposited thin films under varying 550 nm pump fluences from 2.4 – 35.5 μJ/cm^2, showing faster decay under increasing pump fluence.

In order to elucidate the pathway through which C_{60} catalyzes SubPc triplet formation, we investigate the transient absorption data for 1:1 SubPc:C_{60} thin films at various pump-probe delay times (Figure 4.14a). In addition to SubPc triplets, Figure 4.14a shows several induced absorption signals that decay with distinct kinetics. We attribute the peak at 980 nm to C_{60} singlets (Figure 4.8) and the longer-lived peak at 1050 nm to C_{60} anions formed following charge transfer.[223, 250-251] In the visible range, we attribute the peaks around 710 nm and 520 nm primarily to SubPc cations (see Section 4.2.5). We note that the high photogenerated charge density under the conditions of these experiments roughly corresponds to an average distance of ~5 nm between carriers, which is comparable to the distance that one might anticipate for coulomb recapture of conjugate charges in low-dielectric media.[97, 99, 252] This suggests a high likelihood of bimolecular

carrier recombination to create charge-transfer states that may relax to triplet excitons (Path 1 in Figure 4.1a). In fact, we observe fluence-dependent rise times for SubPc triplets, consistent with a bimolecular formation pathway (see Figure C.11 in Appendix C).

Despite the spectral overlap of singlet, triplet, and charge induced absorption signals in Figure 4.14a, we are able to kinetically resolve these states using global target analysis.[247] We arrive at the model shown in Figure 4.14b. Our results suggest that SubPc and C_{60} singlets are both present at early times and decay over tens of picoseconds. In addition, charge carriers are generated on the ultrafast time scale by spin-conserved dissociation of a subset of singlet excitons at SubPc/C_{60} interfaces. Photogenerated charge carriers can then recombine, allowing relaxation to SubPc triplets via triplet charge-transfer states.

We fit our data by assuming that the overall transient signal in Figure 4.14a consists of wavelength-dependent spectral signatures $\sigma(\lambda)$ that decay with time-dependent concentrations C(t) according to Equation 4.2.

$$\Psi_{\mathrm{Total}}(\lambda,t) = [\, C_{\mathrm{SubPc_S}}(t)\sigma_{\mathrm{SubPc_S}}(\lambda) + C_{\mathrm{C60_S}}(t)\sigma_{\mathrm{C60_S}}(\lambda) \,] + C_{\mathrm{SubPc_T}}(t)\sigma_{\mathrm{SubPc_T}}(\lambda) + C_{\mathrm{SubPc_C}}(t)\sigma_{\mathrm{SubPc_C}}(\lambda) + C_{\mathrm{C60_C}}(t)\sigma_{\mathrm{C60_C}}(\lambda) \quad (4.2)$$

In Equation 4.2, the subscripts S, T, and C correspondingly stand for singlet, triplet, and charge. Based on our analysis of the C_{60} triplet spectral line shape in C_{60}:PS films (Figure 4.8), we do not observe significant C_{60} triplet contribution to the transient absorption signal in our vapor-deposited SubPc:C_{60} blends. For this reason, we omit any explicit C_{60} triplet contribution to the transient absorption signal in our model.

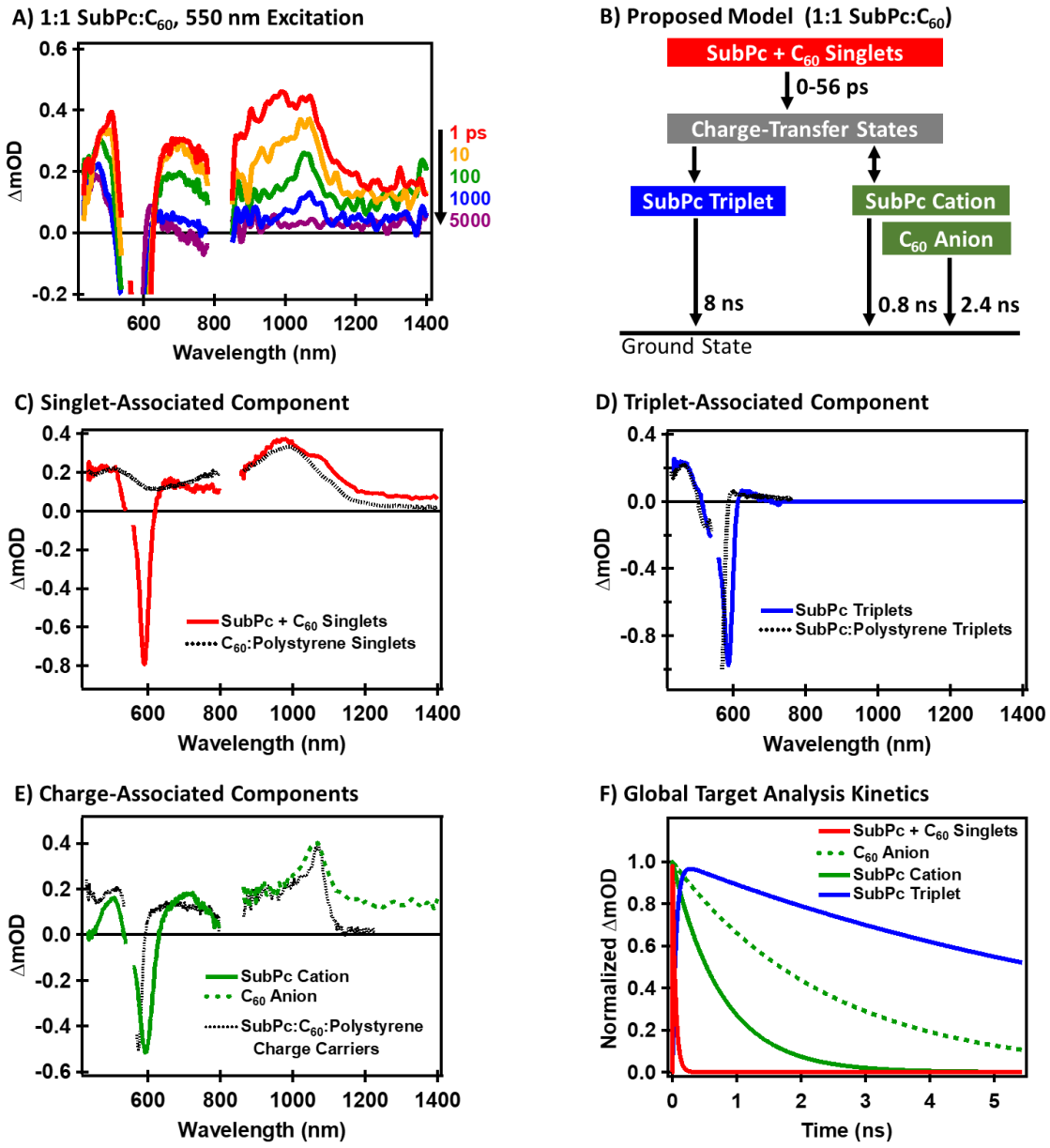

Figure 4.14. (a) Transient absorption spectra taken at 1ps (red), 10 ps (orange), 100 ps (green), 1000 ps (blue), 5000 ps (purple) for 1:1 SubPc:C_{60} films under 550 nm photoexcitation, where the y axis is plotted as the change in optical density (OD). (b) Proposed pathway for generation of charge carriers and SubPc triplets. (c) Component from global target analysis primarily corresponding to SubPc singlet excitons and C_{60} singlet excitons overlaid with the normalized global analysis component for C_{60} singlet excitons in dilute C_{60}:polystyrene films. (d) Component from global target analysis corresponding to SubPc triplet excitons overlaid with the normalized component for SubPc triplet excitons in dilute SubPc:polystyrene films. (e) Component from global target analysis corresponding to SubPc cations and C_{60} anions overlaid with the normalized component for charge carriers in dilute SubPc:C_{60}:polystyrene films. (f) Kinetics from global target analysis corresponding to the spectral components in c-e.

In Figure 4.14c-e we provide the species-associated spectra σ(λ) that we extract from our global target analysis. Figure 4.14c shows a fast-decay spectral component with a 56 ps time constant that we interpret primarily as a superposition of SubPc and C_{60} singlet-associated features. We attribute the negative signal at 605 nm to bleaching of the SubPc ground-state absorption, which overlaps with a broad induced absorption signal over the visible range from C_{60} singlets. In the NIR spectral region, the peak at 980 nm represents C_{60} singlets and is consistent with the C_{60} singlet-associated absorption from dilute C_{60}-only films in polystyrene (Figure 4.8). While the majority of the charge carrier population that we observe decays on the nanosecond time scale (Figure 4.14e), we note that the spectral shape in Figure 4.14c also contains a small contribution from C_{60} anions (1050 nm shoulder) and SubPc cations (Section 4.2.5). These features suggest that a fraction of charge carriers decay on a similar time scale to the singlet excitons in our 1:1 blends.

Figure 4.14d shows a spectral component that grows in over hundreds of picoseconds prior to decaying with an 8 ns lifetime, which we interpret as the SubPc triplet-associated spectrum.[201-202, 227, 249] For comparison, we overlay the normalized triplet-associated spectrum from SubPc-only films in polystyrene (Figure 4.7), showing that the relative peak intensities for the triplet components are similar in both films. The redshifted bleach in the vapor-deposited SubPc:C_{60} films is consistent with a redshift in the ground-state absorption spectrum (Figure C.3 in Appendix C).

Figure 4.14e shows the spectral components that form within our instrument response and decay on the nanosecond time scale, which we interpret as SubPc cation-associated spectra and C_{60} anion-associated spectra. The SubPc cation-associated spectrum exhibits maxima at 520 and 710 nm along with the SubPc bleach from 540 to 630 nm (see Section 4.2.5). The C_{60} anion-associated spectrum shows a sharp peak at 1050 nm.[223, 250-251] For comparison, we overlay the normalized charge-associated spectra from dilute films containing SubPc and C_{60} dispersed in

polystyrene, which we present in Section 4.2.8 to study the effect of disrupted aggregation. Though the dilute films exhibit photoinduced charge transfer to a much lesser extent compared to the vapor-deposited films, we find reasonable agreement for the charge carrier spectral components that we extract for the two types of films.

In Figure 4.14f, we show the decay traces C(t) corresponding to the spectral components in Figure 4.14c-e. We observe ultrafast carrier generation, after which the SubPc cations decay with a 0.8 ns lifetime and C_{60} anions decay with a 2.4 ns lifetime. While few studies simultaneously report both cation and anion kinetics, our results notably return different lifetimes for the positive and negative carriers. This indicates that, in addition to bimolecular recombination returning SubPc cations and C_{60} anions to the ground state at the same rate, other photophysical processes are at play that unequally affect the carriers. One possible source of this imbalance is unintentional doping during materials synthesis and preparation causing defects that preferentially affect either positive or negative carriers through annihilation or trapping.[253-254]

In addition to free carriers, the decay C(t) for the component primarily associated with singlet excitons appears promptly and decays with a 56 ps lifetime. Finally, the SubPc triplet-associated spectrum reaches its maximum amplitude around 250 ps and is the longest-lived spectral feature with an 8 ns lifetime. We find that the triplet rise time depends on pump fluence (Figure C.11), indicating a bimolecular process of carrier recombination to form triplets through charge-transfer states. Our observation of sub-nanosecond triplet formation via charge-transfer state relaxation is consistent with results for other systems where charge generation is efficient.[92, 183, 206]

4.2.7 *Showing 1:2 SubPc:C_{60} Blends Achieve Decreased Recombination to Triplets*

We next investigate the origin of the enhanced photocurrent in our 1:2 SubPc:C_{60} devices by comparing the relative populations of SubPc triplets and SubPc cations between the 1:1 and 1:2 blends (Figure 4.15). While our global target analysis reveals similar dynamic processes leading to charge generation in 1:2 SubPc:C_{60} films (see discussion in Appendix C along with Figure C.13), we observe a significant suppression of the SubPc triplet signal. Figure 4.15a shows the transient absorption data at matched absorbed photon flux for 1:1 and 1:2 blends at 250 ps, when singlet excitons have fully decayed and the triplet signal has reached a maximum amplitude. We overlay these data with the overall fits from our global target analysis, which include a sum of the SubPc triplet and cation spectral components. We observe decreased signal magnitude in the 1:2 blends at the SubPc bleach (580 nm) and the triplet absorption (460 nm), with slightly higher signal magnitude in the cation absorption region (710 nm) at this time slice.

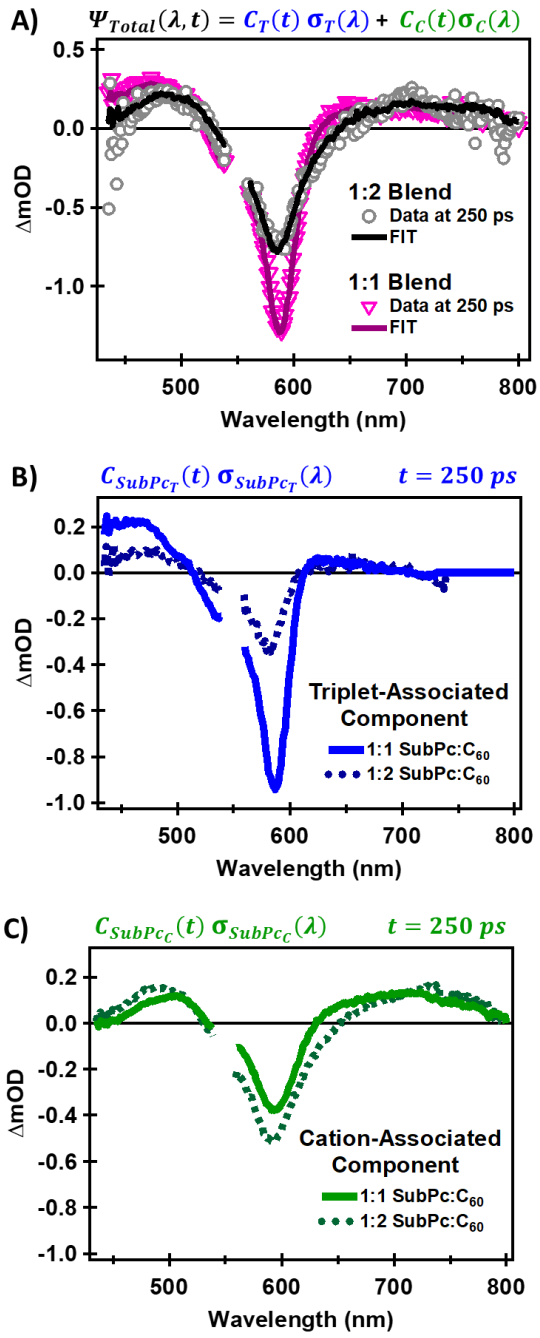

Figure 4.15. (a) Transient absorption data at 250 ps for vapor-deposited SubPc:C_{60} films with 1:1 and 1:2 ratios, overlaid with the overall fit Ψ(λ) from our global target analysis that includes a sum of components associated with SubPc triplets $C_T(t)\sigma_T(\lambda)$ and cations $C_C(t)\sigma_C(\lambda)$ at t = 250 ps. Contribution of the (b) SubPc triplet-associated spectrum and (c) SubPc cation-associated spectrum to the overall fits, showing lower triplet amplitude and higher cation amplitude for the 1:2 blends.

In Figure 4.15b and Figure 4.15c, we show the separate contributions from the spectral components associated with triplets and cations, respectively, to the overall fit at 250 ps where $\Psi_{\mathrm{Total}}(\lambda) = \mathrm{C}_{\mathrm{SubPc_T}}(250\mathrm{ps})\sigma_{\mathrm{SubPc_T}}(\lambda) + \mathrm{C}_{\mathrm{SubPc_C}}(250\mathrm{ps})\sigma_{\mathrm{SubPc_C}}(\lambda)$. Regardless of the fullerene ratio, we extract similar spectral shapes for the cation-associated components and for the triplet-associated components. Figure 4.15b shows a smaller contribution from the SubPc triplet-associated spectra in the 1:2 blends compared to the 1:1 blends, where this decrease in the triplet population accounts for the decrease in the bleach intensity and the decrease in induced absorption at 460 nm that we observe in Figure 4.15a for the 1:2 blends. Figure 4.15c shows a slightly higher contribution from SubPc cation-associated spectra in the 1:2 blends at 250 ps.

We assess the change in SubPc triplet population and in SubPc cation population between the 1:2 and 1:1 blends by evaluating the amplitude ratios ($A_{1:2}/A_{1:1}$) for the spectra associated with each species at their respective maximum concentrations (Figure 4.16). We find that the 1:2 blends exhibit 0.4 ± 0.2 times lower triplet population along with 1.4 ± 0.3 times greater cation population. This result implies a greater branching toward sustained charge generation in the 1:2 blends rather than recombination to SubPc triplets.

Figure 4.16a and Figure 4.16b show how we obtain the amplitude ratios ($A_{1:2}/A_{1:1}$) for SubPc cations and triplets, respectively. We obtain the ratios by dividing the spectral component extracted from our global target analysis of the 1:2 SubPc:C_{60} blends $A_{1:2}\sigma_{1:2}(\lambda)$ by the same spectral component extracted for the 1:1 SubPc:C_{60} blends $A_{1:1}\sigma_{1:1}(\lambda)$, where A is the maximum amplitude of each excited state population. For example, Figure 4.16a shows the result for $A_{1:2,\mathrm{Cation}}\sigma_{1:2,\mathrm{Cation}}(\lambda)$ / $A_{1:1,\mathrm{Cation}}\sigma_{1:1,\mathrm{Cation}}(\lambda)$. In the ideal case, $\sigma_{1:2,\mathrm{Cation}}(\lambda) = \sigma_{1:1,\mathrm{Cation}}(\lambda)$, which would occur if the spectral shape of the cation does not depend on the fullerene content of the film. That would leave us with $A_{1:2,\mathrm{Cation}}/A_{1:1,\mathrm{Cation}} = C$, where C is a constant value describing how much

more transient absorption amplitude we measure from the cations in the 1:2 films compared to the 1:1 films. If this were the case (i.e. perfectly matched cation-associated spectra extracted for the 1:1 and 1:2 films), then we could divide the spectra at any wavelength we please to obtain C. However, we do extract a slightly different spectral shape for our measurements in the 1:1 and 1:2 films, so we would introduce some amount of error if we only chose one wavelength to divide $A_{1:2,Cation}/A_{1:1,Cation}$ to obtain the amplitude ratio. For this reason, we must divide the spectral components at all wavelengths and take a standard deviation to express the amplitude ratio. For the cation spectral component, we obtain a ratio of 1.4 ± 0.3, where we omit the points near 510 nm and 640 nm that correspond to the points where the spectrum is zero. Following the same method, we obtain the triplet amplitude ratio of 0.4 ± 0.2 by dividing $A_{1:2,Triplet}\sigma_{1:2,Triplet}(\lambda)$ / $A_{1:1,Triplet}\sigma_{1:1,Triplet}(\lambda)$.

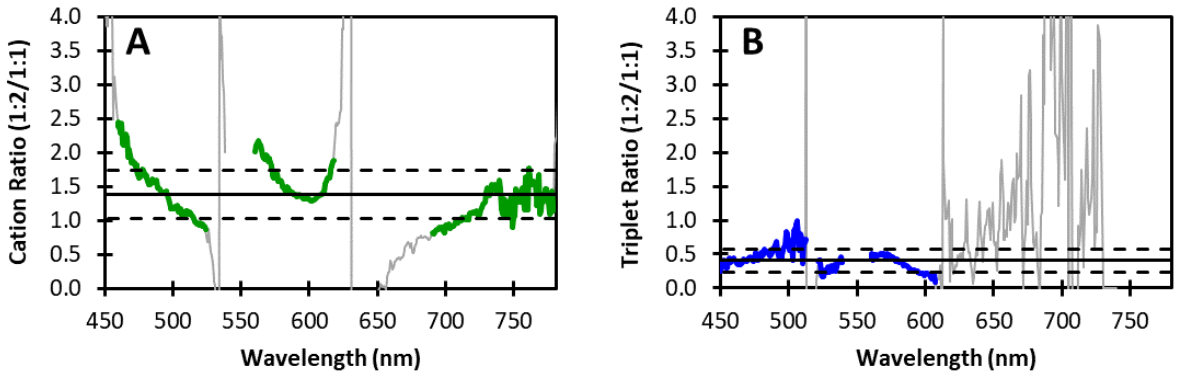

Figure 4.16. Amplitude ratios ($A_{1:2}/A_{1:1}$) for (a) cation-associated spectral components and (b) triplet-associated spectral components between the 1:2 and 1:1 SubPc:C_{60} films, where the solid horizontal line represents the average value and the dotted lines represent standard deviation. The Cation amplitude ratio is 1.4 ± 0.3, and the triplet amplitude ratio is 0.4 ± 0.2.

Considering the prominent C_{60} aggregate peak that we observe in our 1:2 SubPc:C_{60} device EQE, we propose that avoided triplet formation in the 1:2 blends results from electron

delocalization over fullerene aggregates that favors free charge generation and thus improves photocurrent collection.[215, 255] In order to fully investigate the effect of aggregation and charge-transfer states on triplet formation, we next discuss the kinetics at the limit of dilute solid-state mixtures of SubPc and C_{60} with purposefully disrupted aggregation (Section 4.2.8).

4.2.8 *Triplet Formation by Energy Transfer in Dilute SubPc:C_{60}:Polystyrene Blends*

Suppressing aggregation by dispersing small-molecule absorbers in inert matrices has previously been shown to improve photocurrent generation in bilayer devices, where disrupting intermolecular interactions may lessen nonradiative loss pathways.[212, 256] However, as we have demonstrated for blended donor:acceptor devices, aggregation in bulk heterojunctions plays a critical role in driving ultrafast charge transfer, sustaining charge-separated states, and outcompeting alternative interface-mediated loss pathways that remain thermodynamically accessible (i.e. Path 2 in Figure 4.1a). In this section, we further investigate films with disrupted aggregation by dispersing SubPc and C_{60} in polystyrene (PS) in a 1:1 SubPc:C_{60} molar ratio at a total 0.6 wt% in polystyrene (SubPc:C_{60}:PS). In this case, we observe suppressed charge generation along with a significantly slower rise of SubPc triplets. Our global target analysis suggests that in these dilute blends SubPc triplets are populated via Path 2 in Figure 4.1a, including (i) singlet-singlet energy transfer from SubPc to C_{60}, (ii) intersystem crossing centered on C_{60}, and (iii) triplet-triplet energy transfer from C_{60} to SubPc. This energy transfer pathway in dilute blends contrasts with the charge transfer pathway that we observe in the vapor-deposited blends. Our results suggest that Path 2 is a thermodynamically viable pathway for photovoltaic loss via triplets. However, this pathway is kinetically out-competed by charge transfer in the vapor-deposited blends.

Figure 4.17a shows the transient absorption spectra for SubPc:C_{60}:PS films between 1 ps and 9 μs. We attribute the longest-lived signal primarily to SubPc triplets (460 nm maximum, see Section 4.2.3), with a small contribution from C_{60} triplets (760 nm maximum, see Section 4.2.4). We find that the majority of SubPc triplets in the blends originate from fluence-independent processes (Figure C.5) mediated by C_{60} rather than from SubPc intersystem crossing. We conclude that C_{60} catalyzes SubPc triplet formation because ~89% of the initially photoexcited SubPc singlet excitons are quenched by C_{60} in SubPc:C_{60}:PS blends, which results in quenching of the SubPc fluorescence from a 26% quantum yield in SubPc:PS films to 2.8% in SubPc:C_{60}:PS. However, despite the decrease in singlet emission, as well as the decrease in singlet-associated transient absorption in the SubPc:C_{60}:PS blends, the SubPc triplet signal at 9 μs in the SubPc:C_{60}:PS blends remains unquenched (Figure C.6). Taken together, these observations in the dilute polystyrene films suggest that C_{60} quenches SubPc singlets by resonant energy transfer, undergoes intersystem crossing, and sequentially transfers energy back to populate SubPc triplet states.

In addition to the long-lived triplet spectra, Figure 4.17a shows several induced absorption signals that decay with varying kinetics. We assign the negative signal at 500 – 600 nm to the SubPc ground-state bleach, and we attribute the maximum at 612 nm to SubPc singlets (Section 4.2.3).[201-202, 227, 249] In the NIR, the maximum at 980 nm and the shoulder at 1050 nm correspond to C_{60} singlets and anions, respectively.[223, 248, 250-251]

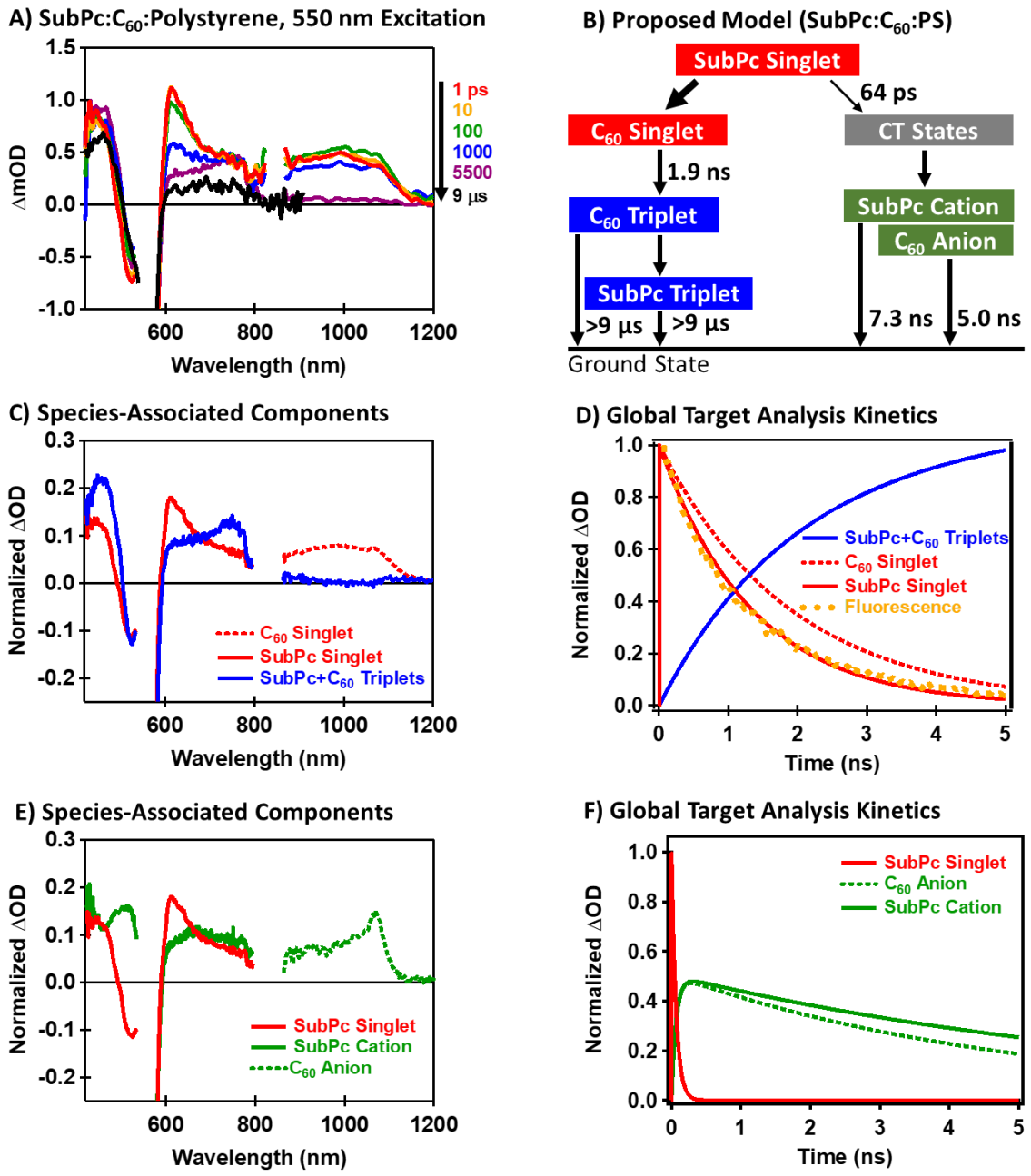

Figure 4.17. (a) Transient absorption spectra taken at 1ps (red), 10 ps (orange), 100 ps (green), 1000 ps (blue), 5500 ps (purple), and 9 us (black) for 0.6 wt% SubPc:C_{60}:polystyrene films under 550 nm excitation. (b) Proposed model for generation of charge carriers and SubPc triplets. (c) Spectral components from global target analysis associated with SubPc singlet excitons (red, solid), C_{60} singlet excitons (red, dotted), and SubPc plus C_{60} triplets (blue). (d) Kinetics from global target analysis corresponding to the spectral components in c. (e) Spectral components from global target analysis associated with SubPc singlets (red), SubPc cations (green, solid) and C_{60} anions (green, dotted). (f) Kinetics from global target analysis corresponding to the spectral components in e.

We note that the C_{60} singlet signal magnitude in Figure 4.17a is more than two times larger than the C_{60} singlet signal in dilute C_{60}-only films under the same excitation conditions (Figure C.8). This larger C_{60} singlet population suggests that additional C_{60} singlets are produced by singlet-singlet energy transfer from SubPc in the dilute blends. We find further evidence of singlet-singlet energy transfer by observing C_{60} fluorescence in the mixed SubPc:C_{60}:PS films, despite no measurable fluorescence in C_{60}:PS films under the same excitation conditions (Figure 4.18). The long-range nature of FRET permits singlet-singlet energy transfer in the dilute films, while other SubPc singlet deactivation pathways, such as charge transfer, occur less readily due to the larger intermolecular spacing. However, the weak C_{60} anion signal at 1050 nm in Figure 4.17a as well as our observation of triplet-triplet energy transfer in these films indicate that a small fraction of SubPc/C_{60} pairs exhibit orbital overlap even at 0.6 wt% in polystyrene.

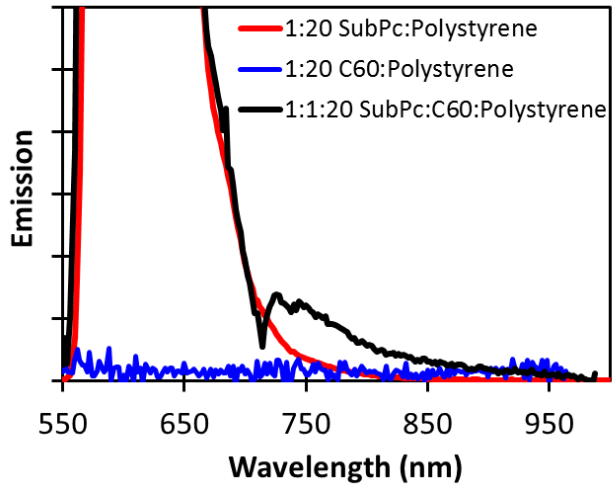

Figure 4.18. Emission spectra under 530 nm photoexcitation at 80 K for SubPc:polystyrene films (red), C_{60}:polystyrene films (blue), and SubPc:C_{60}:polystyrene films (black), showing C_{60} fluorescence at 750 nm in SubPc:C_{60}:polystyrene films due to singlet-singlet energy transfer from SubPc.

We use global target analysis to evaluate the kinetics leading to enhanced SubPc triplet population in the dilute blends, where we fit our transient absorption data according to Equation 4.3.

$$\Psi_{Total}(\lambda, t) = C_{SubPc_S}(t)\sigma_{SubPc_S}(\lambda) + C_{C60_S}(t)\sigma_{C60_S}(\lambda) + \left[C_{SubPc_T}(t)\sigma_{SubPc_T}(\lambda) + C_{C60_T}(t)\sigma_{C60_T}(\lambda)\right] + C_{SubPc_C}(t)\sigma_{SubPc_C}(\lambda) + C_{C60_C}(t)\sigma_{C60_C}(\lambda). \quad (4.3)$$

Figure 4.17b summarizes the final result of our model, which suggests that the majority of SubPc triplets rise on the nanosecond time scale following Path 2 with intersystem crossing centered on C_{60}. Our analysis indicates approximately 72% of the transient absorption amplitude associated with SubPc singlets decays by the energy transfer pathway, and the remaining 28% decays more quickly due to charge transfer with C_{60}.

In Figure 4.17c and Figure 4.17e we present the species-associated spectra σ(λ) that we extract from our analysis, and in Figure 4.17d and Figure 4.17f we provide the corresponding time-dependent concentration C(t) profiles for these species. For the sake of clarity, we separately depict the process that we interpret as triplet population through Path 2 in Figure 4.17c-d, and we depict the process that we interpret as charge transfer in Figure 4.17e-f. However, all results in Figure 4.17 are obtained simultaneously from the same analysis and represent dynamic processes that occur concomitantly following photoexcitation.

In Figure 4.17c, we show the spectral components that we associate with SubPc singlets, C_{60} singlets, and an overlap of SubPc and C_{60} triplets. The SubPc singlet-associated spectrum exhibits a similar line shape to the singlet-associated spectrum for SubPc:PS films that we obtain in Section 4.2.3, including the SubPc bleach from 500 – 600 nm, an induced absorption maximum at 612 nm, and a weaker maximum at 450 nm. In the NIR, the spectrum resembles C_{60} singlet

absorption with a maximum at 980 nm. The spectrum that we extract for triplets is in good agreement with a scaled sum of the SubPc and C_{60} triplet-associated spectra, with a maximum at 460 nm primarily due to SubPc triplet absorption and a maximum at 760 nm primarily due to C_{60} triplet absorption. In Figure 4.19a, we directly overlay our SubPc singlet-associated spectra for SubPc:PS films and from the SubPc:C_{60}:PS films, showing good agreement between the two spectra. In Figure 4.19b, we overlay our fitting results for the triplet-associated spectrum in the SubPc:C_{60}:PS films with scaled triplet-associated spectra from SubPc:PS and C_{60}:PS, showing that both SubPc and C_{60} triplets contribute to the SubPc:C_{60}:PS triplet-associated spectrum.

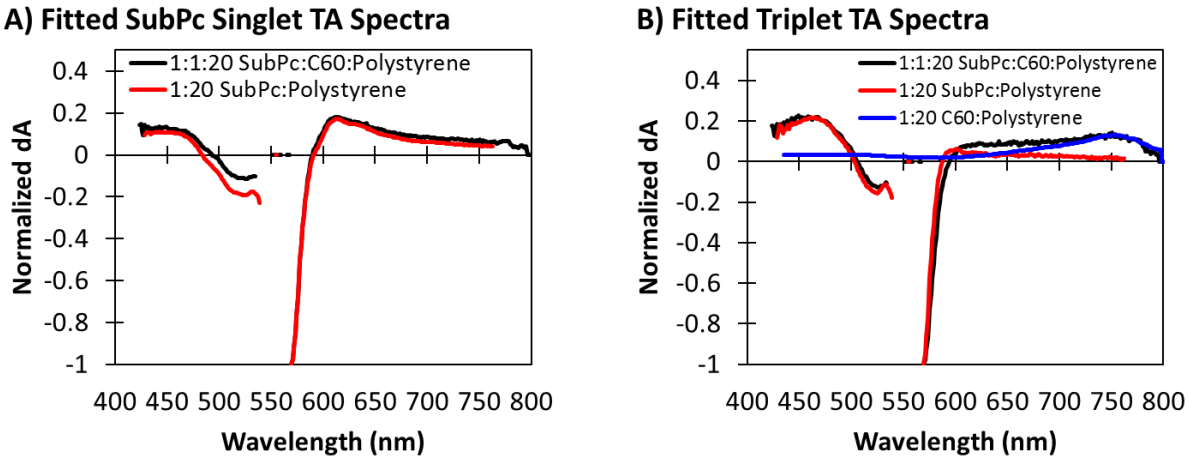

Figure 4.19. Comparison of (a) singlet-associated spectra and (b) triplet-associated spectra obtained through global target analysis for the SubPc:C_{60}:polystyrene (black), SubPc:polystyrene (red), and C_{60}:polystyrene (blue) films. Global target analysis for SubPc:polystyrene and C_{60}:polystyrene films are described in further detail in Sections 4.2.3 and 4.2.4, respectively.

Figure 4.17d shows the kinetic traces corresponding to the singlet and triplet spectral components in Figure 4.17c, along with the normalized SubPc fluorescence kinetics in the blended film. We find that the component consisting of overlapping SubPc and C_{60} triplet-associated spectra grows in as a result of C_{60} intersystem crossing, rising with a 1.89 ns time constant.

Interestingly, the C_{60} singlet decay of 1.89 ns is longer than the native 1.20 ns C_{60} intersystem crossing time (Figure 4.8). We attribute this apparently longer C_{60} singlet decay to repopulation of C_{60} singlets by energy transfer from SubPc singlets. The SubPc singlets decay with a faster lifetime of 1.34 ns, which is well represented in both the transient absorption and fluorescence data in Figure 4.17d.

Figure 4.17e-f represent the 28% of the transient absorption amplitude associated with SubPc singlets that undergo charge transfer rather than energy transfer. In Figure 4.17e, we present the identical SubPc singlet-associated spectral shape to that in Figure 4.17c along with the spectral components that we associate with the SubPc cations and C_{60} anions. The C_{60} anion exhibits a sharp peak at 1050 nm, and the SubPc cation-associated component exhibits maxima around 510 and 675 nm along with the SubPc bleach at 530-600 nm. In Figure 4.17f, we show that a fraction of SubPc singlets decay over 64 ps to generate charge carriers. The C_{60} anion decays with a 5.0 ns lifetime, and the SubPc cation decays with a 7.3 ns lifetime.

4.3 CONCLUSIONS

Our results demonstrate a kinetic competition between charge (re)dissociation versus recombination to triplet excitons in small-molecule organic photovoltaics, where photocurrent enhancement and suppressed recombination correlate with fullerene aggregation in our devices. We present two thermodynamically accessible pathways for SubPc triplet formation facilitated by C_{60} in photovoltaic blends, including recombination through charge-transfer states (Path 1) or, alternatively, an energy transfer pathway (Path 2) that proceeds via (i) singlet-singlet energy transfer from SubPc to C_{60}, (ii) intersystem crossing on C_{60}, and (iii) triplet-triplet energy transfer from C_{60} to SubPc. In vapor-deposited blends, SubPc triplets are populated primarily by charge

recombination, a process which proceeds via triplet charge-transfer states. However, this loss pathway becomes suppressed when we increase the fullerene fraction in the blend, which enhances molecular aggregation and yields photovoltaic devices with larger photocurrent collection efficiencies. Our results suggest that the improved device performance and suppressed triplet formation may be linked to charge delocalization over fullerene aggregates that support more efficient charge separation in small-molecule OPVs. This finding is analogous to the kinetic competition between charge separation and triplet recombination that has been observed in polymer/fullerene blend solar cells.[80] We further study the role of aggregation in SubPc triplet generation by analyzing transient absorption spectra for dilute films with disrupted aggregation. In this case, we find that triplets form on the nanosecond time scale via an energy transfer pathway (Path 2). Our results provide an important example demonstrating that losses to triplet states can be kinetically outcompeted by charge separation in small-molecule blends with optimized morphologies, despite the presence of multiple thermodynamically-accessible loss pathways for triplet formation.

4.4 MATERIALS

Chloroboron subphthalocyanine (85%) and bathocuproine (96%) were purchased from Sigma Aldrich and purified by thermal gradient sublimation. Anhydrous solvents (chlorobenzene, dichloromethane, and tetrahydrofuran), 1,8-iiodooctane, polystyrene (10,000 g/mol), and triethyloxonium hexachloroantimonate were purchased from Sigma Aldrich and used without further purification. Molybdenum(VI) oxide (99.9995%) and aluminum wire (99.999%) were purchased from Alfa Aesar. C_{60} (99.9%, sublimed) was purchased from Materials and

Electrochemical Research Corporation. Patterned indium tin oxide substrates (1.5 x 1.5 cm) were purchased from Thin Film Devices Inc.

4.5 EXPERIMENTAL METHODS

4.5.1 *Thermal Gradient Sublimation Purification*

SubPc and bathocuproine were purified by thermal gradient sublimation in a Lindberg/Blue M tube furnace using a series 58434C three-zone temperature controller. Each material for purification was loaded into a 5 mL glass vial that was slid into the sealed end of a 1-inch diameter pyrex tube. Glass wool was placed into the open end of the 1-inch pyrex tube. This tube was then loaded into a larger 4-inch diameter pyrex tube inside of the furnace, where the 4-inch diameter tube was equipped with metal KF flange attachments fused onto each end. This tube was sealed on one end with a blank KF flange, and attached on the other end to a vacuum pumping system. A liquid nitrogen trap was placed in-line between the tube and turbo pump (Leybold-Heraeus Turbovac 50), and a molecular sieve trap was placed in-line between the turbo pump and two-stage rotary vane vacuum pump (Fischer Scientific Maxima C Plus). The system was evacuated to 1 x 10^{-6} Torr vacuum prior to heating. The temperature zones were 290 K / 240 K / 120 K for SubPc and 250 K / 190 K / 120 K for bathocuproine. The purification for bathocuproine was generally completed in approximately 3 hours, and the purification for SubPc took place over several days. Purified bathocuproine was obtained as light yellow crystals, and purified SubPc was obtained as shiny gold crystals.

4.5.2 *Preparation of Dilute SubPc and C_{60} in Polystyrene Films*

In an argon glove box, 20 molar equivalents (eq.) of polystyrene with molecular weight of 10,000 g/mol were dissolved in anhydrous chlorobenzene along with either SubPc (1 eq), C_{60} (1 eq), or SubPc/C_{60} (1/1 eq). This results in films with 0.2 wt% SubPc in polystyrene, 0.4 wt% C_{60} in polystyrene, or 0.6 combined wt% of 1:1 SubPc:C_{60} in polystyrene. The molar ratios between the films were kept constant, rather than the weight percent, in order to ensure matched optical densities between the films (see Figure S2). The concentration of the solutions prior to film fabrication was 28 mg/mL. The solutions were stirred overnight, after which 120 µL of each solution was drop cast onto a 1.5 x 1.5 cm^2 glass substrate. These samples were held on a hot plate at 40°C in the argon glove box for several hours to evaporate the excess chlorobenzene. The samples were then placed in a vacuum chamber at 30 mTorr overnight. A subset of films were prepared with the addition of diiodooctane (DIO) as a heavy atom source to promote emissive triplet decay. For these films, 24 mg/mL of DIO were added to the solution prior to drop casting. For C_{60}:PS films with DIO and thick C_{60}:PS films in Figure S1, several sequential layers were drop cast in order to increase the optical density for measurement of weak absorption or emission signals.

4.5.3 *Vapor Deposition of Thin Films*

Glass substrates were cleaned by sonicating sequentially in acetone and isopropyl alcohol for 10 minutes followed by air plasma treatment for 10 minutes. Substrates and evaporation materials were loaded into an Amod thermal evaporator (Angstrom Engineering) located inside of a nitrogen glovebox. Vapor deposition was carried out under high vacuum at base pressure < 2 x 10^{-6} Torr. Materials (SubPc, C_{60}, bathocuproine, and molybdenum oxide) were deposited from a

tantalum baffle box at a rate of approximately 0.3 Å/s. For 1:2 SubPc:C_{60} blends, the C_{60} deposition rate was doubled.

4.5.4 *SubPc:C_{60} Bulk Heterojunction Photovoltaic Device Fabrication*

Indium tin oxide coated glass substrates were cleaned by sonicating sequentially in acetone and isopropyl alcohol for 10 minutes followed by air plasma treatment for 10 minutes. Devices were prepared by vapor deposition in an Amod thermal evaporator (Angstrom Engineering) contained within a nitrogen glove box. Vapor deposition was carried out under high vacuum at base pressure < 2 x 10^{-6} Torr. Following deposition of 12 nm molybdenum oxide, the SubPc:C_{60} active layer was created by simultaneously vaporizing SubPc and C_{60} from separate sources. For both 1:1 and 1:2 blends, the SubPc content was held constant corresponding to 13 nm SubPc thickness and C_{60} content was varied. A 10 nm layer of bathocuproine was then added, followed by a 100 nm thick layer of aluminum deposited through an 8-pixel shadow mask which defined the active area of each pixel as 0.1 cm^2.

4.5.5 *Photovoltaic External Quantum Efficiency Measurement*

Photocurrent was detected using a Kiethley 2400 source meter. The device was photoexcited using monochromated light from an Acton TS-428 tungsten-halogen lamp, employing a SpectraPro SP-2155 monochromator purchased from Princeton Instruments. A calibrated OSI optoelectronics silicon photodiode was used to record the lamp power density and calculate external quantum efficiency values. The calibrated photodiode and device pixels were

each masked to 1.2 mm^2 area. The devices were held under static 35 mTorr vacuum during the measurement.

4.5.6 *Current-Voltage Characterization*

The current-voltage curves were measured using a Keithley 2400 source meter under AM1.5 illumination conditions with light intensity of 100 mW cm^{-2} created by a Xenon arc lamp purchased from Solar Light Co. Appropriate short-circuit current values were confirmed by integrating the photovoltaic external quantum efficiency curves.

4.5.7 *Steady-State Absorption Measurement*

Ground-state absorption measurements were carried out using Avantes detectors (AvaSpec NIR-256, and Avaspec 2048L) and light sources (Avalight HAL-S, and Avalight DHS-DUV).

4.5.8 *Steady-State Photoluminescence Measurement*

Steady-state photoluminescence spectra were measured at 80 K with the samples under positive nitrogen pressure in a Janis ST100 open-flow cryostat. The samples were photoexcited using a 447 nm LED (Luxeon Rebel, 700mW, LXML-PR01-0425) modulated at 200 Hz using a Stanford Research Systems SR540 chopper. Luminescence was recorded through an Acton monochromator with a Si/InGaAs dual-band photodiode (ThorLabs, DSD2). The current response from the photodiode was amplified and converted to a voltage signal using a Stanford Research Systems SR570 low-noise current preamplifier, and the signal was measured on a Stanford

Research Systems SR830 lock-in amplifier. The lock-in phase was set using reflected LED light such that the signal was entirely in the positive X-channel (in-phase). Photoluminescence spectra were corrected for detector response using a calibrated LS-1-CAL Ocean Optics light source.

4.5.9 *Photoluminescence Quantum Yield Measurement*

Photoluminescence quantum yields were measured using an absolute quantum yield system purchased from Hamamatsu (C9920-02), which employs a Xenon lamp as the excitation light source passing through a monochromator and incident on the sample using a fiber optic routed into an integrating sphere. The excitation wavelength was 520 nm.

4.5.10 *Photoluminescence Quantum Yield Measurement*

For chemical oxidation of SubPc solutions, 20-120 uL of a 9 mg/mL triethyloxonium hexachloroantimonate solution in dichloromethane was added to a SubPc solution in dichloromethane while simultaneously measuring the steady-state absorption spectrum. Differential absorption spectra were obtained by subtracting the steady-state absorption before and after chemical oxidation.

4.5.11 *Transient Absorption Spectroscopy*

Kinetics were characterized using pump-probe transient absorption spectroscopy. Pump pulses were generated from a tunable-wavelength Coherent/Light Conversion OPerA Solo optical parametric amplifier with input from a Coherent Libra Ti:Sapphire amplifier (800 nm, 50 fs, 1

kHz). For ultrafast measurements (femtoseconds to 5.5 nanoseconds), white-light supercontinuum probe pulses were generated by focusing a portion of the amplifier output onto a sapphire plate (visible range 430-750 nm, near infrared range 850-1600 nm). The pump-probe delay up to 5.5 ns was set using a mechanical translation stage prior to white light generation. Detection and data acquisition were carried out using the HELIOS system purchased from Ultrafast Systems Inc. For the nanosecond to microsecond time range, white-light probe pulses and electronic delays were generated using the EOS system purchased from Ultrafast Systems Inc. In both cases, data were recorded using random time steps to minimize any influence from pump power fluctuation. Samples for transient absorption measurements were prepared in a nitrogen glove box and epoxy-sealed between two glass substrates to minimize exposure to air. Unless otherwise noted, the pump used for the vapor-deposited films is at 550 nm and 11.6 $\mu J/cm^2$ incident photon flux, and the pump used for the polystyrene films is 550 nm and 57.8 $\mu J/cm^2$.

4.5.12 *Time-Resolved Photoluminescence Spectroscopy*

A Hamamatsu streak camera (C10910) equipped with a synchroscan insert (M10913-02) was used to acquire time-resolved photoluminescence data. Samples were excited with 50 fs pulses at 1 kHz from a Coherent/Light Conversion OPerA Solo optical parametric amplifier. Samples for time-resolved photoluminescence were identical to those used in transient absorption, prepared in a nitrogen glove box and epoxy-sealed between two glass substrates.

4.5.13 *Laser Beam Characterization*

Pump and probe beams were characterized at the sample position using the BC106N-VIS CCD Camera Beam Profiler purchased from Thorlabs. Spatial beam images and spot size calculations were obtained from Thorlabs' standard beam profiler software package. Average power was measured using the Coherent FieldMate laser power meter equipped with the OP-2 VIS high sensitivity sensor purchased from Edmond Optics.

Table 4.2 summarizes the beam radii, areas, and incident photon flux for the laser photoexcitations used in our transient absorption and time-resolved photoluminescence experiments. We report the spot sizes by calculating the area of the ellipse with radii defined by $1/e^2$ of the peak intensities of the Gaussian fits given in the spatial distribution profiles shown in Figure 4.20 - Figure 4.23.

Table 4.2. Pump radii, area, and incident power values measure at the sample positions for transient absorption (TA) and time-resolved photoluminescence (PL) experiments

Pump	Diameter µm	Diameter µm	Area cm^2	µW	$\mu W/cm^2$	$\mu J/cm^2$	photons/cm^2
550 nm TA	580.46	380.04	0.0017317	10	5774.7	5.77	1.60 E+13
				20	11549.4	11.55	3.20 E+13
				50	28873.5	28.87	7.99 E+13
				100	57746.9	57.75	1.60 E+14
550 nm PL	390.14	460.3	0.0014097	10	7093.6	7.09	1.96 E+13
				20	14187.3	14.19	3.93 E+13
				50	35468.2	35.47	9.81 E+13
				100	70936.4	70.94	1.96 E+14
365 nm TA	410.98	186.96	0.0006032	50	82895.5	82.90	2.29 E+14
365 nm PL	368.02	519.62	0.0015012	50	33307.6	33.31	9.22 E+13

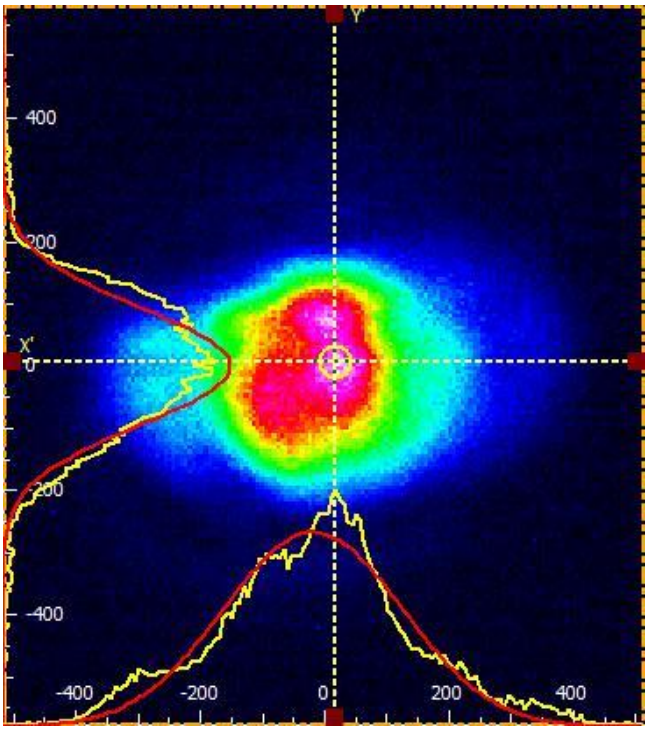

Figure 4.20. 550 nm pump beam at the sample position for transient absorption measurements. Axes are in units of micrometers.

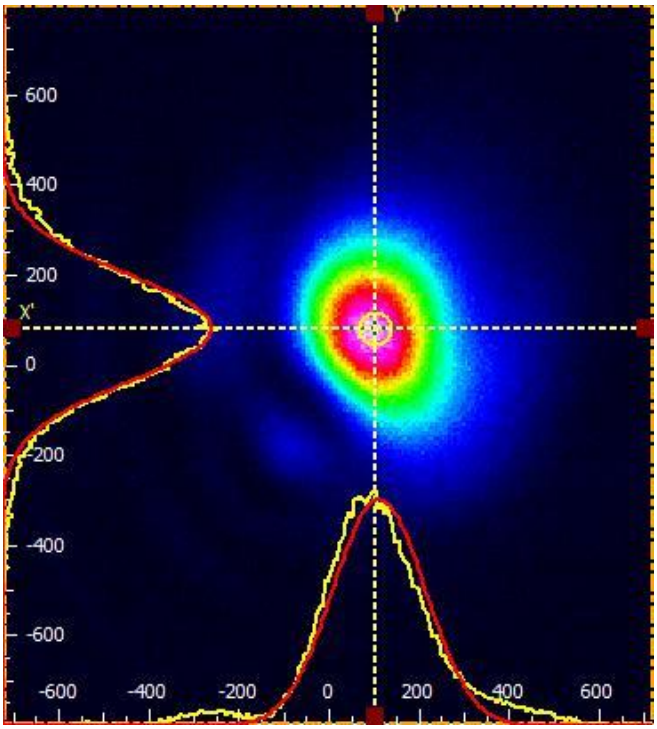

Figure 4.21. 550 nm pump beam at the sample position for time-resolved photoluminescence measurements. Axes are in units of micrometers.

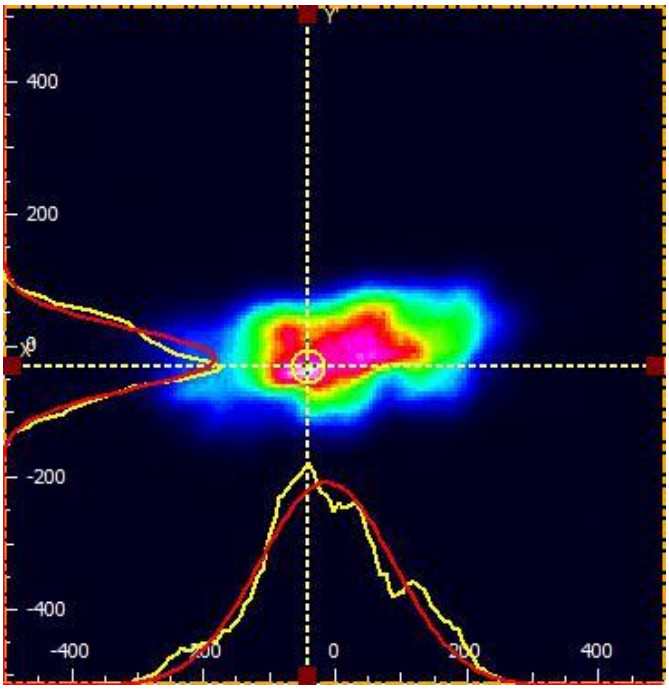

Figure 4.22. 365 nm pump beam at the sample position for transient absorption measurements. Axes are in units of micrometers.

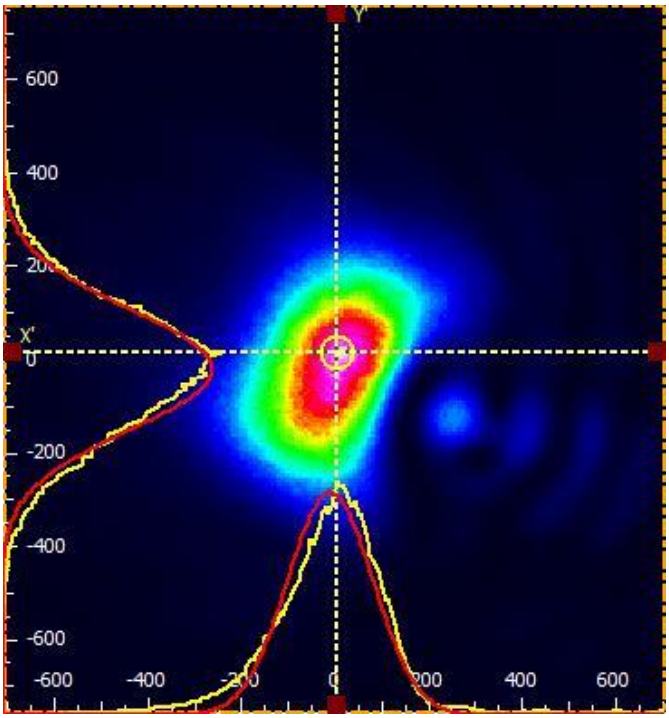

Figure 4.23. 365nm pump beam at the sample position for time-resolved photoluminescence measurements. Axes are in units of micrometers.

Chapter 5. CONCLUSIONS AND FUTURE OUTLOOK

The work in this thesis has shown significant progress toward understanding and further developing the efficient operation of organic photovoltaic (OPV) devices by characterizing the various excited states formed following photoexcitation and during interfacial charge transfer in bulk heterojunction active materials. In Chapter 1, we described the large scale of global energy consumption, motivating the development of emergent photovoltaic technologies. With a goal of designing better OPV devices through selective modification of the appropriate molecular parameters (chemical structure, film morphology, and photophysics), we described the operating principles of organic photovoltaics and the complex landscape of photoexcited states. In Chapter 2 – Chapter 4, we detailed our experimental results that provide new insight into excited-state energetics and kinetics along with their impact on achievable photovoltage and photocurrent from operating solar cells. In this chapter, we discuss our results in the context of future studies that may continue advancing our ability to improve OPV device operation.

We developed structure-function correlations in Chapter 2, relating the heteroatom along the polymer backbone (selenium versus sulphur) with the achievable open-circuit voltages in bulk heterojunction devices. We measured a larger voltage deficit ($q^{-1}E_{CT} - V_{OC}$) for devices employing selenium-substituted polymers, which we attributed to energetic loss in the quasi-fermi level splitting caused by increasing the density of charge-transfer states (N_{CT}). This result was surprising, since variations in open-circuit voltages have been more traditionally described by changes in the charge-transfer state energy (E_{CT}) and electronic coupling (V). Our results further provide new understanding of the spatial nature of charge-transfer states by suggesting that charge-transfer interactions can extend beyond nearest-neighbor donor/acceptor pairs. While carrier delocalization is generally considered beneficial in organic electronics, we propose that the

simultaneous increase of both charge-transfer state delocalization and molecular mixing may increase N_{CT} and cause recombination losses. Moving forward, we propose that morphological control of N_{CT} in addition to the more traditional optimization of energetic parameters may enable higher efficiency OPV devices. Toward this goal, we suggest that future studies focus on relating N_{CT}, E_{CT}, and V to the changes in thin-film morphology under different processing conditions in addition to chemical changes in polymer structure.

Although the role of charge-transfer states in OPV device operation is most often inferred from singlet charge-transfer state properties,[38, 41, 179] in Chapter 3 we showed that triplet charge-transfer states may play a different role in the ability to extract photocurrent form OPV devices. The majority of present studies assume that singlet and triplet charge-transfer states rapidly interconvert,[92] which implies that charge extraction should proportionately counteract decay via both singlet and triplet charge-transfer states. Interestingly, under charge-extraction voltages, we observe *different* voltage dependence for the singlet and triplet charge-transfer state spectroscopic indicators, suggesting that these states may not always rapidly equilibrate. Our results challenge the extent of rapid spin interconversion within the charge-transfer manifold, creating a framework for more detailed investigation of the differing roles that singlet and triplet intermediate states may play in photocurrent generation. To build on our observations, we propose that the time scale and temperature dependence for charge-transfer state spin interconversion should be further characterized in relation to the separate rates of singlet charge-transfer state decay to the ground state and triplet charge-transfer state decay to localized triplet excitons. Detailing the relative rate of spin interconversion in this way may help to explain cases such as PIDT-PhanQ/PC_{71}BM where applied biases unequally affect the singlet and triplet charge-transfer state populations.

We further investigated the morphological factors that influence carrier relaxation via triplet charge-transfer states to form to localized triplet excitons in Chapter 4. We showed that fullerene aggregation in small-molecule OPV blends correlates with photocurrent enhancement, which we attribute to kinetically avoiding recombination to thermodynamically-favored triplet states. Our results suggest that carrier delocalization over aggregates helps to sustain the free charge population and suppress recombination through the triplet charge-transfer manifold. We propose that future studies extend this concept further to compare the effect of aggregation on recombination via both singlet and triplet charge-transfer states. On one hand, delocalization over aggregates may suppress relaxation of the charge-transfer states, and this could influence singlet and triplet charge-transfer states to different extents. On the other hand, delocalization may prevent free carriers from forming interfacial charge-transfer states in the first place. Furthermore, our data support the important influence of electron delocalization over fullerene aggregates, though donor molecule aggregation may also aid in hole delocalization. Since previous studies suggest that fullerene aggregation induces ordered structure into the donor phases,[215] we propose that future studies should elaborate on relative importance of delocalization in both the donor and acceptor phases. This would be especially insightful for small-molecule systems, where donor molecules have a higher likelihood of forming ordered phases.

In conclusion, the work in this thesis provides important links between materials structural parameters and the photophysical processes that mediate photovoltaic device operation. This knowledge serves as an important component to rationally design materials and accelerate organic photovoltaics toward the efficiencies necessary for wider-spread commercialization. The further development of this technology promises a wider pallet of renewable energy options for decreasing pollution and increasing national energy independence.

Appendix A. SUPPORTING INFORMATION FOR CHAPTER 2: *OPEN-CIRCUIT VOLTAGE LOSSES IN SELENIUM-SUBSTITUTED ORGANIC PHOTOVOLTAIC DEVICES FROM INCREASED DENSITY OF CHARGE-TRANSFER STATES*

A.2 ADDITIONAL POLYMER/FULLERENE BLEND CHARACTERIZATION

Figure A.1 shows red-shifted absorption for that selenophene bulk heterojunction blends with $PC_{61}BM$ compared to the neat polymer. Selenophene/C_{60} bilayers do not exhibit the red-shifted absorption peak, suggesting that the absorption originates from charge-transfer states in intermixed polymer/fullerene regions.

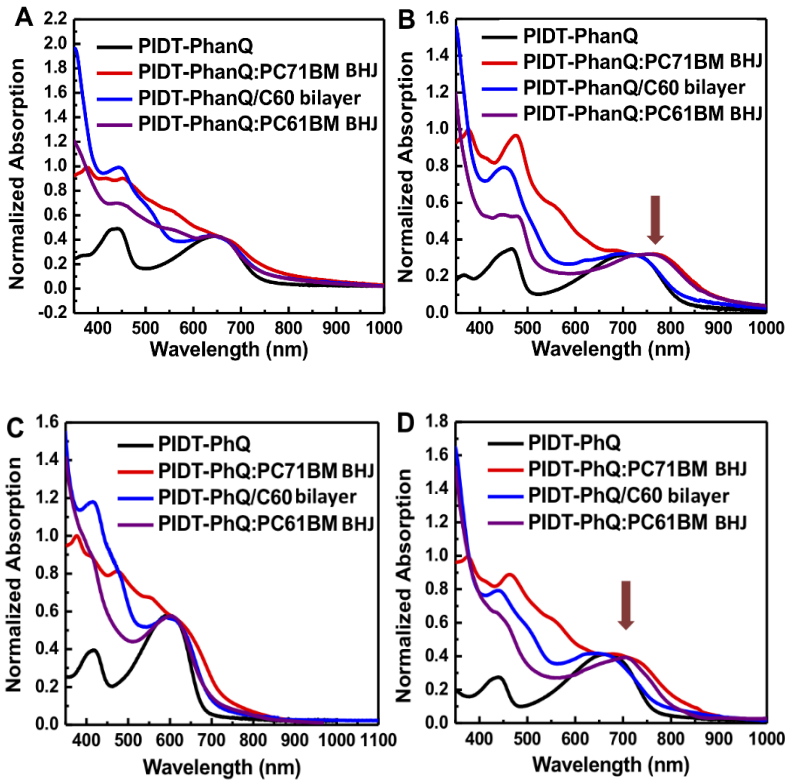

Figure A.1. Normalized thin film absorbance spectra of (a) neat PIDT-PhanQ film, 1:3 PIDT-PhanQ:$PC_{71}BM$ bulk heterojunction (BHJ), PIDT-PhanQ/C_{60} bilayer, and 1:3 PIDT-PhanQ:$PC_{61}BM$ BHJ; (b) neat PIDSe-PhanQ film, 1:3 PIDSe-PhanQ:$PC_{71}BM$ BHJ, PIDSe-PhanQ/C_{60} bilayer, and 1:3 PIDSe-PhanQ:$PC_{61}BM$ BHJ; (c) neat PIDT-PhQ film, 1:3 PIDT-

PhQ:$PC_{71}BM$ BHJ, and 1:3 PIDT-PhQ:$PC_{61}BM$ BHJ; (d) neat PIDSe-PhQ film, 1:3 PIDSe-PhQ:$PC_{71}BM$ BHJ, PIDSe-PhQ/C_{60} bilayer, and 1:3 PIDSe-PhQ:$PC_{61}BM$ BHJ.

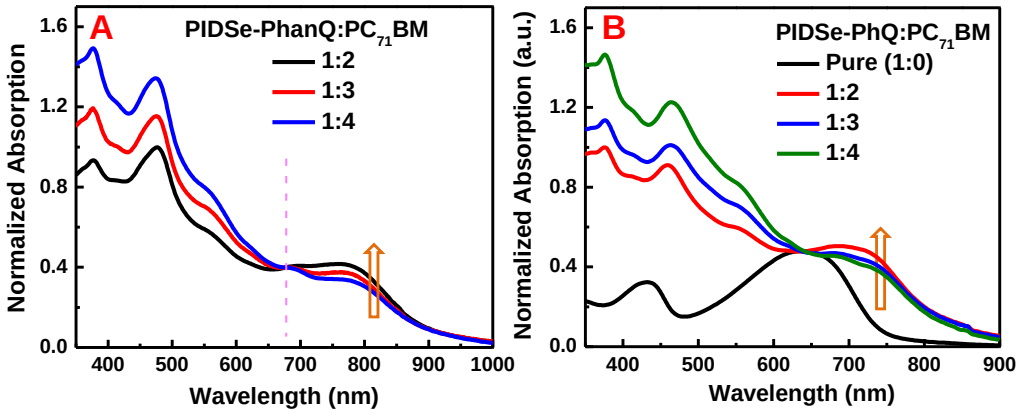

Figure A.2. Absorption spectra for (a) PIDSe-PhanQ: $PC_{71}BM$ films and (b) PIDSe-PhQ: $PC_{71}BM$ films in different blending ratios, showing different trends in sub-gap charge-transfer state absorption compared to neat material absorption with blend ratio.

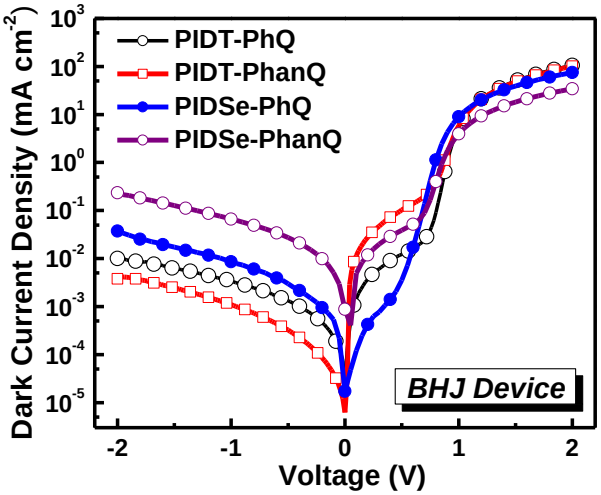

Figure A.3. Dark current of the bulk heterojunction devices including PIDT-PhQ:$PC_{71}BM$ (black circles), PIDT-PhanQ:$PC_{71}BM$ (red squares), PIDSe-PhQ:$PC_{71}BM$ (blue circles), and PIDSe-PhanQ:$PC_{71}BM$ (purple circles).

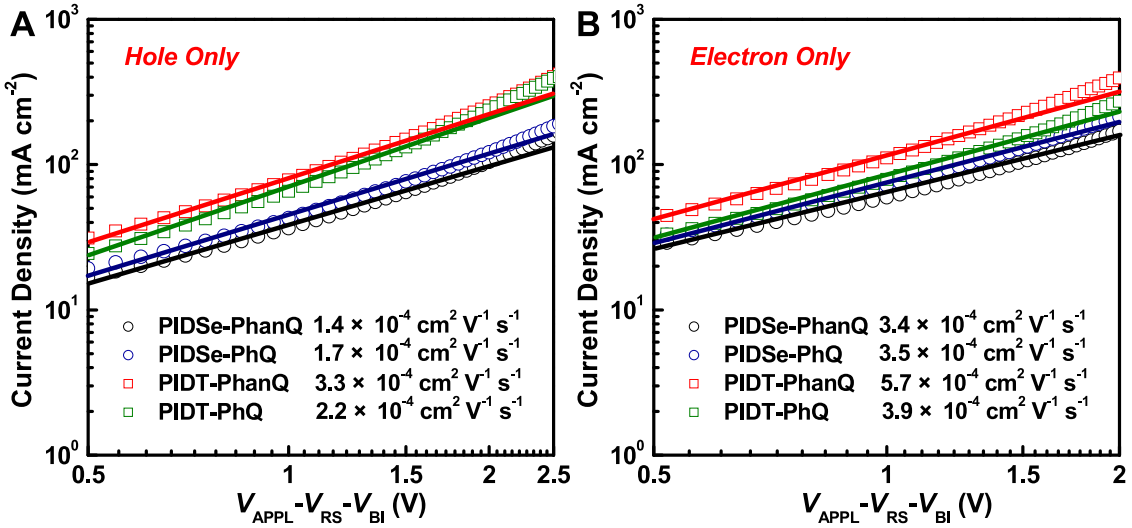

Figure A.4. Charge carrier mobilities for bulk heterojunction films measured with space charge limited current (SCLC) including PIDSe-PhanQ:$PC_{71}BM$ (black circles), PIDSe-PhQ:$PC_{71}BM$ (blue circles), PIDT-PhanQ:$PC_{71}BM$ (red squares), and PIDT-PhQ:$PC_{71}BM$ (green squares).

A.3 ELECTROLUMINESCENCE SPECTRA

Figure A.5 – Figure A.8 show electroluminescence spectra recorded over a constant current density range approximately 1 – 10 times J_{SC}, or 8.3 – 175 mA/cm^2. This current density range corresponds to forward biases near V_{OC}. We indicate forward biases and absolute current in Figure A.5 – Figure A.8 for each electroluminescence spectrum. Tables Table A.2 – Table A.5 show $EL_{max} = E_{CT} + \lambda$ values obtained from fitting all electroluminescence spectra over this charge injection range with Equation 2.1 from Chapter 2. We find that E_{CT} and λ do vary systematically with bias/charge density. This variation may result from an increased effective temperature upon higher charge injection biases. However, it is often necessary to record spectra across a wide range of current densities because of poor signal intensities at very low injected current density. Despite this variation in E_{CT} and λ, we find much smaller standard deviation for the peak position of maximum emission intensity (EL_{max}) across injected current densities compared to fitted values of

E_{CT} or λ alone. We therefore fix the average value of $EL_{max} = (E_{CT} - \lambda)$ as a constraint for fitting the CT absorption region of EQE_{PV} in Chapter 2.

When carrying out the EQE_{PV} fitting procedure in Chapter 2, we obtain values for the coupling constant and charge transfer energy as outlined in Table A.1. We note that the ~10 meV decrease in charge-transfer state energy upon Se substitution in PhanQ systems and the ~50 meV decrease in PhQ systems is consistent with the similar shift in electroluminescence peak position. As the electroluminescence peak width is reasonably comparable for all devices, we would indeed expect the shift in E_{CT} to be mirrored in the shift in the electroluminescence peak position.

Table A.1. Fitting results for the coupling constant (f), charge-transfer state energy (E_{CT}) and electroluminescence peak position (EL_{MAX}).

	Coupling constant, f (eV^2)	**CT Energy, E_{CT}** (eV)	**EL_{MAX}** (eV)
PIDSe-PhanQ BHJ	[8.4 +/- 0.2] E-2	1.42 +/- 0.01	1.23 +/- 0.01
PIDT-PhanQ BHJ	[4.6 +/- 0.3] E-3	1.43 +/- 0.02	1.26 +/- 0.01
PIDSe-PhQ BHJ	[1.4 +/- 0.1] E-2	1.35 +/- 0.02	1.19 +/- 0.00
PIDT-PhQ BHJ	[5.0 +/- 0.2] E-3	1.41 +/- 0.01	1.23 +/- 0.00

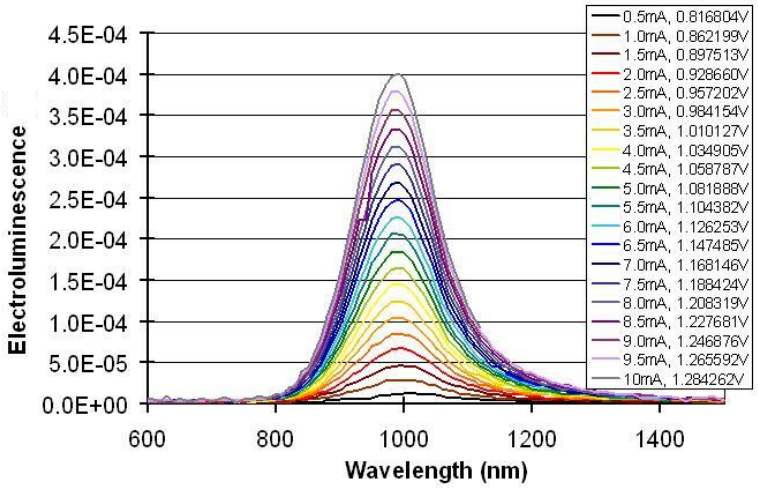

Figure A.5. PIDSe-PhanQ:$PC_{71}BM$ bulk heterojunction electroluminescence spectra.

Table A.2. Electroluminescence peak energy (EL_{MAX}) with increasing injected current.

Current (mA)	**EL_{MAX} (eV)**
0.5	1.082
1	1.197
1.5	1.222
2	1.224
2.5	1.227
3	1.230
3.5	1.231
4	1.233
4.5	1.235
5	1.235
5.5	1.236
6	1.236
6.5	1.237
7	1.238
7.5	1.238
8	1.239
8.5	1.238
9	1.240
9.5	1.240
10	1.240
Average	**1.232**
St Dev:	**0.0101**

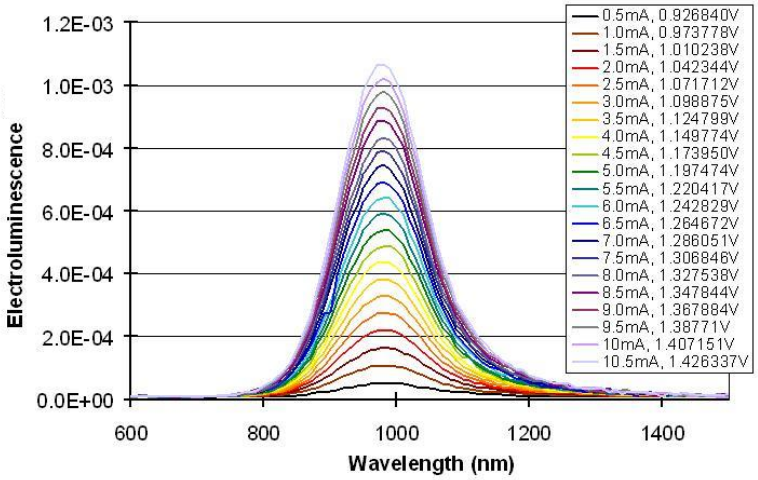

Figure A.6. PIDT-PhanQ:$PCB_{71}M$ bulk heterojunction electroluminescence spectra.

Table A.3. Electroluminescence peak energy (EL_{MAX}) with increasing injected current.

Current (mA)	**EL_{MAX} (eV)**
0.5	1.195
1	1.237
1.5	1.246
2	1.250
2.5	1.253
3	1.254
3.5	1.255
4	1.255
4.5	1.255
5	1.257
5.5	1.258
6	1.258
6.5	1.258
7	1.259
7.5	1.260
8	1.260
8.5	1.260
9	1.261
9.5	1.261
10	1.261
10.5	1.262
Average	**1.258**
St Dev	**0.00598**

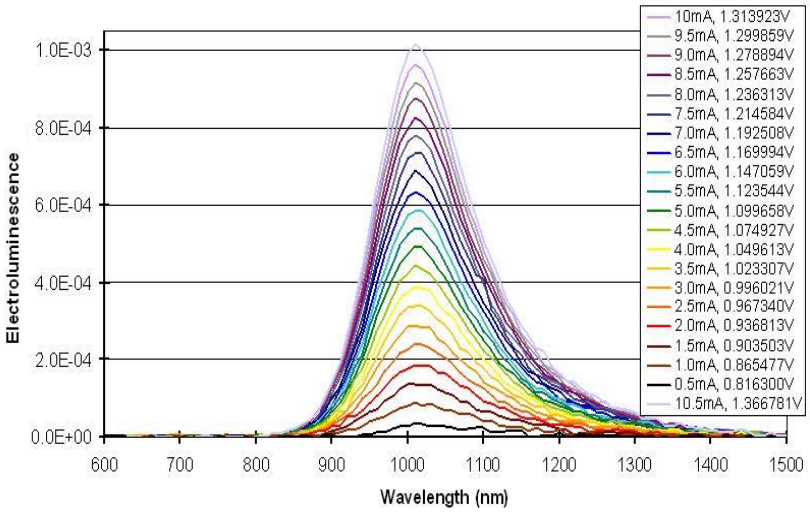

Figure A.7. PIDSe-PhQ:PCBM bulk heterojunction electroluminescence spectra.

Table A.4. Electroluminescence peak energy (EL_{MAX}) with increasing injected current.

Current (mA)	**EL_{MAX} (eV)**
0.5	1.172
1	1.183
1.5	1.185
2	1.185
2.5	1.186
3	1.187
3.5	1.186
4	1.187
4.5	1.187
5	1.188
5.5	1.188
6	1.189
6.5	1.188
7	1.189
7.5	1.188
8	1.189
8.5	1.189
9	1.190
9.5	1.189
10	1.189
10.5	1.190
Average	**1.187**
St Dev	**0.00376**

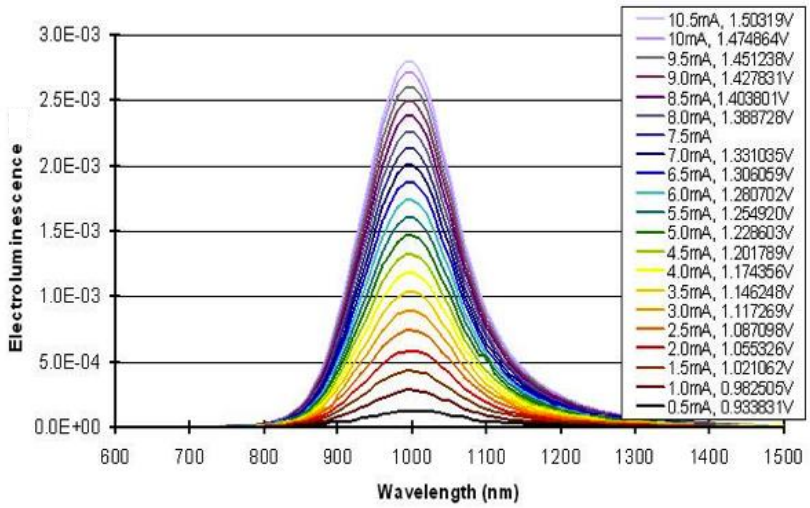

Figure A.8. PIDT-PhQ:$PC_{71}BM$ bulk heterojunction electroluminescence spectra.

Table A.5. Electroluminescence peak energy (EL_{MAX}) with increasing injected current.

Current (mA)	**EL_{MAX} (eV)**
0.5	1.224
1	1.229
1.5	1.230
2	1.230
2.5	1.231
3	1.231
3.5	1.231
4	1.232
4.5	1.232
5	1.231
5.5	1.232
6	1.232
6.5	1.232
7	1.233
7.5	1.233
8	1.233
8.5	1.233
9	1.233
9.5	1.233
10	1.234
10.5	1.234
Average	**1.232**
St Dev	**0.00135**

A.4 UNIT CONVERSIONS

For ease of experimental application, Equations 2.2 and 2.4 in Chapter 2 contain a unit conversion factor [6.24×10^{-25} eVcm^3/D^2]. The unit conversion is necessary because we present energy in units of [eV] while dipole moment is commonly in units of [Debye]. Here we write out the necessary conversion from [Debye] to units compatible with energies in [eV]. We define variables and their units in Chapter 2.

$$f = \eta N_{CTC} 2d \frac{8\pi^3}{3hc} nV^2 \Delta\mu^2 \left[\mathbf{6.24 * 10^{-25}} \frac{\boldsymbol{eVcm^3}}{\boldsymbol{D^2}}\right]$$

$$[eV^2] =$$

$$[cm^{-3}][cm] \frac{1}{[eVs]\left[\frac{cm}{s}\right]} [eV^2][D^2] \left[\frac{\mathbf{10^{-18}}\ \boldsymbol{statC * cm}}{\boldsymbol{D}}\right]^2 \left[\frac{\sqrt{\boldsymbol{erg * cm}}}{\boldsymbol{statC}}\right]^2 \left[\frac{\mathbf{6.24 * 10^{11}} \boldsymbol{eV}}{\boldsymbol{erg}}\right]$$

The unit conversion is the same for the emission equations.

$$f_{emission} = \frac{64\,\pi^4}{3\mathrm{h}^4 c^3} n^3 V^2 \Delta\mu^2 \left[\mathbf{6.24 * 10^{-25}} \frac{\boldsymbol{eVcm^3}}{\boldsymbol{D^2}}\right]$$

$$\left[\frac{1}{eV * s}\right] = \frac{1}{[eVs]^4 \left[\frac{cm}{s}\right]^3} [eV^2][D^2] \left[\frac{\mathbf{10^{-18}}\ \boldsymbol{statC * cm}}{\boldsymbol{D}}\right]^2 \left[\frac{\sqrt{\boldsymbol{erg * cm}}}{\boldsymbol{statC}}\right]^2 \left[\frac{\mathbf{6.24 * 10^{11}} \boldsymbol{eV}}{\boldsymbol{erg}}\right]$$

A.5 PERCENT CONTRIBUTIONS OF N_{CT}, V, AND E_{CT} TO V_{OC} LOSS

We investigate the influence of Se substitution on the open-circuit voltage of bulk heterojunction solar cells in Chapter 2. We measure a decrease in the open circuit voltage (V_{OC}) of 130 mV upon Se-substitution in PhanQ systems and 120 mV in PhQ systems (Figure 2.3 in Chapter 2). We measure several values that could cause lower V_{OC} upon Se-substitution, such as

E_{CT}, N_{CT}, and V. In this section, we calculate which values contribute more to the total V_{OC} loss and we analyze the propagation of error though our calculations.

We calculate V_{OC} from our experimental results by solving Equations 2.5 and 2.4 from Chapter 2 for V_{OC}, and we give the result in Equation A.1.

$$V_{oc} = \frac{E_{\mathrm{CT}}}{q} + \frac{kT}{q}\ln\left(\frac{3J_{sc}h^4c^3}{16\pi^4 q\eta N_{CT} dn V^2 \Delta\mu^2 (E_{\mathrm{CT}}-\lambda)}\right) + \frac{kT}{q}\ln(\mathrm{EQE}_{EL}) \quad \text{(A.1)}$$

Inserting our measured values for each variable into Equation A.1 returns V_{OC} values reported in Chapter 2 (Table 2.2) within +/- 0.029 V error.

We calculate a theoretical value for what V_{OC} would be for the selenophene systems if the values for E_{CT}, N_{CT}, and V were identical to the values measured for the thiophenes. We find that the V_{OC} deficit would be nearly eliminated if E_{CT}, N_{CT}, and V had not changed upon Se substitution. We calculate similar V_{OC} across both systems by inserting the thiophene values for E_{CT}, N_{CT}, and V into equation A.1 while still using the selenophene values for J_{SC}, η, d, EQE_{EL} and λ. This suggests that E_{CT}, N_{CT}, and V account for the majority of V_{OC} loss upon Se substitution. We find that $V_{OC}^{theoretical}$ for PIDSe-PhanQ is 0.85 +/- 0.02 V, compared to V_{OC} of 0.88 +/- 0.01 V for PIDT-PhanQ. We similarly find $V_{OC}^{theoretical}$ for PIDSe-PhQ is 0.85 +/- 0.02 V, compared to 0.87 +/- 0.01 V for PIDT-PhQ. The remainder of the V_{OC} decrease upon Se substitution is due to changes in J_{SC}, η, d, EQE_{EL} and λ.

We next calculate the percent change in V_{OC} when we hold one variable (E_{CT}, N_{CT}, or V) constant across both systems, and we give the results in Table A.6 and Table A.7. For example, to calculate the percent contribution of N_{CT} to the total V_{OC} decrease upon Se substitution, we calculate $V_{OC}^{theoretical}$ from Equation A.1 using constant N_{CT} from the thiophene system and all

other variables as actually measured for the selenophene system. We calculate error bars based on the propagation of error for each experimentally measured or fitted variable.

Table A.6. Values for estimating percent contribution of N_{CT}, E_{CT}, and V to the overall V_{OC} loss upon Se substitution in the PhanQ Systems.

PhanQ Variable	**Total Voc Decrease** (mV)	**Voltage Loss** (mV)	**Percent of Total Voltage Loss**
N_{CT}	130 +/- 14	67 +/- 26	52 +/- 20 %
E_{CT}	130 +/- 14	12 +/- 3.3	9.3 +/- 2.4 %
V	130 +/- 14	18 +/- 4.7	14 +/- 3.2 %

Table A.7. Values for estimating percent contribution of N_{CT}, E_{CT}, and V to the overall V_{OC} loss upon Se substitution in the PhQ systems.

PhQ Variable	**Total Voc Decrease** (mV)	**Voltage Loss** (mV)	**Percent of Total Voltage Loss**
N_{CT}	120 +/- 14	33 +/- 13	27 +/- 11 %
E_{CT}	120 +/- 14	61 +/- 23	51 +/- 20 %
V	120 +/- 14	5.5 +/- 1.8	4.6 +/- 1.4 %

Table A.6 and Table A.7 show that N_{CT} is the major factor causing the 130 mV V_{OC} decrease upon Se substitution in the PhanQ systems and that E_{CT} is the major factor causing the 120 mV V_{OC} decrease upon Se substitution in the PhQ systems. However, we note that N_{CT} contributes significantly more to the V_{OC} decrease than V in both cases. While E_{CT} defines the energetics of the system, we find that N_{CT} represents the major factor causing recombination losses leading to decreased V_{OC} upon Se substitution in both systems.

A.6 DEFINITION OF N_{CT}

To best understand the recombination losses arising from N_{CT}, it is important to carefully define N_{CT}. As noted in Chapter 2, N_{CT} refers to the total available density of charge-transfer states,

not the density of occupied charge-transfer states. The relationship between available and occupied density of charge-transfer states is given by:

$$N_{CT}^{occupied} = N_{CT}^{available}\ \mathrm{A}\ \mathrm{Exp}\left(\frac{\sigma_{CT}^2}{2(kT)^2}\right)\mathrm{Exp}\left(\frac{qV_{OC} - E_{CT}}{kT}\right)$$

where A is the donor/acceptor mixing fraction and σ_{CT} is the energetic disorder.

A.7 INTERNAL QUANTUM EFFICIENCIES AND FILM THICKNESSES

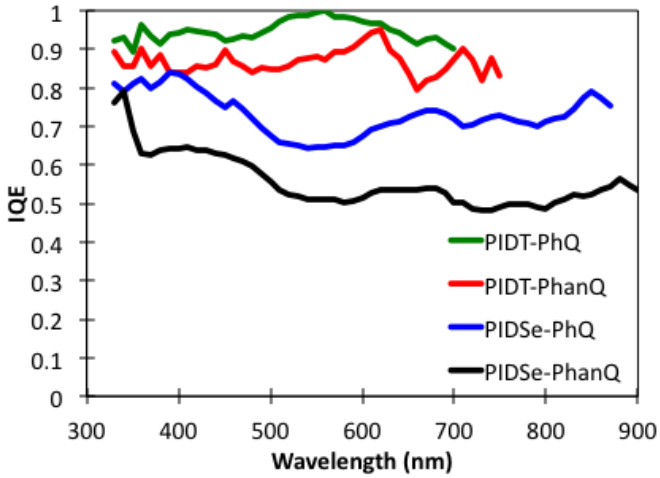

Figure A.9. Internal quantum efficiencies for devices of PIDT-PhQ:PCBM (green), PIDT-PhanQ:PCBM (red), PIDSe-PhQ:PCBM (blue), and PIDSe-PhanQ:PCBM (black).

Table A.8. Film thicknesses measured with profilometer.

PIDSe-PhanQ	Sample 1	Sample 2	Sample 3	
	79.547	76.041	76.057	
	76.213	74.14	76.229	
	77.467	75.471	74.932	
	78.153	73.642	75.848	
Average	**77.845**	**74.824**	**75.767**	**76.145 nm**

PIDT-PhanQ		Sample 1	Sample 2	
		71.867	84.896	
		64.575	80.499	
		67.913	84.935	
		65.064	85.370	
		64.433	85.249	
Average		**65.496**	**84.013**	**74.755 nm**

PIDSe-PhQ	Sample 1	Sample 2	Sample 3	
	87.237	79.887	85.034	
	94.339	82.662	84.311	
	89.173	76.166	85.508	
	92.891	83.496	85.942	
	84.583	78.606	83.686	
Average	**90.247**	**80.233**	**84.862**	**85.114 nm**

PIDT-PhQ		Sample 1	Sample 2	
		77.906	85.435	
		80.464	91.523	
		76.100	88.698	
		75.269	86.743	
		76.259	83.785	
Average		**77.023**	**87.687**	**82.355 nm**

A.8 TIME CORRELATED SINGLE PHOTON COUNTING AND INSTRUMENT RESPONSE FUNCTIONS

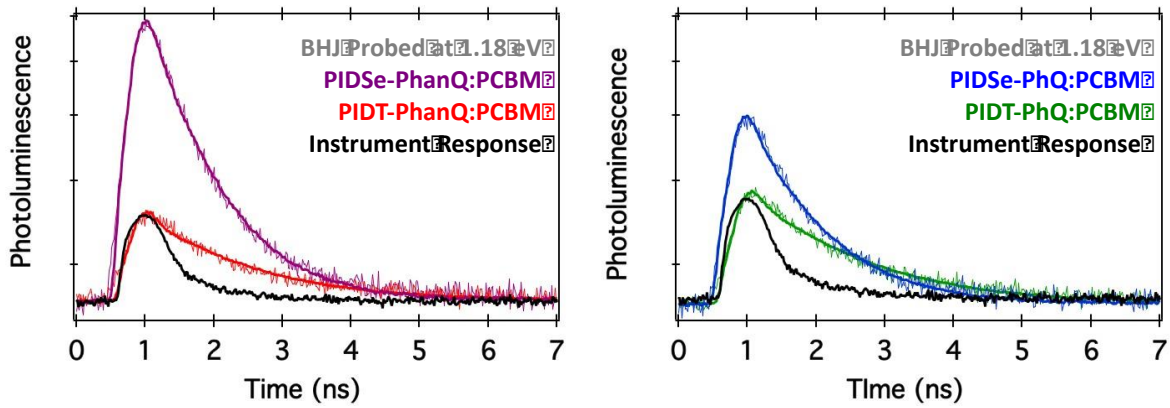

Figure A.10. Time-resolved photoluminescence probed at 1.18 eV, showing charge-transfer state lifetimes and instrument response function measured using the LDS798 fluorophore.

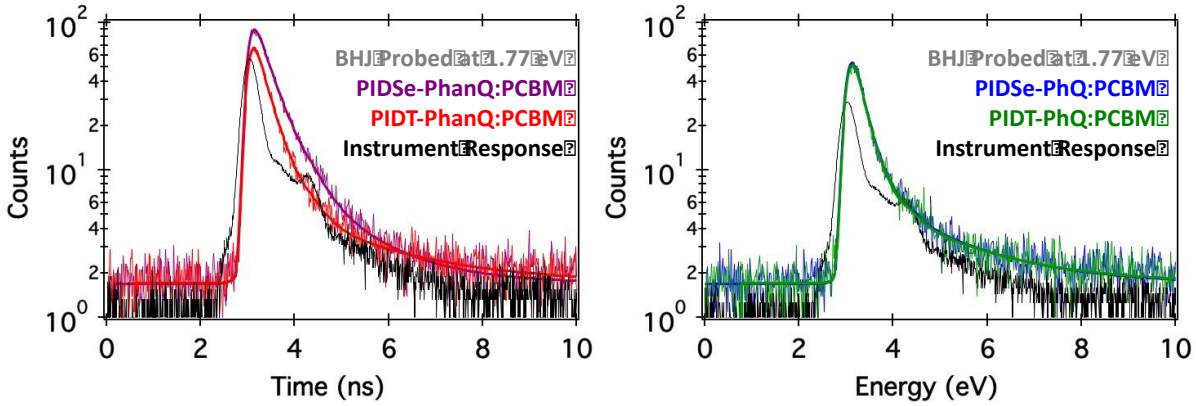

Figure A.11. Time-resolved photoluminescence probed at 1.77 eV, showing lifetimes of unquenched neat materials' excited states and instrument response function measured using scattered laser light from a glass slide.

Figure A.12. Exponential decay time constants (t), amplitude coefficients (A), and fractional intensities for unquenched neat materials' photoluminescence decays probed at 1.77 eV.

Polymer	t_1 (ns)	A_1	Fractional Intensity	t_2 (ns)	A_2	Fractional Intensity
PIDSe-PhanQ	0.3690	2647	77.09%	1.364	212.7	22.91%
PIDT-PhanQ	0.3066	2151	77.42%	2.150	89.40	22.58%
PIDSe-PhQ	0.2391	2052	70.79%	1.811	111.8	29.21%
PIDT-PhQ	0.2407	1999	71.72%	1.882	100.8	28.28%

A.9 GRAZING INCIDENCE WIDE ANGLE X-RAY SCATTERING

We use grazing incidence wide angle x-ray scattering (GIWAXS) to gain more orientational information about the ordered structure in the PIDSe-PhanQ:PCBM bulk heterojunction films. Figure A.13 shows the GIWAXS patterns of the PIDSe-PhanQ:PCBM blend and the neat PIDSe-PhanQ polymer. The GIWAXS pattern of neat PIDSe-PhanQ shows a broad disordered peak at 1.18 nm at X=10°, indicating some in-plane correlation of polymer chains. When blended with fullerene, the broad disordered peak shifts to 1.46 nm at X=10°, suggesting that the presence of fullerene in the BHJ film induces structural reorganization of the disordered polymer regions such that the in-plane correlation distance between polymer segments is larger. Additionally, the PIDSe-PhanQ:PCBM films show a distinct out-of-plane oriented crystalline structure at 1.64 nm at X=80°. This crystalline peak corresponds to the sharp diffraction ring observed in the selected area electron diffraction (SAED) patterns presented in Chapter 2. Figure A.13 shows that the crystalline peak is also absent in GIWAXS for PIDT-PhanQ:PCBM films, which is consistent with the SAED patterns and confirms a unique fullerene-induced crystalline feature present only in the PIDSe-PhanQ:PCBM blends.

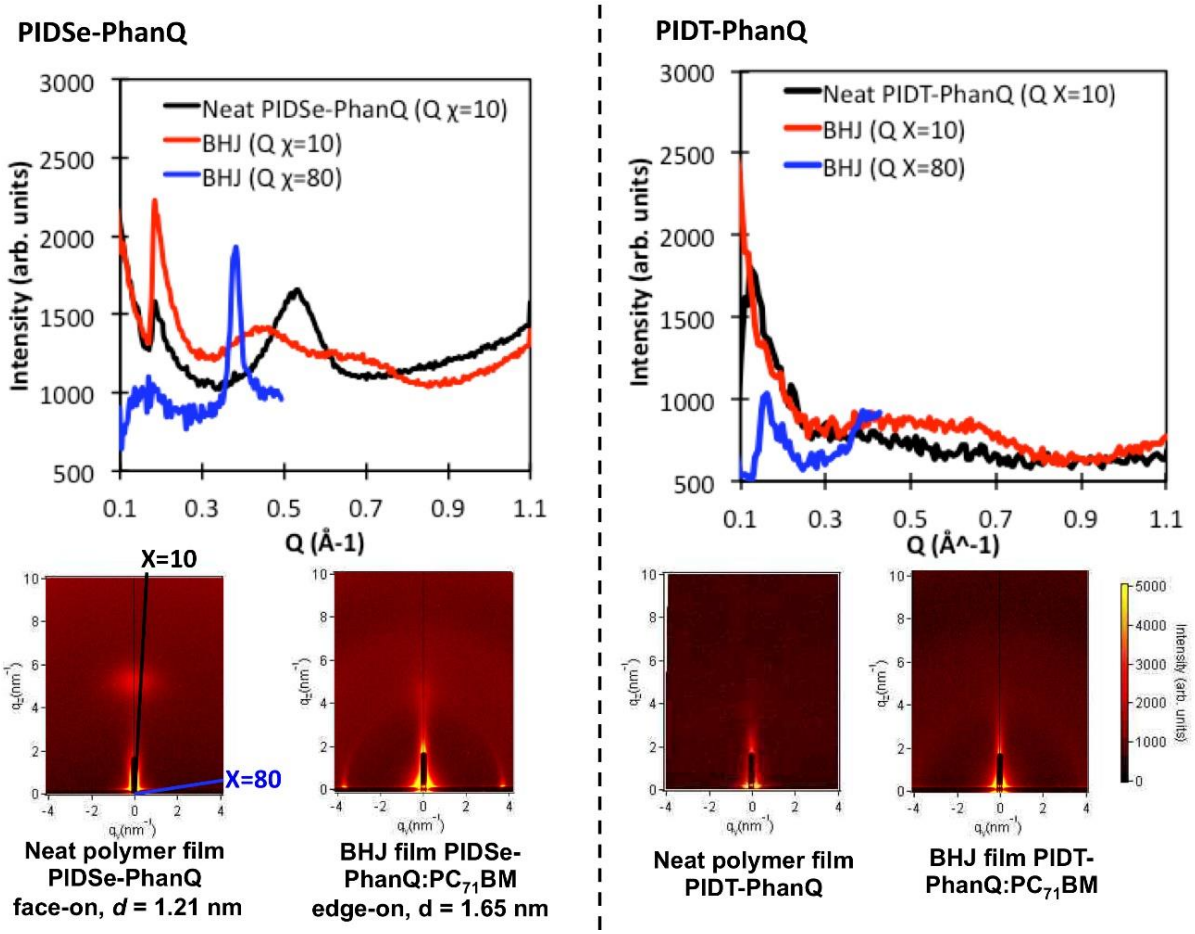

Figure A.13. Grazing Incidence Wide Angle X-ray Scattering (GIWAXS) data for films of neat PIDSe-PhanQ polymer, PIDSe-PhanQ:PCBM, neat PIDT-PhanQ polymer, and PIDT-PhanQ:PCBM, showing ordered features in the PIDSe-PhanQ:PCBM bulk heterojunction (BHJ) films.

Appendix B. **SUPPORTING INFORMATION FOR CHAPTER 3:** *UNEQUILIBRATED SINGLET AND TRIPLET CHARGE-TRANSFER STATES IN ORGANIC BULK HETEROJUNCTIONS*

B.1 **ADDITIONAL STEADY-STATE ABSORPTION SPECTRA**

Figure B.1 shows the absorption spectra for the neat PIDT-PhanQ and $PC_{71}BM$ materials that we used for the study in Chapter 3. Figure B.2 shows the absorption spectra for the 1:3 PIDT-PhanQ:$PC_{71}BM$ films spin-coated from either chloroform ($CHCl_3$) or dichlorobenzene (DCB). We observe increased absorption for the films cast from $CHCl_3$ compared to the films cast from DCB. The higher absorption value for the $CHCl_3$ film is due to increased film thickness. Using atomic force microscopy, we characterized the film thickness as 190 nm for the $CHCl_3$ film and 105 nm for the DCB film.

We note that the increased film thickness has implications for the relative strengths of electric fields resulting from the DC voltage biases that we applied in our study in Chapter 3. The active layer of the thicker sample (processed in $CHCl_3$) would experience a weaker electric field for the same DC voltage bias. We find this observation interesting, as the thicker $CHCl_3$ device nevertheless shows a much stronger voltage dependence both for photocurrent and for the triplet photoinduced absorption signal.

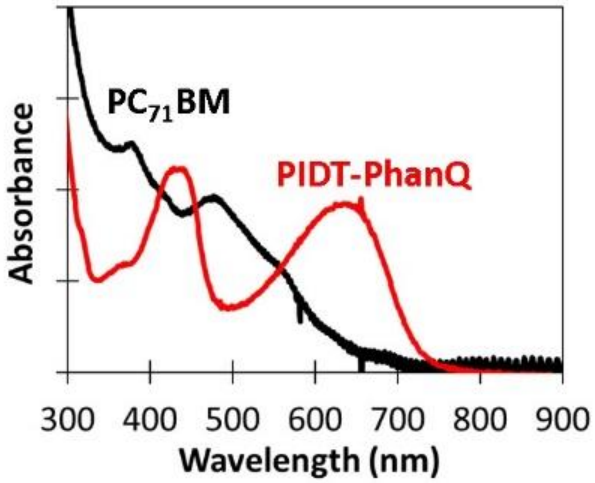

Figure B.1. Absorption spectra for PIDT-PhanQ (red trace) and $PC_{71}BM$ (black trace).

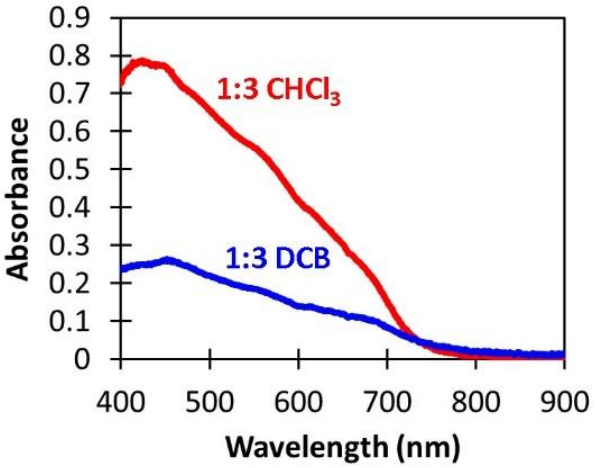

Figure B.2. Absorption Spectra for 1:3 PIDT-PhanQ:$PC_{71}BM$ thin films cast from chloroform ($CHCl_3$, red trace) or dichlorobenzene (DCB, blue trace).

B.2 THIN FILM MORPHOLOGY CHARACTERIZATION WITH ATOMIC FORCE MICROSCOPY

Figure B.3 shows the difference in nanoscale morphology obtained by using either DCB or $CHCl_3$ solvent to spin coat the 1:3 PIDT-PhanQ:$PC_{71}BM$ bulk heterojunction films. We characterize the morphology using transmission electron microscopy (Figure B.3a and Figure

B.3b) and atomic force microscopy (Figure B.3c and Figure B.3d). We observe larger phase separation in the active layer spin coated from $CHCl_3$ compared to that spin coated from DCB.

We note that the large phase separation in the $CHCl_3$ active layer along with the increased film thickness may explain the poor performance for the $CHCl_3$ devices. First, the large phases would not allow complete exciton dissociation, since exciton diffusion is typically on the order of ~10 nm.[210] This loss process would not be recoverable under applied voltage, since neither the diffusion nor the separation of neutral excitons should be influenced by an external field.[41] Furthermore, the large film thickness and isolated fullerene phases may cause charge-extraction issues, which would support our conclusions in Chapter 3 that the applied voltage primarily affects this device by extracting charges.

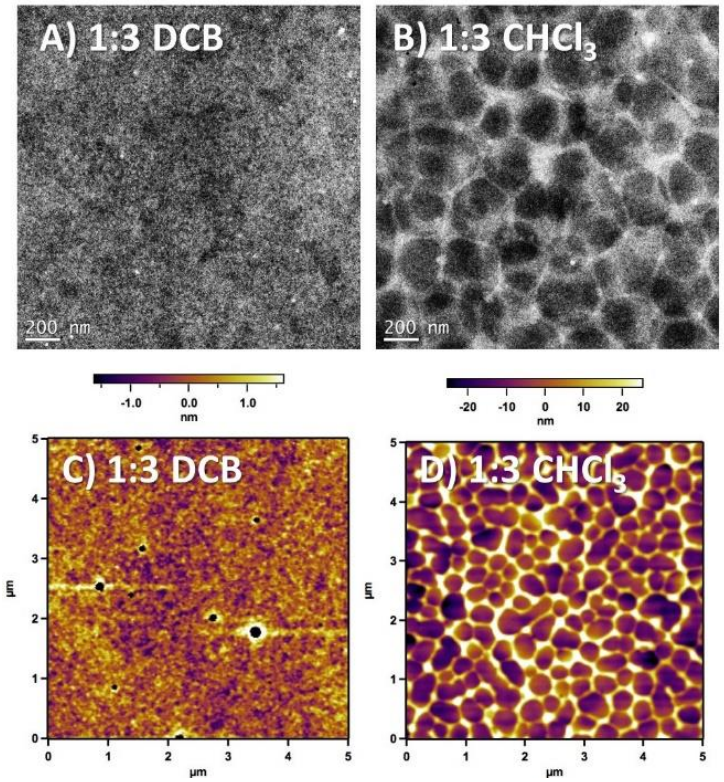

Figure B.3. Transmission electron microscopy images of 1:3 PIDT-PhanQ:$PC_{71}BM$ thin films cast from (a) dichlorobenzene (DCB) and (b) chloroform ($CHCl_3$), and atomic force microscopy images of 1:3 PIDT-PhanQ:$PC_{71}BM$ thin films cast from (c) dichlorobenzene (DCB) or (d) chloroform ($CHCl_3$).

B.3 Soft X-Ray Characterization: Near-Edge X-Ray Absorption Fine Structure, Scanning Transmission X-Ray Microscopy, and Resonant Soft X-Ray Scattering

We further characterize the differences in domain size and purity for the $CHCl_3$ and DCB processed films using soft X-ray techniques. We first measure the near edge X-ray absorption fine structure (NEXAFS) patterns to determine the photon energies that will be used for the analysis. Figure B.4a shows the NEXAFS patterns for the neat polymer and fullerene thin films, highlighting the photon energies characteristic of polymer (292 eV) and fullerene (284.4 eV) absorbance that we later use to quantify the domain composition (Figure B.5). Figure B.4b shows the scattering contrast functions between PIDT-PhanQ and PCBM as well as between the neat materials and vacuum, calculated from the NEXAFS measurements. The contrast functions show that 283 eV is an appropriate photon energy to perform the resonant soft X-ray scattering (RSoXS) measurements, since this maximizes the polymer/fullerene material contrast while minimizing scattering, vacuum contrast, and beam damage from absorption.

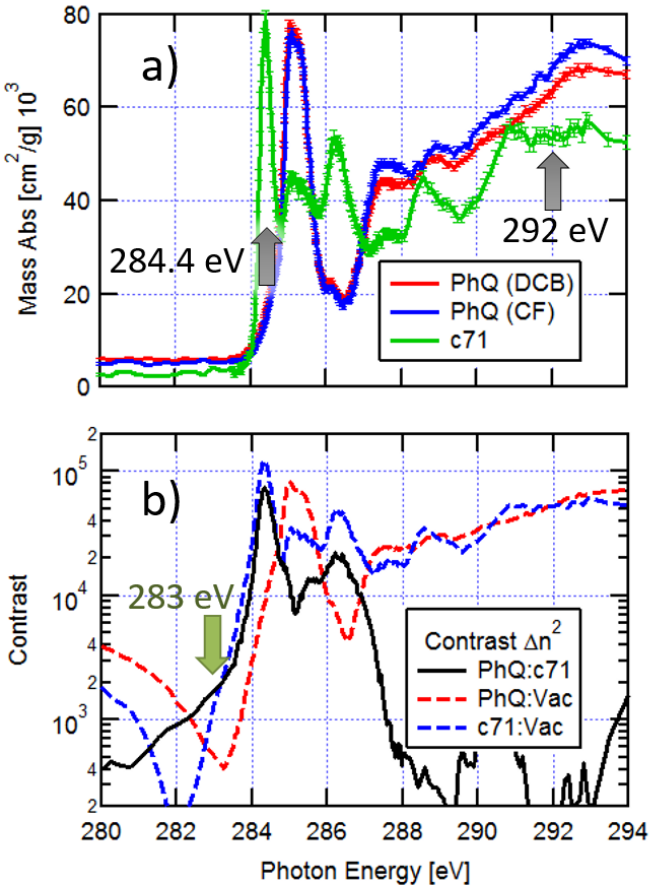

Figure B.4. Near Edge X-ray Absorption Fine Structure (NEXAFS) Spectroscopic analysis of the materials investigated reveals resonant X-ray energies to perform microscopy and scattering experiments. a) Transmission NEXAFS spectra of pure PIDT-PhanQ ("PhQ") cast either from DCB or $CHCl_3$ ("CF") revealing no spectral differences caused by the two casting conditions. NEXAFS spectra of a pure $PC_{71}BM$ ("c71") film is also shown. These data enabled proper choice of photon energies (284.4 eV and 292 eV) used in resonant X-ray microscopy for quantitative compositional analysis (see **Figure B.5**). b) Scattering contrast functions (Δn^2 where n is the complex index of refraction calculated from the NEXAFS measurements). The resonant scattering photon energy of 283 eV was chosen as indicated for this analysis (see **Figure B.6**). This energy maximizes the material contrast ("PhQ:c71", black curve); minimize scattering from roughness or vacuum contrast ("PhQ:Vac" & "c71:Vac", red and blue dashed curves, respectively); and minimize the absorption (and therefore beam damage and X-ray fluorescence signals).

Figure B.5 shows the scanning transmission X-ray microscopy (STXM) analysis of composition and thickness maps for the 1:3 PhanQ:PCBM films processed in $CHCl_3$. We describe the technique and our method of analysis in greater detail in Ref [257]. For the $CHCl_3$ films, our analysis reveals circular domains 300-400 nm in diameter that are largely pure in fullerene, while the matrix is pure in polymer content. Since the DCB-processed films did not image well in the STXM, we used Resonant Soft X-ray Scattering (RSoXS) to probe average profile size scales down to 10 nm in PhanQ:PCBM films of varying polymer:fullerene ratios and solvent processing. We characterize the domain sizes and purities based on the RSoXS Q-positions and total scattering intensities.

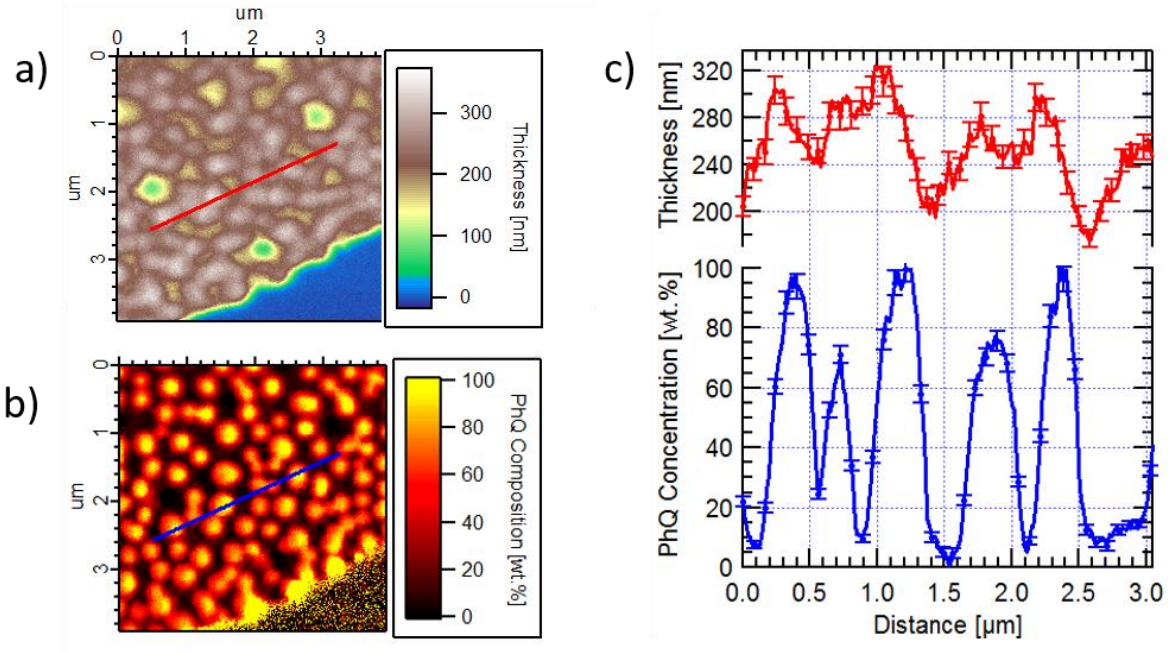

Figure B.5. Quantitative composition maps determine absolute domain composition via Scanning Transmission X-ray Microscopy (STXM). a) Thickness and b) composition maps of a film revealing large circular domains which cause significant film roughness. c) lineouts of a) and b) which show roughness on the order of 100 nm (average thickness of ~250 nm) and nearly pure domains of each constituent molecule (fullerene dispersions and polymer matrix).

Figure B.6 shows the scattering profiles for PhanQ:PCBM films processed in $CHCl_3$ and DCB of varying 1:1 or 1:3 compositions. The profile for the 1:3 PhanQ:PCBM film processed in $CHCl_3$ (C13) revealed features whose Q-positions correspond roughly to domain spacing seen in the STXM, where Q_{C13}=0.0145 nm^{-1} corresponds to characteristic length $l = 2\pi/Q$ of $l_{C13} = 433\ nm$. For the 1:3 PhanQ:PCBM film processed in DCB (D13), we observe smaller domain spacing, where Q_{D13} = 0.119 nm^{-1} corresponds to characteristic length of l_{D13} = 53nm. We also measured 1:1 films processed in $CHCl_3$ (C11) and DCB (D11), where C11 showed Q_{C11} = 0.0838 nm^{-1} with a characteristic length of $l_{C11} = 75nm$, and D11 did not reveal a clear peak. The total scattering intensity (TSI) decreased precipitously following the same order as the domain spacing observed by RSoXS (C13>D13>C11>D11). We quantify total scattering intensity as $TSI = V\Delta n_{12}^2 \phi(1-\phi)$ following the Porod invariant formalism where V the sample volume, ϕ is the volume fraction of one domain, and Δn_{12}^2 is the difference in optical constants between the two domains. Since domain composition $x_{12} \propto n_{12}$, then $\sqrt{TSI} \propto x_{12}$ (although it is also affected by domain volume fraction). The fact that the STXM measurements show pure or nearly pure domains in the 1:3 PhanQ:PCBM film processed in $CHCl_3$ helps to scale the RSoXS measurement of domain composition fluctuation in the other films. Figure S6b shows the relative $\sqrt{TSI}$ for each film, indicating that the D13, D11, and C11 films contain domains either will extremely small volume fraction, or (much more likely) domains which more mixed (less pure) molecular compositions.

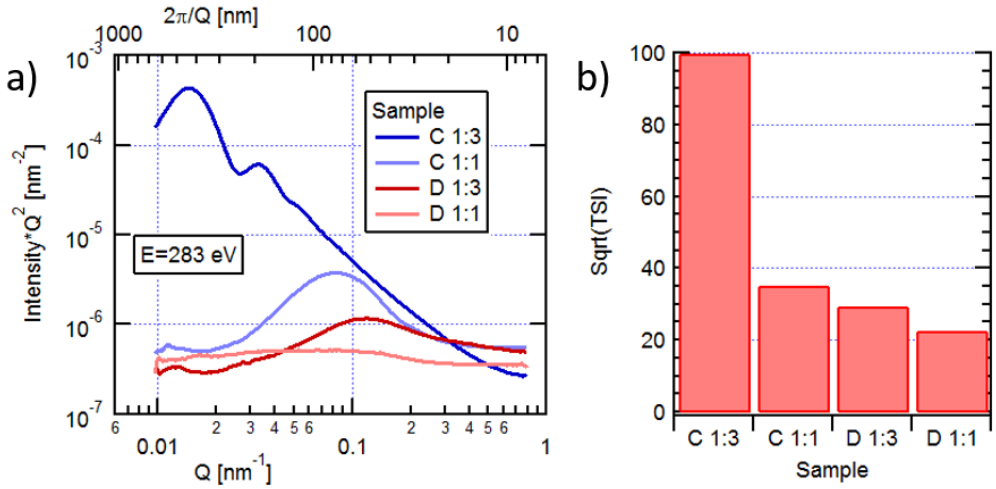

Figure B.6. Resonant Soft X-ray Scattering (RSoXS) reveals domain size and purity. a) Scattering profiles for four samples ("C"=$CHCl_3$, "D"=DCB, "1:3" and "1:1" are the polymer-fullerene ratios) acquired with a photon energy of 283 eV. b) $\sqrt{TSI}$ (total scattering intensity) for each sample which is proportional to domain purity.

Combined analysis of the films indicates domain structures that are highly affected by the processing conditions. The morphology and composition of the domains revealed for the (1:3) films cast from $CHCl_3$ indicate a liquid-like phase separation due to thermodynamic miscibility limits between the two molecules. However, the drastically lower TSI and smaller domains from the (1:3) films cast from DCB seems to indicate that the processing solvent significantly affects the domain purity rather than simply the interaction between the polymer and fullerene. If the solvents were simply neutral spectators, then the DCB-cast films would have the more pure and larger domains given the lower volatility of DCB. The longer evaporation time of DCB would plasticize the film for longer, allowing the molecules to phase separate further as compared with the highly volatile $CHCl_3$ which would vitrify the film quickly. Instead, it is possible (although out of the scope of this investigation to confirm) that $CHCl_3$ is a differential solvent for the molecules compared with DCB, causing one molecule to crash out of solution early.

Importantly, the stark differences in the measured morphology suggests different environments for charge generation within OPV devices. The high purity of the domains in the $CHCl_3$-cast (1:3) film indicates that all the charge separation dynamics will occur only at these discrete interfaces. This contrasts the DCB-cast devices where charge generation/recombination might occur both at domain interfaces and between molecules within mixed domains as well.

B.4 ELECTROLUMINESCENCE QUANTUM YIELDS

Figure B.7 shows that there is little variation in the electroluminescence quantum yield over our measured range of injected current densities, corresponding to a linear relationship between the injected electrons and emitted photon flux. We find that the $CHCl_3$ devices have a slightly higher electroluminescence quantum yield than the DCB-processed devices.

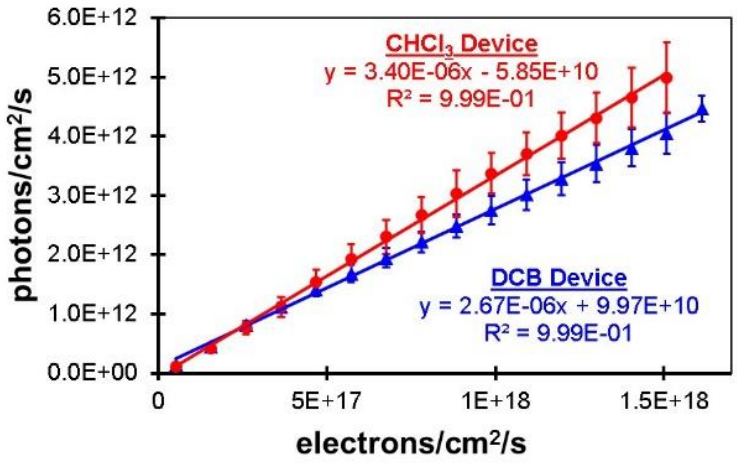

Figure B.7. Electroluminescence quantum yields for the chloroform ($CHCl_3$, red) and dichlorobenzene (DCB, blue) processed devices.

B.5 RECONSTRUCTING SUB-GAP ABSORPTION FROM ELECTROLUMINESCENCE

We provide evidence that charge-transfer states are important for photocurrent generation by relating our data to the reciprocity relation for photon absorption and emission from luminescent charge-transfer states, which was previously derived for organic photovoltaic devices.[157, 258] Following the method of Vandewal et al., we use the electroluminescence spectra given in Section 3.2.8 of Chapter 3 to calculate the sub-gap absorbance A(E) in the 1:3 PhanQ:PCBM films according to Equation B.1.[78]

$$A(E) \sim N(E)E^{-2}Exp\left(\frac{E}{kT}\right) \tag{B.1}$$

In Equation B.1, E is energy, N(E) is the charge-transfer state emission spectrum, k is Boltzmann's constant, and T is temperature.

Figure B.8a and Figure B.8b show the reconstructed absorbance values in open circles or open triangles for the $CHCl_3$ and DCB devices, respectively. As previously outlined by Vandewal et al.,[78] we scaled the reconstructed absorbance values using the overlapping region of the UV-Vis absorbance spectra (shown as solid colored lines in Figure B.8). The UV-Vis absorbance spectra in Figure B.8 show a baseline noise level around ~0.05 absorbance units, although we are able to reconstruct the weakly absorbing sub-gap region down to ~0.001 absorbance units. We also show the EQE curves in Figure B.8 as solid gray lines for both devices. In agreement with the previous results by Vandewal et al., we find that that the reconstructed absorbance spectra follow the same line-shape as the sub-gap region of the EQE curve.[78] We note that the absorbance values in Figure B.8 are multiplied by two in order to offset them from the EQE curves.

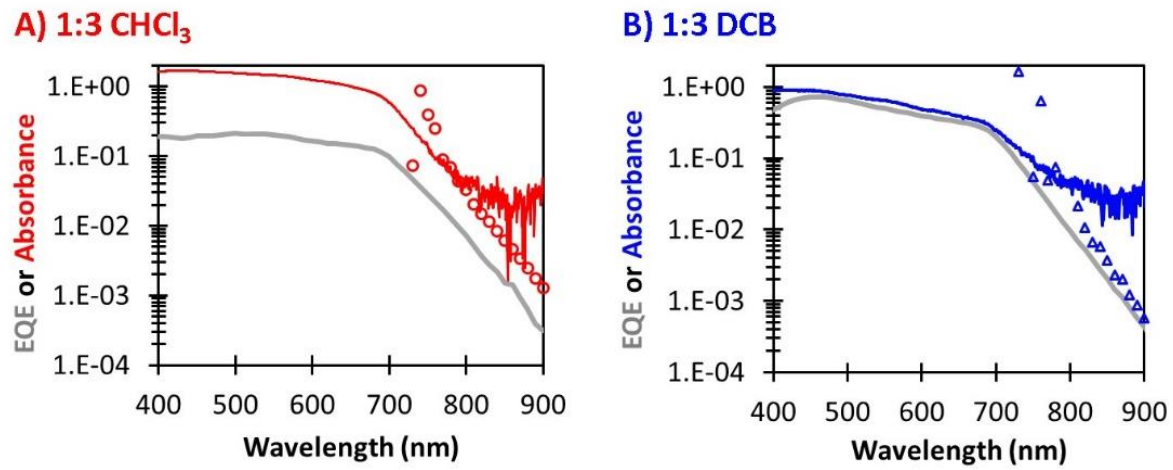

Figure B.8. Measurements on 1:3 PIDT-PhanQ:PCBM thin films and devices spin-cast from (a) chloroform ($CHCl_3$) or (b) dichlorobenzene (DCB) showing the UV-Vis absorption ($CHCl_3$: solid red line, DCB: solid blue line), overlaid with the reconstructed sub-gap absorption ($CHCl_3$: red circles, DCB: blue triangles), as well as the lock-in detected external quantum efficiency (EQE) measured at short circuit and room temperature shown in gray for both devices.

Appendix C. SUPPORTING INFORMATION FOR CHAPTER 4: *KINETIC COMPETITION BETWEEN CHARGE SEPARATION AND TRIPLET FORMATION IN SMALL-MOLECULE PHOTOVOLTAIC BLENDS*

C.1 ADDITIONAL STEADY-STATE ABSORPTION SPECTRA

Figure C.1 shows the absorption spectra for C_{60}:PS films (blue) that we use in Chapter 4 (Section 4.2.4) to characterize the C_{60} native intersystem crossing dynamics, along with thicker C_{60}:PS films (black) created by drop casting several layers at the same wt% in polystyrene (see Section 4.5.2 for film preparation). The thicker film shows higher absorption signal for the symmetry forbidden transition in the 450 – 650 nm region, which we use to find the 0-0 singlet energy reported in the main text. The symmetry forbidden transition in Figure C.1 is different from the C_{60} aggregate absorption peak in Figure C.3.

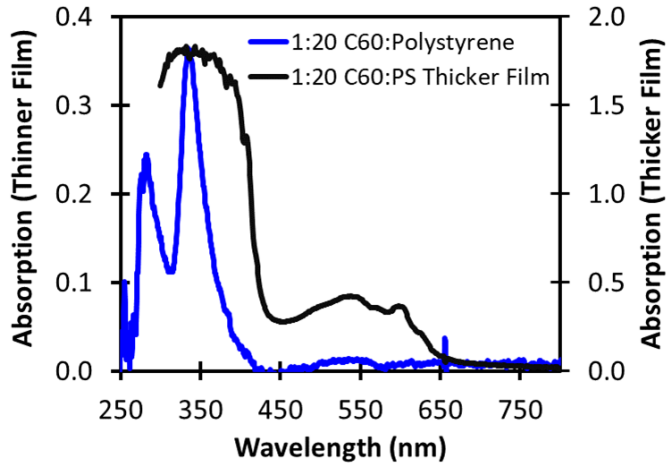

Figure C.1. Absorption spectra for C_{60}:polystyrene (PS) films used in Chapter 4 (blue) and thicker C_{60}:polystyrene films (black) formed by drop casting several layers.

Figure C.2 shows the absorption spectra for dilute films in polystyrene (PS), including 0.2 wt% SubPc:PS, 0.4 wt% C_{60}:PS, and 0.6 wt% SubPc:C_{60}:PS. As we describe in Section 4.5.2 of Chapter 4, these films have matched molar ratios of the active components dispersed in polystyrene, ensuring nearly matched optical densities between the neat (SubPc:PS or C_{60}:PS) and blended (SubPc:C_{60}:PS) films. The difference in wt% between the films is simply due to the higher molecular weight of C_{60} compared to SubPc. Indeed, the SubPc:C_{60}:PS films show similar absorption intensities compared to the dilute SubPc and C_{60} films, allowing us to use similar pump fluences when measuring transient absorption spectra and photoluminescence.

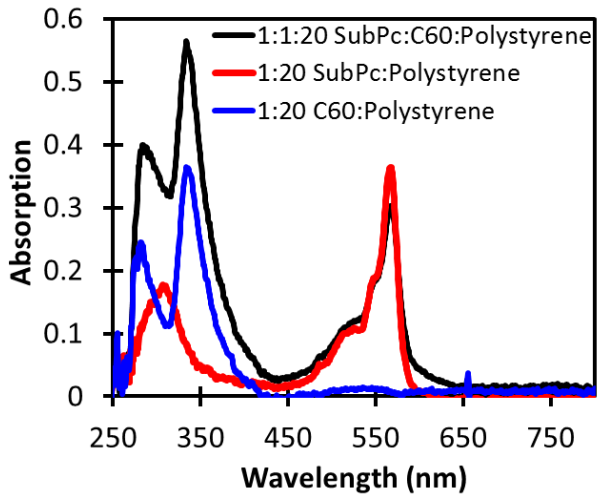

Figure C.2. Absorption spectra for SubPc:polystyrene films (red), C_{60}:Polystyrene films (blue), and SubPc:C_{60}:Polystyrene films (black).

Figure C.3 shows the absorption spectra for the vapor-deposited films used in Chapter 4. We compare the absorption in 1:1 and 1:2 SubPc:C_{60} films as well as neat films of C_{60} and SubPc. The 1:1 and 1:2 films show similar optical density at the SubPc absorption maximum, since we hold the deposited volume of SubPc constant for both films. The 1:2 films show higher absorption in the 250-500 nm region corresponding to increased C_{60} content. Importantly, the 1:2 films exhibit

an enhanced peak at 450 nm corresponding to C_{60} aggregate absorption. The C_{60} aggregate absorption is also visible in the neat C_{60} vapor-deposited films at 450 nm.

In our transient absorption experiments, we excite our samples with 550 nm pump light. As shown in Figure C.3, the 550 nm light primarily photoexcites SubPc rather than C_{60}. Indeed, we measure only weak transient absorption signal for neat C_{60} films under 550 nm excitation (see Figure C.9).

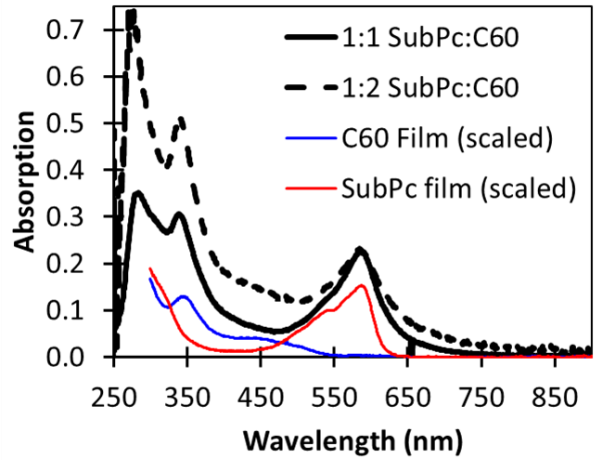

Figure C.3. Absorption spectrum of 1:1 SubPc:C_{60} co-vapor-deposited thin films along with scaled absorption spectra of C_{60} (blue) and SubPc (red) vapor deposited films for comparison.

C.2 ADDITIONAL TRANSIENT ABSORPTION SPECTRA

C.2.1 *SubPc:Polystyrene Films*

Figure C.4 shows the transient absorption spectra in the visible and NIR regions for the SubPc:PS films studied in Chapter 4. We observe minimal transient absorption signal in the NIR region past 800 nm.

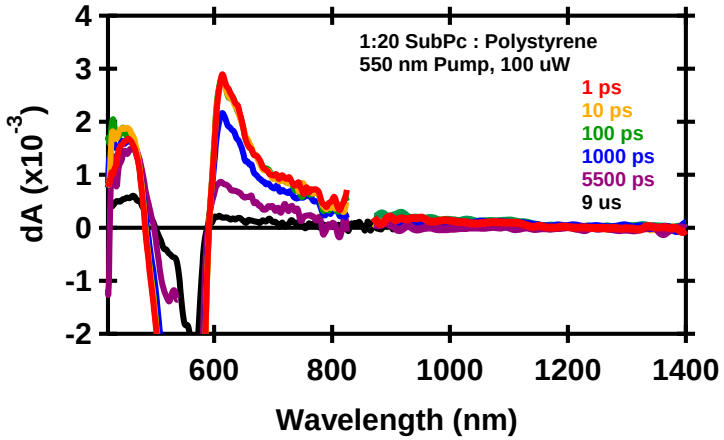

Figure C.4. Transient absorption of SubPc:polystyrene films from 420-1400 nm, showing minimal SubPc signal in the NIR region from 900-1400 nm.

C.2.2 *SubPc:C_{60}:Polystyrene Films*

Figure C.5 shows the normalized transient absorption kinetics at the SubPc bleach position for SubPc:C_{60}:PS films under varying pump fluence. We observe unchanged kinetics for both pump fluences, indicating that the predominant processes in the polystyrene films are monomolecular. This result supports our conclusion that SubPc triplets in the polystyrene blends arise via an energy transfer pathway with intersystem crossing centered on C_{60} rather than from bimolecular recombination through charge-transfer states (which occurs in the vapor-deposited films).

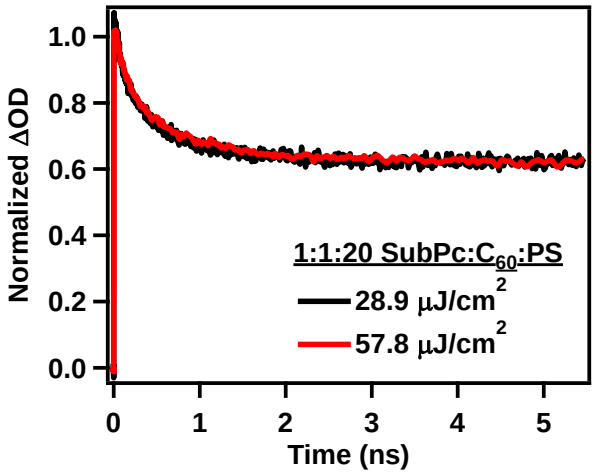

Figure C.5. Normalized transient absorption kinetics at the SubPc ground state bleach for SubPc:C_{60}:PS films at different pump fluences, showing fluence-independent kinetics in the polystyrene films.

Figure C.6 compares the un-normalized transient absorption spectra at 9 μs for dilute polystyrene films of SubPc with and without C_{60} excited at matched absorbed photon flux with a 550 nm pump. The similar transient absorption amplitude and spectral shape that we measure for both films suggests that a similar concentration of long-lived SubPc triplet excitons are generated in both films. Importantly, this is despite ~89% quenching of initially photoexcited SubPc singlets by C_{60} (i.e. a decrease in the photoluminescence quantum yield from 26% in SubPc:PS films to 2.8% in SubPc:C_{60}:PS films). The similar long-lived SubPc triplet transient absorption intensity suggests that SubPc triplets in blends with C_{60} are populated by an additional pathway rather than simply SubPc intersystem crossing, as discussed in Chapter 4.

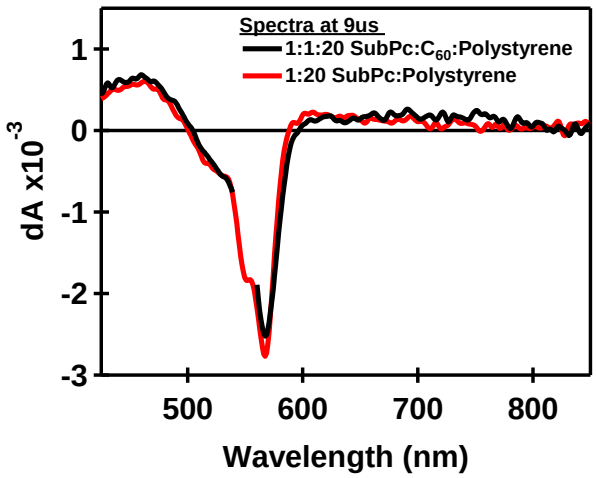

Figure C.6. Transient absorption spectra at 9 μs following 550 nm excitation for SubPc:C_{60}:polystyrene films (black) and SubPc:polystyrene films (red).

Figure C.6 shows a small difference between the long-lived transient absorption spectra for SubPc:PS and SubPc:C_{60}:PS, including slightly higher signal for the SubPc:C_{60}:PS blends near 440 and 750 nm. In Figure C.7, we show that this variation can be accounted for by a small contribution from C_{60} triplet absorption. In Figure C.7, we overlay the 9 μs SubPc:C_{60}:PS spectrum (black trace) with a sum (green dots) of the scaled triplet spectra for SubPc:PS (red) and C_{60}:PS (blue). While the majority of the SubPc:C_{60}:PS spectrum is due to SubPc triplet absorption, there is a small contribution from C_{60} triplets.

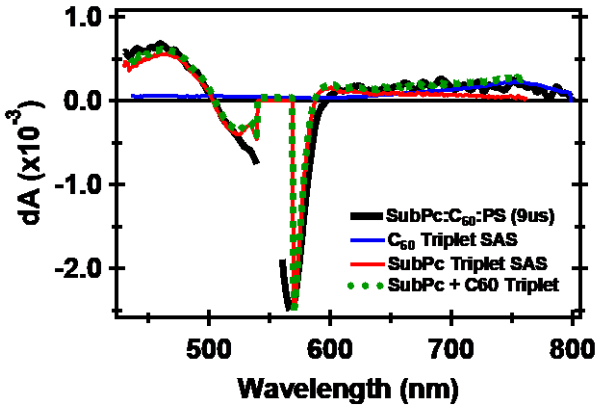

Figure C.7. Reconstruction (green dots) of transient absorption spectrum for SubPc:C_{60}:PS films at 9us (black) obtained by summing fitted spectra for SubPc triplets (red) and C_{60} triplets (blue). SubPc triplet and C_{60} triplet spectra are from SubPc:PS and C_{60}:PS samples, respectively, presented in Sections 4.2.3 and 4.2.4 of Chapter 4.

We note that the contribution from C_{60} triplets in the SubPc:C_{60}:PS triplet-associated spectrum that we present in Chapter 4 is greater than the C_{60} triplet contribution that we observe at 9 μs in Figure C.7. We note that our fitting procedure in Chapter 4 is over the 0 – 5.5 ns time range, suggesting that there is a greater contribution from C_{60} triplets at earlier times (0 – 5.5 ns) compared to later times (9 μs). This likely indicates that C_{60} triplets decay more quickly compared to SubPc triplets. This result is consistent with our proposal of triplet-triplet energy transfer from C_{60} to SubPc. However, the difference in decay rates for the two triplet spectra over the 0 – 5.5 ns time window is not significant enough to distinguish between SubPc and C_{60} spectral shapes in our fitting procedure, resulting in non-separable line shapes in our analysis.

C.2.3 *C_{60}:Polystyrene Films*

Figure C.8 shows transient absorption spectra for C_{60}:PS films under 550 nm photoexcitation at the same incident photon flux that we use for our transient absorption analysis

in Chapter 4 for the SubPc:C_{60}:PS films. We observe a weak induced absorption signal from C_{60} singlet excitons at 980 nm that is approximately half the intensity of the C_{60} singlet signal that we measure in SubPc:C_{60}:PS films (see Figure 4.17 in Chapter 4). This result supports our conclusion that a small amount of C_{60} singlets are photoexcited directly by C_{60} absorption, but that additional C_{60} singlets are populated by energy transfer from SubPc.

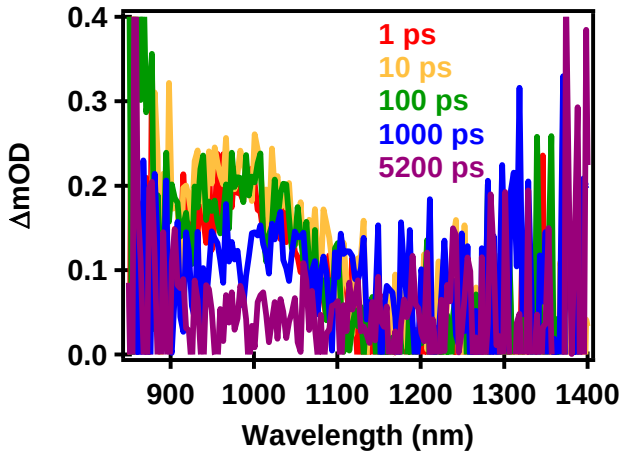

Figure C.8. Transient Absorption spectra for a C_{60}:PS film under 550 nm photoexcitation, showing weak transient absorption signal.

C.2.4 *Vapor-Deposited C_{60} Films*

Figure C.9 shows transient absorption spectra for 35 nm thick vapor-deposited C_{60} films under 550 nm photoexcitation at the same incident photon flux that we use for our transient absorption analysis for SubPc:C_{60} films in Chapter 4. We note that the C_{60}-only films in Figure C.9 contain ~2.7 times more C_{60} material than that used for the 1:1 SubPc:C_{60} films presented in Figure 4.14 of Chapter 4. In Figure C.9, we observe a broad induced absorption from the C_{60} films. Despite the higher C_{60} optical density in the C_{60}-only films measured in Figure C.9, this transient absorption signal is weaker than the C_{60} induced absorption measured in SubPc:C_{60} films (Figure

4.14). This result supports our conclusion that a small amount of C_{60} singlets are photoexcited directly by C_{60} absorption, but that additional C_{60} singlets are populated by energy transfer from SubPc. We note that this singlet-singlet energy transfer from SubPc to C_{60} appears to occur in both the dilute polystyrene films and in the vapor-deposited SubPc:C_{60} films.

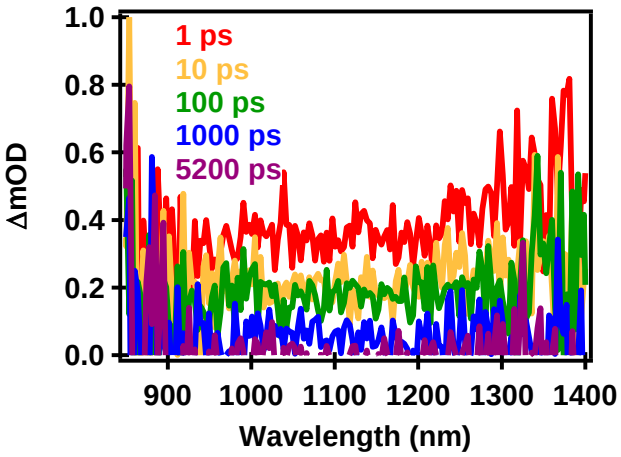

Figure C.9. Transient absorption spectra for a 35 nm thick vapor-deposited C_{60} film under 550 nm photoexcitation, showing weak transient absorption signal.

Figure C.10 shows the transient absorption spectra for vapor-deposited C_{60} films (35 nm thick) under 365 nm photoexcitation. The transient absorption spectrum for aggregated C_{60} films is significantly different from the spectra that we record for films of C_{60} dispersed in polystyrene (Figure 4.8 of Chapter 4). This is consistent with previous studies, where the negative signal around 400-500 nm is attributed to aggregate bleaching and the induced absorption signals have been attributed to a mix of aggregate singlet absorption and electroabsorption.[223, 246, 259]

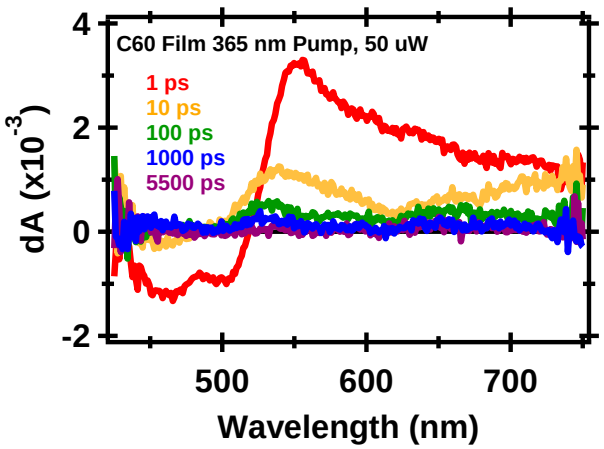

Figure C.10. Transient absorption spectra for a 35 nm thick C_{60} vapor-deposited films under 365 nm photoexcitation

C.2.5 *Vapor-Deposited 1:1 SubPc:C_{60} Films*

In Figure C.11, we present a global target analysis of the transient absorption spectra for 1:1 SubPc:C_{60} films under varying pump fluence, showing that the rise time for SubPc triplets depends on pump fluence, as expected for a bimolecular process. We performed the fluence-dependent studies on thicker (150 nm) SubPc:C_{60} films compared to those presented in Chapter 4 in order to measure a reasonable transient absorption signal at lower absorbed photon densities. Figure C.11a shows a later rise time for the triplet spectral component with decreasing incident photon flux from 28.9 to 5.8 μJ/cm^2. In Figure C.11b, we show that the SubPc triplet spectral component that we extract from our analysis is similar for all pump fluences that we measure, and that the spectral shape matches the triplet component that we present for the thinner films in Figure 4.14 of Chapter 4.

Figure C.11c shows the fast-decay spectral component that relaxes with a ~30 ps time constant, which we attribute to a mix of SubPc singlets and cations. In addition, Figure C.11d shows a component with a similar line shape to Figure C.11c that decays with a slower 0.7-2 ns

lifetime, which we assign to the SubPc cations. We find reasonable agreement of the cation spectral component that we extract for the 150 nm thick SubPc:C_{60} films with the cation component that we extract for the thinner 26 nm SubPc:C_{60} films in the main text, with the exception of a decrease in the 650 nm induced absorption for the 26 nm SubPc:C_{60} films. We speculate that this difference in the spectral line shape could have some contribution from optical interference effects that vary with film thickness and may occur in samples containing multiple layers (such as our epoxy-sealed glass substrates).[241] We test this possibility of a difference in optical interference effects for the epoxy-sealed samples by comparing the normalized ground-state absorption profiles in Figure C.12 for the 26 nm and 150 nm films. Indeed, Figure C.12 shows a difference in the normalized shape of the ground state absorption profiles for the epoxy-sealed SubPc:C_{60} films of different thickness, including a deviation in the 650-750 nm region.

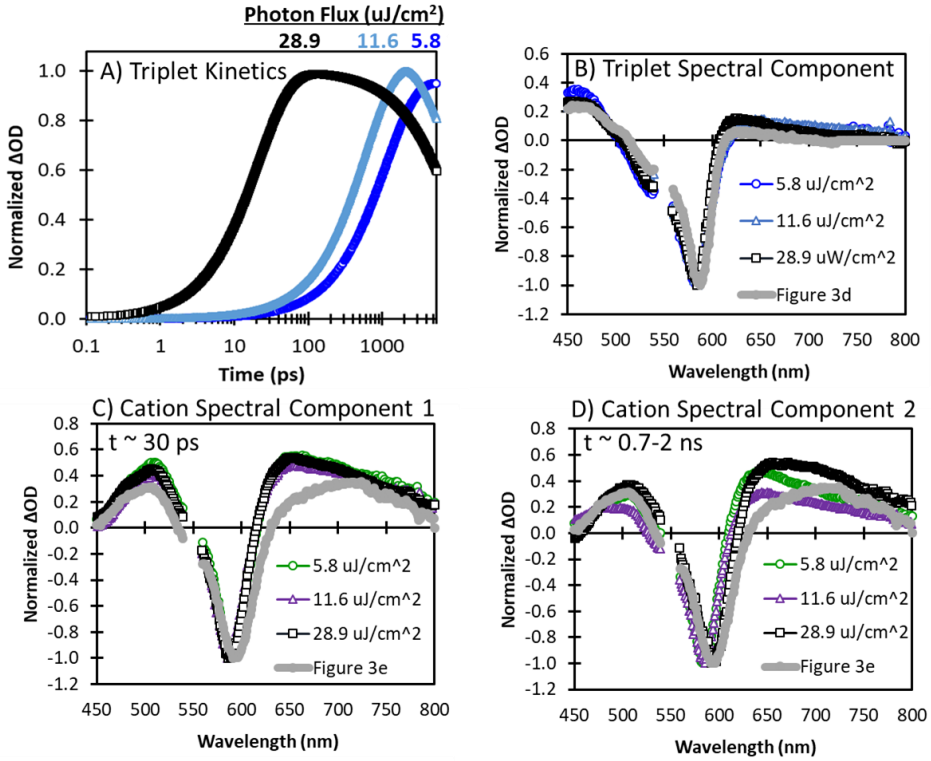

Figure C.11. Global target analysis for 1:1 SubPc:C_{60} vapor deposited films (150 nm thick) under varying pump fluences highlighting a fluence-dependent rise time for SubPc triplets

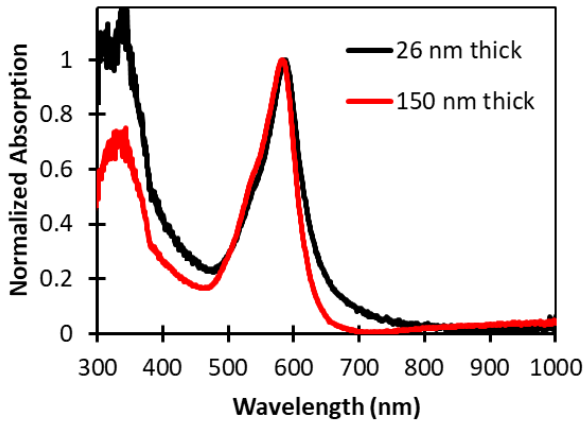

Figure C.12. Normalized absorption spectra of epoxy-sealed samples used for transient absorption measurements of 1:1 SubPc:C_{60} vapor-deposited films of 26 m and 150 nm thickness.

C.2.6 *Vapor-Deposited 1:2 SubPc:C_{60} Films*

Figure C.13 shows the results for our global target analysis of the 1:2 SubPc:C_{60} vapor-deposited films. The triplet and cation spectral shapes in Figure C.13 a are in good agreement with the spectral shapes that we extract for the 1:1 blends. However, the fast decay component (lifetime of 35 ps) has a different spectral shape compared to the fast decay component that we extract for the 1:1 blend in Figure 4.15 of Chapter 4. We attribute the different spectral shape for the fast decay component to greater contribution from C_{60} induced absorption signals in the 1:2 films. The negative signal at 450 nm and positive signal at 540 nm are in good agreement with the spectral shape that we observe for C_{60}-only thin films (Figure C.10). In addition, we attribute the dip near 580 nm to the SubPc ground state bleach.

Figure C.13b shows similar kinetics in the 1:2 film compared to the 1:1 film at matched absorbed photon flux (Figure 4.15 of Chapter 4). The fast decay component has a lifetime of 35 ps, the SubPc cation decays with a lifetime of 0.7 ps, and the SubPc triplet has a lifetime greater than 5 ns.

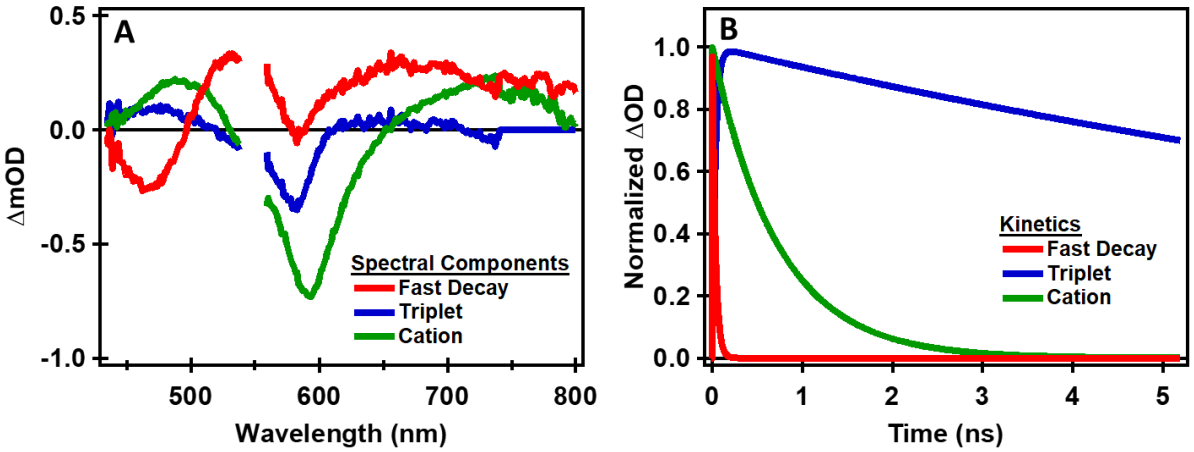

Figure C.13. Global target analysis for transient absorption data of 1:2 SubPc:C_{60} vapor-deposited films including (a) spectral components and (b) kinetics

C.3 ADDITIONAL TIME-RESOLVED PHOTOLUMINESCENCE MEASUREMENTS

Figure C.14 shows the lifetime for SubPc singlet decay measured at the SubPc fluorescence maximum (600-650 nm) in SubPc:PS and SubPc:C_{60}:PS films under 550 nm photoexcitation. The lifetime decreases in films with C_{60}, confirming that C_{60} quenches SubPc singlets.

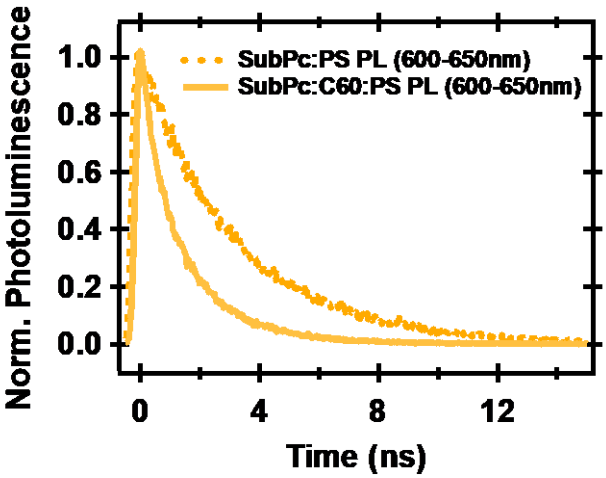

Figure C.14. Comparison of photoluminescence kinetics for SubPc:C_{60}:PS films (solid yellow, τ = 3.14 ns) and SubPc:PS films (dotted yellow τ = 1.34 ns).

REFERENCES

1. Turro, N. J.; Ramamurthy, V.; Scaiano, J. C., *Principles of Molecular Photochemistry*. University Science Books: Sausalita, California, 2009.

2. Nelson, J., *The Physics of Solar Cells*. Imperial College Press: 2003.

3. Levine, I. N., *Quantum Chemistry 6th Ed*. Prentice-Hall Of India Pvt. Limited: 2009.

4. McQuarrie, D. A., *Quantum Chemistry*. University Science Books: 2008.

5. Key World Energy Statistics. International Energy Agency, Ed. Paris, France, 2016.

6. Key World Energy Statistics. International Energy Agency, Ed. Paris, France, 2015.

7. 2014 Key World Energy Statistics. International Energy Agency, Ed. Paris, France, 2014

8. 2013 Key World Energy Statistics. International Energy Agency, Ed. Paris, France, 2013.

9. 2012 Key World Energy Statistics. International Energy Agency, Ed. Paris, France, 2012.

10. International Monetary Fund, Real Gdp Growth, Imf Data Mapper. 2017.

11. Olivier, J. G. J.; Janssens-Maenhout, G.; Muntean, M.; Peters, J. A. H. W., Trends in Global Co2 Emissions: 2016 Report. PBL Netherlands Environmental Assessment Agency European Commission Joint Research Centre, Ed. The Hague, Netherlands, 2016; pp 1-86.

12. International Energy Agency, Iea Finds Co2 Emissions Flat for Third Straight Year Even as Global Economy Grew in 2016. March 17 2017.

13. European Parliament Council of the European Union, Directive 2009/28/Ec of the European Parliament and of the Council of 23 April 2009 on the Promotion of the Use of Energy from Renewable Sources and Amending and Subsequently Repealing Directives 2001/77/Ec and 2003/30/Ec. 2009.

14. Adoption of the Paris Agreement. United Nations Framework Convention on Climate Change, Ed. Paris, France, December 11 2015.

15. Solar Jobs Census - 2016 Economic Impact Analysis. The Solar Foundation, Ed. Washington, DC, 2016.

16. Søndergaard, R.; Hösel, M.; Angmo, D.; Larsen-Olsen, T. T.; Krebs, F. C. Roll-to-Roll Fabrication of Polymer Solar Cells. *Mater. Today* **2012**, *15*, 36-49.

17. Woodhouse, M.; Jones-Albertus, R.; Reldman, D.; Fu, R.; Horowitz, K.; Chung, D.; Jordan, D.; Kurtz, S., On the Path to Sunshot: The Role of Advancements in Solar Photovoltaic Efficiency, Reliability, and Costs. National Renewable Energy Laboratory, Ed. Golden, CO, 2016.

18. Lizin, S.; Van Passel, S.; De Schepper, E.; Maes, W.; Lutsen, L.; Manca, J.; Vanderzande, D. Life Cycle Analyses of Organic Photovoltaics: A Review. *Energy Environ. Sci.* **2013**, *6*, 3136-3149.

19. New Heliatek Solar Energy Facade on Engie's Research Center. http://www.heliatek.com/en/press/press-releases/details/new-heliatek-solar-energy-facade 06/30/2017.

20. Cheng, P.; Zhan, X. Stability of Organic Solar Cells: Challenges and Strategies. *Chem. Soc. Rev.* **2016**, *45*, 2544-2582.

21. Dou, L.; You, J.; Hong, Z.; Xu, Z.; Li, G.; Street, R. A.; Yang, Y. 25th Anniversary Article: A Decade of Organic/Polymeric Photovoltaic Research. *Adv. Mater.* **2013**, *25*, 6642-6671.

22. Yao, H.; Ye, L.; Zhang, H.; Li, S.; Zhang, S.; Hou, J. Molecular Design of Benzodithiophene-Based Organic Photovoltaic Materials. *Chem. Rev.* **2016**, *116*, 7397-7457.

23. Lu, L.; Zheng, T.; Wu, Q.; Schneider, A. M.; Zhao, D.; Yu, L. Recent Advances in Bulk Heterojunction Polymer Solar Cells. *Chem. Rev.* **2015**, *115*, 12666-12731.

24. Xiao, X.; Lee, K.; Forrest, S. R. Scalability of Multi-Junction Organic Solar Cells for Large Area Organic Solar Modules. *Applied Physics Letters* **2015**, *106*.

25. Tang, C. W. Two-Layer Organic Photovoltaic Cell. *Applied Physics Letters* **1986**, *48*, 183-185.

26. de Jong, M. P.; van IJzendoorn, L. J.; de Voigt, M. J. A. Stability of the Interface between Indium-Tin-Oxide and Poly(3,4-Ethylenedioxythiophene)/Poly(Styrenesulfonate) in Polymer Light-Emitting Diodes. *Applied Physics Letters* **2000**, *77*, 2255-2257.

27. Lock, J. P.; Im, S. G.; Gleason, K. K. Oxidative Chemical Vapor Deposition of Electrically Conducting Poly(3,4-Ethylenedioxythiophene) Films. *Macromolecules* **2006**, *39*, 5326-5329.

28. Taohong, W.; Changbo, C.; Kunping, G.; Guo, C.; Tao, X.; Bin, W. Improved Performance of Polymer Solar Cells by Using Inorganic, Organic, and Doped Cathode Buffer Layers. *Chinese Physics B* **2016**, *25*, 038402.

29. Yin, Z.; Wei, J.; Zheng, Q. Interfacial Materials for Organic Solar Cells: Recent Advances and Perspectives. *Advanced Science* **2016**, *3*, 1500362.

30. Zhou, Y.; Fuentes-Hernandez, C.; Shim, J.; Meyer, J.; Giordano, A. J.; Li, H.; Winget, P.; Papadopoulos, T.; Cheun, H.; Kim, J., et al. A Universal Method to Produce Low–Work Function Electrodes for Organic Electronics. *Science* **2012**, *336*, 327.

31. Shockley, W. The Theory of P-N Junctions in Semiconductors and P-N Junction Transistors. *Bell System Technical Journal* **1949**, *28*, 435-489.

32. Liu, C.; Yi, C.; Wang, K.; Yang, Y.; Bhatta, R. S.; Tsige, M.; Xiao, S.; Gong, X. Single-Junction Polymer Solar Cells with over 10% Efficiency by a Novel Two-Dimensional Donor–Acceptor Conjugated Copolymer. *ACS Appl. Mater. Interfaces* **2015**, *7*, 4928-4935.

33. He, Z.; Xiao, B.; Liu, F.; Wu, H.; Yang, Y.; Xiao, S.; Wang, C.; Russell, T. P.; Cao, Y. Single-Junction Polymer Solar Cells with High Efficiency and Photovoltage. **2015**, *9*, 174.

34. Zhao, J.; Li, Y.; Yang, G.; Jiang, K.; Lin, H.; Ade, H.; Ma, W.; Yan, H. Efficient Organic Solar Cells Processed from Hydrocarbon Solvents. **2016**, *1*, 15027.

35. Liang, C.; Wang, Y.; Li, D.; Ji, X.; Zhang, F.; He, Z. Modeling and Simulation of Bulk Heterojunction Polymer Solar Cells. *Sol. Energy Mater. Sol. Cells* **2014**, *127*, 67-86.

36. Giebink, N. C.; Wiederrecht, G. P.; Wasielewski, M. R.; Forrest, S. R. Ideal Diode Equation for Organic Heterojunctions. I. Derivation and Application. *Phys. Rev. B* **2010**, *82*, 155305.

37. Giebink, N. C.; Lassiter, B. E.; Wiederrecht, G. P.; Wasielewski, M. R.; Forrest, S. R. Ideal Diode Equation for Organic Heterojunctions. II. The Role of Polaron Pair Recombination. *Phys. Rev. B* **2010**, *82*, 155306.

38. Vandewal, K.; Tvingstedt, K.; Gadisa, A.; Inganas, O.; Manca, J. V. Relating the Open-Circuit Voltage to Interface Molecular Properties of Donor:Acceptor Bulk Heterojunction Solar Cells. *Phys. Rev. B* **2010**, *81*, 125204.

39. Lunt, R. R.; Giebink, N. C.; Belak, A. A.; Benziger, J. B.; Forrest, S. R. Exciton Diffusion Lengths of Organic Semiconductor Thin Films Measured by Spectrally Resolved Photoluminescence Quenching. *J. Appl. Phys.* **2009**, *105*, 053711.

40. Tamai, Y.; Ohkita, H.; Benten, H.; Ito, S. Exciton Diffusion in Conjugated Polymers: From Fundamental Understanding to Improvement in Photovoltaic Conversion Efficiency. *J. Phys. Chem. Lett.* **2015**, *6*, 3417-3428.

41. Tvingstedt, K.; Vandewal, K.; Zhang, F. L.; Inganas, O. On the Dissociation Efficiency of Charge Transfer Excitons and Frenkel Excitons in Organic Solar Cells: A Luminescence Quenching Study. *J. Phys. Chem. C* **2010**, *114*, 21824-21832.

42. Li, H.; He, D.; Zhou, Q.; Mao, P.; Cao, J.; Ding, L.; Wang, J. Temperature-Dependent Schottky Barrier in High-Performance Organic Solar Cells. **2017**, *7*, 40134.

43. Dibb, G. F. A.; Muth, M. A.; Kirchartz, T.; Engmann, S.; Hoppe, H.; Gobsch, G.; Thelakkat, M.; Blouin, N.; Tierney, S.; Carrasco-Orozco, M., et al. Influence of Doping on Charge Carrier Collection in Normal and Inverted Geometry Polymer: Fullerene Solar Cells. *Sci. Rep.* **2013**, *3*, 3335.

44. Koster, L. J. A.; Smits, E. C. P.; Mihailetchi, V. D.; Blom, P. W. M. Device Model for the Operation of Polymer/Fullerene Bulk Heterojunction Solar Cells. *Phys. Rev. B* **2005**, *72*, 085205.

45. Trukhanov, V. A.; Bruevich, V. V.; Paraschuk, D. Y. Effect of Doping on Performance of Organic Solar Cells. *Phys. Rev. B* **2011**, *84*, 205318.

46. Reference Solar Spectral Irradiance: Air Mass 1.5. http://rredc.nrel.gov/solar/spectra/am1.5/ (accessed 10/04/2017).

47. Cook, S.; Ohkita, H.; Kim, Y.; Benson-Smith, J. J.; Bradley, D. D. C.; Durrant, J. R. A Photophysical Study of PCBM Thin Films. *Chem. Phys. Lett.* **2007**, *445*, 276-280.

48. Kazaoui, S.; Minami, N.; Tanabe, Y.; Byrne, H.; Eilmes, A.; Petelenz, P. Comprehensive Analysis of Intermolecular Charge Transfer Excited States in C60 and C70 Films. *Phys. Rev. B* **1998**, *58*, 7689-7700.

49. Kobayashi, N.; Ishizaki, T.; Ishii, K.; Konami, H. Synthesis, Spectroscopy, and Molecular Orbital Calculations of Subazaporphyrins, Subphthalocyanines, Subnaphthalocyanines, and Compounds Derived Therefrom by Ring Expansion1. *J. Am. Chem. Soc.* **1999**, *121*, 9096-9110.

50. Foster, M. E.; Zhang, B. A.; Murtagh, D.; Liu, Y.; Sfeir, M. Y.; Wong, B. M.; Azoulay, J. D. Solution-Processable Donor–Acceptor Polymers with Modular Electronic Properties and Very Narrow Bandgaps. *Macromol. Rapid Commun.* **2014**, *35*, 1516-1521.

51. Steckler, T. T.; Henriksson, P.; Mollinger, S.; Lundin, A.; Salleo, A.; Andersson, M. R. Very Low Band Gap Thiadiazoloquinoxaline Donor–Acceptor Polymers as Multi-Tool Conjugated Polymers. *J. Am. Chem. Soc.* **2014**, *136*, 1190-1193.

52. Oosterhout, S. D.; Kopidakis, N.; Owczarczyk, Z. R.; Braunecker, W. A.; Larsen, R. E.; Ratcliff, E. L.; Olson, D. C. Integrating Theory, Synthesis, Spectroscopy and Device Efficiency to Design and Characterize Donor Materials for Organic Photovoltaics: A Case Study Including 12 Donors. *J. Mat. Chem. A* **2015**, *3*, 9777-9788.

53. Gibson, G. L.; McCormick, T. M.; Seferos, D. S. Atomistic Band Gap Engineering in Donor–Acceptor Polymers. *J. Am. Chem. Soc.* **2012**, *134*, 539-547.

54. Casey, A.; Dimitrov, S. D.; Shakya-Tuladhar, P.; Fei, Z.; Nguyen, M.; Han, Y.; Anthopoulos, T. D.; Durrant, J. R.; Heeney, M. Effect of Systematically Tuning Conjugated Donor Polymer Lowest Unoccupied Molecular Orbital Levels Via Cyano Substitution on Organic Photovoltaic Device Performance. *Chem. Mater.* **2016**, *28*, 5110-5120.

55. London, A. E.; Huang, L.; Zhang, B. A.; Oviedo, M. B.; Tropp, J.; Yao, W.; Wu, Z.; Wong, B. M.; Ng, T. N.; Azoulay, J. D. Donor-Acceptor Polymers with Tunable Infrared Photoresponse. *Polym. Chem.* **2017**, *8*, 2922-2930.

56. Street, R. A.; Khlyabich, P. P.; Rudenko, A. E.; Thompson, B. C. Electronic States in Dilute Ternary Blend Organic Bulk Heterojunction Solar Cells. *J. Phys. Chem. C* **2014**, *118*, 26569-26576.

57. Banerji, N. Sub-Picosecond Delocalization in the Excited State of Conjugated Homopolymers and Donor-Acceptor Copolymers. *Journal of Materials Chemistry C* **2013**, *1*, 3052-3066.

58. Hilczer, M.; Tachiya, M. Unified Theory of Geminate and Bulk Electron−Hole Recombination in Organic Solar Cells. *J. Phys. Chem. C* **2010**, *114*, 6808-6813.

59. Djurovich, P. I.; Mayo, E. I.; Forrest, S. R.; Thompson, M. E. Measurement of the Lowest Unoccupied Molecular Orbital Energies of Molecular Organic Semiconductors. *Org. Electron.* **2009**, *10*, 515-520.

60. Franck, J.; Dymond, E. G. Elementary Processes of Photochemical Reactions. *Transactions of the Faraday Society* **1926**, *21*, 536-542.

61. Condon, E. A Theory of Intensity Distribution in Band Systems. *Physical Review* **1926**, *28*, 1182-1201.

62. Smith, M. B.; Michl, J. Singlet Fission. *Chem. Rev.* **2010**, *110*, 6891-6936.

63. Busby, E.; Xia, J.; Wu, Q.; Low, J. Z.; Song, R.; Miller, J. R.; Zhu, X. Y.; Campos, Luis M.; Sfeir, M. Y. A Design Strategy for Intramolecular Singlet Fission Mediated by Charge-Transfer States In donor-Acceptor Organic Materials. *Nat. Mater.* **2015**, *14*, 426-433.

64. Weaver, M. S.; Kwong, R. C.; Adamovich, V. A.; Hack, M.; Brown, J. J. Recent Advances in Phosphorescent Oleds for Small- and Large-Area-Display Sizes. *Journal of the Society for Information Display* **2006**, *14*, 449-452.

65. Chen, T.; Zheng, L.; Yuan, J.; An, Z. F.; Chen, R. F.; Tao, Y.; Li, H. H.; Xie, X. J.; Huang, W. Understanding the Control of Singlet-Triplet Splitting for Organic Exciton Manipulating: A Combined Theoretical and Experimental Approach. *Sci. Rep.* **2015**, *5*, 10923.

66. Kohler, A.; Beljonne, D. The Singlet-Triplet Exchange Energy in Conjugated Polymers. *Adv. Funct. Mater.* **2004**, *14*, 11-18.

67. Pandey, A. K. Highly Efficient Spin-Conversion Effect Leading to Energy Up-Converted Electroluminescence in Singlet Fission Photovoltaics. *Sci. Rep.* **2015**, *5*, 7787

68. Chang, W.; Congreve, D. N.; Hontz, E.; Bahlke, M. E.; McMahon, D. P.; Reineke, S.; Wu, T. C.; Bulovic, V.; Van Voorhis, T.; Baldo, M. A. Spin-Dependent Charge Transfer State Design Rules in Organic Photovoltaics. *Nat. Commun.* **2015**, *6*, 6415.

69. Ohkita, H.; Cook, S.; Astuti, Y.; Duffy, W.; Heeney, M.; Tierney, S.; McCulloch, I.; Bradley, D. D. C.; Durrant, J. R. Radical Ion Pair Mediated Triplet Formation in Polymer-Fullerene Blend Films. *Chem. Commum.* **2006**, *0*, 3939-3941.

70. Köhler, A.; Bässler, H. Triplet States in Organic Semiconductors. *Materials Science and Engineering: R: Reports* **2009**, *66*, 71-109.

71. Dimitrov, D. S.; Schroeder, C. B.; Nielsen, B. C.; Bronstein, H.; Fei, Z.; McCulloch, I.; Heeney, M.; Durrant, R. J. Singlet Exciton Lifetimes in Conjugated Polymer Films for Organic Solar Cells. *Polymers* **2016**, *8*, 14.

72. Reineke, S.; Baldo, M. A. Room Temperature Triplet State Spectroscopy of Organic Semiconductors. **2014**, *4*, 3797.

73. Burke, T. M.; Sweetnam, S.; Vandewal, K.; McGehee, M. D. Beyond Langevin Recombination: How Equilibrium between Free Carriers and Charge Transfer States Determines the Open-Circuit Voltage of Organic Solar Cells. *Adv. Energy Mater.* **2015**, *5*, 1500123.

74. Vandewal, K.; Tvingstedt, K.; Gadisa, A.; Inganas, O.; Manca, J. V. On the Origin of the Open-Circuit Voltage of Polymer-Fullerene Solar Cells. *Nat Mater* **2009**, *8*, 904-909.

75. Sulas, D. B.; Yao, K.; Intemann, J. J.; Williams, S. T.; Li, C. Z.; Chueh, C. C.; Richards, J. J.; Xi, Y. Y.; Pozzo, L. D.; Schlenker, C. W., et al. Open-Circuit Voltage Losses in Selenium-Substituted Organic Photovoltaic Devices from Increased Density of Charge-Transfer States. *Chem. Mater.* **2015**, *27*, 6583-6591.

76. Leblebici, S.; Lee, J.; Weber-Bargioni, A.; Ma, B. Dielectric Screening to Reduce Charge Transfer State Binding Energy in Organic Bulk Heterojunction Photovoltaics. *J. Phys. Chem. C* **2017**, *121*, 3279-3285.

77. Liu, X.; Ding, K.; Panda, A.; Forrest, S. R. Charge Transfer States in Dilute Donor–Acceptor Blend Organic Heterojunctions. *ACS Nano* **2016**, *10*, 7619-7626.

78. Vandewal, K.; Albrecht, S.; Hoke, E. T.; Graham, K. R.; Widmer, J.; Douglas, J. D.; Schubert, M.; Mateker, W. R.; Bloking, J. T.; Burkhard, G. F., et al. Efficient Charge Generation by Relaxed Charge-Transfer States at Organic Interfaces. *Nature Materials* **2014**, *13*, 63-68.

79. Bakulin, A. A.; Rao, A.; Pavelyev, V. G.; van Loosdrecht, P. H. M.; Pshenichnikov, M. S.; Niedzialek, D.; Cornil, J.; Beljonne, D.; Friend, R. H. The Role of Driving Energy and Delocalized States for Charge Separation in Organic Semiconductors. *Science* **2012**, *335*, 1340-1344.

80. Rao, A.; Chow, P. C. Y.; Gelinas, S.; Schlenker, C. W.; Li, C. Z.; Yip, H. L.; Jen, A. K. Y.; Ginger, D. S.; Friend, R. H. The Role of Spin in the Kinetic Control of Recombination in Organic Photovoltaics. *Nature* **2013**, *500*, 435-439.

81. Tvingstedt, K.; Vandewal, K.; Gadisa, A.; Zhang, F. L.; Manca, J.; Inganas, O. Electroluminescence from Charge Transfer States in Polymer Solar Cells. *J. Am. Chem. Soc.* **2009**, *131*, 11819-11824.

82. Vandewal, K.; Widmer, J.; Heumueller, T.; Brabec, C. J.; McGehee, M. D.; Leo, K.; Riede, M.; Salleo, A. Increased Open-Circuit Voltage of Organic Solar Cells by Reduced Donor-Acceptor Interface Area. *Adv Mater* **2014**, *26*, 3839-43.

83. Graham, K. R.; Erwin, P.; Nordlund, D.; Vandewal, K.; Li, R. P.; Ndjawa, G. O. N.; Hoke, E. T.; Salleo, A.; Thompson, M. E.; McGehee, M. D., et al. Re-Evaluating the Role of Sterics and Electronic Coupling in Determining the Open-Circuit Voltage of Organic Solar Cells. *Adv Mater* **2013**, *25*, 6076-6082.

84. Ripolles-Sanchis, T.; Raga, S. R.; Guerrero, A.; Welker, M.; Turbiez, M.; Bisquert, J.; Garcia-Belmonte, G. Molecular Electronic Coupling Controls Charge Recombination Kinetics in Organic Solar Cells of Low Bandgap Diketopyrrolopyrrole, Carbazole, and Thiophene Polymers. *J Phys Chem C* **2013**, *117*, 8719-8726.

85. Jarzab, D.; Cordella, F.; Gao, J.; Scharber, M.; Egelhaaf, H. J.; Loi, M. A. Low-Temperature Behaviour of Charge Transfer Excitons in Narrow-Bandgap Polymer-Based Bulk Heterojunctions. *Advanced Energy Materials* **2011**, *1*, 604-609.

86. Bernardo, B.; Cheyns, D.; Verreet, B.; Schaller, R. D.; Rand, B. P.; Giebink, N. C. Delocalization and Dielectric Screening of Charge Transfer States in Organic Photovoltaic Cells. *Nat. Commun.* **2014**, *5*, 3245.

87. Hoke, E. T.; Vandewal, K.; Bartelt, J. A.; Mateker, W. R.; Douglas, J. D.; Noriega, R.; Graham, K. R.; Frechet, J. M. J.; Salleo, A.; McGehee, M. D. Recombination in Polymer:Fullerene Solar Cells with Open-Circuit Voltages Approaching and Exceeding 1.0 V. *Adv. Energy Mater.* **2013**, *3*, 220-230.

88. Marsh, R. A.; Hodgkiss, J. M.; Friend, R. H. Direct Measurement of Electric Field-Assisted Charge Separation in Polymer: Fullerene Photovoltaic Diodes. *Advanced Materials* **2010**, *22,* 3672-+.

89. Chen, X. K.; Wang, T. H.; Bredas, J. L. Suppressing Energy Loss Due to Triplet Exciton Formation in Organic Solar Cells: The Role of Chemical Structures and Molecular Packing. *Adv. Energy Mater.* **2017**, *7,* 1602713.

90. Chen, P.; Peng, Q.; Yao, L.; Gao, N.; Li, F. Identifying the Efficient Inter-Conversion between Singlet and Triplet Charge-Transfer States by Magneto-Electroluminescence Study. *Applied Physics Letters* **2013**, *102,* 063301.

91. Armin, A.; Durrant, J. R.; Shoaee, S. Interplay between Triplet-, Singlet-Charge Transfer States and Free Charge Carriers Defining Bimolecular Recombination Rate Constant of Organic Solar Cells. *J. Phys. Chem. C* **2017**, *121,* 13969-13976.

92. Dimitrov, S. D.; Wheeler, S.; Niedzialek, D.; Schroeder, B. C.; Utzat, H.; Frost, J. M.; Yao, J. Z.; Gillett, A.; Tuladhar, P. S.; McCulloch, I., et al. Polaron Pair Mediated Triplet Generation in Polymer/Fullerene Blends. *Nat. Commun.* **2015**, *6,* 6501.

93. Schlenker, C. W.; Chen, K. S.; Yip, H. L.; Li, C. Z.; Bradshaw, L. R.; Ochsenbein, S. T.; Ding, F. Z.; Li, X. S. S.; Gamelin, D. R.; Jen, A. K. Y., et al. Polymer Triplet Energy Levels Need Not Limit Photocurrent Collection in Organic Solar Cells. *J. Am. Chem. Soc.* **2012**, *134,* 19661-19668.

94. Menke, S. M.; Ran, N. A.; Bazan, G. C.; Friend, R. H. Understanding Energy Loss in Organic Solar Cells: Toward a New Efficiency Regime. *Joule* **2017**.

95. Zhang, J.; Jakowetz, A. C.; Li, G.; Di, D.; Menke, S. M.; Rao, A.; Friend, R. H.; Bakulin, A. A. On the Energetics of Bound Charge-Transfer States in Organic Photovoltaics. *J. Mat. Chem. A* **2017**, *5*, 11949-11959.

96. Menke, S. M.; Sadhanala, A.; Nikolka, M.; Ran, N. A.; Ravva, M. K.; Abdel-Azeim, S.; Stern, H. L.; Wang, M.; Sirringhaus, H.; Nguyen, T. Q., et al. Limits for Recombination in a Low Energy Loss Organic Heterojunction. *Acs Nano* **2016**, *10*, 10736-10744.

97. Hood, S. N.; Kassal, I. Entropy and Disorder Enable Charge Separation in Organic Solar Cells. *J. Phys. Chem. Lett.* **2016**, *7*, 4495-4500.

98. Muntwiler, M.; Yang, Q.; Tisdale, W. A.; Zhu, X. Y. Coulomb Barrier for Charge Separation at an Organic Semiconductor Interface. *Phys. Rev. Lett.* **2008**, *101*, 196403.

99. Clarke, T. M.; Durrant, J. R. Charge Photogeneration in Organic Solar Cells. *Chem. Rev.* **2010**, *110*, 6736-6767.

100. Niedzialek, D.; Duchemin, I.; de Queiroz, T. B.; Osella, S.; Rao, A.; Friend, R.; Blase, X.; Kümmel, S.; Beljonne, D. First Principles Calculations of Charge Transfer Excitations in Polymer–Fullerene Complexes: Influence of Excess Energy. *Adv. Funct. Mater.* **2015**, *25*, 1972-1984.

101. Park, S. H.; Roy, A.; Beaupré, S.; Cho, S.; Coates, N.; Moon, J. S.; Moses, D.; Leclerc, M.; Lee, K.; Heeger, A. J. Bulk Heterojunction Solar Cells with Internal Quantum Efficiency Approaching 100%. **2009**, *3*, 297.

102. Gelinas, S.; Rao, A.; Kumar, A.; Smith, S. L.; Chin, A. W.; Clark, J.; van der Poll, T. S.; Bazan, G. C.; Friend, R. H. Ultrafast Long-Range Charge Separation in Organic Semiconductor Photovoltaic Diodes. *Science* **2014**, *343*, 512-516.

103. Causa, M.; De Jonghe-Risse, J.; Scarongella, M.; Brauer, J. C.; Buchaca-Domingo, E.; Moser, J. E.; Stingelin, N.; Banerji, N. The Fate of Electron-Hole Pairs in Polymer:Fullerene Blends for Organic Photovoltaics. *Nat. Commun.* **2016**, *7*, 12556.

104. Wilcox, D. E.; Lee, M. H.; Sykes, M. E.; Niedringhaus, A.; Geva, E.; Dunietz, B. D.; Shtein, M.; Ogilvie, J. P. Ultrafast Charge-Transfer Dynamics at the Boron Subphthalocyanine Chloride/C-60 Heterojunction: Comparison between Experiment and Theory. *J. Phys. Chem. Lett.* **2015**, *6*, 569-575.

105. Few, S.; Frost, J. M.; Nelson, J. Models of Charge Pair Generation in Organic Solar Cells. *Phys. Chem. Chem. Phys.* **2015**, *17*, 2311-2325.

106. Kaake, L. G.; Barbara, P. F.; Zhu, X. Y. Intrinsic Charge Trapping in Organic and Polymeric Semiconductors: A Physical Chemistry Perspective. *J. Phys. Chem. Lett.* **2010**, *1*, 628-635.

107. Athanasopoulos, S.; Tscheuschner, S.; Bässler, H.; Köhler, A. Efficient Charge Separation of Cold Charge-Transfer States in Organic Solar Cells through Incoherent Hopping. *J. Phys. Chem. Lett.* **2017**, *8*, 2093-2098.

108. Chow, P. C. Y.; Gelinas, S.; Rao, A.; Friend, R. H. Quantitative Bimolecular Recombination in Organic Photovoltaics through Triplet Exciton Formation. *J. Am. Chem. Soc.* **2014**, *136*, 3424-3429.

109. Wang, Y. F.; Sahin-Tiras, K.; Harmon, N. J.; Wohlgenannt, M.; Flatte, M. E. Immense Magnetic Response of Exciplex Light Emission Due to Correlated Spin-Charge Dynamics. *Phys Rev X* **2016**, *6*.

110. Bittner, E. R.; Lankevich, V.; Gelinas, S.; Rao, A.; Ginger, D. A.; Friend, R. H. How Disorder Controls the Kinetics of Triplet Charge Recombination in Semiconducting Organic Polymer Photovoltaics. *Phys. Chem. Chem. Phys.* **2014**, *16*, 20321-20328.

111. Difley, S.; Beljonne, D.; Van Voorhis, T. On the Singlet−Triplet Splitting of Geminate Electron−Hole Pairs in Organic Semiconductors. *J. Am. Chem. Soc.* **2008**, *130*, 3420-3427.

112. Brédas, J. L.; Scott, J. C.; Yakushi, K.; Street, G. B. Polarons and Bipolarons in Polypyrrole: Evolution of the Band Structure and Optical Spectrum Upon Doping. *Phys. Rev. B* **1984**, *30*, 1023-1025.

113. Di Nuzzo, D.; Aguirre, A.; Shahid, M.; Gevaerts, V. S.; Meskers, S. C. J.; Janssen, R. A. J. Improved Film Morphology Reduces Charge Carrier Recombination into the Triplet Excited State in a Small Bandgap Polymer-Fullerene Photovoltaic Cell. *Adv. Mater.* **2010**, *22*, 4321-+.

114. Tautz, R.; Da Como, E.; Limmer, T.; Feldmann, J.; Egelhaaf, H.-J.; von Hauff, E.; Lemaur, V.; Beljonne, D.; Yilmaz, S.; Dumsch, I., et al. Structural Correlations in the Generation of Polaron Pairs in Low-Bandgap Polymers for Photovoltaics. *Nat Commun* **2012**, *3*, 970.

115. He, X.; Zhu, G.; Yang, J.; Chang, H.; Meng, Q.; Zhao, H.; Zhou, X.; Yue, S.; Wang, Z.; Shi, J., et al. Photogenerated Intrinsic Free Carriers in Small-Molecule Organic Semiconductors Visualized by Ultrafast Spectroscopy. *Sci. Rep.* **2015**, *5*, 17076.

116. Bredas, J. L.; Street, G. B. Polarons, Bipolarons, and Solitons in Conducting Polymers. *Acc. Chem. Res.* **1985**, *18*, 309-315.

117. Beljonne, D.; Cornil, J.; Sirringhaus, H.; Brown, P. J.; Shkunov, M.; Friend, R. H.; Bredas, J. L. Optical Signature of Delocalized Polarons in Conjugated Polymers. *Adv. Funct. Mater.* **2001**, *11*, 229-234.

118. Zojer, E.; Cornil, J.; Leising, G.; Bredas, J. L. Theoretical Investigation of the Geometric and Optical Properties of Neutral and Charged Oligophenylenes. *Phys. Rev. B* **1999**, *59,* 7957-7968.

119. Salaneck, W. R.; Friend, R. H.; Brédas, J. L. Electronic Structure of Conjugated Polymers: Consequences of Electron–Lattice Coupling. *Physics Reports* **1999**, *319,* 231-251.

120. Salem, L., *The Molecular Orbital Theory of Conjugated Systems*. W. A. Benjamin, Inc.: Reading, MA, 1974.

121. Khatib, O.; Mueller, A. S.; Stinson, H. T.; Yuen, J. D.; Heeger, A. J.; Basov, D. N. Electron and Hole Polaron Accumulation in Low-Bandgap Ambipolar Donor-Acceptor Polymer Transistors Imaged by Infrared Microscopy. *Phys. Rev. B* **2014**, *90*.

122. Sandanayaka, A. S. D.; Yoshida, K.; Matsushima, T.; Adachi, C. Exciton Quenching Behavior of Thermally Activated Delayed Fluorescence Molecules by Charge Carriers. *J. Phys. Chem. C* **2015**, *119,* 7631-7636.

123. Xu, H.; Jiang, Y.; Li, J.; Ong, B. S.; Shuai, Z.; Xu, J.; Zhao, N. Spectroscopic Study of Electron and Hole Polarons in a High-Mobility Donor–Acceptor Conjugated Copolymer. *J. Phys. Chem. C* **2013**, *117,* 6835-6841.

124. Fishchuk, I. I.; Kadashchuk, A.; Hoffmann, S. T.; Athanasopoulos, S.; Genoe, J.; Bässler, H.; Köhler, A. Unified Description for Hopping Transport in Organic Semiconductors Including Both Energetic Disorder and Polaronic Contributions. *Phys. Rev. B* **2013**, *88,* 125202.

125. He, Z. C.; Zhong, C. M.; Su, S. J.; Xu, M.; Wu, H. B.; Cao, Y. Enhanced Power-Conversion Efficiency in Polymer Solar Cells Using an Inverted Device Structure. *Nat Photonics* **2012**, *6,* 591-595.

126. Zhang, S. Q.; Ye, L.; Zhao, W. C.; Liu, D. L.; Yao, H. F.; Hou, J. H. Side Chain Selection for Designing Highly Efficient Photovoltaic Polymers with 2d-Conjugated Structure. *Macromolecules* **2014**, *47*, 4653-4659.

127. Ye, L.; Zhang, S. Q.; Zhao, W. C.; Yao, H. F.; Hou, J. H. Highly Efficient 2d-Conjugated Benzodithiophene-Based Photovoltaic Polymer with Linear Alkylthio Side Chain. *Chem Mater* **2014**, *26*, 3603-3605.

128. You, J. B.; Dou, L. T.; Yoshimura, K.; Kato, T.; Ohya, K.; Moriarty, T.; Emery, K.; Chen, C. C.; Gao, J.; Li, G., et al. A Polymer Tandem Solar Cell with 10.6% Power Conversion Efficiency. *Nat. Commun.* **2013**, *4*, 1446.

129. Giebink, N. C.; Wiederrecht, G. P.; Wasielewski, M. R.; Forrest, S. R. Thermodynamic Efficiency Limit of Excitonic Solar Cells. *Phys Rev B* **2011**, *83*, 195326.

130. Scharber, M. C.; Sariciftci, N. S. Efficiency of Bulk-Heterojunction Organic Solar Cells. *Prog Polym Sci* **2013**, *38*, 1929-1940.

131. Servaites, J. D.; Ratner, M. A.; Marksb, T. J. Practical Efficiency Limits in Organic Photovoltaic Cells: Functional Dependence of Fill Factor and External Quantum Efficiency. *Appl Phys Lett* **2009**, *95*, 163302.

132. Zhang, G. Y.; Huber, R. C.; Ferreira, A. S.; Boyd, S. D.; Luscombe, C. K.; Tolbert, S. H.; Schwartz, B. J. Crystallinity Effects in Sequentially Processed and Blend-Cast Bulk-Heterojunction Polymer/Fullerene Photovoltaics. *J Phys Chem C* **2014**, *118*, 18424-18435.

133. Hedley, G. J.; Ward, A. J.; Alekseev, A.; Howells, C. T.; Martins, E. R.; Serrano, L. A.; Cooke, G.; Ruseckas, A.; Samuel, I. D. W. Determining the Optimum Morphology in High-Performance Polymer-Fullerene Organic Photovoltaic Cells. *Nat Commun* **2013**, *4*, 2867.

134. Yang, B.; Yuan, Y. B.; Huang, J. S. Reduced Bimolecular Charge Recombination Loss in Thermally Annealed Bilayer Heterojunction Photovoltaic Devices with Large External Quantum Efficiency and Fill Factor. *J Phys Chem C* **2014**, *118,* 5196-5202.

135. Knesting, K. M.; Ju, H. X.; Schlenker, C. W.; Giordano, A. J.; Garcia, A.; Smith, O. L.; Olson, D. C.; Marder, S. R.; Ginger, D. S. Ito Interface Modifiers Can Improve V-Oc in Polymer Solar Cells and Suppress Surface Recombination. *J Phys Chem Lett* **2013**, *4,* 4038-4044.

136. Shao, G.; Glaz, M. S.; Ma, F.; Ju, H.; Ginger, D. S. Intensity-Modulated Scanning Kelvin Probe Microscopy for Probing Recombination in Organic Photovoltaics. *ACS nano* **2014**, *8,* 10799-807.

137. Chen, L. M.; Xu, Z.; Hong, Z. R.; Yang, Y. Interface Investigation and Engineering - Achieving High Performance Polymer Photovoltaic Devices (Vol 20, Pg 2575, 2010). *J Mater Chem* **2010**, *20,* 10947-10947.

138. Vandewal, K.; Tvingstedt, K.; Inganas, O. Polarization Anisotropy of Charge Transfer Absorption and Emission of Aligned Polymer: Fullerene Blend Films. *Phys Rev B* **2012**, *86,* 035212.

139. Deibel, C.; Strobel, T.; Dyakonov, V. Role of the Charge Transfer State in Organic Donor-Acceptor Solar Cells. *Adv Mater* **2010**, *22,* 4097-4111.

140. Provencher, F.; Berube, N.; Parker, A. W.; Greetham, G. M.; Towrie, M.; Hellmann, C.; Cote, M.; Stingelin, N.; Silva, C.; Hayes, S. C. Direct Observation of Ultrafast Long-Range Charge Separation at Polymer-Fullerene Heterojunctions. *Nat Commun* **2014**, *5,* 4288.

141. Lee, J.; Vandewal, K.; Yost, S. R.; Bahlke, M. E.; Goris, L.; Baldo, M. A.; Manca, J. V.; Van Voorhis, T. Charge Transfer State Versus Hot Exciton Dissociation in Polymer-Fullerene Blended Solar Cells. *J. Am. Chem. Soc.* **2010**, *132,* 11878-11880.

142. Piersimoni, F.; Chambon, S.; Vandewal, K.; Mens, R.; Boonen, T.; Gadisa, A.; Izquierdo, M.; Filippone, S.; Ruttens, B.; D'Haen, J., et al. Influence of Fullerene Ordering on the Energy of the Charge-Transfer State and Open-Circuit Voltage in Polymer:Fullerene Solar Cells. *J Phys Chem C* **2011**, *115*, 10873-10880.

143. Vandewal, K.; Gadisa, A.; Oosterbaan, W. D.; Bertho, S.; Banishoeib, F.; Van Severen, I.; Lutsen, L.; Cleij, T. J.; Vanderzande, D.; Manca, J. V. The Relation between Open-Circuit Voltage and the Onset of Photocurrent Generation by Charge-Transfer Absorption in Polymer: Fullerene Bulk Heterojunction Solar Cells. *Adv Funct Mater* **2008**, *18,* 2064-2070.

144. Perez, M. D.; Borek, C.; Forrest, S. R.; Thompson, M. E. Molecular and Morphological Influences on the Open Circuit Voltages of Organic Photovoltaic Devices. *J Am Chem Soc* **2009**, *131,* 9281-9286.

145. Zhang, Y.; Zou, J. Y.; Yip, H. L.; Chen, K. S.; Zeigler, D. F.; Sun, Y.; Jen, A. K. Y. Indacenodithiophene and Quinoxaline-Based Conjugated Polymers for Highly Efficient Polymer Solar Cells. *Chem. Mater.* **2011**, *23,* 2289-2291.

146. Heeney, M.; Zhang, W.; Crouch, D. J.; Chabinyc, M. L.; Gordeyev, S.; Hamilton, R.; Higgins, S. J.; McCulloch, I.; Skabara, P. J.; Sparrowe, D., et al. Regioregular Poly(3-Hexyl) Selenophene: A Low Band Gap Organic Hole Transporting Polymer. *Chem Commun* **2007**, 5061-5063.

147. Marcus, R. A. Relation between Charge-Transfer Absorption and Fluorescence-Spectra and the Inverted Region. *J Phys Chem-Us* **1989**, *93,* 3078-3086.

148. Gould, I. R.; Noukakis, D.; Gomez-Jahn, L.; Young, R. H.; Goodman, J. L.; Farid, S. Radiative and Nonradiative Electron-Transfer in Contact Radical-Ion Pairs. *Chem Phys* **1993**, *176,* 439-456.

149. Burke, T. M.; Sweetnam, S.; Vandewal, K.; McGehee, M. D. Beyond Langevin Recombination: How Equilibrium between Free Carriers and Charge Transfer States Determines the Open-Circuit Voltage of Organic Solar Cells. *Adv Energy Mater* **2015**, *5*, 1500123.

150. Street, R. A.; Krakaris, A.; Cowan, S. R. Recombination through Different Types of Localized States in Organic Solar Cells. *Adv Funct Mater* **2012**, *22*, 4608-4619.

151. Street, R. A.; Khlyabich, P. P.; Rudenko, A. E.; Thompson, B. C. Electronic States in Dilute Ternary Blend Organic Bulk Heterojunction Solar Cells. *J Phys Chem C* **2014**, *118*, 26569-26576.

152. Blakesley, J. C.; Neher, D. Relationship between Energetic Disorder and Open-Circuit Voltage in Bulk Heterojunction Organic Solar Cells. *Phys Rev B* **2011**, *84*.

153. Lee, C. C.; Su, W. C.; Chang, W. C.; Huang, B. Y.; Liu, S. W. The Effect of Charge Transfer State on Open-Circuit Voltage of Small-Molecular Organic Photovoltaic Devices: A Comparison between the Planar and Bulk Heterojunction Using Electroluminescence Characterization. *Org Electron* **2015**, *16*, 1-8.

154. Sutton, C.; Sears, J. S.; Coropceanu, V.; Bredas, J. L. Understanding the Density Functional Dependence of Dft-Calculated Electronic Couplings in Organic Semiconductors. *J Phys Chem Lett* **2013**, *4*, 919-924.

155. Kawatsu, T.; Coropceanu, V.; Ye, A. J.; Bredas, J. L. Quantum-Chemical Approach to Electronic Coupling: Application to Charge Separation and Charge Recombination Pathways in a Model Molecular Donor-Acceptor System for Organic Solar Cells. *J Phys Chem C* **2008**, *112*, 3429-3433.

156. Liu, T.; Troisi, A. Absolute Rate of Charge Separation and Recombination in a Molecular Model of the P3ht/PCBM Interface. *J Phys Chem C* **2011**, *115*, 2406-2415.

157. Rau, U. Reciprocity Relation between Photovoltaic Quantum Efficiency and Electroluminescent Emission of Solar Cells. *Phys Rev B* **2007**, *76*.

158. Vandewal, K.; Tvingstedt, K.; Gadisa, A.; Inganas, O.; Manca, J. V. Relating the Open-Circuit Voltage to Interface Molecular Properties of Donor:Acceptor Bulk Heterojunction Solar Cells. *Phys Rev B* **2010**, *81*.

159. Loi, M. A.; Toffanin, S.; Muccini, M.; Forster, M.; Scherf, U.; Scharber, M. Charge Transfer Excitons in Bulk Heterojunctions of a Polyfluorene Copolymer and a Fullerene Derivative. *Adv. Funct. Mater.* **2007**, *17*, 2111-2116.

160. Di Nuzzo, D.; Wetzelaer, G. J. A. H.; Bouwer, R. K. M.; Gevaerts, V. S.; Meskers, S. C. J.; Hummelen, J. C.; Blom, P. W. M.; Janssen, R. A. J. Simultaneous Open-Circuit Voltage Enhancement and Short-Circuit Current Loss in Polymer: Fullerene Solar Cells Correlated by Reduced Quantum Efficiency for Photoinduced Electron Transfer. *Adv. Energy Mater.* **2013**, *3*, 85-94.

161. Tedlla, B. Z.; zhu, F.; Cox, M.; Drijkoningen, J.; Manca, J.; Koopmans, B.; Goovaerts, E. Understanding Triplet Formation Pathways in Bulk Heterojunction Polymer:Fullerene Photovoltaic Devices. *Adv Energy Mater* **2014**, *4*, 1401109.

162. Gould, I. R.; Noukakis, D.; Gomezjahn, L.; Young, R. H.; Goodman, J. L.; Farid, S. Radiative and Nonradiative Electron-Transfer in Contact Radical-Ion Pairs. *Chem Phys* **1993**, *176*, 439-456.

163. Gould, I. R.; Young, R. H.; Mueller, L. J.; Albrecht, A. C.; Farid, S. Electronic-Structures of Exciplexes and Excited Charge-Transfer Complexes. *J Am Chem Soc* **1994**, *116*, 8188-8199.

164. Carsten, B.; Szarko, J. M.; Son, H. J.; Wang, W.; Lu, L. Y.; He, F.; Rolczynski, B. S.; Lou, S. J.; Chen, L. X.; Yu, L. P. Examining the Effect of the Dipole Moment on Charge Separation in

Donor-Acceptor Polymers for Organic Photovoltaic Applications. *J. Am. Chem. Soc.* **2011**, *133*, 20468-20475.

165. Mayer, A. C.; Toney, M. F.; Scully, S. R.; Rivnay, J.; Brabec, C. J.; Scharber, M.; Koppe, M.; Heeney, M.; McCulloch, I.; McGehee, M. D. Bimolecular Crystals of Fullerenes in Conjugated Polymers and the Implications of Molecular Mixing for Solar Cells. *Adv. Funct. Mater.* **2009**, *19*, 1173-1179.

166. Kittel, C., Introduction to Solid State Physics. 6 ed.; John Wiley & Sons, Inc.: 1986; pp 127-135.

167. Orapunt, F.; O'Leary, S. K. Optical Transitions and the Mobility Edge in Amorphous Semiconductors: A Joint Density of States Analysis. *J Appl Phys* **2008**, *104*, 073513.

168. Loper, P.; Muller, R.; Hiller, D.; Barthel, T.; Malguth, E.; Janz, S.; Goldschmidt, J. C.; Hermle, M.; Zacharias, M. Quasi-Fermi-Level Splitting in Ideal Silicon Nanocrystal Superlattices. *Phys Rev B* **2011**, *84*, 195317.

169. Jiang, C. W.; Green, M. A. Silicon Quantum Dot Superlattices: Modeling of Energy Bands, Densities of States, and Mobilities for Silicon Tandem Solar Cell Applications. *J Appl Phys* **2006**, *99*, 114902.

170. Miller, N. C.; Cho, E.; Junk, M. J. N.; Gysel, R.; Risko, C.; Kim, D.; Sweetnam, S.; Miller, C. E.; Richter, L. J.; Kline, R. J., et al. Use of X-Ray Diffraction, Molecular Simulations, and Spectroscopy to Determine the Molecular Packing in a Polymer-Fullerene Bimolecular Crystal. *Adv Mater* **2012**, *24*, 6071-+.

171. Scarongella, M.; Paraecattil, A. A.; Buchaca-Domingo, E.; Douglas, J. D.; Beaupre, S.; McCarthy-Ward, T.; Heeney, M.; Moser, J. E.; Leclerc, M.; Frechet, J. M. J., et al. The Influence

of Microstructure on Charge Separation Dynamics in Organic Bulk Heterojunction Materials for Solar Cell Applications. *J Mater Chem A* **2014**, *2*, 6218-6230.

172. Liao, H. C.; Tsao, C. S.; Shao, Y. T.; Chang, S. Y.; Huang, Y. C.; Chuang, C. M.; Lin, T. H.; Chen, C. Y.; Su, C. J.; Jeng, U. S., et al. Bi-Hierarchical Nanostructures of Donor-Acceptor Copolymer and Fullerene for High Efficient Bulk Heterojunction Solar Cells. *Energ Environ Sci* **2013**, *6*, 1938-1948.

173. Intemann, J. J.; Yao, K.; Yip, H. L.; Xu, Y. X.; Li, Y. X.; Liang, P. W.; Ding, F. Z.; Li, X. S.; Jen, A. K. Y. Molecular Weight Effect on the Absorption, Charge Carrier Mobility, and Photovoltaic Performance of an Indacenodiselenophene-Based Ladder-Type Polymer. *Chem Mater* **2013**, *25*, 3188-3195.

174. Luchowski, R.; Szabelski, M.; Sarkar, P.; Apicella, E.; Midde, K.; Raut, S.; Borejdo, J.; Gryczynski, Z.; Gryczynski, I. Fluorescence Instrument Response Standards in Two-Photon Time-Resolved Spectroscopy. *Appl Spectrosc* **2010**, *64*, 918-922.

175. Richards, J. Structural Characterization of Composite Thin-Film and Dispersed Phase Conjugated Polymer/Fullerene Composites. Thesis, University of Washington, Seattle, WA, 2014.

176. Zhang, Q.; Kan, B.; Liu, F.; Long, G. K.; Wan, X. J.; Chen, X. Q.; Zuo, Y.; Ni, W.; Zhang, H. J.; Li, M. M., et al. Small-Molecule Solar Cells with Efficiency over 9%. *Nat. Photonics* **2015**, *9*, 35-41.

177. Veldman, D.; Ipek, O.; Meskers, S. C. J.; Sweelssen, J.; Koetse, M. M.; Veenstra, S. C.; Kroon, J. M.; van Bavel, S. S.; Loos, J.; Janssen, R. A. J. Compositional and Electric Field Dependence of the Dissociation of Charge Transfer Excitons in Alternating Polyfluorene Copolymer/Fullerene Blends. *J. Am. Chem. Soc.* **2008**, *130*, 7721-7735.

178. Marsh, R. A.; McNeill, C. R.; Abrusci, A.; Campbell, A. R.; Friend, R. H. A Unified Description of Current-Voltage Characteristics in Organic and Hybrid Photovoltaics under Low Light Intensity. *Nano Lett.* **2008**, *8*, 1393-1398.

179. Bakulin, A. A.; Xia, Y.; Bakker, H. J.; Inganas, O.; Gao, J. Morphology, Temperature, and Field Dependence of Charge Separation in High-Efficiency Solar Cells Based on Alternating Polyquinoxaline Copolymer. *J. Phys. Chem. C* **2016**, *120*, 4219-4226.

180. Marsh, R. A.; Hodgkiss, J. M.; Friend, R. H. Direct Measurement of Electric Field-Assisted Charge Separation in Polymer:Fullerene Photovoltaic Diodes. *Adv. Mater.* **2010**, *22*, 3672-3676.

181. Kraus, H.; Heiber, M. C.; Vath, S.; Kern, J.; Deibel, C.; Sperlich, A.; Dyakonov, V. Analysis of Triplet Exciton Loss Pathways in PTB7:PC71BM Bulk Heterojunction Solar Cells. *Sci. Rep.* **2016**, *6*, 29158.

182. Wang, J.; Chepelianskii, A.; Gao, F.; Greenham, N. C. Control of Exciton Spin Statistics through Spin Polarization in Organic Optoelectronic Devices. *Nat. Commun.* **2012**, *3*, 1191.

183. Schwarz, K. N.; Geraghty, P. B.; Jones, D. J.; Smith, T. A.; Ghiggino, K. P. Suppressing Subnanosecond Bimolecular Charge Recombination in a High-Performance Organic Photovoltaic Material. *J. Phys. Chem. C* **2016**, *120*, 24002-24010.

184. Väth, S.; Tvingstedt, K.; Baumann, A.; Heiber, M. C.; Sperlich, A.; Love, J. A.; Nguyen, T.-Q.; Dyakonov, V. Triplet Excitons in Highly Efficient Solar Cells Based on the Soluble Small Molecule P-Dts(Fbtth2)2. *Adv. Energy Mater.* **2017**, *7*, 1602016.

185. Chow, P. C. Y.; Albert-Seifried, S.; Gelinas, S.; Friend, R. H. Nanosecond Intersystem Crossing Times in Fullerene Acceptors: Implications for Organic Photovoltaic Diodes. *Adv. Mater.* **2014**, *26*, 4851-4854.

186. O'Malley, K. M.; Li, C. Z.; Yip, H. L.; Jen, A. K. Y. Enhanced Open-Circuit Voltage in High Performance Polymer/Fullerene Bulk-Heterojunction Solar Cells by Cathode Modification with a C60 Surfactant. *Adv. Energy Mater.* **2012**, *2,* 82-86.

187. Etzold, F.; Howard, I. A.; Forler, N.; Melnyk, A.; Andrienko, D.; Hansen, M. R.; Laquai, F. Sub-Ns Triplet State Formation by Non-Geminate Recombination in PSBTBT:PC70BM and PCPDTBT:PC60BM Organic Solar Cells. *Energ Environ Sci* **2015**, *8,* 1511.

188. Burkhard, G. F.; Hoke, E. T.; Beiley, Z. M.; McGehee, M. D. Free Carrier Generation in Fullerene Acceptors and Its Effect on Polymer Photovoltaics. *J. Phys. Chem. C* **2012**, *116,* 26674-26678.

189. Proctor, C. M.; Albrecht, S.; Kuik, M.; Neher, D.; Nguyen, T. Q. Overcoming Geminate Recombination and Enhancing Extraction in Solution-Processed Small Molecule Solar Cells. *Adv. Energy Mater.* **2014**, *4,* 1400230.

190. Bartesaghi, D.; Perez, I. D.; Kniepert, J.; Roland, S.; Turbiez, M.; Neher, D.; Koster, L. J. A. Competition between Recombination and Extraction of Free Charges Determines the Fill Factor of Organic Solar Cells. *Nat. Commun.* **2015**, *6,* 7083.

191. Dibb, G. F. A.; Jamieson, F. C.; Maurano, A.; Nelson, J.; Durrant, J. R. Limits on the Fill Factor in Organic Photovoltaics: Distinguishing Nongeminate and Geminate Recombination Mechanisms. *J. Phys. Chem. Lett.* **2013**, *4,* 803-808.

192. Foertig, A.; Kniepert, J.; Gluecker, M.; Brenner, T.; Dyakonov, V.; Neher, D.; Deibel, C. Nongeminate and Geminate Recombination in PTB7: PCBM Solar Cells. *Adv. Funct. Mater.* **2014**, *24,* 1306-1311.

193. Proctor, C. M.; Kim, C.; Neher, D.; Nguyen, T. Q. Nongeminate Recombination and Charge Transport Limitations in Diketopyrrolopyrrole-Based Solution-Processed Small Molecule Solar Cells. *Adv. Funct. Mater.* **2013**, *23*, 3584-3594.

194. Deibel, C.; Strobel, T.; Dyakonov, V. Origin of the Efficient Polaron-Pair Dissociation in Polymer-Fullerene Blends. *Phys. Rev. Lett.* **2009**, *103*, 036402.

195. Dutta, P.; Xie, Y.; Kumar, M.; Rathi, M.; Ahrenkiel, P.; Galipeau, D.; Qiao, Q. Q.; Bommisetty, V. Connecting Physical Properties of Spin-Casting Solvents with Morphology, Nanoscale Charge Transport, and Device Performance of Poly(3-Hexylthiophene):Phenyl-C-61-Butyric Acid Methyl Ester Bulk Heterojunction Solar Cells. *J. Photonics Energy* **2011**, *1*, 011124.

196. Osasa, T.; Yamamoto, S.; Matsumura, M. Photocurrents Generated under Forward Biases in Organic Thin-Film Solar Cells with Organic Heterojunction Structure. *Jpn. J. Appl. Phys. 1* **2006**, *45*, 3762-3765.

197. Brenner, T. J. K.; Li, Z.; McNeill, C. R. Phase-Dependent Photocurrent Generation in Polymer/Fullerene Bulk Heterojunction Solar Cells. *J. Phys. Chem. C* **2011**, *115*, 22075-22083.

198. Jeong, W. I.; Lee, Y. E.; Shim, H. S.; Kim, T. M.; Kim, S. Y.; Kim, J. J. Photoconductivity of C60 as an Origin of Bias-Dependent Photocurrent in Organic Photovoltaics. *Adv. Funct. Mater.* **2012**, *22*, 3089-3094.

199. Lee, J.; Jadhav, P.; Reusswig, P. D.; Yost, S. R.; Thompson, N. J.; Congreve, D. N.; Hontz, E.; Van Voorhis, T.; Baldo, M. A. Singlet Exciton Fission Photovoltaics. *Acc. Chem. Res.* **2013**, *46*, 1300-1311.

200. Sauve, G.; Dimitrijevic, N. M.; Kamat, P. V. Singlet and Triplet Excited-State Behaviors of C-60 in Nonreactive and Reactive Polymer-Films. *J. Phys. Chem.* **1995**, *99*, 1199-1203.

201. Feng, L.; Rudolf, M.; Trukhina, O.; Slanina, Z.; Uhlik, F.; Lu, X.; Torres, T.; Guldi, D. M.; Akasaka, T. Tuning Intramolecular Electron and Energy Transfer Processes in Novel Conjugates of La-2@C-80 and Electron Accepting Subphthalocyanines. *Chem. Commum.* **2015**, *51,* 330-333.

202. Zango, G.; Zirzlmeier, J.; Claessens, C. G.; Clark, T.; Martinez-Diaz, M. V.; Guldi, D. M.; Torres, T. A Push-Pull Unsymmetrical Subphthalocyanine Dimer. *Chem. Sci.* **2015**, *6,* 5571-5577.

203. Ford, T. A.; Avilov, I.; Beljonne, D.; Greenham, N. C. Enhanced Triplet Exciton Generation in Polyfluorene Blends. *Phys. Rev. B* **2005**, *71,* 125212.

204. Schueppel, R.; Schmidt, K.; Uhrich, C.; Schulze, K.; Wynands, D.; Bredas, J. L.; Brier, E.; Reinold, E.; Bu, H. B.; Baeuerle, P., et al. Optimizing Organic Photovoltaics Using Tailored Heterojunctions: A Photoinduced Absorption Study of Oligothiophenes with Low Band Gaps. *Phys. Rev. B* **2008**, *77*, 085311.

205. Schueppel, R.; Uhrich, C.; Pfeiffer, M.; Leo, K.; Brier, E.; Reinold, E.; Baeuerle, P. Enhanced Photogeneration of Triplet Excitons in an Oligothiophene–Fullerene Blend. *ChemPhysChem* **2007**, *8,* 1497-1503.

206. Etzold, F.; Howard, I. A.; Forler, N.; Melnyk, A.; Andrienko, D.; Hansen, M. R.; Laquai, F. Sub-Ns Triplet State Formation by Non-Geminate Recombination in PSBTBT: PC70BM and PCPDTBT:PC60BM Organic Solar Cells. *Energy Environ. Sci.* **2015**, *8,* 1511-1522.

207. Kang, H.; Uddin, M. A.; Lee, C.; Kim, K.-H.; Nguyen, T. L.; Lee, W.; Li, Y.; Wang, C.; Woo, H. Y.; Kim, B. J. Determining the Role of Polymer Molecular Weight for High-Performance All-Polymer Solar Cells: Its Effect on Polymer Aggregation and Phase Separation. *J. Am. Chem. Soc.* **2015**, *137,* 2359-2365.

208. Chang, J.-F.; Clark, J.; Zhao, N.; Sirringhaus, H.; Breiby, D. W.; Andreasen, J. W.; Nielsen, M. M.; Giles, M.; Heeney, M.; McCulloch, I. Molecular-Weight Dependence of Interchain Polaron

Delocalization and Exciton Bandwidth in High-Mobility Conjugated Polymers. *Phys. Rev. B* **2006**, *74*, 115318.

209. Paterson, A. F.; Treat, N. D.; Zhang, W.; Fei, Z.; Wyatt-Moon, G.; Faber, H.; Vourlias, G.; Patsalas, P. A.; Solomeshch, O.; Tessler, N., et al. Small Molecule/Polymer Blend Organic Transistors with Hole Mobility Exceeding 13 Cm2 V−1 S−1. *Adv. Mater.* **2016**, *28*, 7791-7798.

210. Luhman, W. A.; Holmes, R. J. Investigation of Energy Transfer in Organic Photovoltaic Cells and Impact on Exciton Diffusion Length Measurements. *Adv. Funct. Mater.* **2011**, *21*, 764-771.

211. Cnops, K.; Rand, B. P.; Cheyns, D.; Verreet, B.; Empl, M. A.; Heremans, P. 8.4% Efficient Fullerene-Free Organic Solar Cells Exploiting Long-Range Exciton Energy Transfer. *Nat. Commun.* **2014**, *5*, 3406.

212. Menke, S. M.; Luhman, W. A.; Holmes, R. J. Tailored Exciton Diffusion in Organic Photovoltaic Cells for Enhanced Power Conversion Efficiency. *Nat. Mater.* **2013**, *12*, 152-157.

213. Lee, M. H.; Geva, E.; Dunietz, B. D. Calculation from First-Principles of Golden Rule Rate Constants for Photoinduced Subphthalocyanine/Fullerene Interfacial Charge Transfer and Recombination in Organic Photovoltaic Cells. *J. Phys. Chem. C* **2014**, *118*, 9780-9789.

214. Beaumont, N.; Castrucci, J. S.; Sullivan, P.; Morse, G. E.; Paton, A. S.; Lu, Z. H.; Bender, T. P.; Jones, T. S. Acceptor Properties of Boron Subphthalocyanines in Fullerene Free Photovoltaics. *J. Phys. Chem. C* **2014**, *118*, 14813-14823.

215. Pandey, R.; Gunawan, A. A.; Mkhoyan, K. A.; Holmes, R. J. Efficient Organic Photovoltaic Cells Based on Nanocrystalline Mixtures of Boron Subphthalocyanine Chloride and C60. *Adv. Funct. Mater.* **2012**, *22*, 617-624.

216. Rhoda, H. M.; Kayser, M. P.; Wang, Y. F.; Nazarenko, A. Y.; Belosludov, R. V.; Kiprof, P.; Blank, D. A.; Nemykin, V. N. Tuning up an Electronic Structure of the Subphthalocyanine Derivatives toward Electron-Transfer Process in Noncovalent Complexes with C-60 and C-70 Fullerenes: Experimental and Theoretical Studies. *Inorg. Chem.* **2016**, *55*, 9549-9563.

217. Lee, C. C.; Su, W. C.; Chang, W. C.; Huang, B. Y.; Liu, S. W. The Effect of Charge Transfer State on the Open-Circuit Voltage of Small-Molecular Organic Photovoltaic Devices: A Comparison between the Planar and Bulk Heterojunctions Using Electroluminescence Characterization. *Org. Electron.* **2015**, *16*, 1-8.

218. Lin, C. F.; Nichols, V. M.; Cheng, Y. C.; Bardeen, C. J.; Wei, M. K.; Liu, S. W.; Lee, C. C.; Su, W. C.; Chiu, T. L.; Han, H. C., et al. Chloroboron Subphthalocyanine/C60 Planar Heterojunction Organic Solar Cell with N,N-Dicarbazolyl-3,5-Benzene Blocking Layer. *Sol. Energy Mater. Sol. Cells* **2014**, *122*, 264-270.

219. Williams, R.; Chen, H.-C.; Di Nuzzo, D.; Meskers, S. C. J.; Janssen, R. A. J. Ultrafast Charge and Triplet State Formation in Diketopyrrolo-Pyrrole Low Band Gap Polymer/Fullerene Blends: Influence of Nanoscale Morphology of Organic Photovoltaic Materials on Charge Recombination to the Triplet State. *J. Spectrosc.* **2017**, *2017*, 6867507.

220. Thomas, A. K.; Brown, H. A.; Datko, B. D.; Garcia-Galvez, J. A.; Grey, J. K. Interchain Charge-Transfer States Mediate Triplet Formation in Purified Conjugated Polymer Aggregates. *J. Phys. Chem. C* **2016**, *120*, 23230-23238.

221. Xu, Z.; Hu, B. Photovoltaic Processes of Singlet and Triplet Excited States in Organic Solar Cells. *Adv. Funct. Mater.* **2008**, *18*, 2611-2617.

222. Rudolf, M.; Trukhina, O.; Perles, J.; Feng, L.; Akasaka, T.; Torres, T.; Guldi, D. M. Taming C-60 Fullerene: Tuning Intramolecular Photoinduced Electron Transfer Process with Subphthalocyanines. *Chem. Sci.* **2015**, *6*, 4141-4147.

223. Keiderling, C.; Dimitrov, S.; Durrant, J. R. Exciton and Charge Generation in PC60BM Thin Films. *J. Phys. Chem. C* **2017**, *121*, 14470-14475.

224. Gobeze, H. B.; Bandi, V.; D'Souza, F. Bis(Subphthalocyanine)-Azabodipy Triad for Ultrafast Photochemical Processes. *Phys. Chem. Chem. Phys.* **2014**, *16*, 18720-18728.

225. El-Khouly, M. E.; Fukuzumi, S. Light Harvesting Phthalocyanine/Subphthalocyanine System: Intermolecular Electron-Transfer and Energy-Transfer Reactions Via the Triplet Subphthalocyanine. *J. Porphyrins Phthalocyanines* **2011**, *15*, 111-117.

226. del Rey, B.; Keller, U.; Torres, T.; Rojo, G.; Agullo-Lopez, F.; Nonell, S.; Marti, C.; Brasselet, S.; Ledoux, I.; Zyss, J. Synthesis and Nonlinear Optical, Photophysical, and Electrochemical Properties of Subphthalocyanines. *J. Am. Chem. Soc.* **1998**, *120*, 12808-12817.

227. Gonzalez- Rodriguez, D.; Torres, T.; Guldi, D. M.; Rivera, J.; Herranz, M. A.; Echegoyen, L. Subphthalocyanines: Tuneable Molecular Scaffolds for Intramolecular Electron and Energy Transfer Processes. *J. Am. Chem. Soc.* **2004**, *126*, 6301-6313.

228. Koeppe, R.; Sariciftci, N. S. Photoinduced Charge and Energy Transfer Involving Fullerene Derivatives. *Photochem. Photobiol. Sci.* **2006**, *5*, 1122-1131.

229. Trinh, C.; Kirlikovali, K. O.; Bartynski, A. N.; Tassone, C. J.; Toney, M. F.; Burkhard, G. F.; McGehee, M. D.; Djurovich, P. I.; Thompson, M. E. Efficient Energy Sensitization of C-60 and Application to Organic Photovoltaics. *J. Am. Chem. Soc.* **2013**, *135*, 11920-11928.

230. Orlandi, G.; Negri, F. Electronic States and Transitions in C60 and C70 Fullerenes. *Photochem. Photobiol. Sci.* **2002**, *1*, 289-308.

231. Ćavar, E.; Blüm, M.-C.; Pivetta, M.; Patthey, F.; Chergui, M.; Schneider, W.-D. Fluorescence and Phosphorescence from Individual C60 Molecules Excited by Local Electron Tunneling. *Phys. Rev. Lett.* **2005**, *95*, 196102.

232. Kim, D.; Lee, M.; Suh, Y. D.; Kim, S. K. Observation of Fluorescence Emission from Solutions of C60 and C70 Fullerenes and Measurement of Their Excited-State Lifetimes. *J. Am. Chem. Soc.* **1992**, *114*, 4429-4430.

233. Vandenheuvel, D. J.; Chan, I. Y.; Groenen, E. J. J.; Schmidt, J.; Meijer, G. Phosphorescence of C(60) at 1.2-K. *Chem. Phys. Lett.* **1994**, *231*, 111-118.

234. Prat, F.; Marti, C.; Nonell, S.; Zhang, X.; Foote, C. S.; Moreno, R. G.; Bourdelande, J. L.; Font, J. C60 Fullerene-Based Materials as Singlet Oxygen O2(1[Delta]G) Photosensitizers: A Time-Resolved near-IR Luminescence and Optoacoustic Study. *Phys. Chem. Chem. Phys.* **2001**, *3*, 1638-1643.

235. Lee, G. H.; Han, M. G.; Leem, D.-S.; Lim, S.-J.; Yun, S.; Lee, K.-H.; Bulliard, X.; Park, K.-B.; Yagi, T.; Choi, Y. S., et al. Energy Gap between Photoluminescence and Electroluminescence as Recombination Indicator in Organic Small-Molecule Photodiodes. *J. Phys. Chem. C* **2016**, *120*, 10176-10184.

236. Graham, K. R.; Ndjawa, G. O. N.; Conron, S. M.; Munir, R.; Vandewal, K.; Chen, J. J.; Sweetnam, S.; Thompson, M. E.; Salleo, A.; McGehee, M. D., et al. The Roles of Structural Order and Intermolecular Interactions in Determining Ionization Energies and Charge-Transfer State Energies in Organic Semiconductors. *Adv. Energy Mater.* **2016**, *6*, 1601211.

237. Lin, Y. L.; Fusella, M. A.; Kozlov, O. V.; Lin, X.; Kahn, A.; Pshenichnikov, M. S.; Rand, B. P. Morphological Tuning of the Energetics in Singlet Fission Organic Solar Cells. *Adv. Funct. Mater.* **2016**, *26*, 6489-6494.

238. Gonzalez-Rodriguez, D.; Carbonell, E.; Guldi, D. M.; Torres, T. Modulating Electronic Interactions between Closely Spaced Complementary Pi Surfaces with Different Outcomes: Regio- and Diastereomerically Pure Subphthalocyanine-C-60 Tris Adducts. *Angew. Chem. Int. Ed.* **2009**, *48*, 8032-8036.

239. Jakowetz, A. C.; Bohm, M. L.; Sadhanala, A.; Huettner, S.; Rao, A.; Friend, R. H. Visualizing Excitations at Buried Heterojunctions in Organic Semiconductor Blends. *Nat. Mater.* **2017**, *16*, 551-557.

240. Wang, T.; Kafle, T. R.; Kattel, B.; Chan, W.-L. A Multidimensional View of Charge Transfer Excitons at Organic Donor–Acceptor Interfaces. *J. Am. Chem. Soc.* **2017**, *139*, 4098-4106.

241. Gommans, H.; Schols, S.; Kadashchuk, A.; Heremans, P.; Meskers, S. C. J. Exciton Diffusion Length and Lifetime in Subphthalocyanine Films. *J. Phys. Chem. C* **2009**, *113*, 2974-2979.

242. Ma, Y. Z.; Xiao, K.; Shaw, R. W. Exciton-Exciton Annihilation in Copper-Phthalocyanine Single-Crystal Nanowires. *J. Phys. Chem. C* **2012**, *116*, 21588-21593.

243. Caplins, B. W.; Mullenbach, T. K.; Holmes, R. J.; Blank, D. A. Femtosecond to Nanosecond Excited State Dynamics of Vapor Deposited Copper Phthalocyanine Thin Films. *Phys. Chem. Chem. Phys.* **2016**, *18*, 11454-11459.

244. Caplins, B. W.; Mullenbach, T. K.; Holmes, R. J.; Blank, D. A. Intermolecular Interactions Determine Exciton Lifetimes in Neat Films and Solid State Solutions of Metal-Free Phthalocyanine. *J. Phys. Chem. C* **2015**, *119*, 27340-27347.

245. Montero-Alejo, A. L.; Menendez-Proupin, E.; Fuentes, M. E.; Delgado, A.; Montforts, F. P.; Montero-Cabrera, L. A.; Garcia de la Vega, J. M. Electronic Excitations of C60 Aggregates. *Phys. Chem. Chem. Phys.* **2012**, *14*, 13058-13066.

246. Clements, A. F.; Haley, J. E.; Urbas, A. M.; Kost, A.; Rauh, R. D.; Bertone, J. F.; Wang, F.; Wiers, B. M.; Gao, D.; Stefanik, T. S., et al. Photophysical Properties of C60 Colloids Suspended in Water with Triton X-100 Surfactant: Excited-State Properties with Femtosecond Resolution. *J. Phys. Chem. A* **2009**, *113*, 6437-6445.

247. Snellenburg, J. J.; Laptenok, S. P.; Seger, R.; Mullen, K. M.; van Stokkum, I. H. M. Glotaran: A Java-Based Graphical User Interface for the R Package Timp. *J. Stat. Softw.* **2012**, *49*, 1-22.

248. Park, J.; Ramirez, J. J.; Clikeman, T. T.; Larson, B. W.; Boltalina, O. V.; Strauss, S. H.; Rumbles, G. Variation of Excited-State Dynamics in Trifluoromethyl Functionalized C-60 Fullerenes. *Phys. Chem. Chem. Phys.* **2016**, *18*, 22937-22945.

249. Winterfeld, K. A.; Lavarda, G.; Guilleme, J.; Sekita, M.; Guldi, D. M.; Torres, T.; Bottari, G. Subphthalocyanines Axially Substituted with a Tetracyanobuta-1,3-Diene–Aniline Moiety: Synthesis, Structure, and Physicochemical Properties. *J. Am. Chem. Soc.* **2017**, *139*, 5520-5529.

250. Nakanishi, I.; Ohkubo, K.; Fujita, S.; Fukuzumi, S.; Konishi, T.; Fujitsuka, M.; Ito, O.; Miyata, N. Direct Detection of Superoxide Anion Generated in C60-Photosensitized Oxidation of NADH and an Analogue by Molecular Oxygen. *J. Chem. Soc., Perkin Trans. 2* **2002**, 1829-1833.

251. D'Souza, F.; Ito, O. Photosensitized Electron Transfer Processes of Nanocarbons Applicable to Solar Cells. *Chem. Soc. Rev.* **2012**, *41*, 86-96.

252. Gregg, B. A. Entropy of Charge Separation in Organic Photovoltaic Cells: The Benefit of Higher Dimensionality. *J. Phys. Chem. Lett.* **2011**, *2*, 3013-3015.

253. Oosterhout, S. D.; Ferguson, A. J.; Larson, B. W.; Olson, D. C.; Kopidakis, N. Modeling the Free Carrier Recombination Kinetics in PTB7:PCBM Organic Photovoltaics. *J. Phys. Chem. C* **2016**, *120*, 24597-24604.

254. Gregg, B. A. Charged Defects in Soft Semiconductors and Their Influence on Organic Photovoltaics. *Soft Matter* **2009**, *5*, 2985-2989.

255. Savoie, B. M.; Rao, A.; Bakulin, A. A.; Gelinas, S.; Movaghar, B.; Friend, R. H.; Marks, T. J.; Ratner, M. A. Unequal Partnership: Asymmetric Roles of Polymeric Donor and Fullerene Acceptor in Generating Free Charge. *J. Am. Chem. Soc.* **2014**, *136*, 2876-2884.

256. Menke, S. M.; Mullenbach, T. K.; Holmes, R. J. Directing Energy Transport in Organic Photovoltaic Cells Using Interfacial Exciton Gates. *ACS Nano* **2015**, *9*, 4543-4552.

257. Collins, B. A.; Li, Z.; Tumbleston, J. R.; Gann, E.; McNeill, C. R.; Ade, H. Organic Solar Cells: Absolute Measurement of Domain Composition and Nanoscale Size Distribution Explains Performance in PTB7:PC71BM Solar Cells (Adv. Energy Mater. 1/2013). *Adv. Energy Mater.* **2013**, *3*, 1-1.

258. Wurfel, P. The Chemical Potential of Radiation. *Journal of Physics C: Solid State Physics* **1982**, *15*, 3967.

259. Dowgiallo, A.-M.; Mistry, K. S.; Johnson, J. C.; Reid, O. G.; Blackburn, J. L. Probing Exciton Diffusion and Dissociation in Single-Walled Carbon Nanotube–C60 Heterojunctions. *J. Phys. Chem. Lett.* **2016**, *7*, 1794-1799.